Modeling of electrical manipulation in silicon spin qubits

Léo Bourdet

Communauté
UNIVERSITÉ Grenoble Alpes

THÈSE

Pour obtenir le grade de

DOCTEUR DE LA COMMUNAUTE UNIVERSITE GRENOBLE ALPES

Spécialité : Physique théorique

Arrêté ministériel : 25 mai 2016

Présentée par

Léo Bourdet

Thèse dirigée par **Yann-Michel Niquet**

préparée au sein du **Laboratoire de Simulation Atomistique, service Modélisation et Exploration des Matériaux, CEA/INAC**

dans **l'École Doctorale de Physique de Grenoble**

Modeling of electrical manipulation in silicon spin qubits

Modélisation de la manipulation électrique du spin dans les qubits silicium

Thèse soutenue publiquement le **22 novembre 2018**, devant le jury composé de :

Madame Maria-José CALDERÓN
Tenured scientist, Instituto de Ciencia de Materiales de Madrid (ICMM), Rapporteure
Monsieur Christophe DELERUE
Directeur de Recherche, CNRS – IEMN, Rapporteur
Monsieur Patrice BERTET
Chargé de Recherche, CEA, Examinateur
Monsieur Hervé COURTOIS
Professeur des Universités, Université Grenoble Alpes et CNRS/Institut Néel, Président

Remerciements

Les travaux présentés dans ce manuscrit ont été conduits dans le cadre de ma thèse de doctorat, menée au sein du CEA Grenoble dans le laboratoire de simulation atomistique (L_Sim). Plus généralement elle s'inscrit dans un effort commun à Grenoble autour des technologies quantiques, tirant parti des technologies de la microélectronique développés au CEA Leti. J'ai donc eu la chance d'être inclus dans une large équipe, qui a largement contribué à la réussite de cette thèse et que je souhaiterais remercier ici.

Avant cela je souhaite remercier chaleureusement l'ensemble des membres du jury pour avoir accepté d'évaluer ce travail. Merci à eux pour leur bienveillance et leurs questions et remarques judicieuses lors de la soutenance. Je remercie en particulier les rapporteurs, Christophe Delerue et María Calderón, pour leur travail et commentaires sur le manuscrit.

Je remercie mon directeur de thèse Yann-Michel Niquet, pour son encadrement quotidien, sa sympathie, sa pédagogie, et sa connaissance incroyable de la physique et des simulations numériques. J'ai énormément appris à son contact, et il était toujours disponible et enthousiaste pour des discussions sur nos travaux, ce qui a été pour moi une grande source de motivation. Je remercie également les gens de « l'équipe TB_Sim », avec qui j'ai partagé le quotidien (et notre petit bureau !) : François, Zaiping, Daniel, Jing, et Benjamin. J'ai apprécié travailler avec vous dans une très bonne ambiance, et je vous remercie pour l'aide que vous avez pu m'apporter.

Si cette thèse a été si enrichissante pour moi, c'est avant tout grâce aux nombreuses interactions que j'ai pu avoir avec les scientifiques du groupe 'Quantum Silicon' de Grenoble, et j'ai pu apprécier leur bienveillance, leur curiosité et leur dévouement. Je pense d'une part aux gens du Leti : Maud, Louis et Benoit. Merci d'avoir toujours été attentifs à nos idées pas toujours réalistes, et d'avoir donné de l'importance à la simulation. J'ai d'ailleurs trouvé que nos échanges designs-simus fonctionnait très bien. Merci également de m'avoir initié au monde étrange des brevets !

Bien entendu suit la grande équipe du LaTEQs : Marc, Xavier, Silvano, Heorhii, Andrea, Romain, Alessandro, Rami et Agostino! C'était très agréable de travailler avec vous, et de ressentir l'excitation de voir des chouettes expériences qui marchent (sans le

bruit de la pompe du cryostat, la bonding machine, les longues heures de manip... je ne m'en sors pas mal). Les discussions sur les mesures, les dispos, et bien sûr les mystères de l'edsr et de la g-potato sont pour moi de très bons souvenirs. Finalement je remercie les théoriciens de l'INAC avec qui j'ai travaillé (trop peu, mais trois ans ça peut être court !), Mireille et Vincent.

D'autre part j'ai beaucoup apprécié pendant cette thèse l'environnement offert par les laboratoires du CEA dans lesquels j'ai évolué, et qui m'ont fait me sentir bien pendant ces trois années. Pour cela je remercie les membres du L_Sim, en particulier pour la période de mon stage de master au cours de laquelle j'étais vraiment dans les locaux du laboratoire. Je remercie en particulier Thierry pour ses conseils et son suivi.

Je remercie bien sûr tous les membres du LSM, le laboratoire qui m'a accueilli physiquement pendant toute la durée de la thèse. Merci aux permanents Jean-Charles, Thierry, Pascal, Pierrette, Sébastien, Joris, Luca, Philippe, Jean-Philippe, Benoit, Marianne, Hélène (merci pour la relecture du manuscrit !), Olga, Anne-Sophie et Marina, et aux thésards et postdocs : Gabriel, Anthony, Kiki, François, Neil, Alberto, Eamon, Corentin, Saurabh. J'ai passé de très bons moments avec vous, et les pauses cafés, les repas, les discussions, en bref la super ambiance du labo vont définitivement me manquer ! Enfin je remercie la fine bande de Grenoble qui m'a aidé à me sentir bien pendant ces trois années: Thomas, Charly, Léo, Joris, Fred, Lise, Quentin, Laure, Antoine, Pauline B, Pauline T, Claudia, Julien, Kasma, Antoine, Nicolas, Jessy, Marine, Kevin, Hélène, Fabien, Etienne, Charlotte, Yann, Thibault, Damien, Marie, Evan, Bérengère, Laura, Franck, Fabrice, Marc, Carine, et le meilleur pour la fin Guillaume (j'espère que ça te fait plaisir). Big up à Damir et Loïc. Merci et bonne chance à Hocine et Zélie. Merci aux Moules à Facettes, je suis sûr que Rolling Stone annoncera notre reformation... Finalement, merci à ma famille pour leur soutien, et à Mathilde, pour tout.

*One shouldn't work on semiconductors, that is a filthy mess;
who knows whether any semiconductors exist.*
Wolfgang Pauli, Letter to Peierls

Contents

Contents

Contents

Chapter 1

Introduction

Nous introduisons dans ce chapitre le contexte dans lequel s'inscrit cette thèse, l'ordinateur quantique. L'idée a été proposée à l'origine par Richard Feynman : puisqu'il semble impossible à un ordinateur classique de simuler un système quantique (notamment d'un certain nombre de particules quantiques interagissantes), Feynman suggéra d'utiliser les propriétés de la physique quantique pour créer un système capable de simuler un autre système quantique. Les propriétés en question sont le principe de superposition et l'intrication. Cette proposition de simulateur quantique est toujours un sujet de recherche actif, mais une autre classe d'ordinateur quantique a également fait son apparition à la fin des années 90 avec les travaux de Peter Shor. Ce dernier a montré qu'il était possible de tirer parti du parallélisme quantique pour réaliser la factorisation de grands entiers plus rapidement qu'un ordinateur classique. C'est dans ce cadre que ce situe ce travail de thèse, dont le sujet est plus particulièrement l'élément de base de l'ordinateur quantique, le quantum bit (ou qubit). Après avoir présenté rapidement les conditions pour réaliser un ordinateur quantique, nous décrirons le cas particulier du qubit de spin. En effet, un des travaux fondateurs publié par Loss et DiVincenzo [1] montre qu'il est possible de réaliser un ordinateur quantique à partir de spin dans des boîtes quantiques dans des matériaux semiconducteurs. Nous présentons rapidement les caractéristiques générales de ces qubits de spin, notamment leur manipulation par un champ magnétique oscillant, la décohérence de spin, la lecture du qubit, ainsi que les interactions entre qubits.

1.1 A new computing paradigm

1.1.1 Context

Indisputably one of the greatest technological and theoretical achievement of the twentieth century was the invention of computers, with in particular the work of Alan Turing. The practical implementation of powerful computers was linked to another invention of great importance, the transistor, discovered in 1947 by John Bardeen, William Shockley and Walter Brattain. An outstanding property of transistors is that reducing their length typically allows for an increase of drive current and switching speed, and for an increase of the number of transistors (and functions) per chip. Then, from 1970 to 2000, the performance of computers has been growing extremely fast: the main technological requirement was only to improve the lithography techniques. This lead to the famous Moore's law: "the number of transistors on a chip double every two years", and a steady economic growth of 10% per year for the microelectronics industry. When the transistor length reached $\simeq 50$ nm, short channels effects and issues related to thermal dissipation started to limit the performance, therefore the processor clock frequencies stagnated to $\simeq 4$ GHz since 2005. The reduction of the size of the transistors is not anymore the principal driving force of performance enhancement. As the transistors are reaching nanometric size, quantum effects such as tunneling [2] or even Coulomb blockade [3, 4] start to interfere, and to limit the size reduction. Each new generation of transistors requires more time and more investment. Ultimately it will be impossible to reduce the size below a few nanometers, because of direct source-drain tunneling, and even extremely difficult to reach the 10 nm limit [5, 6].

With the end of Moore's law the top microelectronics companies are looking for new markets. One way for this is to create new applications, as it is done today with the Internet of Things. Another way is to investigate new computation paradigms, such as neuromorphic computing, reversible computing, or quantum computing. The latter emerged from the idea that we could use the peculiar properties of quantum systems in order to make a new kind of computer. What are these properties? Let us start by defining a quantum bit (or qubit) by analogy with a classical bit. A classical bit can take two values, 0 and 1. A quantum bit is based on two quantum states $|0\rangle$ and $|1\rangle$. According to quantum mechanics, the state $|\Psi\rangle$ of the qubit is as a superposition of these two states:

$$|\Psi\rangle = \alpha|0\rangle + \beta|1\rangle \tag{1.1}$$

with α, β two complex numbers such that $|\alpha|^2 + |\beta|^2 = 1$. We can thus rewrite Eq. 1.1 as

$$|\Psi\rangle = \cos\frac{\theta}{2}|0\rangle + e^{i\phi}\sin\frac{\theta}{2}|1\rangle \tag{1.2}$$
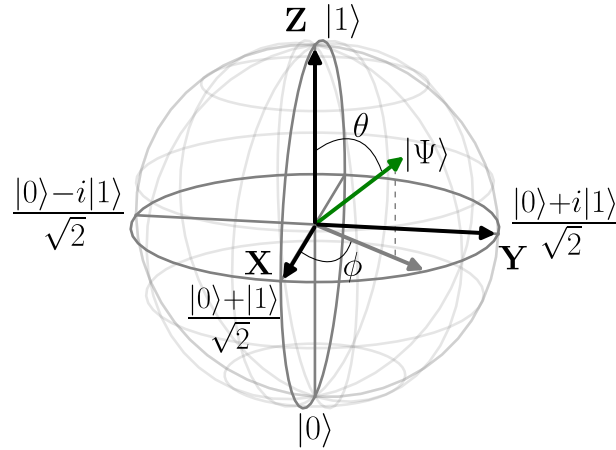
Figure 1.1: Bloch sphere representation of a two-level quantum state.

The information carried by the quantum bit can thus be mapped onto a continuous ensemble of values, and thus contain much more information than a classical bit. The qubit state can be represented as a function of the phases θ, ϕ in the so-called Bloch sphere, shown Fig. 1.1. If we now have two qubits, their coherent state is a superposition of the states $\{|00\rangle, |10\rangle, |01\rangle, |11\rangle\}$:

$$|\Psi\rangle = \alpha_1|00\rangle + \alpha_2|10\rangle + \alpha_3|01\rangle + \alpha_4|11\rangle \tag{1.3}$$

so is described by 2^2 complex amplitudes $(\alpha_{1,2,3,4})$. More generally, a system with n qubits can be represented by 2^n complex amplitudes. Finally the last property that will be harnessed in a quantum computer is the quantum parallelism. In a classical computer, applying a function f to two different bits x and y (that is computing $f(x)$ and $f(y)$) must be done either sequentially or in two different computers simultaneously. Classical parallelism then consists in connecting several computers. In a quantum computer, if we start from $|x\rangle$, a register of n qubits in superposition, and apply a function f (which is a series of unitary operations), we end up with an output register $f(|x\rangle)$, which is a superposition of all outputs. We have thus applied f only once and can obtain 2^n outputs: this is quantum parallelism. Of course, the output register $f(|x\rangle)$ then needs to be measured, which yields only one value. All the difficulty of quantum algorithms is to build a series of operations that grant a more important probability to be measured to the desired result.

All of this can make a quantum computer very different from a classical one. Our computers are Turing Machines: ultimately, if one of them is able to solve a problem of a given complexity, then any other computer potentially can. Another way to say it is that you can potentially emulate any computer with another (provided you have enough memory). It seems that a quantum computer does not belong to the same category: it is practically impossible for a classical computer to simulate a system of many entangled

particles. For instance, a system with 50 interacting spin-1/2 particles, requires $2^{50} \simeq 10^{15}$ numbers in a classical memory, that is a few hundreds petabytes. Calculating its time evolution requires the exponentiation of a $2^{50} \times 2^{50}$ matrix. This is already close to the limits of classical capabilities, and the complexity is exponentially growing with the number of particles in the system. Feynman in his famous lecture of 1959 "There's plenty of room at the bottom" [7] conjectured that it is possible to circumvent this exponential explosion by using a tunable, measurable quantum system to simulate another one. In his own terms:

> "Nature isn't classical, dammit, and if you want to make a simulation of Nature you better make it quantum mechanical, and by golly it's a wonderful problem, because it doesn't look so easy."

Lloyd proved this conjecture in 1996 [8]: quantum computers can be programmed to simulate any local quantum systems. This class of quantum computers are nowadays called *quantum simulators*.

Another class of quantum computers also emerged from the idea to exploit the quantum parallelism. Indeed, in the 1980's David Deutsch examined the possibility to achieve significant speedups on some problems using quantum algorithms [9,10]. Such a quantum computer consists in a collection of qubits and logical operations, called gates (unitary transformations). In a quantum computer, single-qubit and two-qubits operations are needed. Single-qubit gates are any possible rotation on the Bloch sphere. At minimum, one kind of two-qubits gate is needed, the CNOT (controlled-not), which acts on the state of one qubit depending on the state of the other one. With this system, Shor showed in 1999 an algorithm for the prime factorization of large integers [11]. This algorithm provides an exponential speed-up compared to the best known classical algorithm. This may have important implications in everyday life since our safest encryption method (RSA algorithm) is based on the fact that factoring a big number into two prime numbers is a problem impossible to solve by any classical computer. Another example is Grover's algorithm, which consists in searching for an element in a list of N elements. The quantum speed-up is more modest, in average $\sqrt{N}$ steps are needed on a quantum computer against N on a classical one, and that is the best acceleration that can be achieved.

At this point, an important fact needs to be stressed out. The Grover algorithm illustrates that a quantum computer cannot, as often wrongly stated, look at many possible solutions to a problem in parallel (doing so would be a technological and philosophical revolution!). To be more precise, the general agreement is that a quantum computer cannot rapidly solve a particularly difficult set of problems called NP-complete problems [12]. These problems (of which a famous example is the traveling salesman problem), are believed to not have a deterministic solution in polynomial time. No, up to today's knowledge, a quantum computer can only be used on a specific class of problems where they

could provide a substantial acceleration of the resolution over a classical computer. To our understanding, some problems are classically hard, and some are quantumly hard.

1.1.2 Is a quantum computer practically feasible?

Quantum systems interacting with the external environment are prone to decoherence. That means that we are not able to put the system in a specific superposition for an infinite time. The coupling with the environment is noisy and unknown, so unanticipated errors will occur. Moreover, the no-cloning theorem states that in quantum physics, an unknown state cannot be copied. Therefore it is not possible to detect the errors like in classical computing, for instance by performing parity check on a byte with its copy.

In quantum computers decoherence is a major problem that limits the number of reliable operations, so it needs to be circumvented. For that purpose, error-correction codes have been developed. In these schemes, many physical qubits encode the information of one logical qubit. A quantum error correction code is applied to the physical qubits. The threshold theorem [13] then states that providing that the error per physical qubit per gate operation is below some threshold (which depends on the specifications of the code and qubits), increasing the number of physical qubits allow to preserve the information on the logical qubits. More precisely, quantum error correction theory predicts that the precision of the logical qubit improves exponentially with the number of physical qubits. If the assumptions of the theorem hold, quantum computing is "just" transformed into an engineering problem: produce enough qubits with good characteristics. In 2000, David DiVincenzo summarized the requirements to physically implement a quantum computer in a series of 5 criteria [14]: 1) A scalable physical system with well characterized qubits 2) The ability to initialize the state of qubits in a well-known state 3) Decoherence times much longer than the gate operation time 4) A "universal" set of quantum gates[1] 5) The ability to measure individual qubits. In this thesis, we focus on criteria 1) and 3) in a spin qubit in a silicon quantum dot.

With today's technologies and current algorithms, this engineering problem is an incredible challenge. The number of physical qubits per logical qubit is at least of 10000 in the most optimistic scenarios with realistic qubits characteristics [15,16]. Several big companies are engaged in this race for quantum computing: IBM, Google, Intel, Microsoft. They have already fabricated some quantum computers, however with yet insufficient performances. A recent demonstration is the 20-qubits quantum computer from IBM, available on the cloud, and announcements have been made of 50-qubits and 72-qubits quantum computers, respectively by IBM and Google.

Whether quantum computing will be possible or not is debated. Some criticisms have been expressed on the assumptions behind the threshold theorem [17, 18]. First,

---

[1]An arbitrary set of gates to which any possible unitary operation on the quantum computer can be reduced.
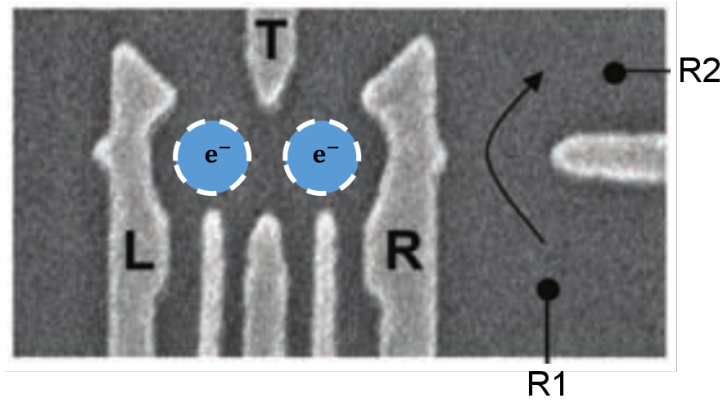
Figure 1.2: SEM picture of a double quantum dot device in a GaAs/AlGaAs heterostructure. Electrostatic gates (light gray) on top of a 2D electron gas define two quantum dots. The gates L and R control the number of electrons in each dot, and gate T controls the tunnel coupling between them. The conductance is measured between R1 and R2 and allow to measure the charge in the right dot. Adapted from Ref. [19].

the quantum computer is an analog computer, so each of the qubit states are known with finite precision, whereas the threshold theorem assumes infinite (same goes for the readout fidelities). Some types of errors are also not taken into account by error-correction codes [18].

Leaving aside these rather complex considerations on quantum computing, this thesis is dedicated to the most elementary building block, the physical quantum bit. From what we have seen, these qubits need to be well-controlled, scalable, and not strongly subjected to errors. In this thesis we focus on a qubit made of a spin inside a quantum dot, and more particularly on the electrical spin manipulation. Therefore the next part will elaborate more on the characteristics of such qubits and the historical achievements.

1.2   The spin quantum bit

We have introduced quantum computers and what they are capable of. As we have seen a quantum computer is composed of quantum bits which are two-levels system, thus, any quantum two-levels systems can in principle be used for quantum information storage and manipulation. In a seminal paper [1], Loss and DiVincenzo have shown that it was possible to realize quantum computation with spins inside semiconductor quantum dots.

The spin qubits in semiconductor quantum dots were first studied in III-V heterostructures, notably in GaAs which is a good material for confining electrons thanks to its low effective mass. In these devices the bandgap mismatch between two III-V materials is responsible for a quantum well at the heterointerface, forming a 2D electron gas. Then, it is possible to use metallic gates deposited on top to deplete the electron gas, thus forming quantum dots. An example of a double quantum dot device is shown in Fig. 1.2. These two dots are tunnel-coupled to each other and to the neighboring reservoirs. These

couplings can be tuned to reach the Coulomb blockade regime, with a fixed number of electrons in each dot.

Once a single electron (or hole) is isolated in the Coulomb blockade regime, the states of a spin qubit are defined in presence of a magnetic field B. Indeed, at $B = 0$ each orbital state is spin-degenerate (this is called Kramers degeneracy), hence does not make a two-level system. A finite B splits a Kramers pair into the qubits states spin up $|1\rangle = |\uparrow\rangle$ and spin down $|0\rangle = |\downarrow\rangle$, separated by the Zeeman energy $E_z = g\mu_B B$, where g is the Landé factor. We have now a system that can be represented in the Bloch sphere of Fig. 1.1. Importantly, the spin state precesses around the **Z** axis of the Bloch sphere at the Larmor frequency $f_L = g\mu_B B/h$. Therefore, all the qubit operations implicitly takes place in the Bloch sphere rotating around **Z** at frequency f_L ("rotating Bloch sphere").

Now that the qubit states are properly defined, let us review the essential properties of spin manipulation, decoherence, readout, and two-qubit interactions in these systems.

1.2.1 Spin manipulation

The spin is a magnetic dipole so the most natural way to manipulate it is to couple it to a magnetic field. The method to do this is called electron spin resonance (ESR). It consists in applying a static magnetic field B_0 along **z** to separate the spin states, and an oscillating magnetic field $B(t) = B_{ac}\cos(\omega t)$ perpendicular to **z**, let's say along **x**. The static magnetic field makes the spin precess around the **Z** axis of the Bloch sphere at the Larmor frequency ω_L. If $\omega = \omega_L$ the oscillating magnetic field interacting with the spin can be represented in the $\{|\downarrow\rangle, |\uparrow\rangle\}$ by the operator:

$$H_{\text{int}} = \begin{pmatrix} 0 & \omega_R \cos(\omega_L t) \\ \omega_R \cos(\omega_L t) & 0 \end{pmatrix} = \frac{\omega_R}{2} \begin{pmatrix} 0 & e^{i\omega_L t} + e^{-i\omega_L t} \\ e^{i\omega_L t} + e^{-i\omega_L t} & 0 \end{pmatrix} \quad (1.4)$$

with $\omega_R = \frac{g\mu_B B_{ac}}{2\hbar}$. Working now in the rotating Bloch sphere, so $H_{\text{int}} \to e^{i\omega_L/2\sigma_z} H_{\text{int}} e^{-i\omega_L/2\sigma_z}$, we have:

$$H_{\text{int}} = \omega_R \begin{pmatrix} 0 & e^{2i\omega_L t} + 1 \\ e^{-2i\omega_L t} + 1 & 0 \end{pmatrix} \quad (1.5)$$

Assuming $\omega_R \ll \omega_L$, we neglect the fast terms $e^{\pm i\omega_L t}$ (rotating wave approximation) and we have simply $H_{\text{int}} = \omega_R \sigma_x$. Then we solve the time-dependent Schrödinger equation, $\frac{\partial |\Psi\rangle}{\partial t} = \frac{-i}{\hbar} \omega_R \sigma_x |\Psi\rangle$, which yields:

$$|\Psi\rangle(t) = e^{-i\omega_R \sigma_x t} |\Psi\rangle(0) \quad (1.6)$$
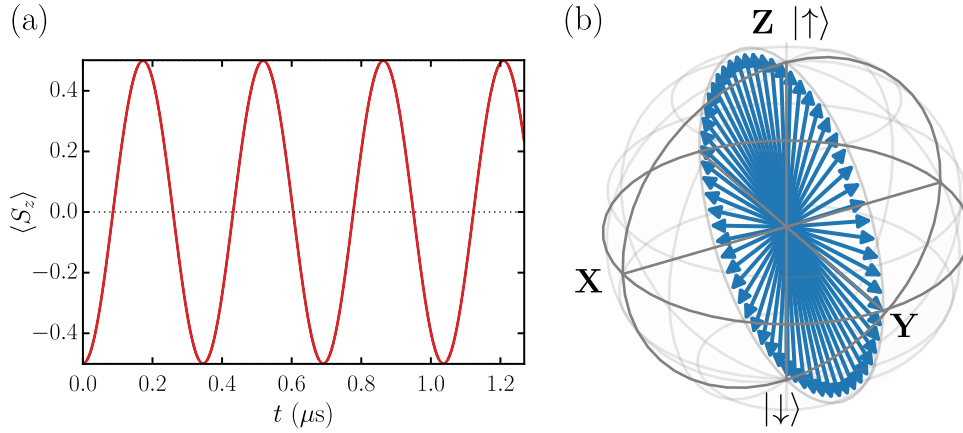
Figure 1.3: (a) Expected value of the spin along z, exhibiting Rabi oscillations. (b) Representation of the state evolution (in blue) in the rotating Bloch sphere.

Therefore, a resonant transverse magnetic field drives rotations of the spin around the **X** axis of the rotating Bloch sphere, called Rabi oscillations, shown in Fig. 1.3. The frequency of these oscillations, called the Rabi frequency, is $f_R = \omega_R/2\pi$. Rabi oscillations in semiconductor quantum dots were first demonstrated experimentally by Koppens *et al* [20]. Importantly, one can also drive rotations around another axis of the Bloch sphere by changing the phase φ of $B_1(t) = B_{ac}\cos(\omega t + \varphi)$: for $\varphi = \pi/2$, **Y** is the rotation axis. This gives full control of the spin state on the Bloch sphere.

In the prospect of a scalable spin qubit architecture, the use of magnetic fields to control the spin raises several issues. It is indeed technically almost impossible to localize a magnetic field in order to affect only one qubit and not its neighbors. Moreover, as f_R depends linearly only on B_{ac} (which cannot be very large), it is typically limited to a few MHz.

Another possibility to manipulate the spin, very similar to ESR, is to use an oscillating electric field, which in comparison can be generated much more easily by exciting a local gate electrode. This effect, called electric-dipole spin resonance (EDSR), requires a mechanism that couples the spin of the electron to its motion induced by the electric field. Several mechanisms were investigated. One of them, theoretically discussed by Rashba and Efros [21], is to use the intrinsic spin-orbit interaction (SO). The spin-orbit coupling can be described semi-classically in the following way: due to a relativistic effect, an electron moving in an electric field (created by the nucleus of the crystal) experiences in its reference frame an effective magnetic field which couples to its spin. The SO-driven EDSR was observed by Nowack *et al* in GaAs [22], and the first spin-orbit qubit was made by Nadj-Perge *et al* [23]. In another work, Laird *et al* used the hyperfine interaction in GaAs to drive spin rotations with electric fields [24]: they took advantage of the inhomogeneity of the Overhauser field generated by the nuclear spins. The moving electron feels an effective, position-dependent magnetic field, thus the spin and orbital degrees of

freedom are hybridized. On a similar idea, Pioro-Ladrière *et al* [25] engineered a slanting magnetic field with Co micromagnets, which also acts effectively as a spin-orbit coupler. All these mechanisms behave similarly to ESR: Eq. 1.6 is still valid for EDSR, however ω_R depends this time on the amplitude of the oscillating electric field and on the strength of the spin-orbit coupling mechanism.

The use of EDSR opens up interesting perspectives for the fast and local manipulation of spins. However, as EDSR calls for a mechanism coupling the spin and orbital motion, this comes at a price: the spin is now sensitive to electrical perturbations in the environment which will induce decoherence.

1.2.2 Spin decoherence

As for any other quantum system, it is not possible to isolate completely the spins from their environment. They interact in a random way, so that the quantum information is lost: this is called decoherence. It is convenient to separate decoherence in two processes: relaxation and dephasing. Relaxation corresponds to the dissipative process $|\uparrow\rangle \to |\downarrow\rangle$, that is the classical loss of information of the spin, and associated with a characteristic time T_1. On the Bloch sphere, it corresponds to a path of the state along a meridian, *i.e.* a change of θ. On the contrary, dephasing corresponds to a change in the phase ϕ, a path along a parallel of the Bloch sphere. It is associated with a characteristic time T_2 (whose value may depend strongly on the measurement procedure). These two processes are represented on Fig. 1.4.

An expected advantage of a spin qubit is that it should be coupled only to its magnetic environment. The main source of magnetic noise is the random nuclear spins, which act on the electron spin via the hyperfine interaction. In III-V materials, this is considered as the main source of decoherence [26]. Another source could be the presence of magnetic impurities nearby the device. However, as we have discussed, spin-orbit effects make the spin state sensitive to noises which affects the real space motion of the electron, such as phonons or electrical noises. In semiconductor quantum dots, sources of electrical noise include notably the Johnson-Nyquist noise (thermal noise generating gate-voltage fluctuations on the gates), or the capture-release of charges by traps nearby the device, which generate random telegraph noise or 1/f noise.

The decoherence of a spin qubit needs to be carefully evaluated, taking into account all the possible sources of noise. To make an efficient quantum bit the decoherence times T_1 and T_2 need to be increased as much as possible while keeping the ability to perform fast rotations. Therefore the relevant figure of merit for single-qubits operations is the number of operations that can be performed before decoherence, that is $Q = f_R \times T_2$ (assuming $T_2 \ll T_1$). This is related to the third DiVincenzo criteria, and is one of the main issues of the chapter 5 of this thesis.
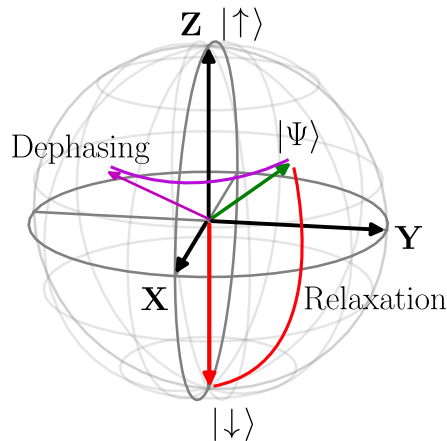
Figure 1.4: Bloch sphere of the spin qubit with sketch of a relaxation process (in red), and of a dephasing process (in violet).

1.2.3 Spin readout

Since it is very difficult to measure the magnetic moment of an individual spin, readout schemes rely on indirect measurement via spin-to-charge conversion: the spin-dependent movement of a charge is detected.

One method is to couple the qubit to a charge sensor, such as a single electron transistor (SET). Then if the electrochemical potential of the SET lies in between the spin down and spin up states of the qubit, only the spin up state can tunnel out and be detected, hence the spin-to-charge conversion [27–29]. A different possibility is to use the Pauli principle to implement Pauli spin blockade, as first demonstrated by Ono *et al* [30]. In the simplest picture, with two quantum dots in series containing each one electron, the transition of the spin of the left dot to the right dot is forbidden by Pauli exclusion principle if the two spins are parallel. Then the presence or absence of transition between dots is measured by a charge-sensing technique.

1.2.4 Two-qubit gates

In order to achieve a universal set of operations, two-qubit gates are needed in addition to the single-qubit gates.

The most used way of achieving this is to rely on the exchange interaction J between two spins, given by the Heisenberg interaction $H_{12} = J\mathbf{S_1}\cdot\mathbf{S_2}$. In the case of two electrons inside two quantum dots, $J \simeq 4t^2/U$, where t is the tunnel coupling between the dots and U the charging energy of the dots. Therefore, as first suggested by Loss and DiVincenzo [1], one could use a gate voltage to tune the shape of the barriers between the dots, and thus the tunnel coupling. That way it is possible to switch between a situation with a high barrier potential, so uncoupled spins ($J \simeq 0$), and a situation with a low barrier potential so that the spins are coupled by the exchange interaction. This is illustrated in
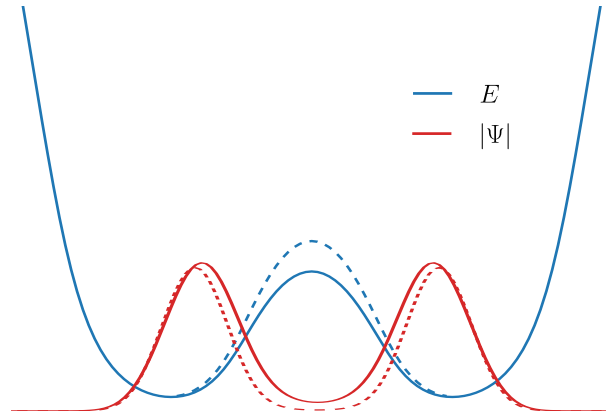
Figure 1.5: Sketch of two qubits coupled by exchange interaction. The height of the barrier between dots tunes t and thus J. Dotted lines correspond to the high-barrier regime ($t \simeq 0$) and full lines to the the low-barrier regime (finite t).

Fig. 1.5. Similarly, it also possible to use the detuning between dots to control J, as it was done in the first demonstration of controlled exchange by Petta *et al* [19], in the context of singlet-triplet qubits (qubit in which the information is encoded into the singlet and triplet states of two entangled spins). The first CNOT-gate in semiconductor spin qubits using exchange interaction has been made by Brunner *et al* [31].

Another possibility for two-qubit gates has emerged recently: the use of circuit quantum electrodynamics. It consists in coupling the spin state of an electron in a quantum dot to microwave photons in a superconducting cavity. First experimental evidences have been given in a InAs quantum dot [32], as well as in silicon [33–35], however two-qubits still need to be demonstrated. The advantage of this approach is that it enables in principle long distance coupling between qubits.

1.3 This thesis

In this thesis we focus on quantum computing with spin qubits in silicon. In particular, we concentrate on the single qubit level, and we study numerically and theoretically the electrical spin manipulation.

In chapter 2 we discuss the peculiarities of silicon and what makes it a material of choice for quantum computation. We also present the paths taken by the main groups towards quantum computing in silicon, as well as the strategy adopted by the teams at CEA Grenoble.

In chapter 3 we present the numerical methods we use throughout the thesis. They allow to model the potential, electronic structure, and many-body interactions in silicon qubits, and to perform time-dependent numerical experiments.

In chapter 4, we start by presenting an interesting experimental results obtained at CEA, the EDSR of electron spins in a double quantum dot. We develop an analytical

model validated by tight-binding simulations. We discuss the origin of the unexpectedly strong spin-orbit interaction.

In chapter 5, we propose a scheme for an electrically-driven electron spin qubit, based on the coupling with the valley states. We study with simulations the characteristics of this qubit, give hints for optimization, and assess its feasibility. We compare tight-binding simulations to a recent experimental result that established a first step for the realization of this scheme.

In chapter 6, we study a hole spin qubit. In particular we analyze the experimental measurements of the dependence of the Rabi frequency with the magnetic field orientation. In order to interpret it, we develop a formalism allowing to separate the Rabi frequency into two relevant contributions. Finally we propose an interpretation of the results with $\mathbf{k.p}$ calculations.

Chapter 2

Silicon

Le silicium est devenu ces dernières années un matériau de choix pour l'implémentation des qubits de spin. Les qubits silicium sont l'un des compétiteurs majeurs pour la course à l'ordinateur quantique, aux côtés des jonctions supraconductrices et des atomes froids. Il y a plusieurs raisons à cela. Tout d'abord, le silicium est un matériau bien connu et massivement utilisé dans l'industrie de la microélectronique, il bénéficie donc d'un savoir-faire et d'une qualité de fabrication exceptionnels, qui pourraient faciliter l'intégration à grande échelle des qubits. D'autre part le silicium possède certaines propriétés intrinsèques très intéressantes pour le calcul quantique. Notamment, le silicium peut être purifié isotopiquement en son isotope le plus abondant, le ^{28}Si. Ce dernier ne contient aucun spin nucléaire, ce qui lui confère de très bonnes propriétés de cohérence, un net avantage sur les semiconducteurs III-V. Nous présentons dans la première partie du chapitre les propriétés liées à la structure de bande du silicium qui sont pertinentes pour l'information quantique, en distinguant la bande de conduction (pour les qubits de spin d'électrons) et la bande de valence (pour les qubits de spin de trous). Dans la bande de conduction il s'agit en particulier des états de vallée, qui constituent un degré de liberté supplémentaire pour un qubit, ainsi que du très faible couplage spin-orbite. Au contraire dans la bande de valence, le couplage spin-orbite est relativement important.

Ces propriétés peuvent être des avantages ou des contraintes pour les qubits de spins en fonction de la manière dont elles sont exploitées et de l'architecture choisie. Nous présentons dans une deuxième partie du chapitre les différentes architectures utilisées par la communauté scientifique puis le cas particulier des dispositifs développés au CEA Grenoble. Une approche assez répandue est celle proposée par Kane [36] : des électrons sont liés à des dopants placés de manière déterministe en réseau sous une surface. Sur la surface sont disposées des grilles qui contrôlent la probabilité de présence sur le dopant ainsi que les interactions d'échange entre plus proches voisins. Le contrôle du spin d'un qubit spécifique se fait par l'application d'un champ magnétique oscillant résonant (ESR: electron spin resonance). Une autre approche consiste à utiliser des grilles métalliques pour définir électrostatiquement des boîtes quantiques. Une stratégie répandue est alors

de chercher à manipuler le spin avec un champ électrique, plus local qu'un champ magnétique. Pour pallier au faible couplage spin-orbite de la bande de conduction, un couplage artificiel est en général implémenté via des micros-aimants qui génèrent un gradient de champ magnétique.

L'approche du CEA est relativement différente. Les dispositifs quantiques utilisés sont basés sur les technologies du Leti de transistors trigate sur isolant légèrement modifiés. Il s'agit d'un nanofil gravé sur un substrat de SiO_2 avec une grille arrière ("backgate"), une grille métallique recouvre trois des interfaces du nanofil. Pour obtenir des qubits, cette géométrie de base est adaptée pour permettre la localisation d'électrons uniques (par blocage de Coulomb). D'autres grilles peuvent être ajoutées afin de créer des systèmes de boîtes quantiques couplées. Dans ces dispositifs, la stratégie du CEA est d'utiliser au maximum les spécificités du silicium pour avoir une architecture simple et donc qui puisse permettre l'intégration à grande échelle. En particulier l'idée est d'utiliser le couplage spin-orbite (pour les trous comme pour les électrons) pour contrôler le spin par EDSR (electric dipole spin resonance).

Any two-levels quantum system could be used as a qubit. There is indeed in the literature an incredible zoology of proposals: superconducting junctions, spins in various semiconductors, photons, trapped ions, and many more [1, 37–42]. Therefore, why does silicon stand out as a serious candidate?

There is first a pragmatic answer: because it is a well-known material, which benefits from all the know-how and technological advances of the microelectronics industry. In particular the control on the quality of materials, on the Si/SiO_2 interface, on the lithography, should make possible the fabrication of quantum dots in silicon with the desired properties. The quantum circuits also need to be scalable in order to reach the high number of qubits needed for error-correction codes, and up to now such high density of components and interconnections can only be found on a silicon chip. Moreover, by using a silicon CMOS platform it is in principle possible to co-integrate the qubits with the classical electronics needed for their control.

Some physical properties also make silicon a good candidate for quantum computing: the peculiarities of its bandstructure and the fact that its most abundant isotope, ^{28}Si, has no nuclear spin. First of all, we are going to present the specific properties of silicon, as a bulk material and in nanostructures. Then, we will outline the different strategies adopted by the main groups working on silicon spin qubits as well as the particular approach adopted by CEA.

2.1 Silicon properties

Silicon belongs to group IV semiconductors. It is a crystalline material with the diamond lattice structure and cubic symmetry. The band structure of bulk silicon is shown in Fig. 2.1, with a zoom on the top of the valence band and the bottom of the conduction band. Silicon is an indirect band gap semiconductor. The maximum of the valence band is at the Γ point ($\mathbf{k} = 0$), whereas the minima of the conduction band are closer to the X points, at $|\mathbf{k_0}| = 0.85 \times 2\pi/a_0$, with $a_0 = 0.5431$ nm. The band gap of silicon is $E_g = 1.17$ eV at $T = 0$ K.

An important property of silicon is the fact that its dominant isotope, ^{28}Si, does not have a nuclear spin. Indeed, natural silicon is made of 92 % of ^{28}Si, 3 % of ^{30}Si with also zero nuclear spins, and only 4 % of ^{29}Si which 1/2 nuclear spins. The hyperfine interaction is thus very weak in silicon, therefore the coherence times can be very long [44]. Moreover, silicon can be isotopically purified to ^{28}Si with a residual concentration of ^{29}Si of 50 ppm, in order to extend further the coherence times [45, 46]. This grants to silicon a major advantage over III-V semiconductors.

Although we have only discussed electron spin qubits so far in chapter I, it is possible to choose either electron or holes to make a spin qubit. That is why in the next two sections we present the properties of silicon in both the conduction and valence bands.
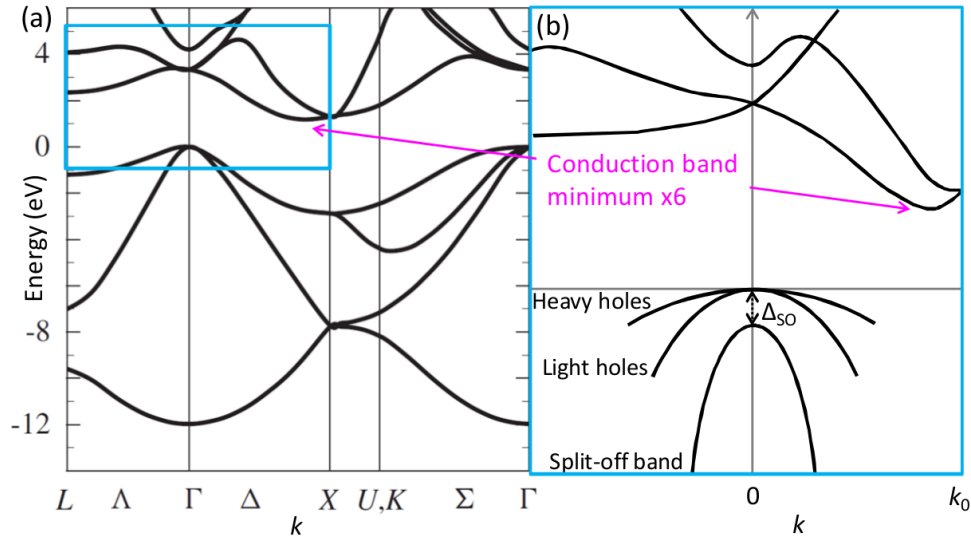
Figure 2.1: (a) Band structure of bulk silicon. (b) Zoom on the conduction band minimum and valence band maximum. From Ref. [43].
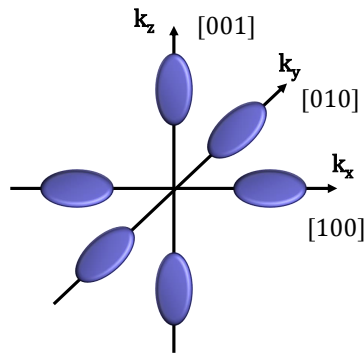
Figure 2.2: Iso-energy surfaces of the six valleys of silicon.

We will discuss the bulk characteristics as well as the effect of confinement in quantum dots.

2.1.1 Conduction band

Because of the cubic symmetry, the conduction band minimum is six-fold degenerate and these minima are called valleys. They are located at $\pm k_0 \mathbf{x}$, $\pm k_0 \mathbf{y}$, and $\pm k_0 \mathbf{z}$. In the k-space, the surfaces of constant energy are ellipsoids (Fig. 2.2), because the effectives masses in each valley are anisotropic (the longitudinal mass is $m_l^* = 0.98 m_0$, and the transverse mass is $m_t^* = 0.2 m_0$). The valley degeneracy may be a problem for quantum computation, since we need only two well-defined states to encode the quantum information in a qubit.

In nanostructures such as quantum dots, the confinement and interfaces reduce the symmetry and lift this six-fold degeneracy. First, as the effective masses in the conduction band are anisotropic, a stronger confinement in the $\mathbf{z}$ direction shifts the four $\mathbf{k_x}$ and $\mathbf{k_y}$

$$|v_1\rangle = |k_z\rangle + e^{i\varphi}|-k_z\rangle$$

$$|v_2\rangle = |k_z\rangle - e^{i\varphi}|-k_z\rangle$$
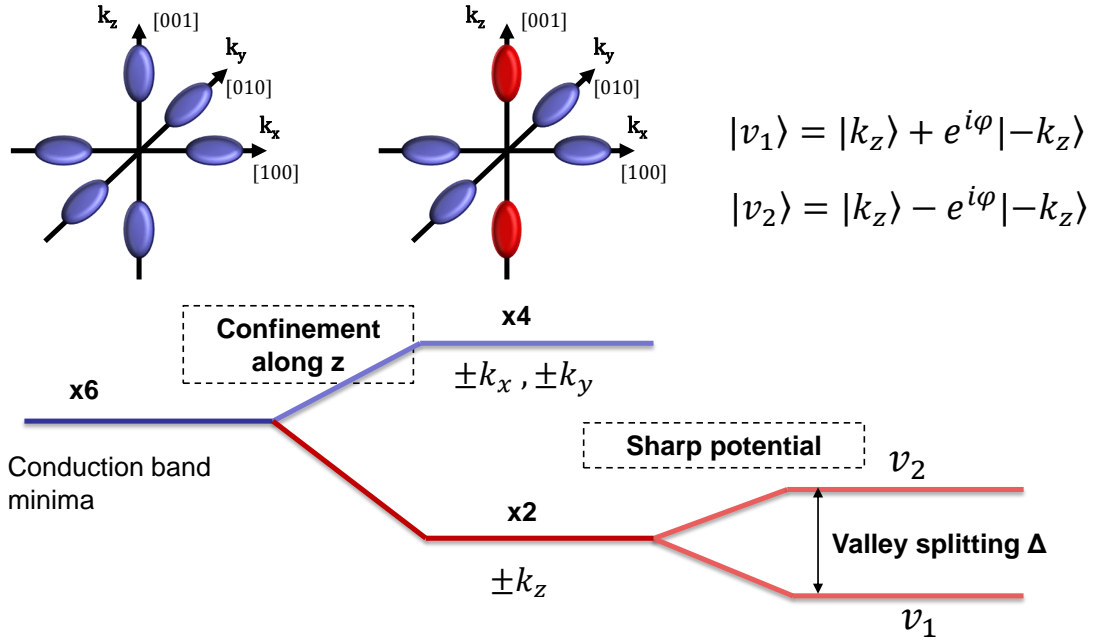
Figure 2.3: Schematic of the effect of the confinement and potential on the valley states and their degeneracy.

valleys well above the two $\mathbf{k_z}$ valleys (typical splitting is $\simeq 10$ meV). Then, the degeneracy of two $\mathbf{k_z}$ valleys can be lifted by inter-valley scattering potentials. As these valleys are distant in k-space, the potential has to vary rapidly along $\mathbf{z}$ to couple them [47–49]. Namely, to achieve sizable coupling, the potential has to show significant variations at the scale of 2 nm along $\mathbf{z}$. Such steep variations can only be produced by dopants, or abrupt interfaces. The resulting states v_1 and v_2 are, in a first approximation, bonding and anti-bonding combinations of the $+\mathbf{k_z}$ and $-\mathbf{k_z}$ states. They are separated by an energy called the valley splitting. Depending on the structure, the valley splitting can be of the same order of magnitude than the orbital splitting and valley-orbit mixing can occur. The effects of confinement and abrupt potentials are summarized in Fig. 2.3. For dopants, the valley splitting reaches a few meV depending on the nature of the impurity. For interfaces, the valley splitting depends a lot on the electric field [50] and on the atomic details of the interfaces [51, 52], as we will see in more detail in chapter 5. For Si/SiO$_2$ interfaces the valley splitting can range from a few tens to a few hundred μeV [50, 53–57], and for Si/SiGe heterostructures it is typically a few tens of μeV [58–62].

As opposed to most III-V semiconductors, another particularity of the silicon conduction band is the fact that is shows a very weak spin-orbit interaction. A reason for this low spin-orbit is that silicon is a relatively light element, with Z $= 14$, so the electric field close to the nucleus is smaller than for heavier atoms. Also, the spin-orbit interaction couples p orbitals of different nature (p_z with p_x for instance). Yet as the conduction band minima are located at large k, the p orbitals are separated in energy and cannot be coupled efficiently by the spin-orbit interaction. Finally, the crystal has centro-symmetry

which suppresses most of the Dresselhaus spin-orbit effects [63]. In quantum dots, the symmetry is in general lower than in the bulk, and in particular the central symmetry can be broken. It has been shown that in certain cases this can lead to a sizable spin-orbit interaction [64, 65].

To summarize, silicon can apparently be the perfect host for an electron spin qubit. As long as the valley splitting is large enough, and thanks to the very low spin-orbit interaction, the spin degree of freedom is a very good quantum number. This makes the spin qubit almost insensitive to electrical noise. As silicon can be purified of nuclear spins, there will not be magnetic noises either. Therefore electron spin qubits can be highly coherent [44–46]. However, in that situation the spin can in principle only be manipulated by magnetic fields. One could also make use of the valley degree of freedom to encode the quantum information, and make a valley qubit. Indeed there have been some proposals in that direction [52, 66, 67]. This kind of qubit is effectively a charge qubit so it does not benefit from the advantages of the spin qubit, but it can be manipulated electrically.

2.1.2   Valence band

In the valence band, the situation is similar to most semiconductors. For bulk silicon, near $\mathbf{k} = 0$, the top of the valence band consists of two bands with different curvatures (the heavy and light holes), which are degenerate at $\mathbf{k} = 0$. A third band called the split-off band, is separated from the other two by the spin-orbit splitting energy $\Delta_{\mathrm{SO}} = 44$ meV. Indeed, in the valence band spin-orbit is generally much stronger than in the conduction band, because it is mostly formed out of bonding linear combinations of p atomic orbitals which are efficiently coupled by the spin-orbit interaction at $\mathbf{k} = 0$.

In a nanostructure the symmetry is lower than in the bulk. This lifts the degeneracy between heavy and light holes at $\mathbf{k} = 0$. The resulting states are combinations of heavy and light holes, which depend on the type of confinement, and also on strain.

Because of the spin-orbit interaction in the valence band, the spin of holes is not a good quantum number. A hole qubit would be effectively a spin-orbit qubit, built out of pseudo-spin states $\{|\Downarrow\rangle, |\Uparrow\rangle\}$ split by a magnetic field. As a result, the qubit can be sensitive to electrical noise, but it can be efficiently manipulated by electric fields.

2.2   Silicon spin qubits.

As we have seen silicon has numerous properties, which can be advantages when making a qubit or constraints that need to be managed. Accordingly, choosing to exploit some
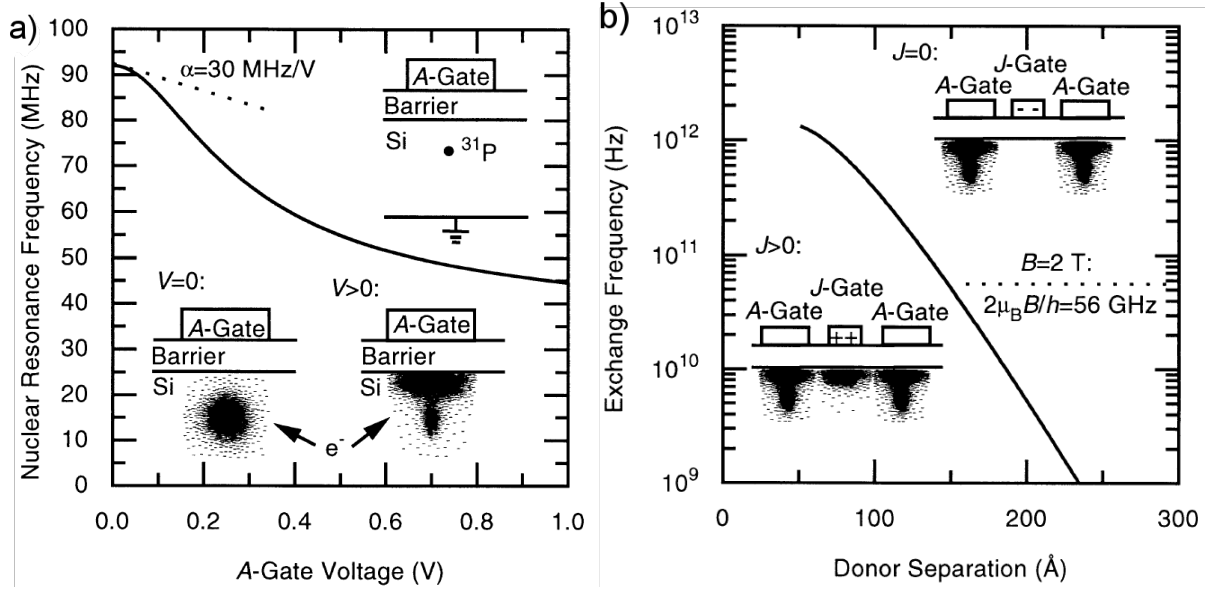
Figure 2.4: Kane quantum computer proposal (a) A-gate, which controls the hyperfine interaction. (b) J-gate, which controls the exchange interaction between two neighboring dots. Both figures are from Ref. [36].

particular properties instead of others (starting with the choice of electrons or holes) leads to different strategies for qubit architectures. In the next paragraphs we are going to describe the major strategies adopted in the silicon qubit community, then the approach undertaken by CEA.

2.2.1 Possible strategies for silicon spin qubits.

One of the first proposals of quantum computer in silicon was made by Kane in 1998 [36]. It consists of an array of deterministically positioned Phosphorus dopants, under a surface were a set of gates are patterned, and the electrons are bound to the donors. An out-of-plane static magnetic field is applied in order to lift the spin degeneracy and define the qubit states, and an in-plane oscillating magnetic field is applied to drive spin rotations. In order to address selectively specific qubits, the resonance frequency of each qubit is controlled. Indeed, the electron spin interact with the nuclear spin of the donor via the hyperfine interaction, $H_{en} = A\mathbf{S}.\mathbf{I}$, where A is the hyperfine constant, $\mathbf{S}$ is the electron spin and $\mathbf{I}$ is the nuclear spin. The hyperfine constant A depends on the probability density of the electron on the donor nucleus, which is tuned by a gate on top of the donor ("A-gate"). This leads to a change of the energy splitting of the electron spin states, so that the A-gates tune the resonance frequency of each qubit. A second set of gates located in between the dopants tune the exchange interaction between two neighbor electrons ("J-gate"), thus allowing for two-qubit operations. These two gates and their effects are depicted in Fig. 2.4. This proposal inspired a lot of experiments on spin qubits with dopants in silicon, in particular in the UNSW group in Sydney. In particular,

electrical control of the spin resonance by the A-gate in a continuous microwave magnetic field has been realized by Laucht *et al.* [68]. One of the main difficulty of the Kane proposal is the need for a precise positioning of the dopants, which critically determines some properties such as the exchange interaction between qubits. Indeed, the valley states oscillate rapidly in space [69], and the exchange interaction depends on the overlap between wavefunctions, so that it also oscillates with the vertical position of dopants [70]. The UNSW group has made great technological progress in that sense, using scanning-tunnelling-microscopy hydrogen lithography [71] as well as precise ion implantation [72]. More recently the idea of coupling a donor to a gate-defined quantum dot has been revived by the demonstration of coherent coupling between a donor-bound electron and a quantum dot bound electron, by Harvey-Collard *et al.* [73], and by some new proposals derived from Kane architecture [74, 75].

Another approach also adopted by many groups is to use only gate-defined quantum dots without any dopants. A natural way in Silicon is to use the Si/SiO$_2$ interface with a set of gates defining the potential landscape that traps one electron, as shown in Fig. 2.5. Some groups are also using Si/SiGe heterostructures, this is notably the strategy adopted now in the Delft and Wisconsin groups [76, 77]. In this kind of proposal it is in principle difficult to control the state by spin-orbit driven EDSR as for III-V quantum bits. Two strategies are then explored by the community: electrical spin resonance (ESR), with dedicated current lines [78] (also shown in Fig. 2.5), or EDSR driven by a slanting magnetic field created by a micromagnet as first demonstrated by Pioro-Ladrière *et al* [25], and then adopted by the Delft and Tarucha groups with recent excellent results [75, 79, 80]. Either approach calls for particular care in the design of ESR lines or micromagnets, especially when it comes to scaling up the devices [81]. Finally, another possibility explored is to encode the quantum information in the states of two or three entangled electron spins. These are the singlet-triplet (two electrons in two dots) [19, 82], or the hybrid qubit (three electrons in two dots) [83, 84].

Finally the last important requirement for quantum computation is the ability to perform two-qubits operations. We have already discussed in Kane's proposal the use of the exchange interaction, which is up to now the most implemented scheme [85, 86]. Another possibility that has recently emerged is to couple two qubits through a superconductor resonator using quantum electrodynamics (QED), as first demonstrated by Mi *et al.* [35]. This allows to envision a new long-distance coupling scheme that could be co-implemented with nearest-neighbor coupling.

There are many degrees of freedom in silicon devices, resulting in a wide variety of strategies to make a spin qubit. The groups working in this subject are trying to make the best out of many worlds. We will see in the next paragraph that CEA approach is quite original on several points.
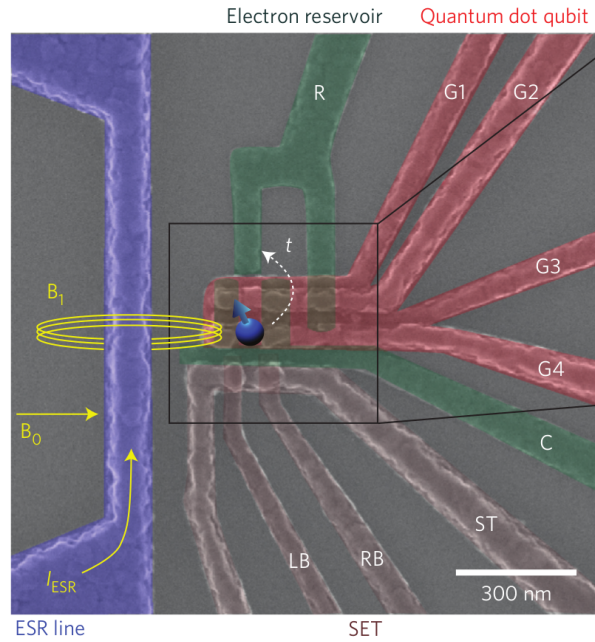
Figure 2.5: Silicon spin qubit. The set of gates define the quantum dot as well as a single electron transistor for readout. On the left, a microwave line is used to create an oscillating magnetic field for spin control. From Ref. [78]

.

2.2.2 Silicon spin qubits in CEA.

In CEA Grenoble there are laboratories of condensed matter and low temperature physics at INAC, and of microelectronics at Leti. Thus, there are historical reasons that guided the technological choices that have been done for quantum bits. In the following, we present the development of qubit devices in CEA and what make them original with respect to the previous approaches we have presented.

In the race for Moore's law, the technology of silicon nanowires has attracted a lot of attention. Especially at CEA Leti, great progress has been made on the fabrication
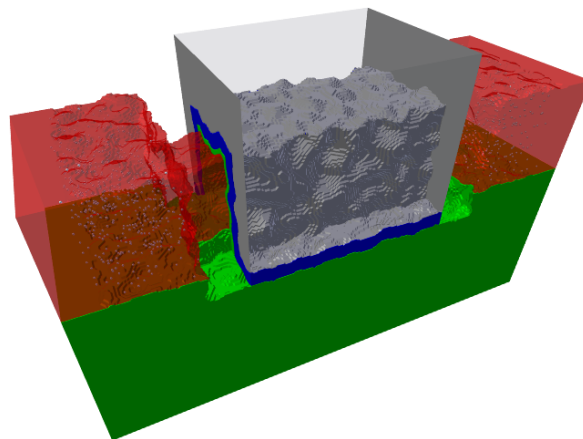
Figure 2.6: 3D schematic of a typical trigate silicon MOSFET from Leti. Silicon is in red, SiO_2 in green, HfO_2 in blue, and the metallic gate is in gray.

of the so-called silicon-on-insulator (SOI) trigate transistor. It consists in a nanowire, first defined on a SOI substrate by standard optical lithography, then chemically etched in order to achieve smaller dimensions (down to $\simeq 10$ nm). The nanowire thus lies on a thick SiO_2 layer, the BOX, with a backgate electrode below. The ends of the nanowire are raised and degenerately doped in order to form the source and drain contacts. A gate is deposited on top of the nanowire, and separated from the source and drain contacts by Si_3N_4 spacers. The gate is used to define a channel in which the density of electrons (or holes) is controlled. The metallic gate is separated from the Si channel by two oxides: a thin (< 1 nm) SiO_2 oxide layer and a thicker ($\simeq 2$ nm) HfO_2 layer which provides a more efficient gate coupling thanks to its higher dielectric constant. The gate is covering three out of the four sides of the nanowire, thus giving an excellent electrostatic control over the channel. The SiO_2 BOX limits the leakage current, and the backgate offers an additional electrostatic knob on the system, for instance allowing for a tuning of the threshold voltage (the limit between the "on" and "off" state of the transistor). These assets make the trigate devices suitable for low-power applications.

Given the small dimensions of these devices, quantum simulations are needed to explain the physics and help the design. In particular, in this group, the quantum transport has been modeled using Non-Equilibrium Green's Function. During my master thesis and at the beginning of my PhD I have studied the access resistance under low and high electric fields [87, 88]. This study is not part of the present manuscript which focuses on quantum bits, but it gave us some insights on their quantum counterparts. In particular, comparison between mobility calculations and measurements allowed us to obtain the surface roughness parameters on the facets of the nanowires [87, 89], that we used for the modeling of the qubit devices.

The approach of CEA is to divert these SOI trigate devices in order to create quantum bits that would be more compact, more reproducible, and consequently more scalable. First, the geometry needs to be modified to make the device operate in the single-electron (or hole) regime. Then, we need a way to measure the spin state and to manipulate it locally, and, finally, a scalable architecture incorporating two-qubit operations. We detail all these points is the following.

A key ingredient for the control of single charges is the design of the spacers (between the source/drain contacts and the gate). Indeed, these spacers control the tunnel barriers between the channel and source/drain reservoirs. If they are long enough, they lead at low temperature to the formation of a quantum dot under the gate in the regime of Coulomb blockade. Acting on the gate potential then controls the number of electrons in the quantum dot. Fig. 2.7 shows an example of device, as well as the measured Coulomb oscillations.

A second step is to introduce another gate in this system, in order to create double quantum dots. For instance in Fig. 2.8 there are two MOS gates in series, so that
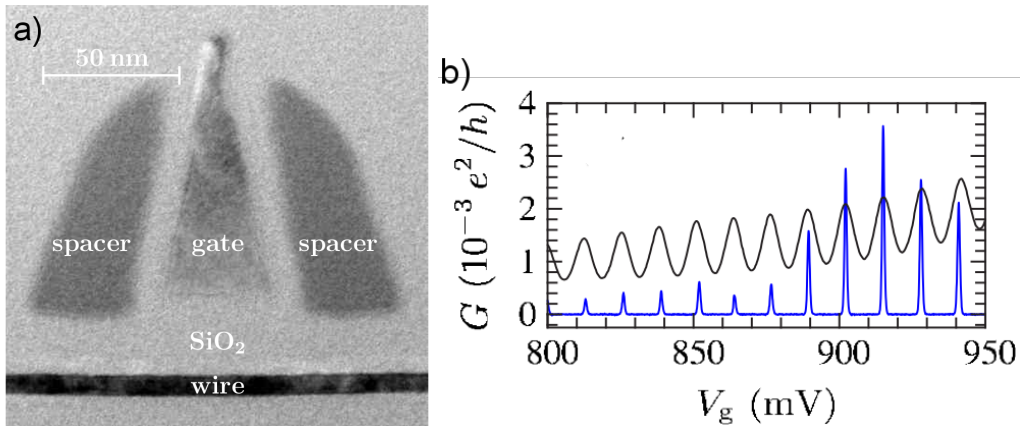
Figure 2.7: (a) MOSFET transistor with long spacers, isolating a quantum dot under the gate, capacitively coupled to the source and drain contacts. (b) Measured Coulomb oscillations at 4.2 K (black curve), and at 400 mK (blue curve). Adapted from Ref. [90].
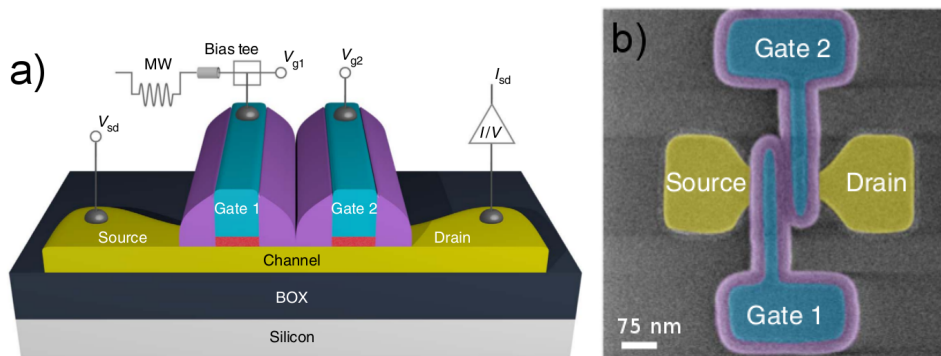
Figure 2.8: (a) 3D schematic of a double quantum dot sample. (b) Top view of the device. From Ref. [93].

one quantum dot is formed under each gate, and they are tunnel coupled. The double quantum system is ideal to study spin quantum bits thanks to the Pauli Spin blockade: the current can only flow if the spins in the two dots are not parallel. A measure of the current thus gives a measure of the spin, and this was demonstrated for electrons [53, 91] as well as for holes [92, 93]. However the current-based detection of Pauli spin blockade is not suited for quantum computation, which requires single-shot readout. Therefore a method for single-shot detection of charge transfer, called gate-reflectometry, is currently implemented [94–96].

At this point we can isolate a single charge and measure its spin state, so that a scheme of spin manipulation is needed to perform single-qubit operations. In order to keep the compactness and scalability of the MOS devices, the main approach of CEA is to perform electrical manipulation via EDSR. To that end, p-type samples have been used to trap holes in the double quantum dot. Then the application of a microwave signal on one of the gates, with a frequency resonant with the Zeeman splitting, leads to EDSR. Maurand *et al.* have demonstrated that way the first hole spin qubit [93]. Fig. 2.9 show
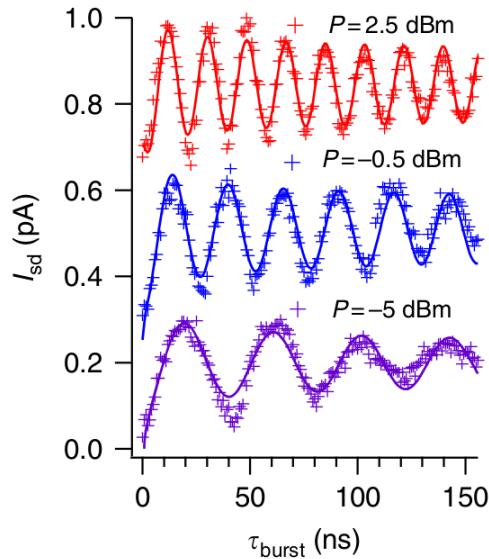
Figure 2.9: Rabi oscillations for different microwave powers. From Ref. [93].

the Rabi oscillations they measured. On that sample, Ramsey measurements were used to estimate $T_2^* = 60$ ns, however since this article much longer coherence times and larger Rabi frequencies have been achieved. More surprisingly, Corna *et al.* [53] managed to take advantage of the small spin-orbit interaction in the conduction band to perform EDSR on electron spins in a *n*-type double quantum dot, using a similar set-up. In this thesis we will study the experiments of spin manipulation on both electron and holes.

Another way of creating double quantum dots has also been implemented in order to have a more scalable architecture than two dots in series. A fabrication process has been developed to create gates in a geometry called 'face-to-face' allowing to localize distinct quantum dots in the two corners of the section of the nanowire [97, 98], as shown Fig. 2.10. These corner quantum dots, confined near two interfaces, are a unique specificity of these devices. Pauli spin blockade between the two corners can be detected by gate reflectometry, as demonstrated by Betz *et al.* [94]. Finally, by duplicating these face-to-face devices along a nanowire, we obtain the structure shown Fig. 2.11, currently under development. Each qubit dot is facing its measurement dot. Moreover, two-qubit gates can be implemented by tuning the exchange interaction between neighboring qubits. The goal is to use this architecture to demonstrate a prototypical quantum algorithm implementation.

The qubit architecture studied at CEA is original in many ways. First, the use of nanowires on silicon on insulator substrates leading to a 2D structural confinement is different from the quantum well and planar MOS devices. This allows for a much more compact structure: for a single qubit, two gates are sufficient for localization, control and measurement (way less than the planar device of Fig. 2.5 for instance). Then, the use of hole spin states is also peculiar and was only recently reproduced by another group in a germanium nanowire [99]. To sum up, the particularity of CEA is to work on devices
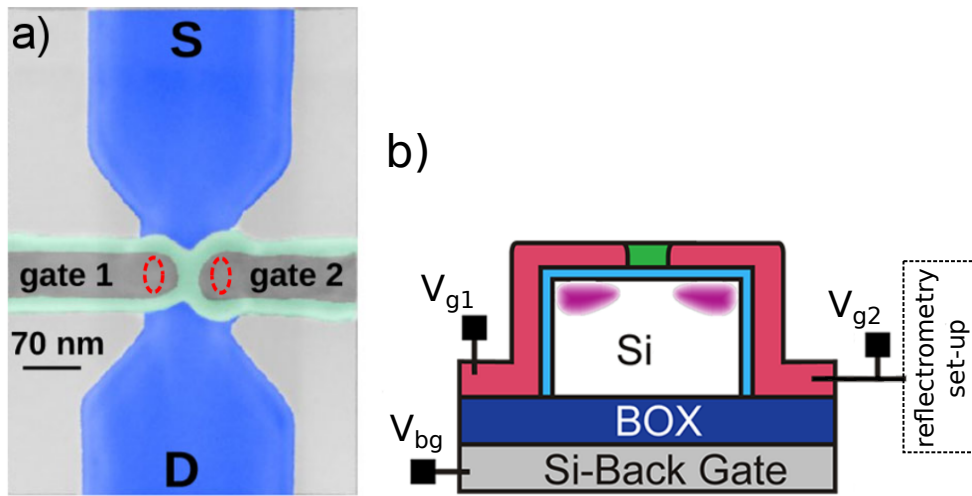
Figure 2.10: (a) Top view of a face-to-face device. The quantum dots approximate locations are shown by red lines. From Ref. [97]. (b) Schematic of the cross-section of the device and set-up. The position of the wavefunctions into the corner states is outlined in pink. Adapted from Ref. [94].
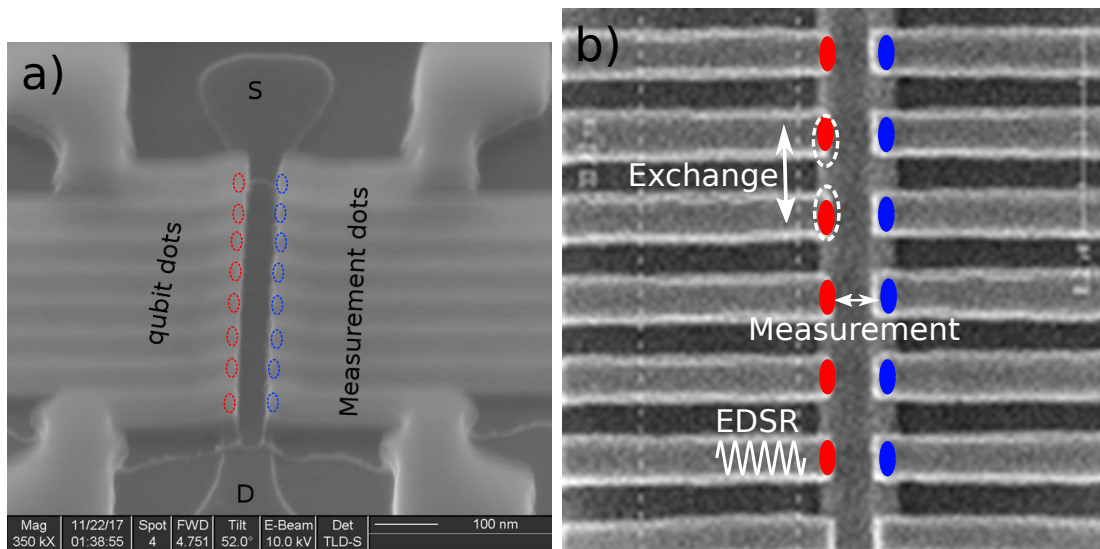
Figure 2.11: (a) SEM tilted top view of an array of face-to-face devices on a single nanowire. Schematics of the dots approximate position are given in red for the qubit dots and in blue for the measurement dots. (b) SEM top view with same color code. The possible operations (spin measurement, single spin control via EDSR, and exchange interaction) are outlined in white.

25

really close to MOSFET devices in order to facilitate the transition towards large scale integration.

In this thesis, we will focus on the modeling of the electrical control of single spins in silicon. The measurement of EDSR in an electron double quantum dot is theoretically studied in chapter 4. We show in particular that EDSR is enabled by the particular symmetry of the corner states. These results are used in chapter 5 to investigate a new scheme for electrical control of a spin qubit, which takes advantage of the backgate of the SOI devices. In chapter 6 we study the spin manipulation in a hole double quantum dot, and in particular the anisotropy of the Rabi frequency with the magnetic field orientation as measured in Ref. [100].

Chapter 3

Numerical Methods

*Dans ce chapitre nous présentons les différentes méthodes numériques (implémentées dans le code TB_Sim développé au CEA Grenoble) qui sont utilisées dans les chapitres suivants pour l'étude des qubits de spins. Nous prenons comme exemple un dispositif typique développé au CEA, constitué d'un nanofil recouvert partiellement par deux grilles métalliques se faisant face. Partant de la géométrie 3D du dispositif, il est possible de calculer le potentiel dans le système en résolvant numériquement l'équation de Poisson, et ce en incluant éventuellement des interfaces rugueuses et des charges ponctuelles comme des dopants. Ce potentiel est ensuite utilisé pour le calcul des premiers états électroniques. Ceci peut être réalisé via une méthode atomistique, la méthode des liaisons fortes, ou bien par des méthodes de milieu continu, les méthodes **k.p**. Une fois obtenues les fonctions d'onde et les énergies, il est possible de calculer les propriétés multi-électroniques du système avec la méthode d'interaction de configuration. Nous donnons une application de cette méthode avec le calcul de l'énergie de charge d'une paire de dopants Bore. Finalement, partant des états à une ou plusieurs particules, il est possible de calculer l'évolution des états en résolvant l'équation de Schrödinger dépendante du temps.*

Le but de ces simulations est d'avoir une description aussi réaliste que possible des dispositifs étudiés, afin de permettre des comparaisons précises avec les mesures expérimentales. Valider ces comparaisons est indispensable pour pouvoir faire des prédictions théoriques et des propositions d'expériences avec les simulations. D'autre part les simulations seront utiles pour la construction et la validation de modèles analytiques dans les prochains chapitres. Le couplage entre les calculs de structure électronique et les simulations dépendantes du temps donnent la possibilité d'effectuer des expériences numériques sur le qubit avec un accès à toutes les observables.

In this chapter we introduce the numerical methods that will be used in chapter 4, 5, and 6. They are all implemented in the TB_Sim code developed at CEA Grenoble. The idea of these simulations is to describe the 3D geometries of the samples (which are more complex than the usual planar devices), to compute the single particle electronic structure, to deal with many-particle interactions if needed, and to perform time-dependent simulations with these inputs. We will use all these methods to characterize single qubits. Two-qubit gates may also be studied with these methods, however going beyond two qubits would be numerically difficult. The methodology we present here is hence adapted to the study of the qubit itself whereas the simulation at the scale of the quantum circuit must be done by other means.

In this chapter, we are first going to present the simulation workflow used to describe the CEA devices, then we will give a short explanation of each method. In order to illustrate this description we give the results of the typical numerical calculation on a representative device, a silicon nanowire on a SOI substrate, with gates in the "face-to-face" geometry presented in the previous chapter.

3.1 Simulation workflow

Let us begin with an overview of the toolbox of the TB_Sim code, and of the logical sequence of possible simulations. This is summarized in Fig. 3.1. We start from an accurate 3D description of the device. We compute the potential in this device with a Poisson solver. Then the electronic states in this potential are calculated using two possible methods: the semi-empirical tight-binding method (atomistic description), or the **k.p** method (continuous medium description). After that, we can, if appropriate, compute the many-particles states using the configuration interaction method. Finally the single or many particles states can be used as inputs for time-dependent simulations. At each step, we can postprocess the data for analysis. In the next paragraphs we are going to present all these steps in more detail.

3.2 Device modeling

We are going to illustrate these different steps on a "face-to-face" device (called that way because two gates are facing each other). It is similar to the devices that will be studied throughout this thesis. The device is shown in Fig. 3.2 with the chosen $\{\mathbf{x}, \mathbf{y}, \mathbf{z}\}$ axes. It consists in a [110]-oriented silicon nanowire with width $W = 40$ nm and height $H = 10$ nm, which lies on a SiO_2 buried oxide layer (BOX) with thickness $t_{BOX} = 25$ nm. The SiO_2 BOX lies on a thick Si substrate (not shown) which can be used as a back gate. In the following the backgate is biased at $V_{bg} = 0$ V. Moreover, two metallic gates cover partially the nanowire. The gate length (in the $\mathbf{x}$ direction) is $L_g = 30$ nm and the two
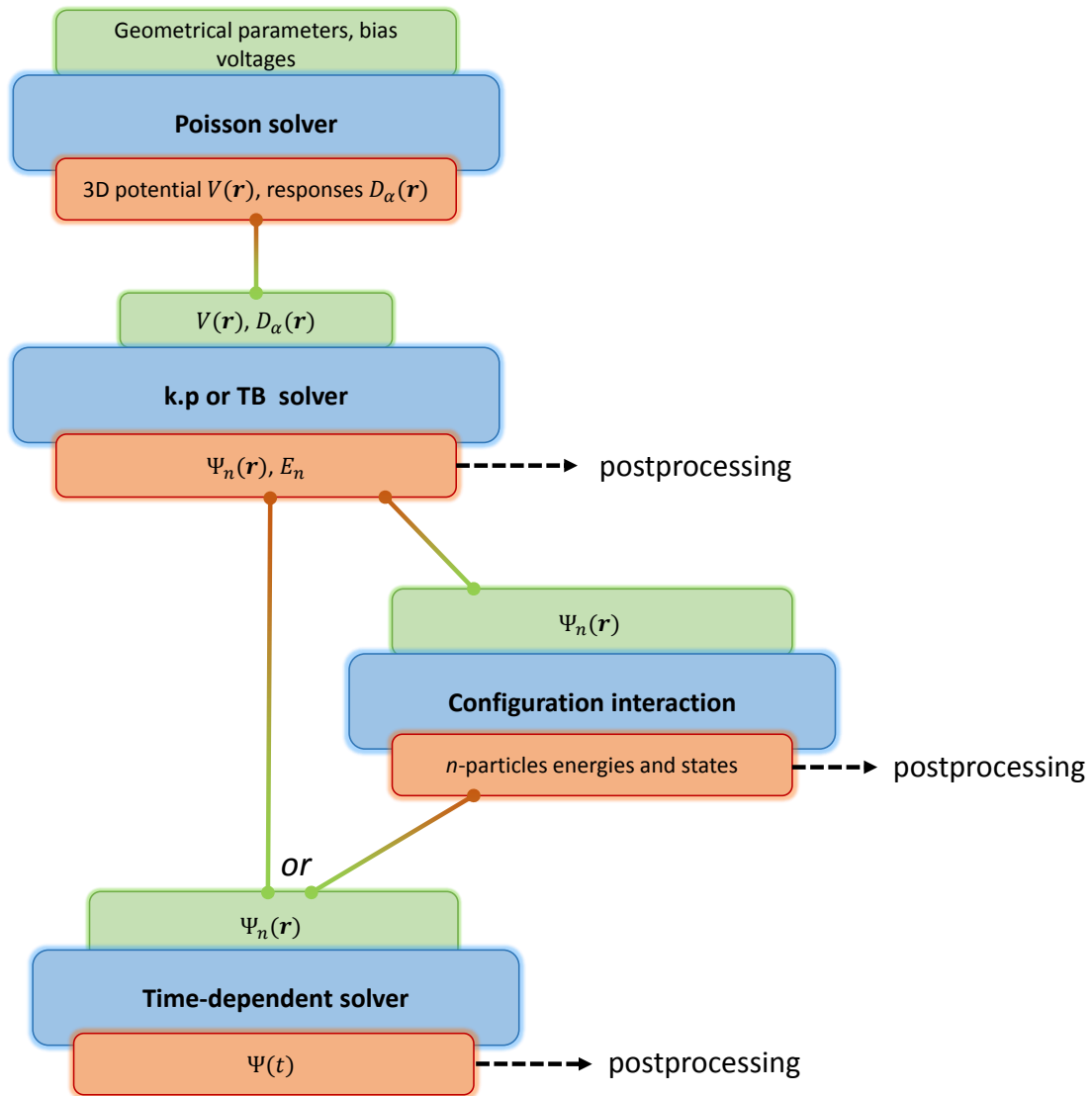
Figure 3.1: Workflow of possible simulations. The solvers are in blue, their inputs are in green and their outputs are in red.
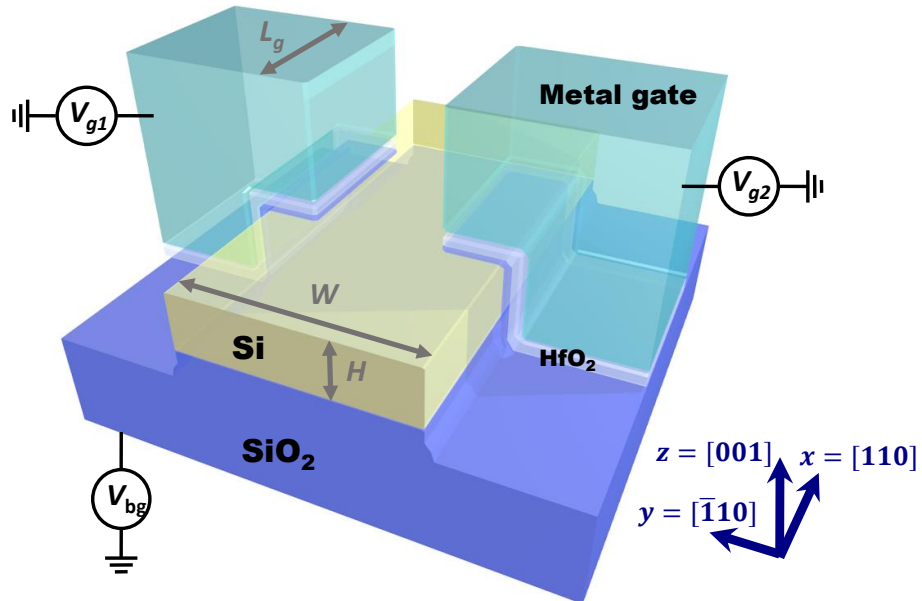
Figure 3.2: Geometry of the "face-to-face" device. The silicon nanowire is in yellow, HfO$_2$ is in light gray, SiO$_2$ is in dark blue and the metal gates are in light blue. The buried SiO$_2$ lies on top of a Si substrate, not shown.

gates are separated by 20 nm (in the **y** direction). The two gates are biased at (V_{g1}, V_{g2}). The metallic gates are separated from the nanowire by one layer of SiO$_2$ (typical thickness $t_{\mathrm{SiO_2}} \simeq 1$ nm) and one layer of HfO$_2$ (typical thickness $t_{\mathrm{HfO_2}} \simeq 2$ nm). The whole device is embedded in Si$_3$N$_4$. We may introduce sources of local disorder, such as interface roughness, dopants, or trapped charges at the interface between the materials. This will be illustrated in the next section.

The dimensions of the structure can be arbitrary as well as the number and position of top gates.

3.3 Potential

The potential $V(\mathbf{r})$ in a continuous medium with a charge density $\rho(\mathbf{r})$ and a dielectric constant $\epsilon(\mathbf{r})$ is the solution of the Poisson equation:

$$\boldsymbol{\nabla}[\epsilon(\mathbf{r})\boldsymbol{\nabla}V(\mathbf{r})] = -4\pi\rho(\mathbf{r}) \tag{3.1}$$

To be solved numerically, this equation is spatially discretized on a mesh. In our case this 3D mesh is a product of three 1D inhomogeneous meshes. The density of the mesh is increased in the region of fast variations of the potential: the silicon nanowire (typical mesh step down to 0.2 nm), and the oxides between gates and silicon. It is relaxed in the region of slow variations of the potential, as in the buried oxide. We assume dielectric constants $\epsilon_{\mathrm{Si}} = 11.7$, $\epsilon_{\mathrm{SiO_2}} = 3.9$, $\epsilon_{\mathrm{HfO_2}} = 20$, and $\epsilon_{\mathrm{Si_3N_4}} = 7.5$ throughout the thesis.

Eq. 3.1 is discretized using the method of the finite volumes. It consists in dividing the space in small volumes centered on the nodes of the mesh. Each node i is characterized by a potential V_i, a charge Q_i and a dielectric constant ϵ_i. We then write Gauss theorem on each elementary volume assuming that the electric field is constant on each face. This leads to a system of equations of the form:

$$AV = 4\pi(Q + Q_b) \tag{3.2}$$

where Q_b, Q, are the vectors which describe respectively the boundary conditions and charge, V is the vector of the unknown potentials, and A is a symmetric matrix. Typically Q_b accounts for the fixed gate potentials and Q accounts for the dopants or individual charges. Finally the linear system of Eq. 3.2 is solved with the conjugate gradient method [101], and as a result we obtain the potential $V(\mathbf{r})$ on the mesh. We apply periodic boundary conditions along the **x** direction (wire axis).

Moreover, as we are interested in this thesis in electrical manipulation, we will need the response of the system to an excitation on the gate. This is described by the gate response potentials D_α. D_α is the electrostatic response of the system to an excitation on gate α: $D_\alpha(\mathbf{r}) = \frac{\partial V(\mathbf{r})}{\partial V_\alpha}$, the partial derivative of the total potential $V(\mathbf{r})$ in the system with respect to the gate potential V_α (α spans all the gates, including the backgate). In practice, as the electrostatics of the system is linear, we compute $D_\alpha(\mathbf{r})$ by solving the Poisson equation with $V_\alpha = 1$ V and all the other gates grounded.

As an illustration we have computed the potential in the face-to-face device, with various sources of disorder usually considered in silicon devices. The results are plotted in Fig. 3.3 with $V_{g1} = 0.2$ V, $V_{g2} = 0.1$ V. In the calculations of b), c), d), we have introduced surface roughness (SR). The rough interface is generated from the target autocorrelation function $C(\mathbf{r}, \mathbf{r}') = \langle \Delta(\mathbf{r}), \Delta(\mathbf{r}') \rangle \simeq \Delta_{SR}^2 \exp[-|\mathbf{r} - \mathbf{r}'|^2/\Lambda_{SR}^2]$ [102, 103], where $\mathbf{r}$, $\mathbf{r}'$ are the 2D position vectors in the interface plane, $\Delta(\mathbf{r})$ is the displacement of the interface, Δ_{SR} is the rms roughness, and Λ_{SR} is a correlation length. Here we took $\Delta_{SR} = 0.35$ nm and $\Lambda_{SR} = 1.5$ nm. In c) we have placed a dopant with charge $+1$ at $(x, y, z) = (0, 9, 0)$ nm. In d) we have placed a distribution of so-called RCS (Remote Coulomb Scattering) charges at the SiO_2/HfO_2 interface, with a density $n_{RCS} = 10^{13}$ cm^{-2}. Room-temperature mobility measurements indeed suggests the presence of such charges in the gate stack [104].
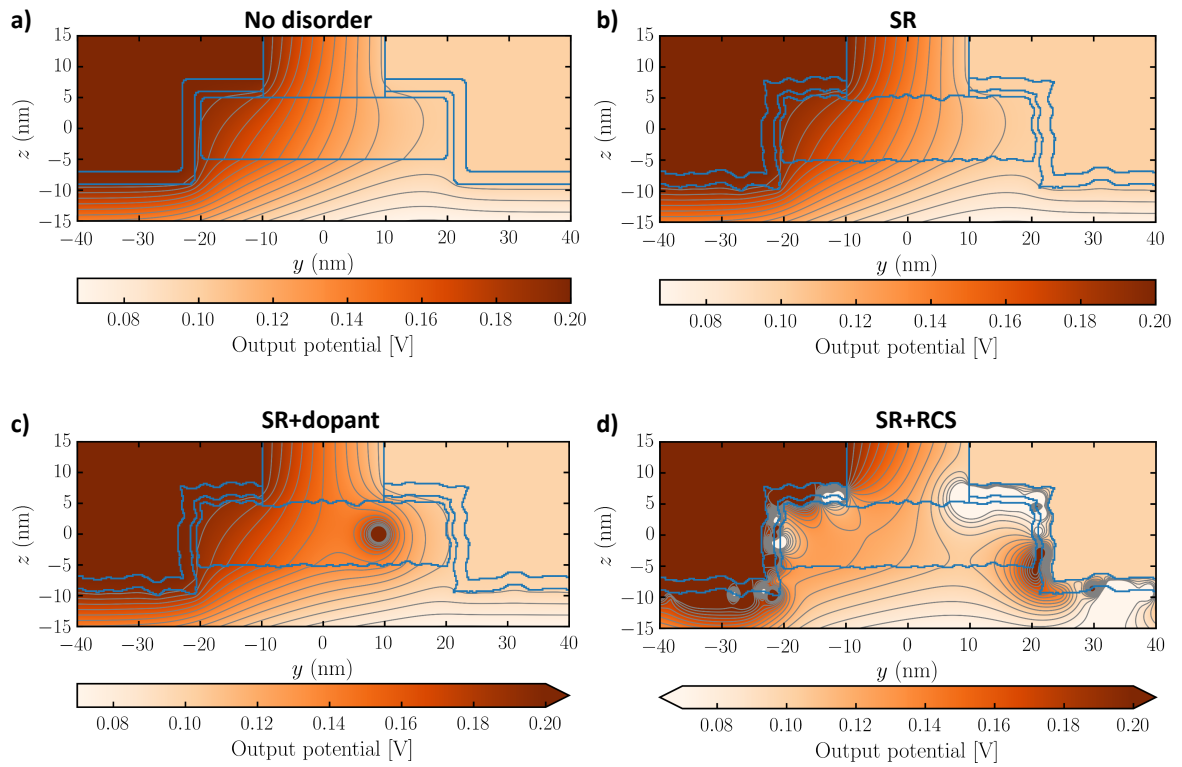
Figure 3.3: Cross-section of the calculated potential in the yz-plane at $x = 0$, for different cases. (a) Perfect device without disorder. (b) Including surface roughness (SR). (c) Including SR and one dopant with charge $+1$ at $(x, y, z) = (0, 9, 0)$ nm. The color scale is the same than (a), with open scale. (d) Including SR and positive RCS charges with surface density $n_{\mathrm{RCS}} = 10^{13}$ cm^{-2}. The color scale is the same than (a), with open scale.

3.4 Electronic structure

The next step in this simulation flow is to use the calculated potential as input for the electronic structure calculations. There are two kinds of methods available. The first kind is an atomistic approach, the semi-empirical tight-binding method [105], which consists in a development of the wavefunction in a basis of atomic orbitals. The second kind are continuous method, such as the effective mass and **k.p** methods [106], which are approximations of the band structure at the top of the valence band or at the bottom of the conduction band. We will detail these two methods in the following.

3.4.1 Atomistic method: tight-binding

The semi-empirical tight-binding method (TB) consists in writing the electron or hole wavefunctions as linear combinations of atomic orbitals [105, 107, 108]:

$$|\Psi\rangle = \sum_{i\alpha} c_{i\alpha} |\phi_{i\alpha}\rangle \tag{3.3}$$

where $i = \{1..n\}$ index the atoms, $\alpha = \{1..m\}$ index the atomic orbitals, and $\phi_{i\alpha}$ is the atomic orbital α centered on atom i. The $\phi_{i\alpha}$ can be chosen orthogonal. Then the Scrödinger equation takes a matrix form:

$$H_{\text{TB}}|\Psi\rangle = \epsilon|\Psi\rangle \tag{3.4}$$

where $|\Psi\rangle$ is the vector of the coefficients $c_{i\alpha}$ and ϵ is the corresponding eigenvalue. H_{TB} can be represented as a $N \times N$ matrix, with $N = nm$:

$$H_{\text{TB}} = \sum_{i\alpha} \epsilon_{i\alpha} |\phi_{i\alpha}\rangle\langle\phi_{i\alpha}| + \sum_{i\alpha,j\beta} t_{i\alpha j\beta} |\phi_{i\alpha}\rangle\langle\phi_{j\beta}| \tag{3.5}$$

where $\epsilon_{i\alpha}$ is the energy of the orbital α of atom i, and $t_{i\alpha j\beta}$ is the hopping integral between $|\phi_{i\alpha}\rangle$ and $|\phi_{i\beta}\rangle$. The number of orbitals per atom depends on the type of atom. In silicon, we use the $sp^3d^5s^*$ model that describes the s, p, d orbitals of the outer shell of silicon, and include an extra s^* orbital. Furthermore, as the orbitals are localized on the Si atoms, we consider only the interactions between first nearest neighbor atoms. That way the matrix H_{TB} is sparse, and can be efficiently stored and diagonalized numerically. The TB parameters ($\epsilon_{i\alpha}, t_{i\alpha j\beta}$) are adjusted to reproduce the whole bulk band structure calculated with advanced *ab initio* methods, such as the many-body GW approximation. The comparison between the band structure of bulk silicon calculated with the GW and TB methods was given in Ref. [109] and is shown in Fig. 3.4. Moreover, a slowly varying potential $V(\mathbf{r})$ can be added to the diagonal of the tight-binding Hamiltonian ($\epsilon_{i\alpha} \rightarrow \epsilon_{i\alpha} + V(\mathbf{R_i})$). In our case this potential is the output of the Poisson solver. The spin-orbit
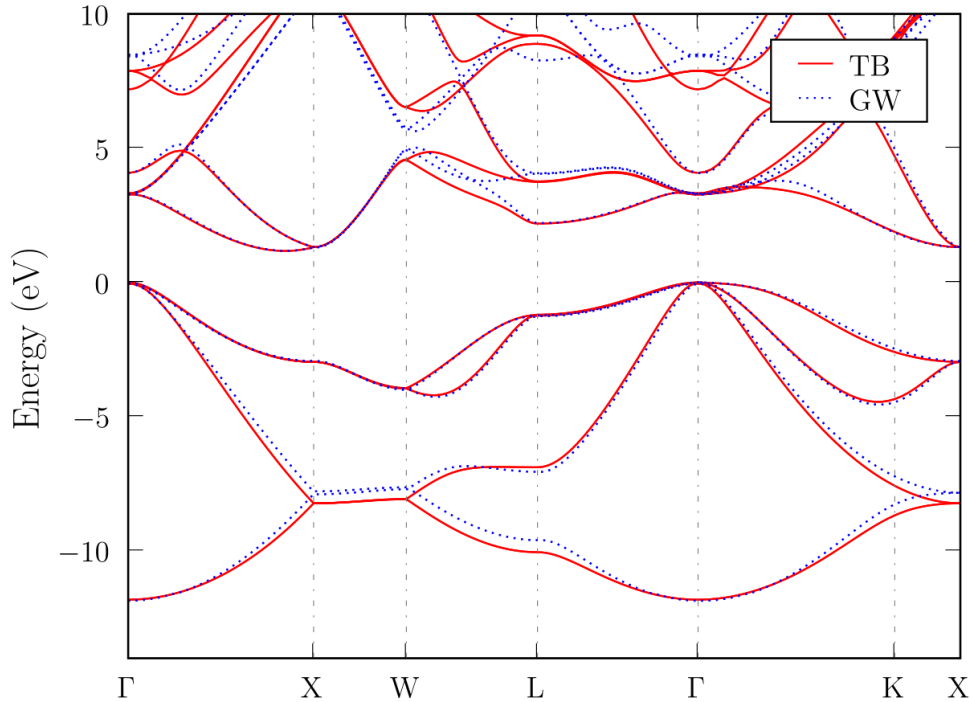
Figure 3.4: Band structure of bulk silicon in the $sp^3d^5s^*$ TB and GW approximations. From Ref [109].

interaction needs also to be included. The general Hamiltonian for SO is:

$$H_{SO} = \frac{\hbar}{2m_0^2 c^2}(\boldsymbol{\nabla} V_c(\mathbf{r}) \times \mathbf{p}).\mathbf{S} \tag{3.6}$$

where m_0 is the electron mass, c is the speed of light, $\mathbf{p}$ is the momentum, and $V_c(\mathbf{r})$ is the potential in the crystal. SO is efficient only when the electric field is strong, that is near the nuclei. In that region we can make the assumption that the potential is central, so that $\boldsymbol{\nabla} V_c(\mathbf{r}) = \frac{1}{r}\frac{\mathrm{d}V_c(r)}{\mathrm{d}r}\mathbf{r}$. Using also that $\mathbf{r} \times \mathbf{p} = \mathbf{L}$, Eq. 3.6 then becomes for one given atom:

$$H_{SO} = \frac{\hbar}{2m_0^2 c^2}\frac{1}{r}\frac{\mathrm{d}V_c(r)}{\mathrm{d}r}\mathbf{L}.\mathbf{S} \tag{3.7}$$

The effects of SO are most important on the p orbitals involved in the sp^3 bonds of silicon. We may therefore rewrite Eq. 3.7 for p orbitals (after summation on the atoms) as:

$$H_{SO} = 2\lambda_{SO}\sum_i \mathbf{L_i}.\mathbf{S} \tag{3.8}$$

where $\mathbf{L_i}$ are the matrices of the angular momentum and λ_{SO} is a constant.

The methodology we have described up to now is valid at zero magnetic field. In presence of a magnetic field $\mathbf{B}$, one has to deal with the following effects: first the coupling between $\mathbf{B}$ and the spin is included via the Zeeman interaction $H_z = g_0\mu_B\mathbf{B}.\mathbf{S}$, where $g_0 = 2.0023$ is the bare Landé gyromagnetic factor, μ_B is Bohr's magneton, and $\mathbf{S}$ is the
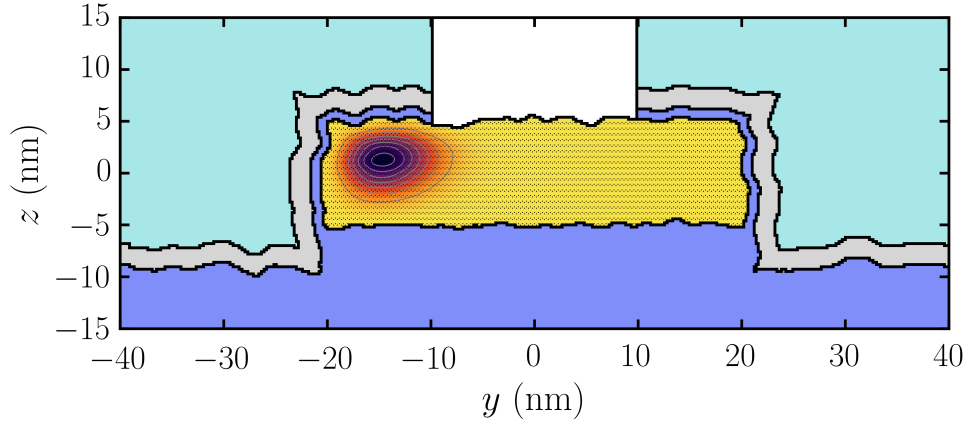
Figure 3.5: Cross-section of the squared TB wavefunction of an electron in the yz-plane at $x = 0$, calculated with the potential of Fig. 3.3b. The iso-probability surfaces are in gray. The Si atoms are the black dots, and the same colors have been used for the other materials as in Fig. 3.2.

spin vector. Second, the coupling between $\mathbf{B}$ and the orbital part of the wavefunctions is described by the substitution $\mathbf{p} \to \mathbf{p} + e\mathbf{A}$. Conveniently, in tight-binding this can be treated by Peierls substitution [110], i.e the orbital effect of the magnetic field can be described by the following transformation on the hopping elements:

$$t_{ij} \to t_{ij} \exp\left[\frac{-ie}{h} \int A(\mathbf{r}')d\mathbf{r}'\right] \simeq t_{ij} \exp\left[\frac{-ie}{h}(\mathbf{R_j} - \mathbf{R_i})\frac{1}{2}(\mathbf{A}(\mathbf{R_i}) + \mathbf{A}(\mathbf{R_j}))\right] \qquad (3.9)$$

where $\int A(\mathbf{r}')d\mathbf{r}'$ is the integral of the vector potential along the hopping path (from the site at position $\mathbf{R}$ to the one at position $\mathbf{R}'$). The approximation of the integral is valid as long as $\mathbf{A}(\mathbf{r})$ is slowly varying.

In a nanostructure such as our nanowire, the dangling bonds at the surfaces are saturated with pseudo-hydrogen atoms[1]. Then we solve numerically Eq. 3.4 to obtain $|\Psi_i\rangle$ and ϵ_i for the first few conduction and valence band states using an iterative Jacobi-Davidson eigensolver [112, 113]. Once the states are converged, we can compute the matrix elements $\langle \Psi_i | D_\alpha | \Psi_j \rangle$ of the response potentials D_α, and the matrix elements of other useful observables such as the position and spin operators.

An example of such simulation is given in Fig. 3.5, for a face-to-face device with surface roughness. At bias voltage bias $(V_{g1}, V_{g2}) = (0.2, 0.1)$ V, the electron is confined in the top left corner of the nanowire, which is typical of this kind of device.

3.4.2 Envelope function methods: effective mass and k.p

In this paragraph we are going to describe the family of $\mathbf{k.p}$ methods, insisting in particular on the 6-bands $\mathbf{k.p}$ scheme that will be used to describe holes in chapter 6. We will start

---

[1]The choice of modeling the interfaces by pseudo-hydrogen atoms can be discussed, however we used also the effective oxide model of Ref. [111] which gave similar trends in our calculations.

by giving the general ideas of the **k.p** methods

For electrons in a periodic crystal, the Hamiltonian reads:

$$\left(\frac{\hat{p}^2}{2m_0} + V_c(\mathbf{r}) \right) \phi(\mathbf{r}) = E\phi(\mathbf{r}) \tag{3.10}$$

where $V_c(\mathbf{r})$ is the periodic potential of the crystal, and $\hat{\mathbf{p}} = -i\hbar\boldsymbol{\nabla}$. According to Bloch's theorem, the eigenstates can be written as the product of a plane wave and a Bloch function which has the periodicity of the lattice:

$$\phi_{n\mathbf{k}}(\mathbf{r}) = e^{i\mathbf{k}.\mathbf{r}}u_{n\mathbf{k}}(\mathbf{r}) \tag{3.11}$$

where n indexes of the bands. Injecting Eq. 3.11 into Eq. 3.10 leads to the following equation for the $u_{n\mathbf{k}}(\mathbf{r})$

$$\frac{1}{2m_0}\left(\hat{p}^2 + \hbar^2 k^2 + 2\hbar\mathbf{k}.\hat{\mathbf{p}} \right) u_{n\mathbf{k}}(\mathbf{r}) = E_{n\mathbf{k}}u_{n\mathbf{k}}(\mathbf{r}) \tag{3.12}$$

The idea is then to treat the $\mathbf{k}.\hat{\mathbf{p}}$ term as a perturbation. This gives an expression for the $u_{n\mathbf{k}}$ and $E_{n\mathbf{k}}$ as a function of the $u_{n\mathbf{k_0}}$ and of $E_{n\mathbf{k_0}}$ at the vicinity of $\mathbf{k} = \mathbf{k_0}$. For the conduction band, the simplest flavor of this method is the effective mass approximation (EMA). In the EMA, for a direct band gap semiconductor, we consider only one band, and the resulting dispersion relation is parabolic:

$$E(\mathbf{k}) = E_0 + \frac{\hbar^2 k^2}{2m^*} \tag{3.13}$$

where m^* is the isotropic effective mass, which can be expressed as a function the matrix elements of the $\hat{\mathbf{p}}$ operator between the $u_{n\mathbf{k_0}}$. Moreover, if we add an external potential $V(\mathbf{r})$ varying slowly compared to $V_c(\mathbf{r})$, we may write the eigenstates as:

$$\Psi_n(\mathbf{r}) = \Phi_n(\mathbf{r})u_{n\mathbf{k_0}}(\mathbf{r})e^{i\mathbf{k_0}.\mathbf{r}} \tag{3.14}$$

where $\Phi_n(\mathbf{r})$ is the envelope function, also slowly varying compared to $u_{n\mathbf{k}}(\mathbf{r})$. The equation for $\Phi_n(\mathbf{r})$ can be obtained by substitution $\mathbf{k} \to -i\boldsymbol{\nabla}$ in Eq. 3.13. In the EMA,

$$H = E_0 - \frac{\hbar^2}{2m^*}\nabla^2 + V(\mathbf{r}) \tag{3.15}$$

For the conduction band of silicon, there are six valleys at $|\mathbf{k}| = 0.85 \times 2\pi/a_0$, with anisotropic effective masses. Considering that the six valleys v are uncoupled, and including the anisotropic effective masses, the EMA Hamiltonian of each valley reads:

$$H^v(\mathbf{r}) = -\frac{\hbar^2}{2}\left(\frac{1}{m_x^{*v}}\frac{\partial^2}{\partial x^2} + \frac{1}{m_y^{*v}}\frac{\partial^2}{\partial y^2} + \frac{1}{m_z^{*v}}\frac{\partial^2}{\partial z^2} \right) + V(\mathbf{r}) \tag{3.16}$$

where m_i^{*v} is the effective mass of valley v in the direction i. To be solved numerically, this Hamiltonian is discretized on a finite difference mesh. An advanced version of this model is the 2-bands **k.p** model which couples the valleys at $\pm k_0$ [114].

Unlike the conduction band, the valence band of silicon cannot be approximated by a one or two-bands model. The heavy-hole and light-hole bands are degenerate at the Γ point, and the split-off band is very close. At $\mathbf{k} = \mathbf{0}$, the $u_{n\mathbf{k}}$ can be mapped onto $|J, m_J\rangle$ the eigenstates of the operators $\mathbf{J} = \mathbf{L} + \mathbf{S}$ and J_z. $|\frac{3}{2}, \pm\frac{3}{2}\rangle$ are the heavy-holes states, $|\frac{3}{2}, \pm\frac{1}{2}\rangle$ are the light-holes states and $|\frac{1}{2}, \pm\frac{1}{2}\rangle$ are the split-off states. Therefore, in order to describe the valence band properly around the Γ point we have to use a 6-bands **k.p** model. In bulk silicon, the 6-bands **k.p** Hamiltonian [115] reads in the $\{u_{n\mathbf{k}}\} = \{|\frac{3}{2}, +\frac{3}{2}\rangle, |\frac{3}{2}, +\frac{1}{2}\rangle, |\frac{3}{2}, -\frac{1}{2}\rangle, |\frac{3}{2}, -\frac{3}{2}\rangle, |\frac{1}{2}, +\frac{1}{2}\rangle, |\frac{1}{2}, -\frac{1}{2}\rangle\}$ Bloch functions basis set [116]:

$$H_{6\text{kp}} = - \begin{pmatrix} P+Q & -S & R & 0 & \frac{1}{\sqrt{2}}S & -\sqrt{2}R \\ -S^* & P-Q & 0 & R & \sqrt{2}Q & -\sqrt{\frac{3}{2}}S \\ R^* & 0 & P-Q & S & -\sqrt{\frac{3}{2}}S^* & -\sqrt{2}Q \\ 0 & R^* & S^* & P+Q & \sqrt{2}R^* & \frac{1}{\sqrt{2}}S^* \\ \frac{1}{\sqrt{2}}S^* & \sqrt{2}Q & -\sqrt{\frac{3}{2}}S & \sqrt{2}R & P+\Delta & 0 \\ -\sqrt{2}R^* & -\sqrt{\frac{3}{2}}S^* & -\sqrt{2}Q & \frac{1}{\sqrt{2}}S & 0 & P+\Delta \end{pmatrix} \tag{3.17}$$

where:

$$P = \frac{\hbar^2}{2m_0}\gamma_1\left(k_x^2 + k_y^2 + k_z^2\right) \tag{3.18a}$$

$$Q = \frac{\hbar^2}{2m_0}\gamma_2\left(k_x^2 + k_y^2 - 2k_z^2\right) \tag{3.18b}$$

$$R = \frac{\hbar^2}{2m_0}\sqrt{3}\left[-\gamma_3\left(k_x^2 - k_y^2\right) + 2i\gamma_2 k_x k_y\right] \tag{3.18c}$$

$$S = \frac{\hbar^2}{2m_0}2\sqrt{3}\gamma_3\left(k_x - ik_y\right)k_z . \tag{3.18d}$$

k_x, k_y, k_z are the components of the wave vector in the axes of Fig. 3.2, γ_1, γ_2 and γ_3 are the Luttinger parameters, and Δ is the spin-orbit coupling parameter. In silicon, $\gamma_1 = 4.285$, $\gamma_2 = 0.339$, $\gamma_3 = 1.446$ and $\Delta = 44$ meV. Again if we add a slowly varying potential, we can write the eigenstates as:

$$\Psi_n(\mathbf{r}) = \sum_n \Phi_n(\mathbf{r}) u_{n\mathbf{k_0}}(\mathbf{r}) e^{i\mathbf{k_0}.\mathbf{r}} \tag{3.19}$$

where $\Phi_n(\mathbf{r})$ are the envelope functions. The equations for the envelope functions are obtained after the substitution $\mathbf{k} \to -i\boldsymbol{\nabla}$ and are discretized on a finite differences mesh. Periodic boundary conditions are applied along the wire axis $\mathbf{x}$. Hard wall boundary
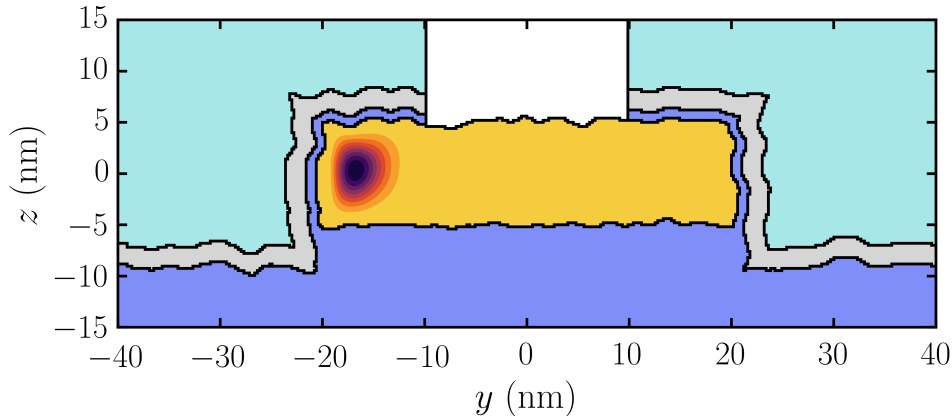
Figure 3.6: Iso-surfaces of the squared wavefunction of a hole obtained from 6-bands **k.p** in the yz-plane at $x = 0$. The same colors have been used for the materials as in Fig. 3.2.

conditions are applied at the surface of the wire (the wave function does not penetrate in the oxides nor in Si_3N_4). As for the treatment of the magnetic field, the effect of the potential vector **A** on the envelope functions is included through Peierls substitution as done in tight-binding [110]. The effect of the magnetic field on the Bloch functions and spin is described by the following Hamiltonian [117]:

$$H_{\text{Bloch}} = -(3\kappa + 1)\mu_B \mathbf{B} \cdot \mathbf{L} + g_0\mu_B \mathbf{B} \cdot \mathbf{S} \qquad (3.20)$$

where **L** is the orbital angular momentum of the Bloch function, **S** its spin, and $\kappa = -0.42$ in silicon. The H_{Bloch} matrices are given in appendix A. Finally, the eigenstates are once again computed with an iterative Jabobi-Davidson eigensolver [112, 113]. As for TB, we then compute the matrix elements $\langle \Psi_i | D_\alpha | \Psi_j \rangle$ from the response potentials D_α.

As an illustration this methodology for the 6-bands **k.p** model is applied to the face-to-face device with surface roughness, with negative bias $(V_{g1}, V_{g2}) = (-0.2, -0.1)$ V, in order to confine a hole state. A cross section of the squared wavefunction is plotted Fig. 3.6, showing the confinement in a corner state, as for electrons.

3.4.3 Comparison of tight-binding and k.p

We have presented two very different methods for the calculations of the electronic states in the system. What are the strengths and weaknesses of each method?

To begin with, tight-binding is a method that provides a faithful description of all bands on a large energy range hence is presumably more accurate in strongly confined systems. In particular, in the conduction band, it describes the valleys and spin-orbit interaction without the need for extra empirical terms in the Hamiltonian. Moreover, TB provides an atomistic description of interfaces and dopants. The main drawback is that it is computationally expensive: the complexity is at best $\mathcal{O}(n)$, for n atoms, which means
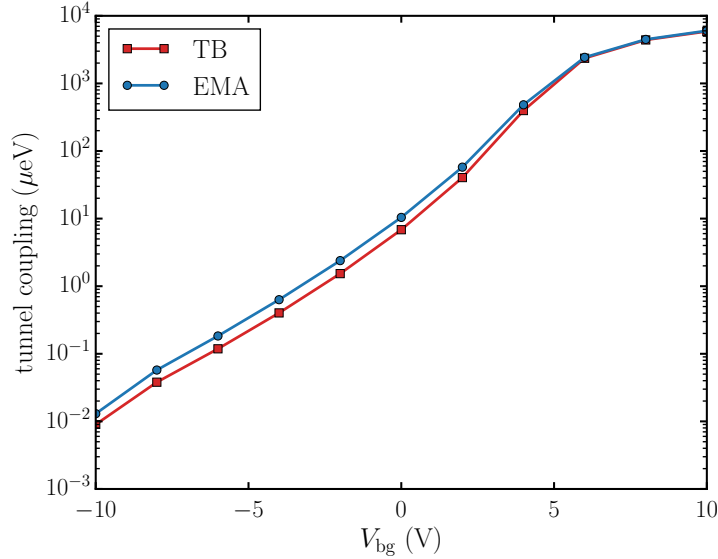
Figure 3.7: Tunnel coupling between the two dots of the face-to-face device as a function of V_{bg}, calculated using TB and EMA.

$\mathcal{O}(d^3)$ with d the typical lateral dimension of the system.

On the other hand, **k.p** gets rid of the underlying atomic lattice, so is less adapted to the study of dopants for instance. In the conduction band, the spin-orbit interaction can only be treated by adding extrinsic Rashba and Dresselhauss Hamiltonians with additional empirical parameters. However, in the valence band, the spin-orbit interaction is well captured by the 6-bands **k.p** model. Moreover, the envelope function formalism is easier to use in analytical models. From the numerical point of view, **k.p** is more tractable than TB, as it is discretized on a mesh which can be adapted to the structures.

Consequently, in the following we use the TB method to study electrons in chapters 4 and 5 in order to have a good description of valley and spin-orbit couplings. We will use the 6-bands **k.p** model in chapter 6, which is dedicated to holes, because it provides an accurate enough description at a much lower cost than TB.

Since both methods should give an accurate description of the envelope functions in weakly confined structures, it is interesting to compare them on a particular calculation, where only the envelope is expected to matter. To that end we have computed the tunnel coupling t between the two corner dots of a face-to-face device as a function of the backgate voltage [98] (contrarily to previous examples, this system has a SiO_2 BOX of 145 nm). When $V_{g1} = V_{g2}$, the first states are the bonding and anti-bonding combinations of the ground states of each isolated dot. Then the difference in energy between the bonding and anti-bonding states is to first order $2t$. We extract t as a function of V_{bg} for electron states using the tight-binding and EMA methods. The results are plotted in Fig. 3.7 and show a very good agreement. This figure also shows that the tunnel coupling can be tuned over several order of magnitude by the electrostatic confinement.

$$D_0 = \frac{1}{\sqrt{2}}\begin{vmatrix} \phi_{0\downarrow}(\boldsymbol{r_1}) & \phi_{0\downarrow}(\boldsymbol{r_2}) \\ \phi_{0\uparrow}(\boldsymbol{r_1}) & \phi_{0\uparrow}(\boldsymbol{r_2}) \end{vmatrix} \qquad D_1 = \frac{1}{\sqrt{2}}\begin{vmatrix} \phi_{0\downarrow}(\boldsymbol{r_1}) & \phi_{0\downarrow}(\boldsymbol{r_2}) \\ \phi_{1\downarrow}(\boldsymbol{r_1}) & \phi_{1\downarrow}(\boldsymbol{r_2}) \end{vmatrix} \qquad D_p = \frac{1}{\sqrt{2}}\begin{vmatrix} \phi_{1\uparrow}(\boldsymbol{r_1}) & \phi_{1\uparrow}(\boldsymbol{r_2}) \\ \phi_{3\downarrow}(\boldsymbol{r_1}) & \phi_{3\downarrow}(\boldsymbol{r_2}) \end{vmatrix}$$
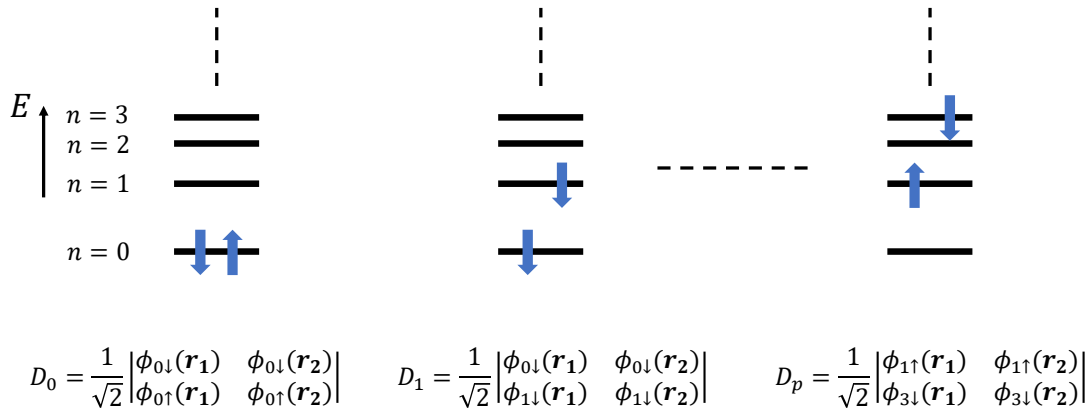
Figure 3.8: Illustrations of a few possible configurations for two-electrons states and their corresponding Slater determinants.

3.5 Many-particles interactions

In our systems, the interactions between two qubits, the Pauli spin blockade, or the effect of the dot's inner electrons (if there are more than one electron in the dot) on the single qubit properties, are all problems that require the description of many-particles interactions. These become too complex very fast with the increasing number of particles. For small numbers of electrons (2 to 4), we use the full configuration interaction method (CI) [118]. The idea of CI is to write the n-particle wavefunctions Ψ_{np} as a linear combination of Slater determinants of the single-particle states.

$$|\Psi_{\mathrm{np}}\rangle = \sum_i c_i |D_i\rangle \tag{3.21}$$

Each Slater determinant D_i correspond to one possible configuration $i.e$ a given occupation of single particle states. A few configurations and their determinants are given in Fig. 3.8. In full CI, we consider all the possible excitations from a set of p single particle states, so for n particles there are $\binom{p}{n}$ Slater determinants in the basis. The Hamiltonian then reads:

$$H|c\rangle = \epsilon|c\rangle \tag{3.22}$$

where $|c\rangle$ is the representation of $|\Psi_{\mathrm{np}}\rangle$ in the basis $\{|D_i\rangle\}$. H features the Coulomb integrals defined by:

$$U_{ijkl} = \int \phi_i^*(\mathbf{r}')\phi_j(\mathbf{r}')W(\mathbf{r}',\mathbf{r})\phi_k^*(\mathbf{r})\phi_l(\mathbf{r})d\mathbf{r}d\mathbf{r}' \tag{3.23}$$

with $W(\mathbf{r},\mathbf{r}')$ the potential created at $\mathbf{r}'$ by a charge at $\mathbf{r}$. They are calculated numerically with the Poisson solver using the single particle wavefunctions. The diagonalization of H thus provides the many-particles energies and the coefficients c_i. Because of the size of the Slater determinants basis is $\binom{p}{n}$, this method has a very high numerical cost even for
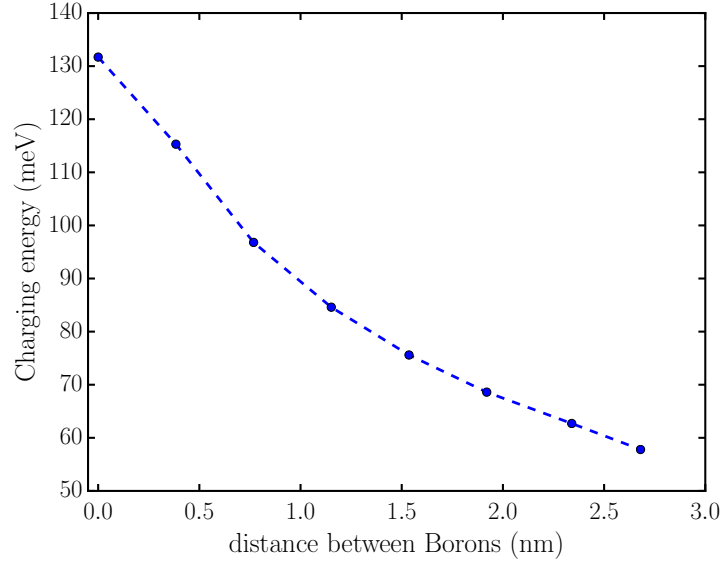
Figure 3.9: Charging energy of states bound to a cluster of two Boron impurities as a function of the distance between them.

a few number of particles.

The current implementation of the method could be improved to enable the description of higher number of particles, for instance to treat the case of a single electron which carries the quantum information, coupled to the dot's inner electrons. To that end we could choose a specific subset of excitations in the Slater determinants.

This method will not be used in the following chapters, which focus on the electrical manipulation of single electrons or holes. However it has been used in some preliminary studies. For instance, in Ref. [92], we have used it to explain the large charging energies observed for the first hole states (up to 70 meV). Here the charging energy is the energy cost when going from one hole to two holes in the dot. The device was doped with Boron atoms, with a high probability of having two dopants closer than 2.5 nm from each other. We used the CI method on top of TB calculations to compute the charging energies of two-particles hole states bounded to cluster of two Boron impurities. The dependence of the charging energy with the distance between dopants is shown Fig. 3.9. According to these calculations, the measured charging energies are compatible with states bound to two dopants distant of $\simeq 2$ nm. Assuming a random distributions of Borons, we have actually estimated that there was a 95 % chance to have two dopants closer than 2.5 nm in such devices.

3.6   Time dependent simulations

In this part we want to describe how the states (computed with one of the previous method) evolve in time when electric signals are applied on the gates. For that purpose, we need to solve the time-dependent Schrödinger equation:

$$H(t)|\Psi(t)\rangle = i\hbar \frac{\partial}{\partial t}|\Psi(t)\rangle. \tag{3.24}$$

We introduce $H_0(V_0)$ the static Hamiltonian at a reference bias point $V_0 \equiv \{V_\alpha^0\}$, with V_α^0 the potential applied on gate α (including the backgate), and $\delta V_\alpha(t) = V_\alpha(t) - V_\alpha^0$. Then we can expand $H(t) = H[V_\alpha(t)]$ to first order:

$$H(t) = H[V_\alpha^0 + \delta V_\alpha(t)] \tag{3.25a}$$

$$= H[V_\alpha^0] + \sum_\alpha \delta V_\alpha(t) \frac{\partial V_{\text{tot}}}{\partial V_\alpha}\Big|_{V_\alpha^0} \tag{3.25b}$$

$$= H_0(V_0) + \sum_\alpha \delta V_\alpha(t) D_\alpha \tag{3.25c}$$

As in section 3.3, $D_\alpha = \frac{\partial V_{\text{tot}}(\mathbf{r})}{\partial V_\alpha}|_{V_0}$ is the derivative of the total potential $V_{\text{tot}}(\mathbf{r})$ with respect to gate α. Eq. 3.25 is exact if the electrostatics is linear with respect to all V_α, which is the case in our simulations.

We solve this equation in the basis of the N lowest eigenstates of the Hamiltonian $H_0(V_0)$. $H_0(V_0)$ is therefore diagonal in this basis set, and all matrix elements of all D_α are precomputed in the tight-binding or **k.p** calculations. We sample the control signal $\delta V_\alpha(t)$ on a regular grid with time step δt. Assuming that the $\delta V_\alpha(t)$ vary slowly enough at the scale of δt, Eq. 3.24 can be integrated as follows:

$$|\Psi(t + \delta t)\rangle = \exp\left[-\frac{i\delta t}{\hbar} H(t + \delta t/2)\right]|\Psi(t)\rangle \tag{3.26}$$

with $H(t + \delta t/2) = [H(t+) + H(t + \delta t)]/2$. The evolution operator $\exp(-iH\delta t/\hbar)$ needs to be computed at each time step. This can be done from an exact diagonalization of the $N \times N$ matrix $H(t + \delta t/2)$, which can be numerically expensive. In our case, we expand the evolution operator as a fast-converging series of Chebyshev polynomials [119]. The use of Chebyshev polynomials is faster than exact diagonalization and ensures a uniform convergence over the whole spectrum of H.

To illustrate this method we use again the face-to-face device. The reference bias applied on the gate is $V_0 = \{V_{g1}, V_{g2}\} = \{0.1, 0.1\}$ V. We apply a sinusoidal signal on gate 1 in order to drive dot 1 - dot 2 transitions. Namely, we apply $\delta V_{g1}(t) = V_{ac} \sin(2\pi f t)$, with $V_{ac} = 15$ mV and $f = 5$ MHz. We solve the time-dependent Schrödinger equation
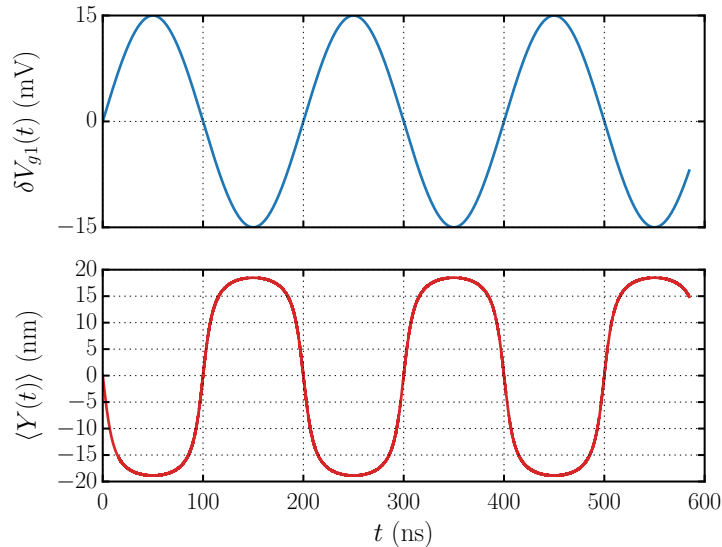
Figure 3.10: Signal on gate 1 $\delta V_{g1}(t)$ and average position $\langle Y(t) \rangle$ as a function of time.

in order to get $|\Psi(t)\rangle$, and we compute the average position $\langle Y(t) \rangle$ on the **y** axis as a function of time. $\delta V_{g1}(t)$ and $\langle Y(t) \rangle$ are plotted in Fig. 3.10 as a function of time. We indeed observe the electron oscillating between the two dots. In this kind of simulation, we can also monitor the spin or the state probabilities as a function of time. This will be used in chapter 5, where a qubit operation is studied using the time-dependent solver.

3.7 Conclusion

We have presented the methodology we are going to use in the chapters 4 to 6, which is well suited to the study of a single qubits. The realistic calculations of the potential and electronic structure enable precise comparisons with experimental measurements. Validating these comparisons is essential as it will allow us to make theoretical predictions and proposals using the simulations. Moreover, the simulations will help in the construction and validation of analytical models. The coupling of the electronic structure calculations to the time-dependent solver gives the possibility to make numerical experiments of qubit control with an access to all observables.

Broadly speaking, the first interest of these simulations is to give different insights on the physics than can be achieved in experiments. The joint use of measurements and simulations can lead to a deep understanding of the qubits behavior. The second interest is that simulations are way faster and cheaper than experiments. Indeed, the fabrication of a batch of qubits using microelectronics techniques can take up to one year, and the low-temperature experiments can take a few months. We can thus explore in advance the influence of the geometrical parameters in order to prepare the design of future devices, propose new experiments, and test the validity of proposals.

Chapter 4

Electrical control of the electron spin

Le spin d'un électron confiné dans le silicium est un candidat intéressant pour stocker de l'information quantique, étant données ses très bonnes propriétés de cohérence, mais pour en faire un quantum bit il est nécessaire de pouvoir le contrôler. Puisque le spin est un dipôle magnétique, un moyen naturel de le manipuler est de le coupler à un champ magnétique oscillant. Cependant, dans la perspective de réaliser un ordinateur quantique, coupler localement le spin à un champ magnétique soulève certains problèmes. Il peut être préférable de coupler le spin à un champ électrique, via le couplage spin-orbite qui peut être intrinsèque ou extrinsèque.

Dans ce chapitre nous présentons et étudions un résultat expérimental d'importance pour les qubits de spin sur silicium : l'observation de résonance électrique de spin (EDSR ou "electric-dipole spin resonance"), sans élément extrinsèque. Le spectre fréquence/champ magnétique montre plusieurs résonances qui sont compatibles avec la présence d'un état de vallée excité et de couplage spin-orbite. Nous reproduisons ces résultats avec des calculs de liaisons fortes et proposons un modèle analytique qui rend compte de la physique de cette manipulation électrique de spin. Le mécanisme en jeu implique une combinaison du couplage dipolaire inter-vallée et du couplage spin-orbite inter-vallée. Cette interaction spin-orbite est responsable d'un anticroisement des états lorsque l'énergie de Zeeman est égale à la séparation entre les vallées (ou "valley splitting"). La dépendance en champ magnétique de la fréquence de Rabi est étudiée et montre une forte non-linéarité au voisinage de cet anticroisement. Par une étude des symétries nous montrons que l'interaction spin-orbite est rendue possible par la faible symétrie des états dans la boîte quantique. Ceci est confirmé par les calculs ainsi que par l'anisotropie mesuré du courant en fonction de l'orientation du champ magnétique.

The spin of the electron in silicon is an interesting candidate for storing quantum information given its excellent coherence properties [45,46], but in order to make quantum bit we have to be able to manipulate it.

Since the spin is a magnetic dipole, the natural way to manipulate it is to couple it to an oscillating magnetic field. However, in the prospect of making a quantum computer, coupling locally a spin qubit to a magnetic field raises some challenges. Although some group choose to address these challenges directly [74,120], coupling the spin to the electric field gives a different pathway that could simplify the design and thus facilitate the large-scale integration. This is possible only if there is a coupling between the orbital motion of the electron and its spin. This coupling can be engineered for instance with a micro-magnet generating a slanting magnetic field [25,76,80,86,121,122], or be intrinsic to the material, that is the spin-orbit coupling (SO). The SO is generally present in atoms and solids: due to a relativistic effect, electrons moving in an electric field experience in their reference frame an effective magnetic field which couples to their spin. In the case of electrons in silicon, however, SO is intrinsically very weak.

In this chapter we will present the first demonstration of the electrical control of the electron spin in silicon without extrinsic elements. We will first present the experimental device and set-up, and then analyse the results of the electric dipole spin resonance (EDSR) measurement. We show that the observed spectrum involves an excited valley state with a small valley splitting (36 μeV), and a spin-orbit effect. We will then explain with tight-binding simulations and an analytical model the physics behind electrical manipulation, and show that it involves a combination of intervalley dipolar and intervalley spin-orbit interactions. We show that this peculiar spin-orbit interaction is only made possible by the low symmetry of the dot. The anisotropy of the measured current with the magnetic field backs up this interpretation.

4.1   Measurement of EDSR in a Silicon MOS double quantum dot

This study of the electrical control of the electron spin in a silicon quantum dot has been motivated by the first experimental observation of electric dipole spin resonance (EDSR) by Andrea Corna during his PhD at CEA INAC [53,123]. He measured a double quantum dot in series in the Pauli spin blockade regime, with, for first intention, to perform an electron spin resonance (ESR) experiment with a nearby antenna. Yet he realized that a microwave signal applied on one of the MOS gates was lifting the blockade, with a clear resonance, signature of EDSR [22,124]. In the following paragraphs we are going to present the protocol and the main results of this experiment.
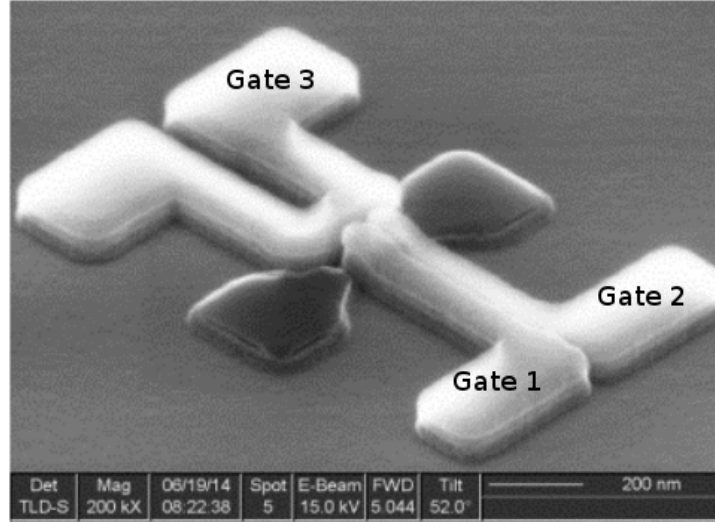
Figure 4.1: SEM image of a similar sample after source/drain epitaxy.
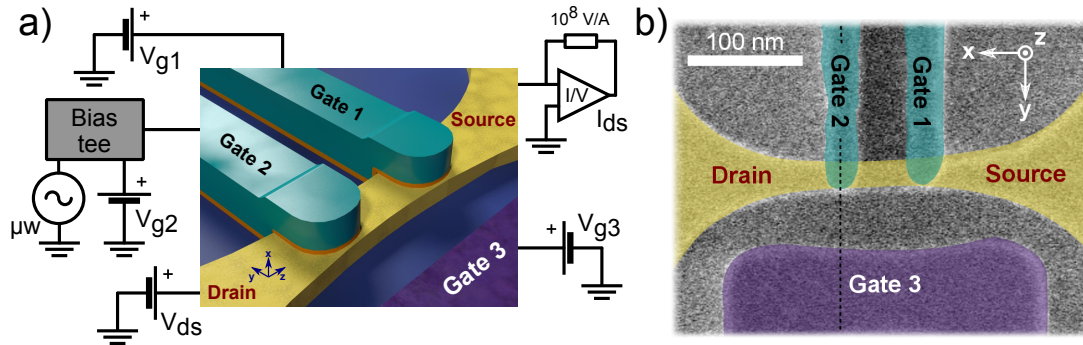
Figure 4.2: (a) Sketch of the sample and measurement setup. The silicon nanowire is coloured in yellow, the two top gates in green and the side gate in violet. The gate oxides are colored in orange and the buried oxide (BOX) is in blue. (b) Colourized device top view obtained by scanning electron microscopy before the deposition of the spacers of a device similar to the one used in the experiment, with same colour code. Adapted from Ref. [53]

The device consists in a silicon nanowire ($H = 12$ nm, $W = 30$ nm) with two metallic gates in series (G1 and G2). The two gates overlap only part of the channel, in order to create two corner quantum dots. They are connected to the source and drain contacts, which are degenerately Arsenic-doped reservoirs of electrons. An additional gate, G3, originally intended to work as an antenna, is located at 50 nm from the channel. G3 is biased at $V_{g3} = -0.28$ V throughout the experiment in order to push the wavefunctions further in the corners. SEM and TEM pictures of the device are shown in Fig. 4.1 and 4.2b, and the device and measurement setup is schematized in Fig. 4.2a. In the Coulomb blockade regime, the potential V_{g1} and V_{g2} are adjusted in order to fill the quantum dots below the gates with small numbers of electrons n_1, n_2. Transports measurement are performed in a dilution fridge at $T = 15$ mK, by setting a small source-drain bias and measuring the current.
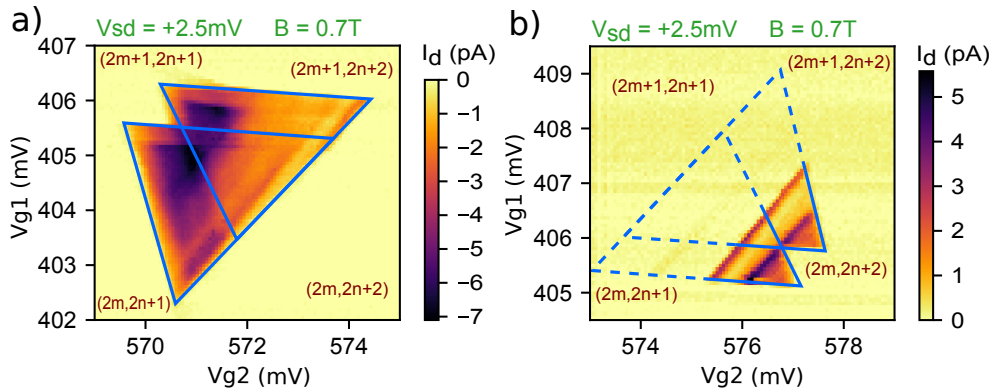
Figure 4.3: Bias triangles. (a) Map of the current I_{ds} as a function of V_{g1} and V_{g2} at finite $V_{ds} = -2.5$ mV around a pair of triangles showing current rectification. The magnetic field $B = 0.7$ T is parallel to $\mathbf{x} - \mathbf{y}$ (see axes on Fig. 4.2). The number of electrons in each dot is given between parentheses. (b) Same as (a) at opposite $V_{ds} = +2.5$ mV. Adapted from Ref. [53]

In this double quantum dot system, the current can flow only if the energy levels of the dots are properly aligned, which results in pairs of triple points [125]. The typical current signature is a couple of conduction triangles in the (V_{g1}, V_{g2}) plane, shown Fig. 4.3a. Under a finite magnetic field, if the triple points correspond to a transition (n_1, n_2) $\rightarrow (n_1 - 1, n_2 + 1)$, with n_1, n_2 odd, the current is blocked in a region at the base of triangle as shown Fig. 4.3b, which is a signature of Pauli spin blockade. For a reverse source-drain bias, the transition $(n_1 - 1, n_2 + 1) \rightarrow (n_1, n_2)$ is never blocked and the current can flow throughout the whole triangle. The Pauli blockade in presence of the valley degree of freedom is actually a bit more complex than the picture that we have drawn in chapter 1. In the appendix B we give a more detailed explanation of the Pauli blockade with spin and valleys. It is very interesting to see that in Fig. 4.3b there is little difference between the background current outside the triangle and within the blocked part, highlighting a nearly perfect blockade. In the qubit perspective, a reliable readout mechanism is very important for the readout fidelity.

In the following, (V_{g1}, V_{g2}) are chosen so that we are in the Pauli blockade regime, and a microwave signal is applied on G2. The frequency ν of the microwave signal and the amplitude B of the magnetic field are swept, and we observe a set of resonance lines in Fig. 4.4 in the current versus ν and B maps. On the lines labelled A, B, C, V, H, the Pauli blockade is lifted and the current is enhanced: we evidenced here electric dipole spin resonance (EDSR). As pure spins are not coupled by an electric field, either an intrinsic or extrinsic spin-orbit effect must be involved. The other regularly spaced horizontal lines are due to resonances in the cables or photon assisted tunnelling. Other than these parasitic lines, the resonance lines are remarkably clear.

The equations for lines A, B, C, appear to be a modified version of the usual resonance
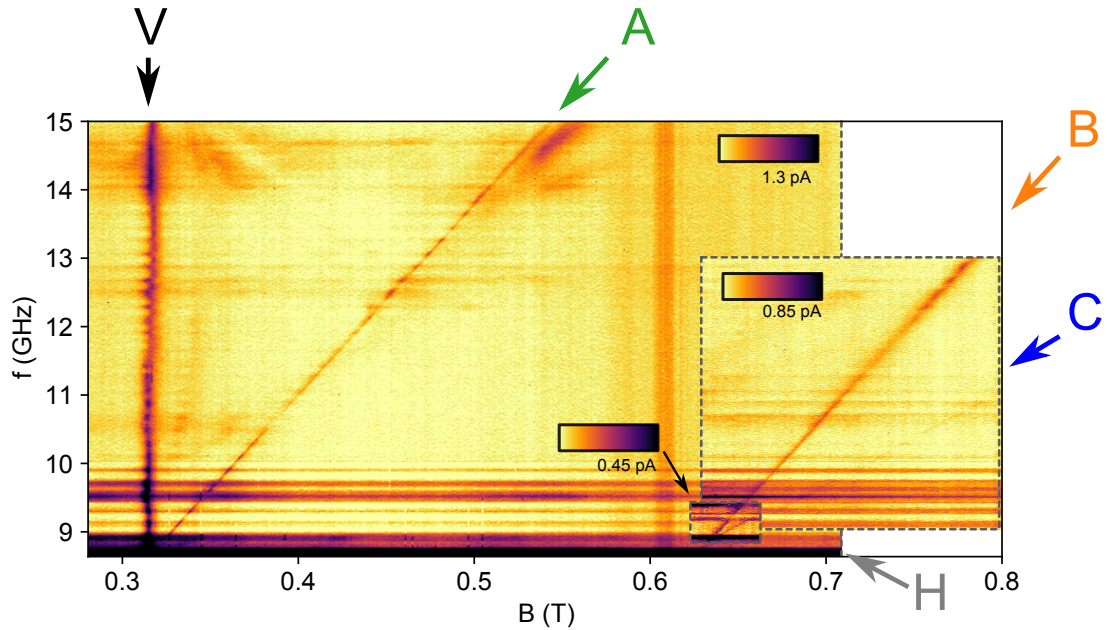
Figure 4.4: Experimental EDSR map. The measured current is plotted as a function of the frequency of the microwave signal and of the magnetic field amplitude. The relevant lines are labelled A, B, C, V, H. Adapted from Ref. [53].
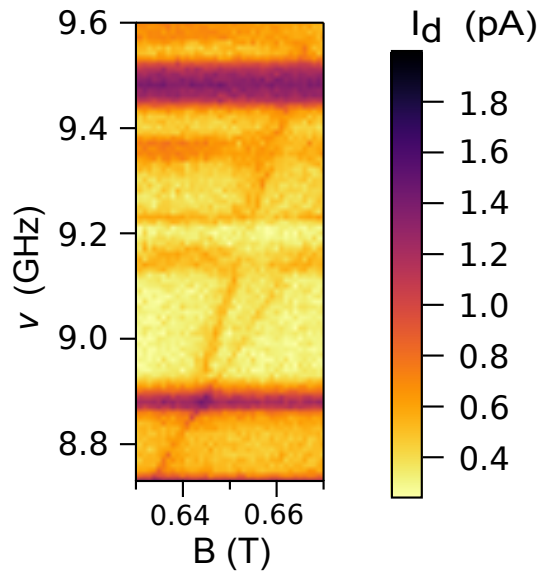

Figure 4.5: Zoom on lines H, B, C of the EDSR map. This scan comes from a different measurement than the one of Fig. 4.4, there are less parasitic lines.

Line	g	K (μeV)
A	1.97 ± 0.005	-0.32
B	2.00 ± 0.01	-36.9
C	0.96 ± 0.01	43×10^{-3}

Table 4.1: Extracted parameters of resonance lines A, B, C.

condition, namely:

$$h\nu = g\mu_B B + K \tag{4.1}$$

where ν is the frequency of the applied microwave signal, g is the gyromagnetic factor, and K is an additional energy splitting independent of the magnetic field. With this equation we extract the slope and intercept of lines A, B, C in Table 4.1. As for the other lines, the vertical line V appears at constant magnetic field $B = 316$ mT independently of the RF frequency. This value correspond to a Zeeman $g\mu_B B \simeq 36.2$ μeV (for $g \simeq 2$). The horizontal line H appears at $\nu = 8.88$ GHz independently of magnetic field, which also corresponds to an energy of 36 μeV. The H line is best visible on another scan, Fig. 4.5, with less parasitic lines. From these data we can ascribe line A to a resonance of the microwave photon with the Zeeman splitting $E_z = g\mu_B B$, with $g = 1.98$ compatible with the reported gyromagnetic factors of electrons in silicon ($g \simeq 2$ [126]), and an offset $K \simeq 0$. The line C is also extrapolating to $h\nu = 0$ at $B = 0$, with half the slope of line A. It can be attributed to a second-harmonic (two-photons) process. Interestingly, line B also has $g \simeq 2.00$ and extrapolates to $h\nu = 36$ μeV at $B = 0$, the same value characteristic of line H and line V. This observation led us to the conclusion that a second orbital state was involved, spaced by 36 μeV from the ground state. Such a small value can only correspond to another valley state as higher orbitals excitations lie way farther in energy, and we will confirm this later by tight-binding simulations.

In order to understand the experimental EDSR spectrum, we neglect in first approximation the hybridization between the two quantum dots and consider only the quantum dot 2 filled with one electron. In this silicon nanowire, the confinement is strongest along the **z** direction (normal to the substrate plane), so that the low-energy levels belong to the $\Delta_{\pm z}$ valleys. Valley coupling at the Si/SiO$_2$ interface lifts the two-fold valley degeneracy [43, 47, 51, 127], resulting in two spin-degenerate valley eigenstates $|v_1\rangle$ and $|v_2\rangle$, with respective energy E_1, E_2. The valley splitting is $\Delta = E_2 - E_1$. In the simplest approximation the states $|v_1\rangle$ and $|v_2\rangle$ are bonding and anti-bonding combinations of the $\Delta_{\pm z}$ states. In presence of a static magnetic field, the state v_1 is then split into $|v_1 \downarrow\rangle$, $|v_1 \uparrow\rangle$ with respective energies $E_1 - \frac{1}{2}\mu_B B$ and $E_1 + \frac{1}{2}\mu_B B$; and the state v_2 is split into $|v_2 \downarrow\rangle$, $|v_2 \uparrow\rangle$ with respective energies $E_2 - \frac{1}{2}\mu_B B$ and $E_2 + \frac{1}{2}\mu_B B$ (the spin being quantized along **B**). When $B = \frac{\Delta}{g\mu_B}$, $|v_1 \uparrow\rangle$ and $|v_2 \downarrow\rangle$ are resonant so they might anticross [50]. Fig. 4.6a shows the energy levels of a one-electron system with two valleys and their evolution with magnetic field, assuming an anticrossing between $|v_1 \uparrow\rangle$ and $|v_2 \downarrow\rangle$. This anticrossing,
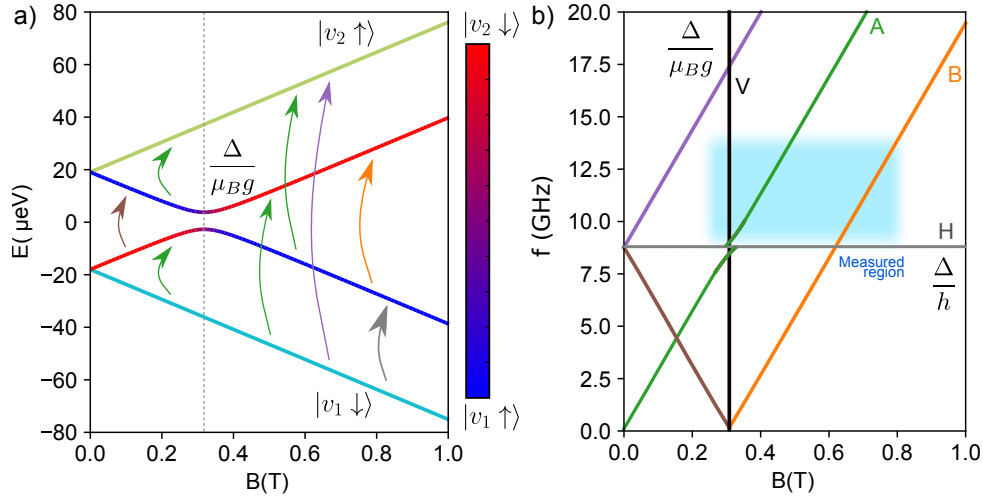
Figure 4.6: (a) Energy diagram of the first four states as a function of the magnetic field amplitude. An avoided crossing is supposed at $B = \Delta/(g\mu_B)$. The energy of $|v_1 \downarrow\rangle$ is in light blue, and the energy of $|v_2 \uparrow\rangle$ is in green. The spin and valley composition of the hybridized states is quantified by a colour scale. (b) Sketch of the possible transitions noted by the arrows in (a). The experimentally measured region is in light blue.

due to spin-orbit interaction, couples $|v_1 \uparrow\rangle$ and $|v_2 \downarrow\rangle$ in mixed spin-valley states. On Fig. 4.6b are shown the expected EDSR lines, with a blue frame highlighting the region measured experimentally.

It is worth noting that some of these resonances were observed in a Si-SiGe planar quantum dot with a micro-magnet by Scarlino *et al* [61]. In this paper they do not measure the H line because their readout mechanism is ineffective in this energy range, however they observe it in simulations. In another paper Hao *et al* [54] have measured similarly the ESR spectrum of a double quantum dot. They do not observe the H line because it is purely an EDSR feature (an oscillating magnetic field cannot couple valley states of same spin). However they detect in the ESR spectrum the anticrossing on line A. They identify this anticrossing as an inter-valley spin-orbit interaction with a strength of 125 neV.

In conclusion we have seen that in a silicon double quantum dot device the spin blockade is lifted by a microwave signal, signature of EDSR. Sweeping the magnetic field results in a rich resonance spectrum showing several state transitions. It indicates the presence of a valley excited state spaced by 36 μeV from the ground state. In the next part we will unveil the physics behind EDSR in the conduction band of silicon through theoretical modeling and tight-binding simulations.

4.2 Model for EDSR with inter-valley spin-orbit interaction.

The spin degree of freedom does not couple with the electric field, so as said earlier, a spin-orbit interaction must be involved to couple the orbital motion of the electron to its spin. To study this in our particular system we performed tight-binding simulations including spin-orbit through the Hamiltonian:

$$H_{SO} = 2\lambda_{SO} \sum_{iat} \mathbf{L_{iat}}.\mathbf{S} \qquad (4.2)$$

with *iat* the atomic index and $\lambda_{SO} = 0.01851$ eV [109] (see chapter 3). Tight-binding is particularly well suited to the descriptions of these silicon devices since it accounts for valley and spin-orbit coupling at the atomistic level. In particular, there is no need for extrinsic terms in the Hamiltonian such as interface terms on the interface for the valley coupling, or Rashba or Dresselhaus terms for the spin-orbit coupling.

We consider the prototypical device of Fig. 4.7a, which consists in a [110] silicon nanowire, $W = 30$ nm wide and $H = 10$ nm thick. It is etched in a (001) silicon-on-insulator film on top of a 25 nm thick buried oxide (BOX). The backgate is polarized at $V_{bg} = 0$ V. The quantum dot is defined by the central, 30 nm long gate. This gate covers only part of the nanowire as in the experiment, in order to confine a corner state. The gate stack consists in a 1 nm layer of SiO_2 and a 2 nm layer of HfO_2. The corner quantum dot is surrounded by two side gates, placed 30 nm on the left and right of the central gate, which control the barrier height between the dots (periodic boundary conditions being applied along the wire). The two side gates are polarized at $V_{s1} = V_{s2} = 0$ V. They mimic here the quasi-metallic source/drain contacts. Finally the atomistic segment of the device considered in the tight-binding calculations is 80 nm long and contains 1 120 000 atoms. The dangling bonds at the surface are saturated with hydrogen atoms.

We compute the first four eigenstates of this device using tight-binding. As explained before, with confinement and at the Si/SiO_2 interface, the first two spin-degenerate states are $|v_1\rangle$ and $|v_2\rangle$, separated by the valley splitting $\Delta = E_2 - E_1$. We apply a magnetic field which splits each spin-degenerate state via the Zeeman interaction. Then the first four eigenstates that we compute are expected to be $\{|v_1 \downarrow\rangle, |v_1 \uparrow\rangle, |v_2 \downarrow\rangle, |v_2 \uparrow\rangle\}$ with respective energy $\{E_1 - \frac{1}{2}g\mu_B B, \ E_1 + \frac{1}{2}g\mu_B B, \ E_2 - \frac{1}{2}g\mu_B B, \ E_2 + \frac{1}{2}g\mu_B B\}$. We may neglect the effects of the magnetic field on the orbital motion of the electrons in a first approximation. The wavefunctions $\varphi_{n,\sigma} = \langle \mathbf{r}|v_n\rangle$ ($n = 1, 2$ and $\sigma = \downarrow, \uparrow$) can then be chosen real.

To understand the role of SO, let us compare calculations of the energy levels with and without SO. The results are shown Fig. 4.8: the SO is responsible for an anti-crossing between states $|v_1 \uparrow\rangle$ and $|v_2 \downarrow\rangle$, thus mixing spins and valleys. From the anti-crossing gap,
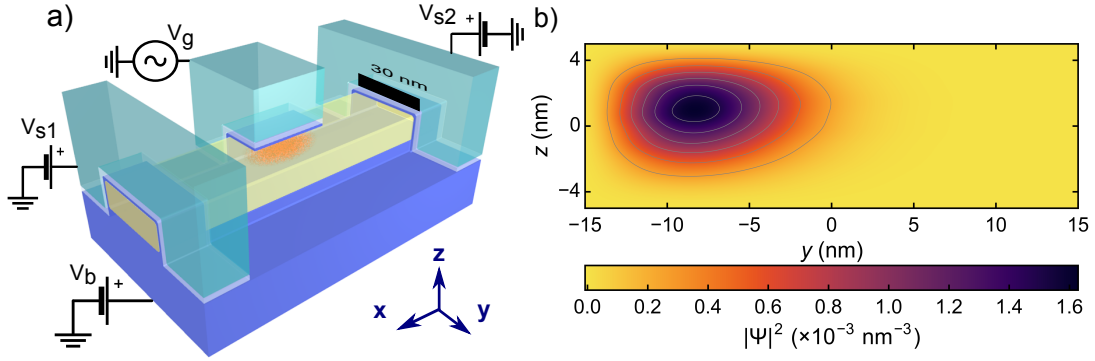
Figure 4.7: (a) Schematics of the device. The silicon nanowire is in yellow, SiO_2 in blue, HfO_2 in light gray and the gate are in dark green. The squared wavefunction is schematized in orange. (b) Cross-section of the squared wavefunction in the (yz) plane, computed with tight-binding.

this SO effect seems small but sizeable compared to what is expected for silicon [128]. This observation incites to build a model dealing with the SO Hamiltonian as a perturbation. A first step is to apply a simple non-degenerate perturbation theory, valid far from the anti-crossing.

In perturbation theory, a perturbed state $|\tilde{\Psi}_k\rangle$ is given to first order as a function of the unperturbed states $\{|\Psi_n\rangle\}$ by:

$$|\tilde{\Psi}_k\rangle = |\Psi_k\rangle + \sum_{n\neq k} \frac{\langle\Psi_n|\tilde{H}|\Psi_k\rangle}{E_k - E_n}|\Psi_n\rangle \tag{4.3}$$

where $\tilde{H}$ is a perturbation. Here, treating H_{SO} as a perturbation yields to first order:

$$|\tilde{\Psi}_{v_1\downarrow}\rangle = |v_1 \downarrow\rangle - \frac{C_{v_1v_2}}{\Delta + g\mu_B B}|v_2 \uparrow\rangle - \frac{iR_{v_1v_2}}{\Delta}|v_2 \downarrow\rangle + ... \tag{4.4a}$$

$$|\tilde{\Psi}_{v_1\uparrow}\rangle = |v_1 \uparrow\rangle + \frac{C^*_{v_1v_2}}{\Delta - g\mu_B B}|v_2 \downarrow\rangle + \frac{iR_{v_1v_2}}{\Delta}|v_2 \uparrow\rangle + ... \tag{4.4b}$$

The sum goes on for the orbital excited states, and we have used the following spin-orbit matrix elements:

$$C_{v_1v_2} = \langle v_2 \uparrow|H_{SO}|v_1 \downarrow\rangle = -\langle v_1 \uparrow|H_{SO}|v_2 \downarrow\rangle \tag{4.5a}$$

$$R_{v_1v_2} = -i\langle v_2 \downarrow|H_{SO}|v_1 \downarrow\rangle \tag{4.5b}$$

The above equalities follow from time-reversal symmetry considerations for real wavefunctions. $C_{v_1v_2}$ is complex and $R_{v_1v_2}$ is real.

We want now to drive spin rotations by applying a microwave signal on the gate, of the form $V_g(t) = V_g^0 + V_{ac}\sin(2\pi\nu t + \varphi)$. When the frequency ν is resonant with the splitting between two states $|\Psi_i\rangle$, $|\Psi_j\rangle$, the frequency of the Rabi oscillations driven by

the electric field read:

$$f_R = \frac{eV_{ac}}{h} |\langle \Psi_i | D | \Psi_j \rangle| \tag{4.6}$$

Here $\hat{D}$ is the gate coupling operator, i.e the electrostatic response of the system to an excitation of the gate: $\hat{D}(r) = \frac{\partial V_{tot}(\mathbf{r})}{\partial V_g}$, formally the partial derivative of the total potential $V_{tot}(\mathbf{r})$ with respect to the gate potential V_g. Coming back to the perturbation theory, we can inject the expression of the first order state into Eq. 4.6. We make the hypothesis that we can restrict the sum over states to to $\{|v_1 \downarrow\rangle, |v_1 \uparrow\rangle, |v_2 \downarrow\rangle, |v_2 \uparrow\rangle\}$, that is the spin and valley states of the first orbital. We use the fact that $\hat{D}$ cannot couple states with opposite spins. This yields:

$$f_R = eV_{ac} \left| \langle \tilde{\Psi}_{v_1\downarrow} | D | \tilde{\Psi}_{v_1\uparrow} \rangle \right| \tag{4.7}$$

$$= \frac{2eV_{ac}}{h} |C_{v_1v_2}| |D_{v_1v_2}| \left| \frac{1}{\Delta - g\mu_B B} + \frac{1}{\Delta + g\mu_B B} \right| \tag{4.8}$$

where we have introduced the electric dipole matrix element between valleys v_1 and v_2:

$$D_{v_1v_2} = \langle v_1\sigma | D | v_2\sigma \rangle = \langle v_2\sigma | D | v_1\sigma \rangle \tag{4.9}$$

We can already notice that $R_{v_1v_2}$ does not contribute to f_R (as it couples states with the same spin). In the case were $|\Delta - g\mu_B B| \gg 0$, we can expand the denominators of Eq. 4.8 to first order in B:

$$f_R = \frac{2eV_{ac}g\mu_B B |C_{v_1v_2}| |D_{v_1v_2}|}{h\Delta^2} \tag{4.10}$$

This simple model gives interesting insights into the physics: the EDSR is mediated by virtual transitions, $|v_1 \downarrow\rangle \xrightarrow{D} |v_2 \downarrow\rangle$ due to inter-valley dipolar coupling, and $|v_2 \downarrow\rangle \xrightarrow{H_{SO}} |v_1 \uparrow\rangle$ due to inter-valley spin-orbit coupling. In other words, the electric field can drive spin rotations only if the spin orbit coupling hybridize spin and valley. We will come back in part 4.3 to the non-trivial origin of the spin-orbit coupling here, which is expected to be small in the conduction band of silicon [50, 54, 64, 129–131]. The dipolar interaction between valleys is less surprising. Indeed the valley wavefunctions feature oscillations in quadrature in the strongest confinement direction, leading to a finite dipolar coupling [52, 132, 133]. This will be discussed in more details in the next chapter. For now, it is illustrated it in Fig. 4.9, in which the p_z orbital component of the $|v_1\rangle$ and $|v_2\rangle$ states is plotted in real space. The interface roughness can also induce dipolar coupling in the other directions [52, 133]. From Eq. 4.10 the Rabi frequency is linear in B when $|\Delta - g\mu_B B| \gg 0$. If $B = 0$, the time-reversal symmetry is not broken and the contributions of terms $\propto C_{v_1v_2}$ in Eqs. 4.4a and 4.4b cancels out so $f_R = 0$. f_R is also linear in V_{ac}, so that in the following we will set $V_{ac} = 1$ mV, and the Rabi frequency can be understood in MHz/mV.

We can compute f_R from Eq. 4.6 with the tight-binding wavefunctions. We have verified that we obtain the same value for f_R with the solution of the time-dependent
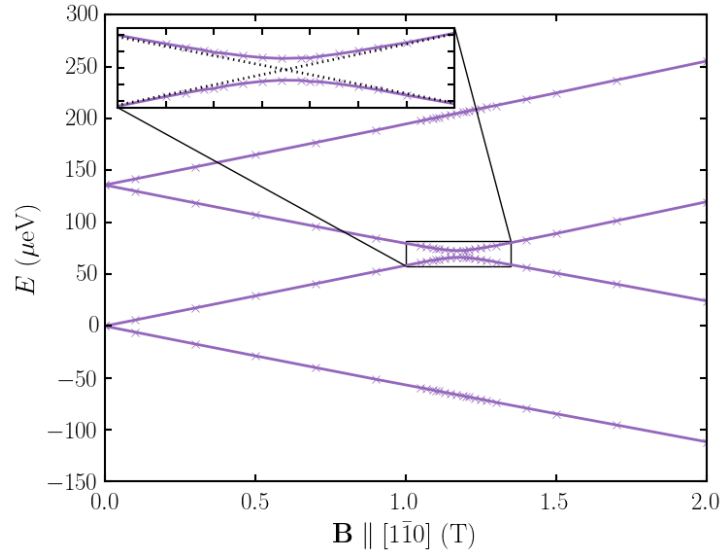
Figure 4.8: Energy levels computed with tight-binding, in violet including spin-orbit coupling. The zoomed part show the anticrossing, with in dotted black the calculations without spin-orbit interaction.
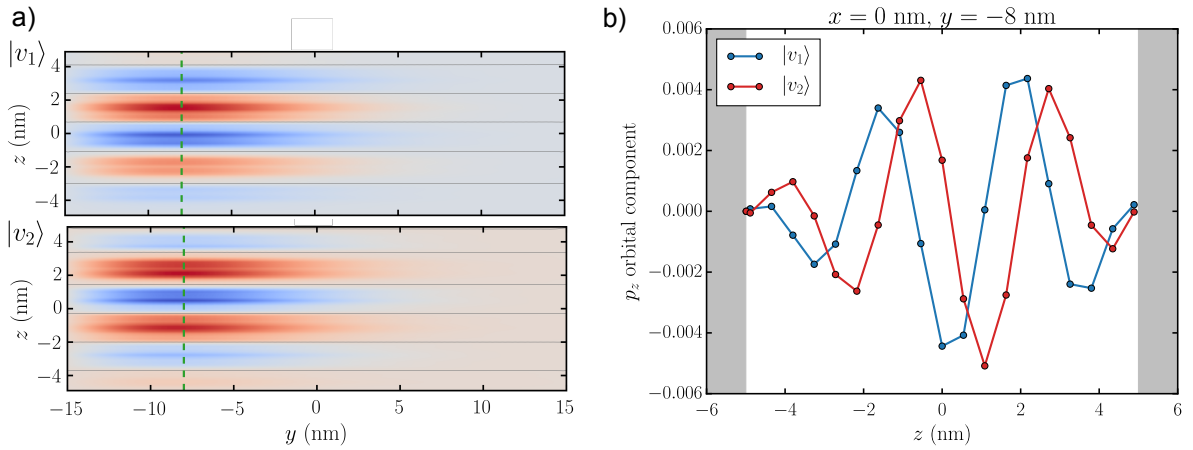
Figure 4.9: (a) p_z atomic orbital component of the $|v_1\rangle$ and $|v_2\rangle$ states in the (yz) plane at $z = 0$ nm. (b) Cut of (a) along the green dashed line at $y = -8$ nm. The two states can be coupled by the potential $V(z) = -eE_z\mathbf{z}$ of an electric field $\mathbf{E}$ along $\mathbf{z}$.
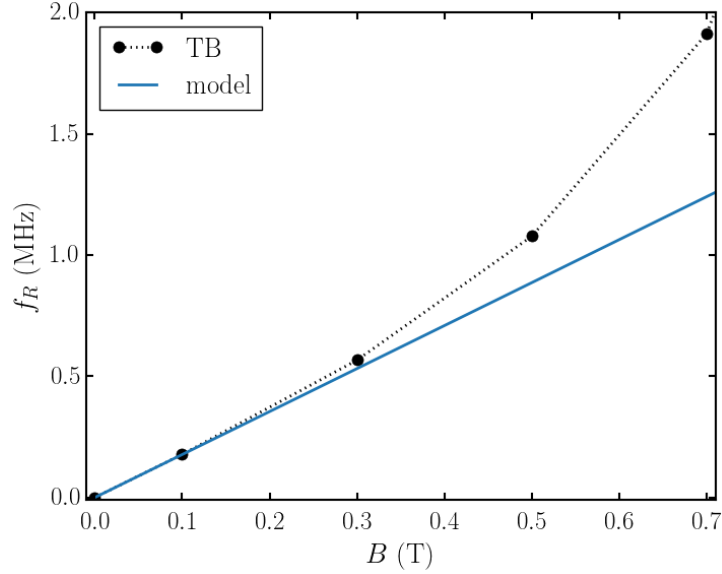
Figure 4.10: Rabi frequency against magnetic field, from direct TB simulations and non-degenerate perturbation theory model.

Schrödinger equation (see chapter 3) as with Eq 4.6. We can also compute $D_{v_1 v_2}$ and $C_{v_1 v_2}$ in tight-binding, by switching off the spin-orbit interaction to calculate the uncoupled states $|v_n \sigma\rangle$ and then get the matrix elements from Eqs. 4.5a and 4.9. We perform the calculation on the device of Fig. 4.7 with $V_g = 0.1$ V. We plug the computed $C_{v_1 v_2}$ and $D_{v_1 v_2}$ into Eq. 4.10, and we compare the outcome to the direct TB calculations in Fig. 4.10. In this calculation $\mathbf{B}$ is parallel to $\mathbf{y}$, $|D_{v_1 v_2}| = 180$ μV/V, $|C_{v_1 v_2}| = 3.25$ μeV, and $\Delta = 136$ μeV. We can see that for $B > 0.3$ T the Rabi frequency starts to move away from the linear perturbation model. This approach is, indeed, not valid when Δ is close to $g\mu_B B$, because one of the terms is diverging in Eq. 4.8. This let us anticipate that there is an enhancement of f_R at this point. We may deal with the anticrossing using degenerate perturbation theory in the $\{|v_1 \uparrow\rangle, |v_2 \downarrow\rangle\}$ subspace, and using non-degenerate perturbation theory for the first and fourth excited states, which are weakly coupled. However such strategy would spoil the cancellations to achieve the proper behaviour $f_R(B \to 0) \to 0$. Consequently a proper way to address this case is to treat the SO Hamiltonian in the basis $\{|v_1 \downarrow\rangle, |v_1 \uparrow\rangle, |v_2 \downarrow\rangle, |v_2 \uparrow\rangle\}$:

$$H = \begin{pmatrix} E_1 - \frac{1}{2}g\mu_B B & 0 & -iR_{v_1 v_2} & C^*_{v_1 v_2} \\ 0 & E_1 + \frac{1}{2}g\mu_B B & -C_{v_1 v_2} & iR_{v_1 v_2} \\ iR_{v_1 v_2} & -C^*_{v_1 v_2} & E_2 - \frac{1}{2}g\mu_B B & 0 \\ C_{v_1 v_2} & -iR_{v_1 v_2} & 0 & E_2 + \frac{1}{2}g\mu_B B \end{pmatrix} \tag{4.11}$$

where the term $R_{v_1 v_2}$ can been set to zero for simplicity because as before it is not contributing to the Rabi frequency as it mixes states with same spin. H can then be split

56

into two blocks in the $\{|v_1 \downarrow\rangle, |v_2 \uparrow\rangle\}$ and $\{|v_1 \uparrow\rangle, |v_2 \downarrow\rangle\}$ subspaces.

First we can diagonalize in the $\{|v_1 \uparrow\rangle, |v_2 \downarrow\rangle\}$ subspace, which yields the energies of the states that anti-cross:

$$E'_{\pm} = \frac{1}{2}(E_1 + E_2) \pm \frac{1}{2}\sqrt{(\Delta - g\mu_B B)^2 + 4|C_{v_1 v_2}|^2} \qquad (4.12)$$

and their wavefunctions:

$$|\psi'_+\rangle = \alpha'|v_1 \uparrow\rangle + \beta'|v_2 \downarrow\rangle \qquad (4.13a)$$

$$|\psi'_-\rangle = \beta'|v_1 \uparrow\rangle - \alpha'^*|v_2 \downarrow\rangle \qquad (4.13b)$$

with:

$$\alpha' = \frac{2C^*_{v_1 v_2}}{(4|C_{v_1 v_2}|^2 + F'^2)^{1/2}} \qquad (4.14a)$$

$$\beta' = \frac{F'}{(4|C_{v_1 v_2}|^2 + F'^2)^{1/2}} \qquad (4.14b)$$

and:

$$F' = \Delta - g\mu_B B + \sqrt{(\Delta - g\mu_B B)^2 + 4|C_{v_1 v_2}|^2} \qquad (4.15)$$

Likewise, diagonalization in the $\{|v_1 \downarrow\rangle, |v_2 \uparrow\rangle\}$ subspace yields the energies of the lowest and highest states:

$$E_{\pm} = \frac{1}{2}(E_1 + E_2) \pm \frac{1}{2}\sqrt{(\Delta + g\mu_B B)^2 + 4|C_{v_1 v_2}|^2} \qquad (4.16)$$

and their wavefunctions:

$$|\psi_+\rangle = \alpha|v_1 \downarrow\rangle + \beta|v_2 \uparrow\rangle \qquad (4.17a)$$

$$|\psi_-\rangle = \beta|v_1 \downarrow\rangle - \alpha^*|v_2 \uparrow\rangle \qquad (4.17b)$$

with:

$$\alpha = \frac{-2C_{v_1 v_2}}{(4|C_{v_1 v_2}|^2 + F^2)^{1/2}} \qquad (4.18a)$$

$$\beta = \frac{F}{(4|C_{v_1 v_2}|^2 + F^2)^{1/2}} \qquad (4.18b)$$

and:

$$F = \Delta + g\mu_b B + \sqrt{(\Delta + g\mu_B B)^2 + 4|C_{v_1 v_2}|^2} \qquad (4.19)$$

From this we can compute the Rabi frequency for resonant transitions between the ground

state $|\Psi_-\rangle \simeq |v_1 \downarrow\rangle$ and the mixed states $|\Psi'_\pm\rangle$ from the $\{|v_1 \uparrow\rangle, |v_2 \downarrow\rangle\}$ subspace:

$$hf_- = eV_{ac} \left|\langle\psi'_-|D|\psi_-\rangle\right| = eV_{ac}|\alpha'\beta + \alpha^*\beta'||D_{v_1v_2}| \tag{4.20a}$$

$$hf_+ = eV_{ac} \left|\langle\psi'_+|D|\psi_-\rangle\right| = eV_{ac}|\alpha\alpha' - \beta\beta'||D_{v_1v_2}|. \tag{4.20b}$$

Let us now compare this model to the tight-binding simulations. We work on the same device (Fig. 4.7) but we added surface roughness (SR), with rms $\Delta_{\mathrm{SR}} = 0.4$ nm and correlation length $\Lambda_{\mathrm{SR}} = 1.5$ nm [87, 102], in order to match the experimental device better. Indeed, in the perfect device the valley splitting is way higher than the experimental value of 36 μeV, and SR is known to decrease Δ [132]. In the SR sample we chose, we compute $C_{v_1v_2} = 1.8$, $D_{v_1v_2} = 70$ μeV/V and $\Delta = 36$ μeV. In Fig. 4.11 we have plotted the energy levels and Rabi frequencies (f_-, f_+). The results are obtained with the full tight-binding calculations at finite field (Eq. 4.6) and with the model (Eq. 4.20). We reach a perfect agreement between the two, thus validating the hypothesis that we have made: it is not necessary to include higher orbital states in Eq. 4.11, and the matrix elements $D_{v_1v_2}$ and $C_{v_1v_2}$ do not depend on B. In a pertubative picture, this is true at least for $B < \frac{\Delta E_{\mathrm{orb}}}{g m u_B} \simeq$ 8 T, where $\Delta E_{\mathrm{orb}} = 1$ meV is the splitting to the nearest orbital state. Higher orbitals might need to be considered in particular systems like in Ref [131] where they are closer in energy.

We can now analyse the particular sigmoid shape of the Rabi frequencies, and to do so we can plot the coefficients $\alpha, \alpha', \beta, \beta'$ as a function of B (Fig. 4.12). For all B, $\alpha \simeq 0$ and $\beta \simeq 1$, meaning that $|\Psi_-\rangle$ is mostly $|v_1 \downarrow\rangle$ and $|\Psi_+\rangle$ is mostly $|v_2 \uparrow\rangle$, as expected since these two states do not anti-cross. As the Rabi frequencies are proportional to $|D_{v_1v_2}|$ the shape of f_- and f_+ are thus respectively given by α' and β' which give the proportion of $|v_2 \downarrow\rangle$ in respectively $|\Psi'_-\rangle$ and $|\Psi'_+\rangle$. When $|\Psi'_-\rangle$ or $|\Psi'_+\rangle$ is purely $|v_2 \downarrow\rangle$ the corresponding Rabi frequency saturates at $|D_{v_1v_2}|/h$.

We now choose to follow the state which has the most $|v_1 \uparrow\rangle$ character, as along line A of the EDSR map (Fig. 4.4), that is $|\Psi\rangle = |\Psi'_-\rangle$ before the anti-crossing and $|\Psi\rangle = |\Psi'_+\rangle$ after. In that case $f_R = \min(f_-, f_+)$, which is plotted along with the energy levels on Fig. 4.13 from the model and the tight-binding simulations. The interesting feature of this plot is the peak of f_R at the anti-crossing. From Eq. 4.20 we can show that the height of the peak is:

$$hf_R = \frac{e|D_{v_1v_2}|}{\sqrt{2}} \tag{4.21}$$

We can also show that the width of the peak is proportional to $C_{v_1v_2}$. The full width at half maximum of the peak is indeed:

$$g\mu_B \Delta B_{\mathrm{FWHM}} = \frac{12|C_{v_1v_2}|}{\sqrt{7}} \tag{4.22}$$
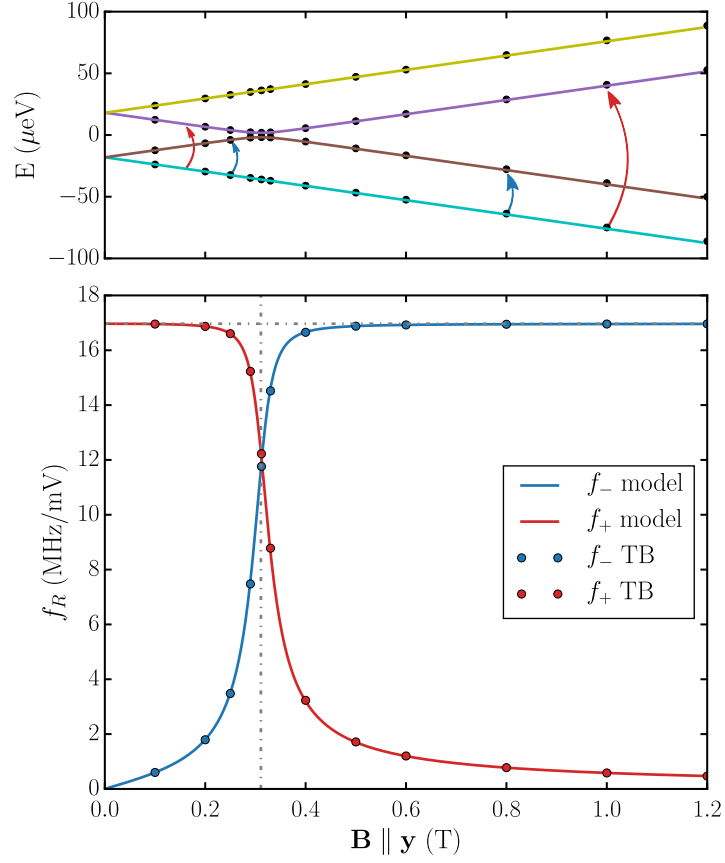
Figure 4.11: Energy levels and f_- and f_+ Rabi frequencies, corresponding to transitions between the ground state and respectively $|\Psi'_-\rangle$ and $|\Psi'_+\rangle$, as highlighted by the blue (f_-) and red (f_+) arrows. Dots are for direct tight-binding calculations, the solid lines are for the analytical model with $C_{v_1 v_2} = 1.8$, $D_{v_1 v_2} = 70$ μeV/V and $\Delta = 36$ μeV, extracted from the TB calculations.
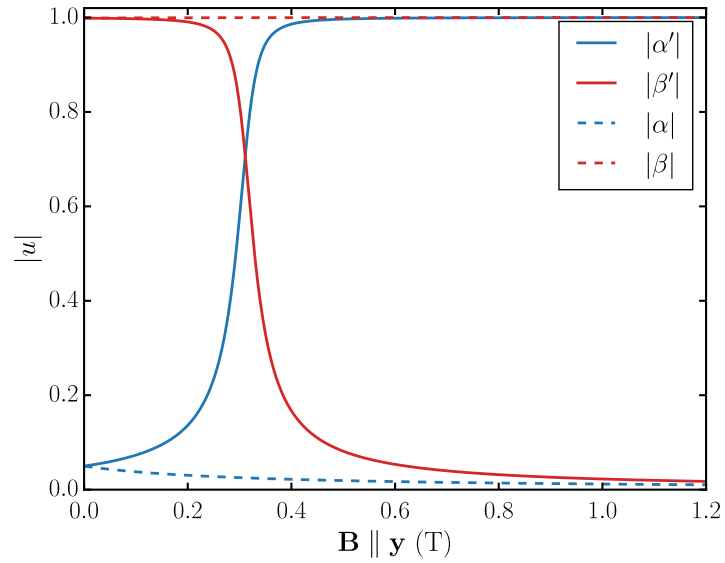
Figure 4.12: Norm of the coefficients α, α', β, β' as a function of magnetic field amplitude.

Figure 4.13: Energy levels and Rabi frequency as a function of magnetic field. Here $f_R = \min(f_-, f_+)$ Coloured lines are from the analytical model, black dots are tight-binding simulations.

The two relations 4.21 and 4.22 may be used to determine the matrix elements experimentally. Nevertheless this peculiar resonance is not observed experimentally on the EDSR map: as the measured region starts after the anti-crossing we should see a decrease of the current when increasing B. The problem is that the power of the microwave signal sent on the gate is not constant with frequency, and the power-frequency dependence is not known. However we will see in the next part how other measurements and the study of symmetries can confirm our model.

4.3 What is the origin of the spin-orbit interaction?

The spin-orbit coupling is a relativistic effect which couples the orbital motion of the electron to its spin. As seen in chapter 2, in bulk silicon the crystal centro-symmetry suppresses most effects of spin-orbit interaction. However, in nanostructures, symmetries can be locally broken and some groups observed (yet small) effects of spin-orbit in group IV materials [50, 54, 130]. Huang *et al.* [131] even proposed a qubit using an inter-orbital inter-valley spin-orbit interaction, based on a coupling with a *p*-like excited orbital enabled

by putting the wavefunction on an interface step. Our model here supposes quite differently that we can have an inter-valley spin-orbit coupling within the same orbital. This coupling may be intrinsic or extrinsic, i.e originating from an inhomogeneous magnetic field. The latter possibility has been envisioned as the metallic TiN gates can be superconducting, and because HfO_2 can be ferromagnetic at low temperature. However we have quantitatively excluded these possibilities [123]. TiN is indeed superconducting but is too thin in the experiment to produce a sizeable gradient of magnetic field. Although rejected here as explanations for spin-orbit interactions these two effects open interesting perspectives for the creation of a local magnetic field gradient, to the condition that they can be engineered properly.

To investigate further the origin of the spin-orbit interaction, we have analysed the effect of the symmetries of the system using group theory. To do so, we are going to study what form the spin-orbit tight-binding Hamiltonian and the dipolar coupling operator can take given the different symmetries of the system. We choose to focus on two different set of symmetries: those of our device and those of a trigate device (which have the same symmetries as a planar quantum dot). The ground state in each device is plotted Fig. 4.14 and Fig. 4.15, highlighting the mirror planes. In the corner geometry the device is invariant by reflection by the (yz) plane, thus belonging to the C_s space group. In the trigate or planar geometry, the device is invariant by reflection by the (yz) and the (xz) planes, as well as by a twofold rotation around the z axis, thus belonging to C_{2v} space group. The table of characters for these two space groups are given Table 4.2. For the corner geometry $|v_1\rangle$ and $|v_2\rangle$ states belong to the A_1 irreducible representation of C_s. For the trigate geometry they belong to the A_1 irreducible representation of C_{2v}. In both cases, the mirror planes transform $|v_1\rangle$ and $|v_2\rangle$ into themselves.

According to group theory, for any observable $\hat{O}$, unitary symmetry operation R, and wavefunctions $|\Psi_1\rangle$ and $|\Psi_2\rangle$ we have the relation:

$$O_{12} = \langle\psi_1|\hat{O}|\psi_2\rangle = \langle R\psi_1|R\hat{O}R^\dagger|R\psi_2\rangle \qquad (4.23)$$

Let us start with the dipolar coupling $D(\mathbf{r}) = \partial V_t(\mathbf{r})/\partial V_g$. For the corner geometry $V_t(\mathbf{r})$ belongs also to the C_s space group so that $\sigma(xy)D\sigma(xy)^\dagger = D$. Therefore, Eq. 4.23 does not set any condition on the $D_{v_1v_2}$ matrix element. The result is the same for the trigate geometry. We now turn to the spin-orbit tight-binding Hamiltonian, which we write:

$$H_{SO}^{TB} = \lambda_{SO}\left(\mathcal{L}_x\sigma_x + \mathcal{L}_y\sigma_y + \mathcal{L}_z\sigma_z\right) \qquad (4.24)$$

where σ_α are the Pauli matrices, $\mathcal{L}_\alpha = \sum_{iat} L_{iat,\alpha}$ and $L_{iat,\alpha}$ is the component $\alpha = x, y, z$ of the angular momentum on atom iat. We neglect here the coupling to d orbitals (see

C_{2v}	E	$\sigma(yz)$	$\sigma(xz)$	$C_2(z)$
A_1	1	+1	+1	+1
A_2	1	−1	−1	+1
B_1	1	+1	−1	−1
B_2	1	−1	+1	−1

C_s	E	$\sigma(yz)$
A_1	1	+1
A_2	1	−1

Table 4.2: Table of characters of (a, left) the C_s and (b, right) the C_{2v} group.

$$L_{iat,x} = \begin{pmatrix} 0 & 0 & 0 \\ 0 & 0 & -i \\ 0 & i & 0 \end{pmatrix} \quad L_{iat,y} = \begin{pmatrix} 0 & 0 & i \\ 0 & 0 & 0 \\ -i & 0 & 0 \end{pmatrix} \quad L_{iat,z} = \begin{pmatrix} 0 & -i & 0 \\ i & 0 & 0 \\ 0 & 0 & 0 \end{pmatrix}$$

Table 4.3: Matrices of $L_{iat,x}$, $L_{iat,y}$ and $L_{iat,z}$ in the $\{p_x, p_y, p_z\}$ basis set.

chapter 2). The matrix element $C_{v_1 v_2} = \langle v_1 \uparrow | H_{SO}^{TB} | v_2 \downarrow \rangle$ reads

$$C_{v_1 v_2} = \lambda_{SO} \sum_\alpha \langle v_1 | \mathcal{L}_\alpha | v_2 \rangle \langle \uparrow | \sigma_\alpha | \downarrow \rangle \tag{4.25}$$

We are now interested in the terms $\langle v_1 | \mathcal{L}_\alpha | v_2 \rangle$. We start with the corner geometry: the plane $\sigma(yz)$ leaves the orbitals $p_{y,z}$ invariant but transforms a p_x orbital into $-p_x$, so that Eq. 4.23 gives $\sigma(yz)\mathcal{L}_{y,z}\sigma(yz) = -\mathcal{L}_{y,z}$ and $\sigma(yz)\mathcal{L}_x\sigma(yz) = \mathcal{L}_x$. Hence using Eq. 4.23, $\langle v_1 | \mathcal{L}_{y,z} | v_2 \rangle = \langle \sigma(yz)v_1 | \sigma(yz)\mathcal{L}_{y,z}\sigma(yz)^\dagger | \sigma(yz)v_2 \rangle = \langle v_1 | -\mathcal{L}_{y,z} | v_2 \rangle = 0$. The inter-valley matrix element therefore reads:

$$C_{v_1 v_2} = \lambda_{SO} \langle v_1 | \mathcal{L}_x | v_2 \rangle \langle \uparrow | \sigma_x | \downarrow \rangle \tag{4.26}$$

As for the trigate geometry, the $\sigma(yz)$ mirror sets the same condition: only $\mathcal{L}_x$ can couple $|v_1\rangle$ and $|v_2\rangle$. Similarly one can show that the $\sigma(xz)$ operation imposes that only the $\langle v_1 | \mathcal{L}_y | v_2 \rangle$ is non zero. Hence $C_{v_1 v_2} = 0$ for the trigate/planar geometry, as these conditions are incompatible. Consequently, the C_{2v} symmetry must be broken in order to get significant intervalley spin-orbit coupling. This is actually achieved in corner dots where the symmetry is lower.

Coming back to the corner geometry, is this result compatible with the measurements? The study of symmetries gave a spin-orbit Hamiltonian proportional to $\langle \uparrow | \sigma_x | \downarrow \rangle$, so when the magnetic field is oriented along the wire axis **x** this coupling is zero. More precisely the expected dependence of $\langle v_1 \uparrow | H_{SO} | v_2 \downarrow \rangle$ with the magnetic field orientation is proportional to $\sin\theta$, with θ the angle between the nanowire axis and the magnetic field. On Fig. 4.16 we compare the measured current on line A, as a function of the magnetic field orientation in the plane of the wafer, to the square of the calculated Rabi frequency, with $\theta = 0$ the nanowire axis. Indeed the current is expected to be $\propto f_R^2$ [134, 135]. We have a perfect agreement between theory and experiment on the $\sin^2\theta$ dependence. We do not have experimental data for **B** out of the plane, but we have verified that we have
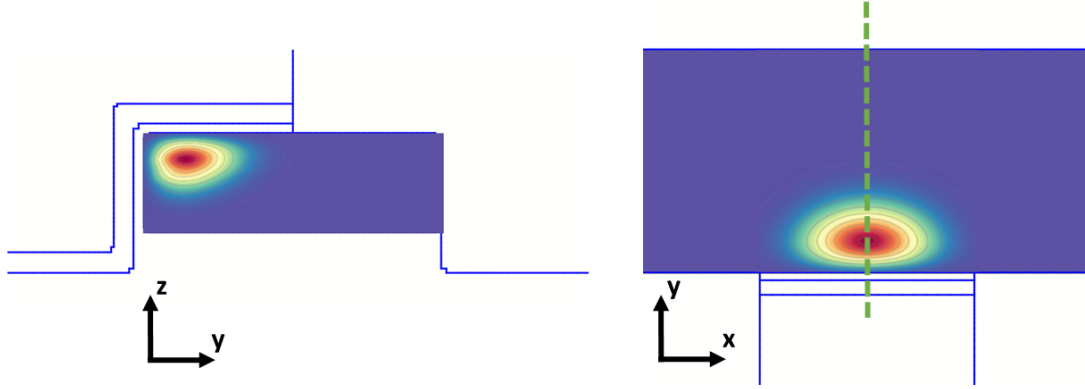
Figure 4.14: Symmetry plane in half-gated device. The mirror planes of the wavefunction are given by the dotted green lines.
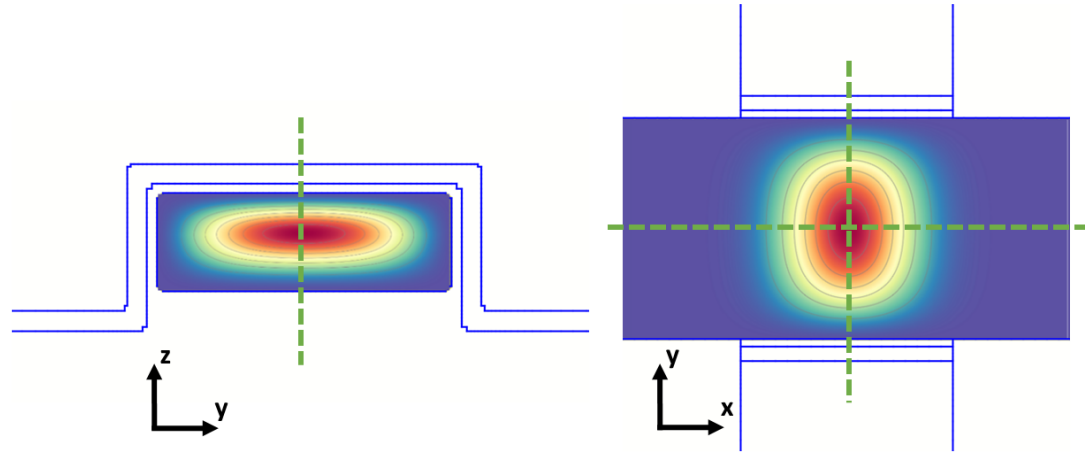
Figure 4.15: Symmetry plane in trigate device. The mirror planes of the wavefunction are given by the dotted green lines.

$\langle v_1 \uparrow | H_{SO} | v_2 \downarrow \rangle \propto \sin\theta$ for any polar angle ϕ in the TB calculation. This confirms that intrinsic spin-orbit coupling is the main driving force for the observed EDSR.

As discussed earlier, some groups have observed the effects of spin-orbit interactions in Si MOS planar quantum dots [50, 54, 136], but it has never been leveraged to perform EDSR. The results of Hao *et al.* [54] give an interesting point of comparison: they measured the ESR spectrum of a silicon gate-defined quantum dot and observed an anticrossing, which they identify as spin-valley mixing. From the position of the anticrossing they extract the valley splitting, 86.2 μeV, comparable to the one we measured. From the anticrossing gap, we can deduce the value of the intervalley spin-orbit coupling: 125 neV. This value is one order of magnitude smaller than what we computed with tight-binding in our device. The reason for that is probably that their system is much more symmetric than a corner state: the asymmetry could only be created by disorder or asymmetric gate potential. In half-gated nanowires, the combination of asymmetric structural and electric
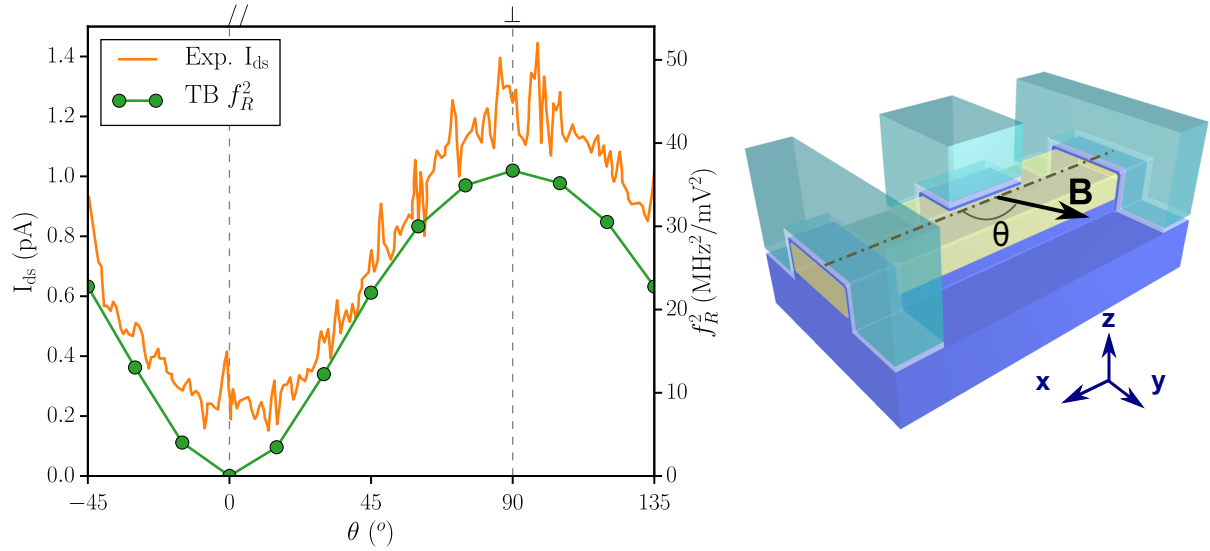
Figure 4.16: Comparison of the dependence with in-plane magnetic orientation of the measured current and of the squared Rabi frequency computed in tight-binding. The directions parallel and perpendicular to the nanowire are highlited with dashed lines. The definition of the angle θ is given in the right panel, on the schematic of the device.

field confinements enhance the spin-orbit interaction much more efficiently.

4.4 Conclusion

We have presented the first experimental observation of EDSR in the conduction band of silicon without intrinsic elements. The measured EDSR spectrum reveals the presence of a valley excited state spaced by 36 μeV from the ground state, and demonstrate that spin and valley degree of freedom are hybridized.

We have presented an analytical model that explains this mixing of spin and valley by the intrinsic spin-orbit interaction, the electric field coupling opposite valleys via a dipolar interaction. This model has been validated by detailed tight-binding simulations. We have studied, in particular, the effect of the magnetic field amplitude and have shown that the Rabi frequency is non-linear with B: the main EDSR line is expected to exhibit a resonance when the Zeeman splitting matches the valley splitting.

By studying the effects of the symmetries of the system, we have shown that the observed anisotropy of EDSR with the magnetic field orientation is compatible with the intrinsic spin-orbit interaction. Furthermore, the symmetry study shows that the spin-orbit coupling is non-zero only if there is no more than one mirror plane in the structure. In corner states, as opposed to planar quantum dots, symmetries are strongly broken, therefore corner states are good candidate for the realization of an all-electrical spin qubit.

However, we have not yet demonstrated a qubit. We know that a strong mixing of spin and valleys is essential for efficient EDSR, but we also expect that it couples the states to parasitic electric fields, thus inducing an enhancement of relaxation and decoherence times [50,129]. In the next chapter we are going to address this issue with a scheme which allows to tune the level of mixing between spin and valleys with the electric field.

Chapter 5

A Spin-Valley qubit

Dans ce chapitre nous utilisons le modèle et les mécanismes développés au chapitre 4 pour proposer un schéma de qubit de spin efficace. Ce schéma consiste à passer de manière réversible entre un qubit de spin, où l'information quantique est protégée, et un qubit de vallée où le qubit peut être manipulé électriquement mais la décohérence est plus importante. Pour ce faire, nous étudions les propriétés du qubit en fonction du champ électrique, qui est contrôlé par le potentiel appliqué sur l'électrode en face arrière, la "backgate". Celle-ci constitue une caractéristique clé des dispositifs du CEA.

Les calculs de liaisons fortes associés à des modèles analytiques et des simulation dépendantes du temps nous cherchons à caractériser de manière exhaustive la physique de ce système. En particulier les simulations dépendantes du temps sont utilisées pour démontrer l'opération du qubit selon le schéma "spin-vallée" en prenant en compte les contraintes d'adiabaticité. Nous cherchons ensuite à étudier la viabilité du schéma. Nous évaluons donc la décohérence causée par l'interaction avec les phonons et le bruit électrique sur les grilles (bruit Johnson-Nyquist), confirmant que les temps caractéristiques sont différents de plusieurs ordres de grandeurs entre les régimes de spin et de vallée. L'impact de la variabilité due à la rugosité des surfaces sur les différents éléments du modèle est évalué. Nous étudions également l'effet de variation de l'épaisseur du nanofil sur le splitting de vallée, qui est expliqué par un modèle analytique simple. Finalement, nous présentons quelques résultats expérimentaux préliminaires qui montrent le bon contrôle du splitting de vallée avec la backgate. Ces résultats peuvent être reproduits par les calculs de liaisons fortes, qui montrent un fort effet des charges piégées à l'interface SiO_2/HfO_2. Il suggèrent que supprimer la couche de HfO_2 de l'empilement de grille permettrait de réduire fortement la variabilité dans ces dispositifs. Ces résultats expérimentaux ainsi que ceux présentés au chapitre 4 constituent une première étape vers la réalisation pratique du schéma de spin-vallée qubit que nous proposons.

The EDSR experiment has been a great occasion to unveil a lot of physics in this system and to gather it in a simple model. In the previous chapter we have shown that the electrical control of the spin can be achieved with the intrinsic spin-orbit coupling that mixes spin of opposite valleys and to the inter-valley dipolar interaction that couples opposite valleys of same spin. That spin-orbit interaction is enhanced by the low symmetry that exists in the corner quantum dots. We have studied the magnetic field dependence of the Rabi frequency and have shown that it exhibits strong non-linearities at the vicinity of the anticrossing between states $|v_1 \uparrow\rangle$ and $|v_2 \downarrow\rangle$.

However the magnetic field is not a convenient local knob, as it affects many qubits at once. It is preferable to achieve an all-electrical control on the qubit. In this part we study the dependence of the properties of the qubit on the electric field in the dot, handily controlled by the potential on the back electrode, a key feature of silicon-on-insulator devices. We try to use it to engineer an efficient qubit based on controlled spin-valley mixing. Indeed we will show that the backgate allows to switch between a spin qubit, in which the quantum information is well-preserved, and a valley qubit, in which the electrical manipulation is fast. We call this scheme the spin-valley qubit.

Our tight-binding calculations combined with analytical models and time-dependent simulations allow a thorough characterization of the physics of the system. In particular we use the time-dependent simulations to demonstrate the qubit operation and adiabatic constraints. After that, in order to give precise boundaries on the feasibility and interest of the proposed scheme, we study the decoherence with some simple sources of noise and the variability due to the surface roughness and the film thickness variations. Finally we present some recent experimental results that show the good control of the valley splitting with the backgate, a first step towards the practical realization of the spin-valley qubit.

5.1 Electric field dependence of the spin-valley system.

5.1.1 Principle

Let us start by giving the main ideas of our qubit proposal taking advantage of the particular physics of this system. In the last chapter we have studied in particular the transition along the line A of the EDSR spectrum, that is between the ground state and the "mostly spin up" state. This was determined by the experiment, but it may not be the best choice for a qubit.

A natural way to build a qubit is to choose its states as the ground and first excited state of the system, in order to avoid enhanced relaxation with an intermediate level. In this chapter we propose a qubit based on the states $|0\rangle \equiv |\Psi_-\rangle$ and $|1\rangle \equiv |\Psi'_-\rangle$, with energy E_0, E_1. The state $|0\rangle$ is in fact almost a pure $|v_1 \downarrow\rangle$ state, whereas the state $|1\rangle$
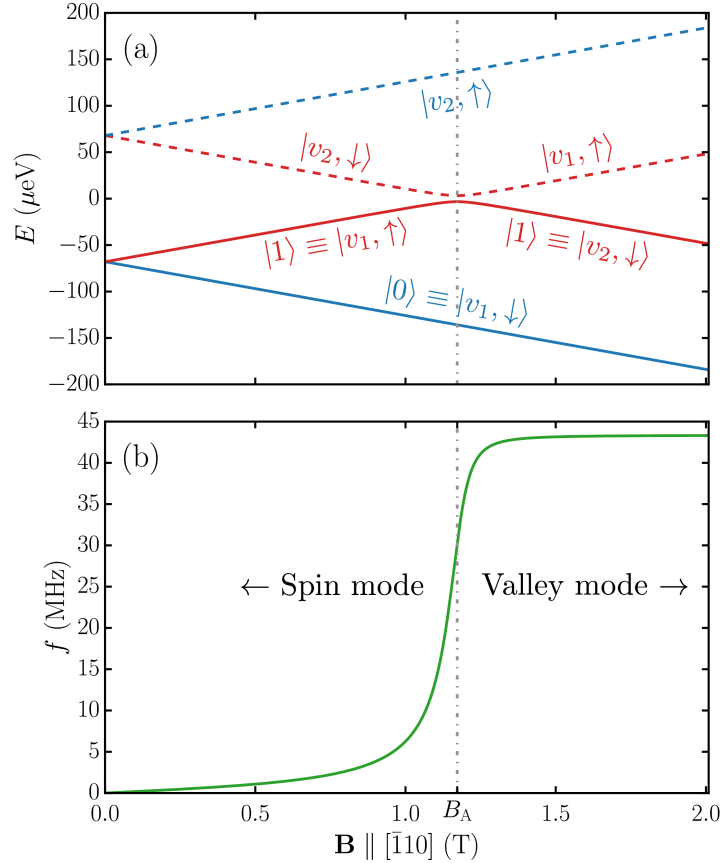
Figure 5.1: (a) Energy levels of the quantum dot in a magnetic field B. The solid blue line is the energy of the $|v_1, \downarrow\rangle$ state, the dotted blue line the energy of the $|v_2, \uparrow\rangle$ state, and the solid and dashed red lines the energies of the $|\psi'_-\rangle$ and $|\psi'_+\rangle$ states (which are mixtures of the $|v_1, \uparrow\rangle$ and $|v_2, \downarrow\rangle$ states that anti-cross at $B = B_A = 1.172$ T). (b) Computed Rabi frequency for the transition between $|0\rangle \equiv |v_1, \downarrow\rangle$ and $|1\rangle \equiv |\psi'_-\rangle$ (solid lines in (a)). The parameters of the model are $\Delta = 136$ μeV, $|C_{v_1 v_2}| = 3.25$ μeV, and $|D_{v_1 v_2}| = 179.26$ μV/V. They have been extracted from tight-binding simulations on the device of chapter 4 (Fig. 4.7) at $V_g = 0.1$ V and $V_{\mathrm{bg}} = 0$ V. The amplitude of the RF excitation on the front gate is $V_{ac} = 1$ mV.

is a combination of $|v_1 \uparrow\rangle$ and $|v_2 \downarrow\rangle$. We remind the expressions of the qubit states from chapter 4:

$$|0\rangle = \beta|v_1 \downarrow\rangle - \alpha^*|v_2 \uparrow\rangle \tag{5.1a}$$

$$|1\rangle = \beta'|v_1 \uparrow\rangle - \alpha'^*|v_2 \downarrow\rangle \tag{5.1b}$$

The coefficients α and β have the following expressions:

$$\alpha = \frac{-2C_{v_1 v_2}}{(4|C_{v_1 v_2}|^2 + F^2)^{1/2}} \tag{5.2a}$$

$$\beta = \frac{F}{(4|C_{v_1 v_2}|^2 + F^2)^{1/2}} \tag{5.2b}$$

with:

$$F = \Delta + g\mu_b B + \sqrt{(\Delta + g\mu_B B)^2 + 4|C_{v_1 v_2}|^2} \tag{5.3}$$

and:

$$\alpha' = \frac{2C_{v_1 v_2}^*}{(4|C_{v_1 v_2}|^2 + F'^2)^{1/2}} \tag{5.4a}$$

$$\beta' = \frac{F'}{(4|C_{v_1 v_2}|^2 + F'^2)^{1/2}} \tag{5.4b}$$

with:

$$F' = \Delta - g\mu_b B + \sqrt{(\Delta - g\mu_B B)^2 + 4|C_{v_1 v_2}|^2} \tag{5.5}$$

When a signal $V_g(t) = V_g^0 + V_{\mathrm{ac}}\sin(2\pi\nu t)$ is applied on the gate, with $h\nu = E_1 - E_0$, the Rabi frequency is:

$$hf_R = eV_{ac}\,|\langle 1|D|0\rangle| = eV_{ac}|\alpha'\beta + \alpha^*\beta'||D_{v_1 v_2}| \tag{5.6}$$

In practice, $|\alpha| \simeq 0$ and $|\beta| \simeq 1$, so that most relevant coefficient in the Rabi frequency is α', the mixing of $|v_2 \downarrow\rangle$ into $|v_1 \uparrow\rangle$. We recall in Fig. 5.1 the energy levels of the system as a function of the magnetic field, and the Rabi frequency in response to the resonant gate excitation. This figure presents clearly two regimes. Left of the avoided crossing, $|1\rangle \simeq |v_1 \uparrow\rangle$, the qubit is effectively a **spin qubit** $\{|v_1\downarrow\rangle, |v_1\uparrow\rangle\}$, which is difficult to manipulate electrically (low Rabi frequency). On the right of the avoided crossing, $|1\rangle \simeq |v_2 \downarrow\rangle$ and the qubit is effectively a **valley qubit** $\{|\mathbf{v_1} \downarrow\rangle, |\mathbf{v_2} \downarrow\rangle\}$ whose manipulation is much faster. In this regime, the Rabi frequency saturates at $f_R^{\max} = eV_{ac}|D_{v_1 v_2}|/h$. We expect the valley qubit to be sensitive to all kinds of electric noises, which are the dominant noises in silicon, especially in pure Silicon 28. On the contrary in the spin mode, the qubit is almost decoupled from electric noises (the residual coupling is proportional to the small $|v_2 \downarrow\rangle$ component of $|1\rangle$).
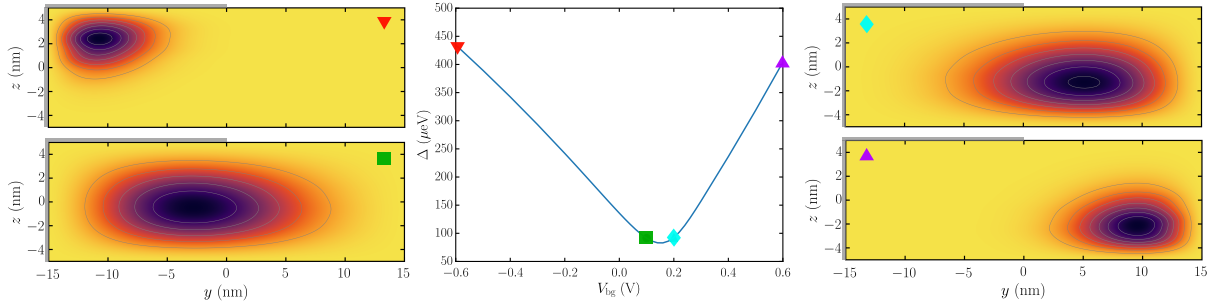
Figure 5.2: (Central panel) valley splitting as a function of backgate potential ($V_g = 0.1$ V). The valley splitting shows a minimum $\Delta^{\mathrm{min}} = 83$ μeV at $V_{\mathrm{bg}}^{\mathrm{min}} = 0.15$ V. (Lateral panels) The squared wavefunction of the ground state $|0\rangle$ is plotted in the (yz) cross section, at the four bias points labelled by the symbols. The thick gray lines outline the position of the front gate.

In this chapter, we try to make the best out of those two worlds. We want to be in the spin mode most of the time to protect the quantum information and switch to the valley mode when necessary for fast electrical control: we want to make a spin-valley qubit.

Then, how to switch between modes? We can already devise from Fig. 5.1 a first easy answer: we can sweep the magnetic field. There are two problems with that option. First the magnetic field would affect many qubits at once, and second in practice changing its amplitude is very slow. The solution we propose is to switch between the two modes using the electric field, which can be handily controlled in silicon-on-insulator devices by the backgate electrode. Indeed, the valley splitting Δ is dependent on the static electric field $\mathbf{E}$ and the anti-crossing position is given by $g\mu_B B = \Delta$. Therefore by controlling Δ at a constant magnetic field we can in principle switch between the two modes: the spin mode at electric field $\mathbf{E_1}$ such that $g\mu_B B < \Delta(\mathbf{E_1})$ and the valley mode at electric field $\mathbf{E_2}$ such that $g\mu_B B > \Delta(\mathbf{E_2})$.

In the following we are going to demonstrate this principle using tight-binding simulations. We will study the dependences of the valley splitting with the backgate potential, and then how to practically operate the qubit.

5.1.2 Electric field control of the qubit.

We are now going to implement this scheme in a quantum dot defined by a gate in a silicon nanowire, and control the vertical electric field with the backgate. The device studied here is the same as the one of the previous chapter. The side gates could in the present case mimic source/drain barriers as well as neighbouring qubits. We have computed the valley splitting as a function of the backgate potential using tight-binding (TB). As in chapter 4, the atomistic segment of the device included in the TB calculation is 80 nm long.

The results are shown Fig. 5.2 along with the wavefunctions at a few bias points. The valley splitting increases as the wavefunction is pushed against one of the interfaces and
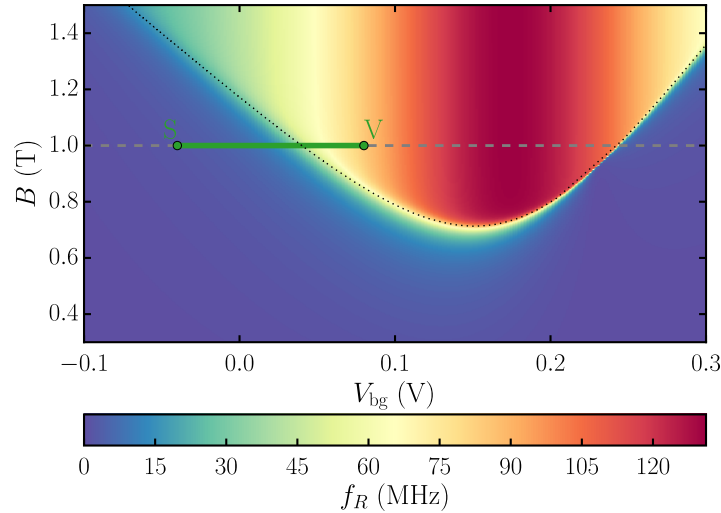
Figure 5.3: Map of Rabi frequency as a function of the magnetic field amplitude and V_{bg}. The dotted black line is the anticrossing condition $E_z = g\mu_B B = \Delta(V_{\text{bg}})$. The RF amplitude is $V_{ac} = 1$ mV. The green line is the path chosen for qubit operation at $B = 1$ T.

is minimum when the state is the most delocalized. More precisely the valley splitting shows a minimum $\Delta^{\min} = 83$ μeV at $V_{\text{bg}}^{\min} = 0.15$ V; for $V_{\text{bg}} \ll V_{\text{bg}}^{\min}$ the electron is pushed in the corner of the front gate, and for $V_{\text{bg}} \gg V_{\text{bg}}^{\min}$ the electron is pulled in the opposite corner near the buried oxide interface. This leads to this particular $\Delta(V_{\text{bg}})$ curve with a crescent shape.

Using Eq. 5.6, we can compute the Rabi frequency as a function of V_{bg} and B, plotted in Fig. 5.3. On this map we easily see the spin-valley transition given by the condition $\Delta = g\mu_B B$ (dotted line). The qubit is in valley mode inside the area enclosed by the line and is is spin mode outside. Remarkably the Rabi frequency can be as high as 124 MHz/mV. The variations of f_R on this map are quite complex, but we will dwell on this later. For now let us set a fixed magnetic field, for instance $B = 1$ T, so that $g\mu_B B > \min(\Delta(V_{\text{bg}}))$. We can then switch between spin and valley modes: acting on the backgate voltage, we follow the path on the dashed line of Fig. 5.3 (the spin S and valley V bias operating points we chose are marked for later use). To illustrate what it means practically let us examine the three first energy levels and the Rabi frequency as a function of V_{bg}, Fig. 5.4. On the energy spectrum we see that we have this time two anticrossings: in between them $|1\rangle \simeq |v_2 \downarrow\rangle$, and outside $|1\rangle \simeq |v_1 \uparrow\rangle$. The Rabi frequency is hence maximum in between the anticrossings, and tends to zero outside. This case is different from a magnetic field sweep (Fig. 5.1), in which the variation of f_R is only due to the proportion $|v_1 \uparrow\rangle/|v_2 \downarrow\rangle$ in $|1\rangle$, the matrix elements $C_{v_1 v_2}$ and $D_{v_1 v_2}$ being independent of B. Here the electric field modifies the shape of the wavefunction, therefore $C_{v_1 v_2}$ and $D_{v_1 v_2}$ are not constant anymore. This way, not only the proportion $|v_1 \uparrow\rangle/|v_2 \downarrow\rangle$ in $|1\rangle$ is controlled by V_{bg} (the anticrossings of Fig. 5.4 do not have the same size), but $f_R^{\max}$
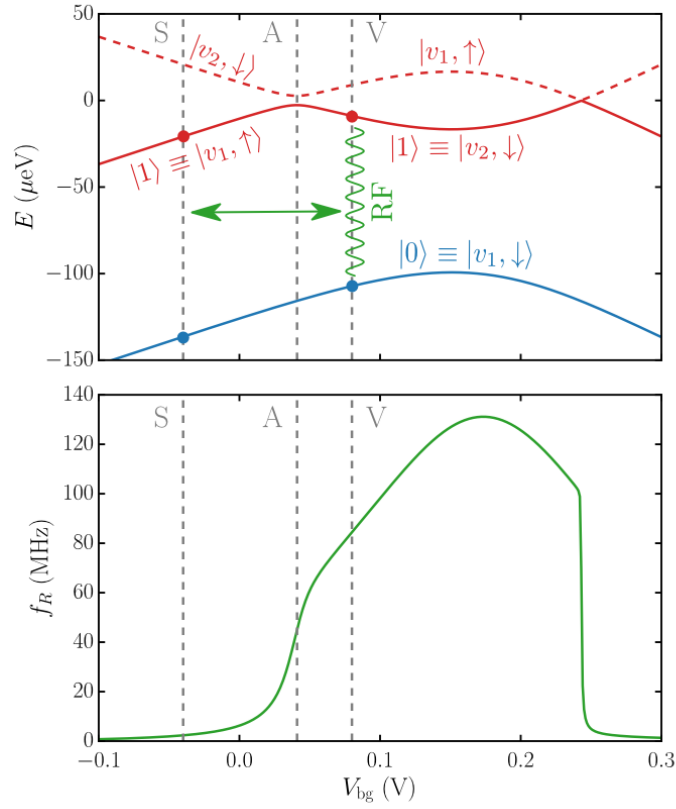
Figure 5.4: (Top panel) Energy levels as a function of V_{bg}. The gray dashed lines highlight the spin (S) and valley (V) mode chosen for the qubit operation and the avoided crossing (A) separating the two regimes. (Bottom panel) Rabi frequency corresponding to the transition $|0\rangle \leftrightarrow |1\rangle$ as a function of V_{bg}.
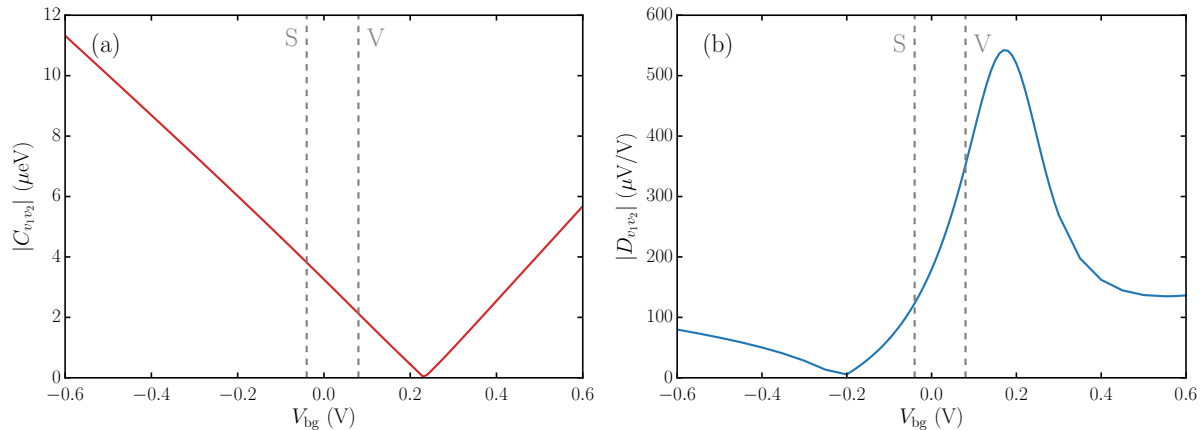
Figure 5.5: (a) Spin-orbit and (b) dipolar inter-valley matrix elements as a function of $V_{\rm bg}$. The gray dashed lines highlight the spin and valley mode arbitrarily chosen for the qubit operation.

changes with $D_{v_1 v_2}$ (even in between the anticrossings f_R is not constant).

The dependence of the matrix elements $D_{v_1 v_2}$ and $C_{v_1 v_2}$ with $V_{\rm bg}$ is plotted Fig. 5.5. Remarkably the SO matrix element is zero at $V_{\rm bg} = 0.23$ V. Indeed at this point the wavefunction gains an additional symmetry plane (perpendicular to $\mathbf{y}$) which kills the coupling, in agreement with our symmetry study of chapter 4. Group theory does not predict the detailed dependence of the SO matrix element, however it is interesting to note that $C_{v_1 v_2}$ increases linearly as the asymmetry increases.

The dependence of $D_{v_1 v_2}$ is more complicated, however a general trend is that it is maximum when the wavefunction is the most delocalized in the $\mathbf{z}$ direction. This is a strong point of this proposal: the Rabi frequency has a maximum in between the anticrossings, that is in the region of the valley mode in which we will perform the manipulation.

In Fig. 5.3 we have highlighted in green the path that we choose to perform the qubit operation. The valley and spin points, S and V, are marked as well on the other figures. In the next part we are going to study the qubit operation along this path, using time-dependent simulations.

5.2 Qubit operation.

We now perform time-dependent simulation in order to study the real time operation of our proposed spin-valley scheme. The inputs of the calculations are the results of the previous static tight-binding simulations, as discussed in chapter 3 (numerical resolution of time-dependent Schrödinger equation). We will use this equation to model the qubit operation, taking care of the adiabatic criteria in this system. Finally the systematic dephasing inherent to the operation will be included in order to control the rotation axis in the Bloch sphere.

5.2.1 Demonstration of qubit operation.

In this part we are going to demonstrate numerically the following operation:

1. Starting from the spin mode, sweep V_{bg} to reach the valley mode.

2. Send an RF excitation on the front gate to drive a $|0\rangle \leftrightarrow |1\rangle$ rotation.

3. Sweep V_{bg} back to the spin mode.

This should result in an effective spin rotation. The chosen spin (S) and valley (V) modes are shown on Figs. 5.3 and 5.4. The time dependent Schrödinger equation is solved in a basis of N low energy single particle states. In order to describe correctly the wavefunction all over the V_{bg} span (from -40 mV to $+80$ mV), we have to use a large enough basis of such states. We actually use 128 states at the middle of the range, $V_{bg} = 20$ mV, in order to achieve convergence on the whole V_{bg} range. We prepare the initial state as $|\Psi(t=0)\rangle = |0\rangle \simeq |v_1 \downarrow\rangle$, and the simulation then gives $|\Psi(t)\rangle$. From $|\Psi(t)\rangle$ we compute the expectation value of S_x, S_y, S_z, as well as $|\langle 1|\Psi(t)\rangle|^2$, the probability to be in $|1\rangle$ state. Starting from $V_{bg} = -40$ mV we apply a square pulse on the backgate electrode in order to reach the valley regime at $V_{bg} = +80$ mV. The pulse is not perfectly square, as the edges have finite slopes in order to ensure that we move adiabatically from S to V (see details in the next section). We apply during the pulse a resonant microwave signal on the main gate to rotate the valley state. Fig. 5.6a show the result of the simulation, exhibiting 8.5 Rabi oscillations and ending in the $|1\rangle$ state. The Rabi frequency extracted from these oscillations, 83.8 MHz, is very close to the direct tight-binding calculation at the S point (84.4 MHz, Eq. 5.6), showing the excellent convergence with $N = 128$ states.

As expected the oscillations of the average spin values are very small as we are mostly driving valley rotations between $|v_1 \downarrow\rangle$ and $|v_2 \downarrow\rangle$. However the spin suddenly changes its value during the ramp as we adiabatically go through the anticrossing back to the spin mode ($|v_2 \downarrow\rangle \rightarrow |v_1 \uparrow\rangle$). This is an interesting feature of this scheme: contrarily to usual EDSR, in which the dipolar and spin-orbit interactions act simultaneously, here their action is separated in time. First we make use of the dipolar interaction to drive valley rotation, then the spin-orbit interaction, to convert the valley rotation into a spin rotation.

5.2.2 Adiabaticity.

Let us now explore a bit more the physics of adiabaticity/diabaticity along this path. Indeed, what we want here is to ensure that a given state at the S point, let's say $|\Psi\rangle = |1\rangle$, stays $|1\rangle$ if no excitation is applied when we switch the system to the V point, back and forth. According to the adiabatic theorem [137], an eigenstate of the initial Hamiltonian will evolve continuously to the corresponding eigenstate of the final Hamiltonian if the

(a) Adiabatic S-V transition.

(b) Non-adiabatic S-V transition.
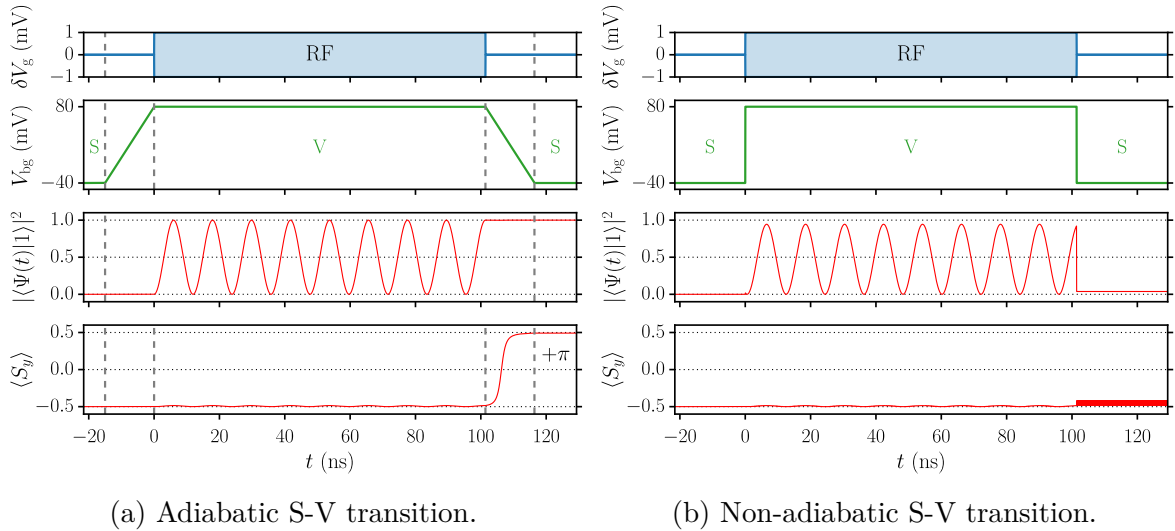
Figure 5.6: Time series for spin manipulations, monitored by the probability $p(|1\rangle)$ to be in the $|1\rangle$ state, and by the expectation value of the spin $\langle S_y \rangle$. Starting from the $|0\rangle = |v_1 \downarrow\rangle$ state at point S, the qubit is pulsed (adiabatically in (a) or diabatically in (b)) to point V by the backgate, and the RF signal with resonant frequency is applied on the front gate to drive rotations between $|0\rangle$ and $|1\rangle$. Once the RF signal is switched off, the qubit is brought back to point S (again adiabatically in (a) or diabatically in (b)).

perturbation is applied slowly enough: this is an adiabatic process. On the contrary, if the perturbation is too fast, the probability density is unchanged, and an initial eigenstate evolves into a linear combination of eigenstates of the final Hamiltonian: this is a diabatic process. The rapidity of the changing perturbation thus determines the type of process. In our case, we can derive the adiabatic condition by using the well-known case of the avoided crossing, treated by Landau and Zener [138,139]. The Hamiltonian for the avoided crossing is:

$$H = \begin{pmatrix} \frac{\alpha}{2} & C \\ C^* & -\frac{\alpha}{2} \end{pmatrix} \tag{5.7}$$

where C is the coupling between the states, and α is the energy splitting between the uncoupled states. The elements on the diagonal are the energies of the diabatic states, which are not eigenvalues of the Hamiltonian. Diagonalization of this Hamiltonian yields the adiabatic states, which form an avoided crossing. The diabatic and adiabatic energies are given in Fig. 5.7. Assuming α can be controlled externally at speed v ($\alpha = vt$), the Landau-Zener formula gives the probability of a diabatic transition. Starting from the lower branch of the anticrossing, the probability of transiting to the upper branch is:

$$P_D = \exp(-2\pi\Gamma) \tag{5.8}$$

with $\Gamma = \frac{|C|^2}{\hbar v}$. This equation can be applied to derive the condition on the adiabatic passage of the state $|1\rangle$, which will be the most limiting since it is the closest in energy
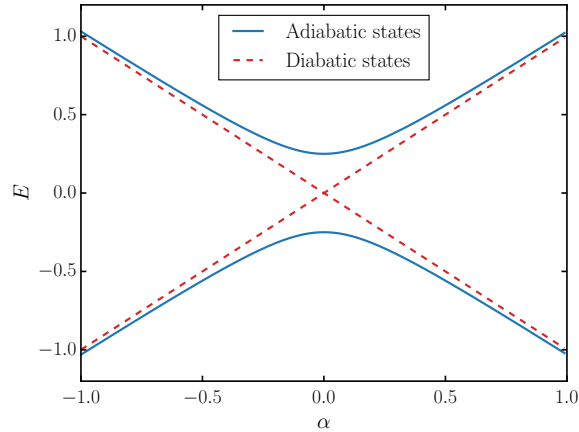
Figure 5.7: Diabatic and adiabatic states of an avoided crossing described by the Hamiltonian of Eq. 5.7.

to the other excited states, in particular at the anticrossing. For this some assumptions are needed. We have to suppose that Δ varies linearly with t, which is almost the case if we apply a linear ramp on V_{bg} during a time τ_R. We also have to neglect the fact that in our case $C_{v_1 v_2}$ depends on time since it depends on V_{bg}. We will hence take as average $C_{v_1 v_2}$ its value at the anticrossing. Then $v = \frac{\Delta^S - \Delta^V}{\tau_R}$ and $\Gamma = \frac{|C_{v_1 v_2}|^2 \tau_R}{\hbar(\Delta^S - \Delta^V)}$, with $\Delta^S = 156.8$ μeV, $\Delta^V = 98.5$ μeV and $|C_{v_1 v_2}| = 2.7$ μeV. We hence get:

$$\tau_R = \frac{-\log(P_D)\hbar(\Delta^S - \Delta^V)}{2\pi |C_{v_1 v_2}|^2} \tag{5.9}$$

If we choose the criteria that $P_D < 10^{-5}$, we get $\tau_R > 9.6$ ns, which gives an approximation of the ramp time we need for an adiabatic passage.

Let us now examine the numerical results. We have plotted on Fig. 5.6b the same simulation than in Fig. 5.6a but with a perfect square pulse. We see that for the first diabatic passage from S to V there is at first sight little difference since we start in the $|v_1 \downarrow\rangle$ state which is well separated from the other states in energy. Nonetheless the Rabi oscillations have a slightly smaller amplitude, indicating that the $|0\rangle$ state has been coupled to some excited states. In the second diabatic passage from V to S, we start from a mostly $|v_2 \downarrow\rangle$ state. During the passage, the state does not follow the $|1\rangle$ branch but retains a large $|v_2 \downarrow\rangle$ component, with $\langle S_y\rangle$ dropping to $\simeq -0.5$. By varying the ramp time τ_R we find that for a good adiabatic passage (with the criteria $P_D = 10^{-5}$) the minimal τ_R time is 9 ns. Eq. 5.9 hence gave a very good estimation, showing that the passage of the anticrossing is the most limiting point.

Consequently we could reduce this time by increasing the value of $C_{v_1 v_2}$ at the anticrossing. For instance, at $B = 1.5$ T, $C_{v_1 v_2} = 4.1$ μeV at the anticrossing. Keeping the same $\Delta^S - \Delta^V$, Eq. 5.9 then gives $\tau_R = 4.2$ ns. Another possibility is to adapt the backgate gate signal to make it slower as we are closer to the anticrossing.

5.2.3   Control of rotation axis.

Now that we have properly calibrated the ramp times, another issue to take care of in designing the control signals arise when we want to chain together two rotations. Indeed when going from S to V and from V to S, the phase of the qubit state drifts for two reasons. First, the precession frequencies are different at point S and at point V, since $hf^S = g\mu_B B/2$ and $hf^V = \Delta/2$. Second, the adiabatic passages add a phase that has two components: the dynamical phase that comes from the time evolution, and the geometric phase that comes from the continuous variation of the eigenstates.

We therefore introduce the time-dependent states $|0\rangle(t) = |v_1 \downarrow\rangle e^{+i\omega_S t/2}$ and $|1\rangle(t) = |v_1 \uparrow\rangle e^{-i\omega_S t/2}$, where $\omega_S/(2\pi)$ is the precession frequency at point S. The projections of the qubit state on $|0\rangle(t)$ and $|1\rangle(t)$ define its representation in the rotating Bloch sphere at point S.

The transformation matrix T for the complete manipulation sequence reads in the $\{|0\rangle(t), |1\rangle(t)\}$ basis set:

$$T = R_Z(\Delta\varphi_{\mathrm{VS}}) R_Z(\Delta\varphi_{\mathrm{V}}) R_{XY}(\alpha, \varphi) R_Z(\Delta\varphi_{\mathrm{SV}}), \tag{5.10}$$

where $R_Z(\alpha)$ is the matrix of a rotation of angle α around the polar axis $\mathbf{Z}$ of the Bloch sphere:

$$R_Z(\alpha) = \begin{pmatrix} e^{i\alpha/2} & 0 \\ 0 & e^{-i\alpha/2} \end{pmatrix}, \tag{5.11}$$

and $R_{XY}(\alpha, \varphi)$ is the matrix of a rotation of angle α around $\mathbf{U} = \cos\varphi \mathbf{X} + \sin\varphi \mathbf{Y}$:

$$R_{XY}(\alpha, \varphi) = \begin{pmatrix} \cos(\alpha/2) & -i\sin(\alpha/2)e^{i\varphi} \\ -i\sin(\alpha/2)e^{-i\varphi} & \cos(\alpha/2) \end{pmatrix}. \tag{5.12}$$

The first rotation, $R_Z(\Delta\varphi_{\mathrm{SV}})$, accounts for the phase drift on the way from S to V. The second, $R_{XY}(\alpha, \varphi)$, accounts for the electrical manipulation at V. The third, $R_Z(\Delta\varphi_{\mathrm{V}})$, accounts for the difference in precession frequencies at V and S. Finally the fourth, $R_Z(\Delta\varphi_{\mathrm{VS}})$, accounts for the phase drift on the way back to S. $\Delta\varphi_{\mathrm{SV}}$ and $\Delta\varphi_{\mathrm{VS}}$ depend on the back gate voltage ramps, while $\Delta\varphi_{\mathrm{V}} = (\omega_{\mathrm{V}} - \omega_{\mathrm{S}})\tau_{\mathrm{V}}$, where $\omega_{\mathrm{V}}/(2\pi)$ and τ_{V} are the precession frequency and the total time spent at point V, respectively. α is controlled by the duration $\tau_\alpha \leq \tau_{\mathrm{V}}$ of the RF pulse at V. The axis of rotation, characterized by φ, can be controlled by the phase of the RF signal, as demonstrated in Fig. 5.8. The above sequence of rotations can be factorized as:

$$T = R_Z(\Delta\varphi_{\mathrm{SV}} + \Delta\varphi_{\mathrm{V}} + \Delta\varphi_{\mathrm{VS}}) R_{XY}(\alpha, \varphi - \Delta\varphi_{\mathrm{SV}}). \tag{5.13}$$

Namely, the net operation appears as a rotation around an axis of the equatorial plane of the Bloch sphere (as expected), followed by a rotation around $\mathbf{Z}$ that outlines the total
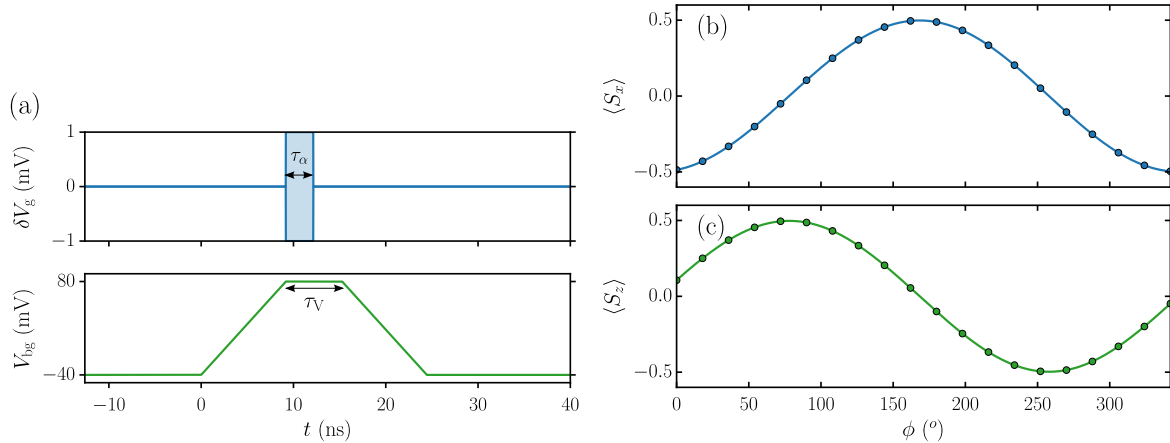
Figure 5.8: (a) Time series for a $\pi/2$ rotation from the $|v_1 \downarrow\rangle$ state (b,c) Expectation value of S_x and S_z in the rotating Bloch sphere after that $\pi/2$ rotation as a function of the phase ϕ of the driving RF signal.

phase accumulated out of the S point. This phase must be accounted for when chaining rotations. Once the ramp time is fixed, $\Delta\varphi_{SV}$ and $\Delta\varphi_{VS}$ are fixed, so the total phase can be compensated by choosing τ_V such that $\Delta\varphi_T = \Delta\varphi_{SV} + \Delta\varphi_V(\tau_V) + \Delta\varphi_{VS} = 2n\pi$ irrespective of the rotation (typically, τ_V must be greater than τ_π so that π rotations can be accommodated within the manipulation window at V).

By varying the phase of the microwave signal we are in principle able to control the axis of rotation of the spin in the Bloch sphere [93] and consequently to perform arbitrary rotations giving a two-axis control on the Bloch sphere. We show in Fig 5.8 the expectation values of S_x and S_z in the rotating Bloch sphere after a $\pi/2$ rotation from the $|v_1 \downarrow\rangle$ state as a function of the phase ϕ of the RF signal on the front gate, namely $\delta V_g(t) \propto \sin(\omega_V t + \phi)$. In this figure, the time τ_V spent at the V point has been adjusted so that two successive $\pi/2$ rotations around the same axis result in a net π rotation, i.e $\Delta\varphi_T = 2n\pi$. Still, the phase ϕ of the second rotation must account for the mismatch in precession frequencies at S and V. For example, if the first rotation at time t_0 is driven by a RF signal $\delta V_g(t) \propto \sin[\omega_V(t - t_0) + \phi]$, the second rotation at time t_1 must be driven by a RF signal $\delta V_g(t) \propto \sin[\omega_V(t - t_0) + \phi + (\omega_S - \omega_V)(t_1 - t_0)]$. Such a phase management is systematic in qubit systems where the precession frequency changes with a tuning parameter.

To conclude we have shown how to operate the spin-valley qubit with gate signals using time-dependent calculations on top of the tight-binding Hamiltonian. We have computed the dynamics of the system and have given the conditions for adiabatic passage of the anticrossing. Finally we have shown that some precautions need to be taken when chaining rotations as our protocol introduces systematic dephasing at each qubit operation. Nonetheless our protocol depends a lot on the amplitude and tunability of the valley splitting, as well as on the existence of sizable intervalley dipolar and spin-orbit

couplings. We will see in part 5.4 and 5.5 that in our system both features depends on the surface roughness and film thickness thus calling for careful design.

5.3   Noise and decoherence

In the previous parts we have shown how to operate the spin-valley qubit in a decoherence-free environment, we will now study the decoherence in both regimes. In silicon devices there are various sources of electric noises with different dynamics, which are not well characterized and depends a lot on the device. Here we choose to study the effects of two simple pervasive noises (Johnson-Nyquist and phonons) on the qubit. We will show, as we first intuitively claimed, that the decoherence is faster in the valley regime than in the spin regime because of the greater sensitivity to electric fields.

Huang and Hu [129] have studied the spin relaxation in a spin-valley system with spin-orbit coupling, and reached good agreement with the measurements of Yang et al [50]. In this paper the relaxation of a spin up is calculated as a function of the magnetic field, showing as in the experiment an enhancement of the relaxation rate at the anticrossing. The relaxation rate T_1^{-1} due to the electron-phonon interactions are

$$
T_{1,l}^{-1} = \frac{\omega_{01}^5}{4\pi\hbar\rho v_l^7} \left[\frac{|Y_{01}|^2 + |Z_{01}|^2}{2} \left(\frac{4}{3}\Xi_d^2 + \frac{8}{15}\Xi_d\Xi_u + \frac{4}{35}\Xi_u^2 \right) \right.
$$
$$
\left. + |X_{01}|^2 \left(\frac{2}{3}\Xi_d^2 + \frac{4}{5}\Xi_d\Xi_u + \frac{2}{7}\Xi_u^2 \right) \right] \coth\left(\frac{\hbar\omega_{01}}{2kT} \right) \tag{5.14}
$$

for the longitudinal phonons, and

$$
T_{1,t}^{-1} = \frac{\omega_{01}^5}{4\pi\hbar\rho v_t^7} \left[\frac{|Y_{01}|^2 + |Z_{01}|^2}{2} \frac{16}{105}\Xi_u^2 + |X_{01}|^2 \frac{4}{35}\Xi_u^2 \right] \coth\left(\frac{\hbar\omega_{01}}{2kT} \right), \tag{5.15}
$$

for the transverse phonons, where $\omega_{10}/(2\pi)$ is the qubit precession frequency, $X_{01} = \langle 0|x|1 \rangle$, $Y_{01} = \langle 0|y|1 \rangle$ and $Z_{01} = \langle 0|z|1 \rangle$ are the dipole matrix elements in the device axis set, $v_l = 9000$ m/s and $v_t = 5400$ m/s are the longitudinal and transverse sound velocities, $\Xi_d = 1.0$ eV and $\Xi_u = 8.6$ eV are the conduction band deformation potentials, $\rho = 2329$ kg/m^3 is the mass density of silicon, and $T = 100$ mK is the temperature.

We follow Refs. [129,140,141] for the relaxation rate T_1^{-1} and dephasing rate T_2^{*-1} due to Johnson-Nyquist noise. Also known as thermal noise, this noise corresponds to the fluctuations of potential due to the thermal agitation and zero-point motion of electrons inside an electrical conductor. In our case the electrical conductor is the metallic gates. We assume a $R = 2k\Omega$ series resistance on the front gate and neglect the noise on the far

less coupled back and lateral gates. Then,

$$T_{1,\text{jn}}^{-1} = \frac{4\pi}{\hbar}\frac{R}{R_0}|D_{01}|^2\hbar\omega_{01}\coth\left(\frac{\hbar\omega_{01}}{2kT}\right)$$

$$T_{2,\text{jn}}^{*-1} = \frac{2\pi}{\hbar}\frac{R}{R_0}|D_{11} - D_{00}|^2 kT\,, \tag{5.16}$$

where $R_0 = h/e^2$, $D_{00} = \langle 0|D|0\rangle$, $D_{11} = \langle 1|D|1\rangle$ and $D_{01} = \langle 0|D|1\rangle$, with $D(\mathbf{r}) = \partial V_{\text{tot}}/\partial V_g$ the gate coupling operator.

The relevant data at the S and V points are given in Table 5.1. As expected, T_1 and T_2^* are much longer in the spin than in the valley regime due to the reduced sensitivity of spin qubits to electric fields. The operation of the qubit is limited by Johnson Nyquist noise, but the calculated $T_{1,\text{jn}}$ remains orders of magnitude larger than the total manipulation time (around 25 ns on Fig. 5.8). The phonon-limited T_1's are also much longer than measured in Ref. [50] because the valley splittings and dipole matrix elements are smaller (in particular, $T_{1,\text{l}}$ and $T_{1,\text{t}}$ scale as Δ^{-5} in the valley regime). Practically, the coherence might be limited by various sources of $1/f$ noise [61, 141], which still need to be carefully characterized. In particular an important expected effect is the noise of the capture-release of charges by traps that are known to exist in standard MOSFETs [142], either as dopants in source/drain or in the gate stack (especially with HfO$_2$ [143]), and are responsible for random telegraph noise. It has been in particular observed in the Coulomb blockade regime by Hofheinz *et al* [144] and more recently by Li *et al* [145]. It is in principle possible to study this effect with the tools we have. We need to compute the matrix elements associated with the change of potential due to the capture-release of a charge by a trap, then add it as a noise with Poisson statistics (with a characteristic time of capture and release) in the time dependent-solver in order to compute T_1 and T_2 numerically. The methodology has been implemented but the study is still ongoing at this time.

The working points of spin and valley mode have been chosen arbitrarily, so the T_1 and T_2^* we have computed are not optimal. Indeed, we have computed T_1 and $T_{2,jn}^*$ as a function of the backgate bias at $B = 1$ T, plotted in Fig. 5.9. We see that we can gain on both times in the spin mode by going further away from the anticrossing at more negative V_{bg}, but the lifetime of the qubit is already pretty long at that point. More interestingly there is a peak on T_2^* at $V_{\text{bg}} \simeq 0.15$ V, which corresponds to a sweet spot in the energy splitting that we can see in Fig. 5.4. Indeed the energy splitting (and thus ω_V) is independent on V_g and V_{bg} to first order, which limits the sensitivity of the qubit to electrical noises and enhances the T_2^*. This could be an interesting working point for the qubit in the valley mode, with improved coherence and fast manipulation.

	S point	V point
$\hbar\omega_{01}$ (μeV)	115.3	98.3
X_{01} (Å)	0.000	0.001
Y_{01} (Å)	0.005	0.050
Z_{01} (Å)	0.011	0.287
D_{01} (μV/V)	9.5	348.9
$|D_{11} - D_{00}|$ (μV/V)	2.4	607.8
$T_{1,l}^{-1}$ (s^{-1})	$1.02{\times}10^{-2}$	3.08
$T_{1,t}^{-1}$ (s^{-1})	0.15	32.8
$T_{1,\mathrm{jn}}^{-1}$ (s^{-1})	15.4	$1.77{\times}10^{4}$
$T_{2,\mathrm{jn}}^{*-1}$ (s^{-1})	$3.64{\times}10^{-2}$	$2.35{\times}10^{3}$

Table 5.1: Precession frequency, dipole and gate coupling matrix elements, inverse relaxation and coherence times at the S and V points of Fig. 5.4.
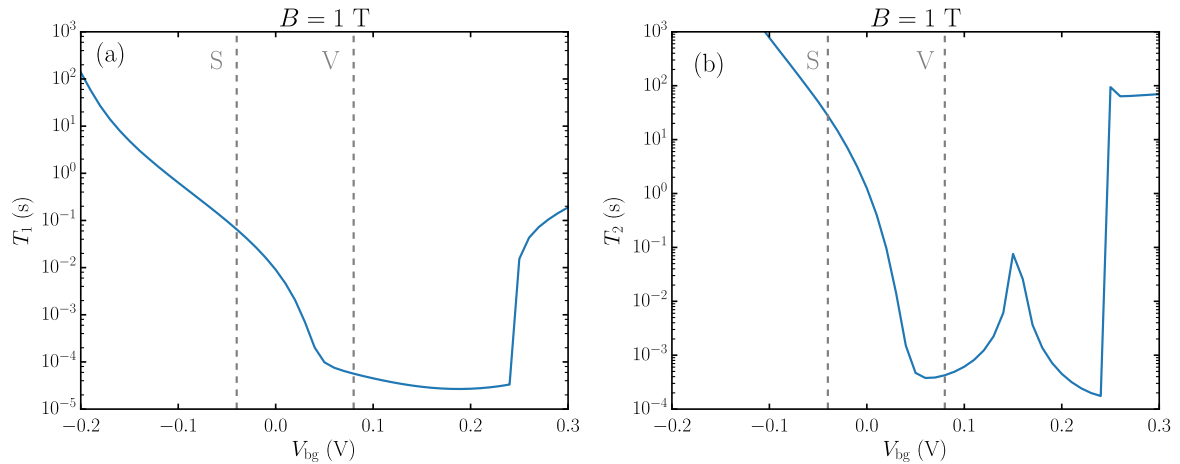

Figure 5.9: (a) Relaxation time including phonons and Johnson-Nyquist noises as a function of V_{bg} (b) Dephasing time for Johnson-Nyquist noise $T_{2,\mathrm{jn}}^{*}$ as a function of V_{bg}. For both panels $B = 1$ T, and the vertical gray dotted lines mark the spin and valley operation points of part 5.2.

5.4 Effect of surface roughness

We have seen in detail how to implement our spin-valley qubit scheme in an ideal device. An important concern on the feasibility of this approach is whether it is still doable in a realistic device. In this part we have thus studied the effect of surface roughness, which is a source of local disorder that is always present, although it can be reduced [146].

We have used realistic surface roughness parameters (but neither state of the art nor optimal) generated from a gaussian spectral density with rms $\Delta_{\text{SR}} = 0.4$ nm on the top and lateral interfaces and $\Delta_{\text{SR}} = 0.25$ nm on the bottom interface, with a correlation length of $\Lambda_{\text{SR}} = 1.5$ nm on all sides. Δ_{SR} lies in the upper range of the values compatible with the carrier mobilities measured in similar devices at room temperature [87, 89]. The description of the surface is critical for the physics of the valley splitting. Here the surface is passivated with pseudo-hydrogen atoms, however we compared our results to test calculations made with the model of Ref. [111] for the Si/SiO_2 interfaces, which show exactly the same trends.

The main elements of the EDSR model (Δ, $C_{v_1 v_2}$, $D_{v_1 v_2}$) have been computed for 16 different samples with surface roughness disorder, as a function of V_{bg}. The results are plotted Fig. 5.10. The Rabi frequency maps (B, V_{bg}) of four of these samples are plotted in Fig. 5.11 as an illustration. The maximal f_R are typically a few tens of MHz, which is significant.

Let us discuss the three elements of the model one by one, starting with the valley splitting. A well-known observation is that Δ is reduced with surface roughness [47, 132, 147], because it disturbs the reflections of the wavefunctions on the interfaces. The variability is low at the minimum of Δ and increases when V_{bg} pulls the wavefunction at the top or bottom interface. This has an important consequence for our scheme: it is always possible to choose a reasonable magnetic field such that $g\mu_B B > \min(\Delta(V_{\text{bg}}))$ for all the devices. As the variability increases away from the minimum, the bias point where the anticrossing occurs (that is $g\mu_B B = \Delta(V_{\text{bg}}^A)$) will be quite different from device to device. Each qubit will thus need an individual calibration, which is almost always the case whatever the qubit architecture.

Concerning the spin-orbit, the $C_{v_1 v_2}$ matrix element has very low variability. It goes to zero at exactly the same V_{bg} for all devices. This is very interesting on the physics side because it means that it does not change with the details of the interface and depends only on the overall confinement.

Finally the surface roughness effect on the dipolar interaction is probably the weakest point of this proposal so far. As the valley splitting, $D_{v_1 v_2}$ is also decreased by the SR disorder. The variability is quite high, because $D_{v_1 v_2}$ is now not only due to the vertical electric field (along $\mathbf{z}$), as the surface roughness also creates non zero intervalley dipolar coupling in the $\mathbf{y}$ direction [52, 133] (the gate electric field being mostly along $\mathbf{z}$ and $\mathbf{y}$).
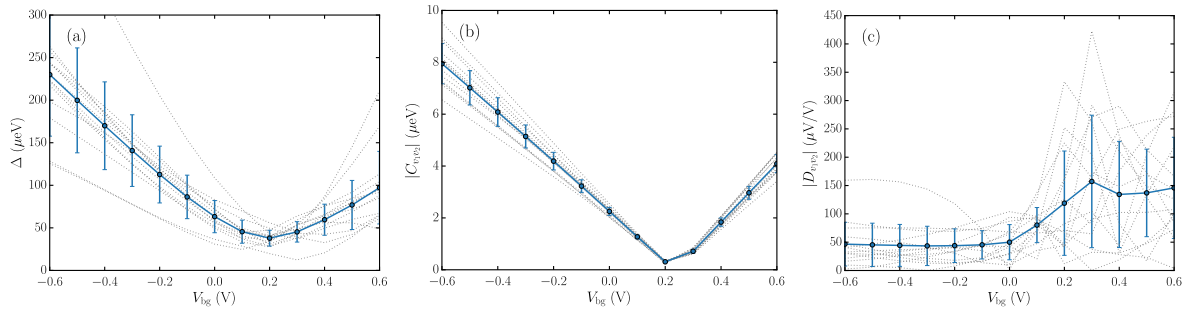
Figure 5.10: (a) Valley splitting Δ as a function of the back gate voltage V_{bg}, for different realizations of the surface roughness disorder (dotted gray lines). The average and standard deviation are plotted as the blue line and error bars. (b) SOC matrix element $C_{v_1 v_2}$ as a function of the back gate voltage V_{bg}, for different realizations of the disorder (c) Gate coupling matrix element $D_{v_1 v_2}$ as a function of the back gate voltage V_{bg}, for different realizations of the disorder. $V_g = 0.1$ V in all plots.

Again, at the price of a bit slower Rabi frequencies (keeping in mind that the time we apply microwave is not the longest time of our scheme) and individual bias calibration of the qubits, our manipulation protocol is still interesting. For all the realizations of the disorder there is always a maximum of the Rabi frequency in the valley mode of at least 20 MHz/mV. This is also the result that can be the most debated, since it depends on the description of the interfaces and on the thickness [64]. For the performances of the qubit as well as for the modeling it is then necessary to delve into the valley physics of these devices. That is the study we started in the next part using a simple two-valleys effective mass analytical model and tight-binding simulations.
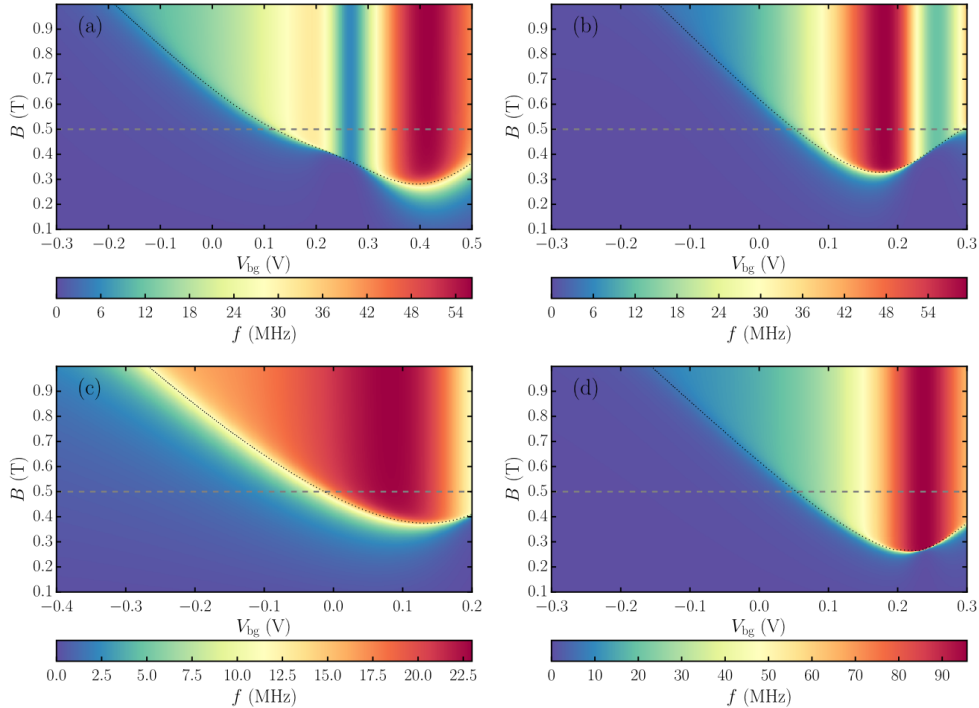
Figure 5.11: Map of the Rabi frequency as a function of the magnetic field and V_{bg}, for different realizations of the disorder. The dotted black line is the anti-crossing condition $E_Z = g\mu_B B = \Delta(V_{\text{bg}})$. The horizontal dashed line is a target magnetic field $B = 0.5$ T for qubit operation. $V_g = 0.1$ V and $\mathbf{B} \parallel y$ in all plots.

5.5 Valley physics and dependence of thickness.

In the following we will give a simple model for the valley physics and use it to explicit the valley splitting. We will study in particular the influence of the interfaces and of the thickness of the nanowire, which are crucial here. Indeed in the last part we have studied the variability due to interface roughness for a given thickness, but the device-to-device variation of the thickness is estimated to be a few Å, depending on the process. It is up to now impossible to control the thickness with atomic precision, so this must be included in the study of variability of the devices.

Let us start from the uncoupled valley solutions in the simple effective mass approximation (EMA). The EMA Hamiltonian is noted H_0, with $H_0\phi_0^\pm = \epsilon_0\phi_0^\pm$, and:

$$\phi_0^\pm(\mathbf{r}) = \phi_0(\mathbf{r})e^{\pm ik_0 z}u_{\pm k_0}(\mathbf{r}) \tag{5.17}$$

We include only the valley mixing effects resulting from the interfaces through the operator:

$$\hat{V}_{if} = \left(\hat{V}_T\delta(z - H/2) + \hat{V}_B\delta(z + H/2)\right)\theta(|y| - W/2) \tag{5.18}$$

85

with

$$\hat{V}_{T,B} = \begin{pmatrix} 0 & \lambda_{T,B} \\ \lambda_{T,B}^* & 0 \end{pmatrix} \tag{5.19}$$

Let us now introduce the matrix element $V = \langle \phi_0^+ | \hat{V}_{if} | \phi_0^- \rangle$ so that in the basis $\{\phi_0^+, \phi_0^-\}$ the Hamiltonian reads:

$$H = \begin{pmatrix} \epsilon_0 & V \\ V^* & \epsilon_0 \end{pmatrix} \tag{5.20}$$

The eigenenergies of this Hamiltonian are

$$E_\pm = \epsilon_0 \pm |V| \tag{5.21}$$

and its eigenfunctions are

$$\Psi_0^\pm(\mathbf{r}) = \frac{1}{\sqrt{2}}(e^{ik_0 z}u_{k_0}(\mathbf{r}) \pm e^{-i\phi_V}e^{-ik_0 z}u_{-k_0}(\mathbf{r}))\phi_0(\mathbf{r}) \tag{5.22}$$

with $\phi_V = \arg(V)$. We can write explicitly the matrix element V:

$$
\begin{aligned}
V &= \int \phi_0^{+*}(\mathbf{r})V_{if}(\mathbf{r})\phi_0^-(\mathbf{r})d\mathbf{r} \\
&= \int |\phi_0(\mathbf{r})|^2\, e^{-2ik_0 z}\, |u_{k_0}(\mathbf{r})|^2\, V_{if}(\mathbf{r})d\mathbf{r} \\
&= \iint_{xy} \left|\phi_0(x,y,\frac{H}{2})\right|^2 \lambda_T e^{-ik_0 H} \;+\; \left|\phi_0(x,y,-\frac{H}{2})\right|^2 \lambda_B e^{ik_0 H} dxdy
\end{aligned}
$$

so that

$$V = \chi_T \lambda_T e^{-ik_0 H} \;+\; \chi_B \lambda_B e^{ik_0 H} \tag{5.23}$$

with

$$\chi_T = \iint_{xy} \left|\phi_0(x,y,\frac{H}{2})\right|^2 dxdy \tag{5.24}$$

$$\chi_B = \iint_{xy} \left|\phi_0(x,y,-\frac{H}{2})\right|^2 dxdy \tag{5.25}$$

The valley splitting is $\Delta = E_+ - E_- = 2\,|V|$, so

$$\Delta = 2\sqrt{\chi_T^2\,|\lambda_T|^2 + \chi_B^2\,|\lambda_B|^2 + 2\chi_T\chi_B\,|\lambda_T|\,|\lambda_B|\cos(2k_0 H + \phi_T - \phi_B)} \tag{5.26}$$

with $\arg(\lambda_{\text{T,B}}) = \phi_{\text{T,B}}$. This general expression for Δ was first given by Nestoklon $et\ al$ [64]. We are now going to look at some limiting cases. The first limit is when the electron is pushed on the top (respectively bottom) interface, so that $\chi_B = 0$ ($\chi_T = 0$), hence only

one term in Eq. 5.26 does not vanish and we are left with:

$$\Delta_{\text{Top/Bottom}} = 2\chi_{T,B} \left| \lambda_{T,B} \right| \tag{5.27}$$

As $\lambda_{T,B}$ is a constant, we expect that the linear dependence of $\Delta(V_{\text{bg}})$ in this regime is due to the linearly increasing charge density on the interface. We have verified this by computing explicitly (in EMA) the wavefunction density at the interface, and find indeed a perfect linear dependence on V_{bg}. A second limiting case is when the wavefunction is symmetric with respect the two interfaces, and $\chi_T = \chi_B$. This should be the case in particular when $\Delta(V_{\text{bg}})$ is minimum. The valley splitting then reads:

$$\Delta = 2\chi_T \sqrt{(\left|\lambda_T\right|^2 + \left|\lambda_B\right|^2) + 2\cos(2k_0 H + \phi_T - \phi_B)} \tag{5.28}$$

Eq. 5.28 shows that Δ should oscillate with the thickness H, but as $\chi_{T,B}$ decreases with increasing H these oscillations must be damped. We have computed the valley splitting as a function of H in the symmetric case. It is important to realize here that in tight-binding H is a multiple of the thickness of one atomic layer, and that the orientation of the surface bonds is shifted by 90 degrees each time we add an atomic layer, as illustrated Fig. 5.12. We call these types of interfaces α, for hydrogen bondings perpendicular to the wire direction, and β, for hydrogen bondings parallel to the wire direction. We have then two orientations for each surface which should give two different phases for $\phi_{T,B}$, but with similar amplitude $\left|\lambda_{T,B}\right|$. In the end there are four possibilities of interfaces: $\alpha\alpha$, $\beta\alpha$, $\alpha\alpha$, $\beta\beta$. For the global decrease of Δ with H, it can be estimated from χ_T. The hard wall boundary conditions $\phi_0(x, y, z = \pm\frac{H}{2}) = 0$ cannot be used because they imply $\chi_{T,B} = 0$ so $\Delta = 0$. We can apply in this case generalized hard wall boundary conditions as given by Volkov and Pinsker [148]:

$$\phi_0(z = \pm\frac{H}{2}) = R\frac{\partial\phi_0}{\partial z}(z = \pm\frac{H}{2}) \tag{5.29}$$

where R is homogeneous to a length [1]. Then,

$$\chi_T = R^2 \iint_{xy} \left| \frac{\partial\phi_0}{\partial z}(x, y, \frac{H}{2}) \right|^2 dxdy \tag{5.30}$$

If we approximate ϕ_0 by the solution of the 3D infinite quantum well, with width W, height H and length L, namely $\phi_0(x, y, z) = \sqrt{\frac{8}{LWH}} \cos(\frac{\pi}{L}x) \cos(\frac{\pi}{W}y) \cos(\frac{\pi}{H}z)$, we get:

$$\chi_T = \frac{2\pi^2 R^2}{H^3} \tag{5.31}$$

---

[1]In a quantum well of width H and with finite depth U_0 such that $\frac{\hbar^2\pi^2}{2mH^2} \ll U_0$, $R \simeq \frac{\hbar}{\sqrt{2mU_0}}$
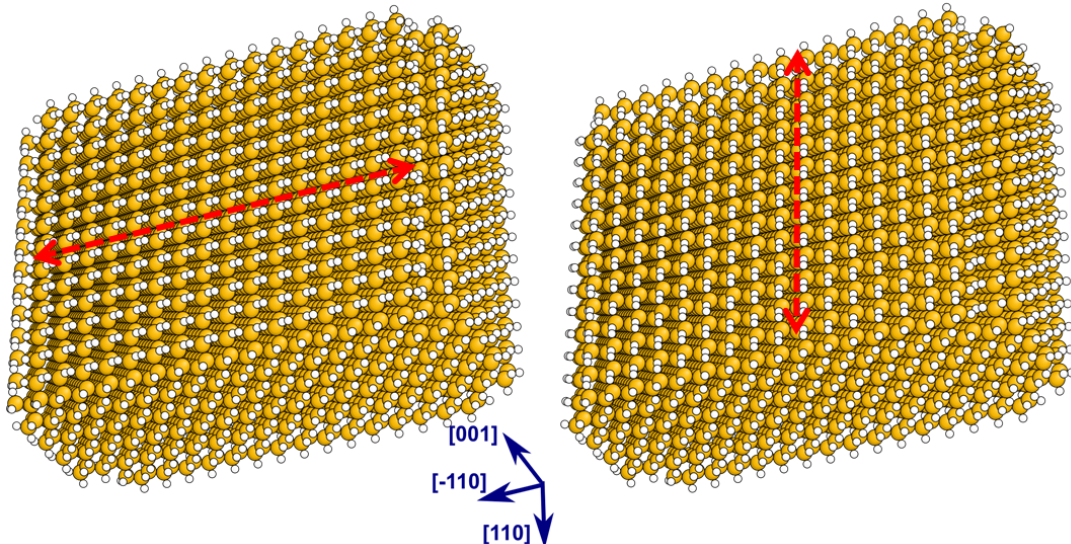
Figure 5.12: Small portion of a silicon nanowire passivated with hydrogen atoms. (Left) Type α interface, the surface bondings are oriented perpendicularly to the wire direction. (Right) Type β interface, the surface bondings are oriented parallel to the wire direction.

In Fig. 5.13a we have plotted the valley splitting at $V_{\mathrm{bg}} = 0.15$ V (symmetric case) as a function of H, for the four sets of interfaces. All the curves show damped oscillations but with different phases. This confirms that the parameters $\phi_{T,B}$ in our model can be related to the surface orientation, and that $|\lambda_{T,B}|$ does not depend on this orientation. The curves for $\alpha\alpha$ and $\beta\beta$ are almost superimposed, as well as the curves for $\alpha\beta$ and $\beta\alpha$. What seems to matter here is if the surface bondings of each interface are parallel or orthogonal.

First, concerning the global decrease of Δ with H, we have fitted the data with a $\propto \frac{1}{H^3}$ envelope, showing excellent agreement, highlighting the relevance of this model (Fig. 5.13). Then, in Fig. 5.13, we have fitted the full model (Eq. 5.28) with damping and oscillations with

$$\Delta = \frac{K}{H^3}\sqrt{A + 2\cos(2k_0 H + \Phi)} \qquad (5.32)$$

We have distinguished between parallel and orthogonal surface bondings. In both cases the parameters K and A are similar. As for the phase, we obtained $\Phi^{\parallel} - \Phi^{\perp} = \pi$, the oscillations in the sets of parallel and perpendicular surface bondings are antiphased. More precisely we have $(\phi_T^{\alpha} - \phi_B^{\alpha}) - (\phi_T^{\alpha} - \phi_B^{\beta}) = \pi$. Assuming that $|\lambda_T| = |\lambda_B|$ because the interfaces are identical, then $\phi_T^{\alpha,\beta} = \phi_B^{\alpha,\beta}$, and the previous relation becomes $\phi_{T,B}^{\beta} - \phi_{T,B}^{\alpha} = \pi$.

This is the case of an ideal device, however in a realistic sample, the interface disorder is expected to decrease the valley splitting as it mixes the interference between the two valleys [52, 132, 147] as we have already observed in part 5.4. However it has never been shown if the oscillations of Δ with H are still present. We have tried to verify this here by computing the valley splitting for different surface roughness profile (with the same
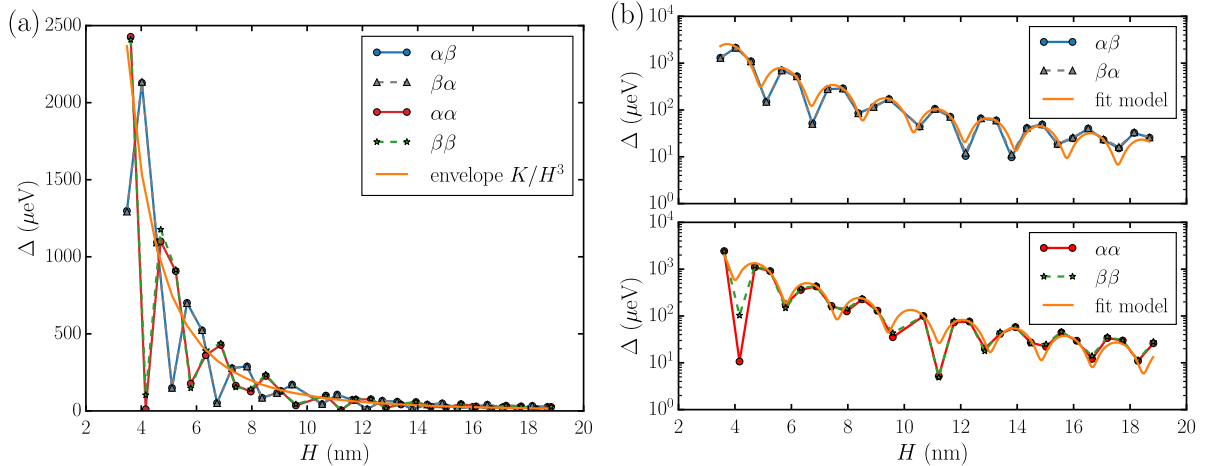
Figure 5.13: Valley splitting as function of the wire thickness H, for four sets of surface termination. The hydrogen bondings of top and bottom surfaces are either parallel (AA or BB) or orthogonal (AB or BA). (a) Linear scale, we fit the envelope from the model of Eq. 5.31. (b) Semilog scale, we fit the full model from Eq. 5.32 for orthogonal surface bondings (top panel) and parallel surface bondings (bottom panel).

parameters as in part 5.4), as a function of H. The results of the calculation of the valley splitting of 11 samples of surface roughness are plotted on Fig. 5.14, along with the average value and standard deviation. Here we plotted Δ at $V_{\mathrm{bg}} = 0.2$ V, which is close to the minimum of $\Delta(V_{\mathrm{bg}})$. We still observe a decrease of $\Delta^{\min}$ with H. The variability is high for small thicknesses, and is decreasing with H. The necessary condition of our scheme is to have $g\mu_B B > \min(\Delta(V_{\mathrm{bg}}))$, and $\min(\Delta(V_{\mathrm{bg}}))$ small enough to allow qubit manipulation at frequencies $\Delta^{\min}/h$ of a few tens of GHz. This is achieved for a thickness higher than 8 nm. Interestingly, the oscillations of $\Delta^{\min}$ with H are still visible. This means that for a random surface profile, the valley phase does not have a totally random value, otherwise the different samples would not have the same oscillations.

Models for the dependence of $D_{v_1 v_2}$ and $C_{v_1 v_2}$ on the thickness are under development in order to reach a comprehensive understanding of the Rabi frequency with the design of the device. Preliminary results indeed show that $C_{v_1 v_2}$ does not depend much on H, whereas $D_{v_1 v_2}$ exhibits large variations with H.
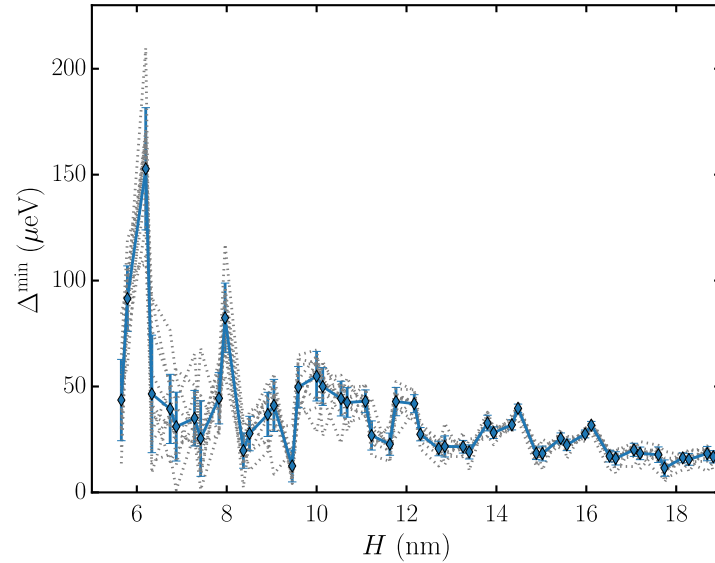
Figure 5.14: Valley splitting as function of the wire thickness H, with surface roughness. The individual samples are in dotted lines, the blue line is for the average valley splitting, and the error bars show the standard deviation.

5.6 Experimental control of valley splitting with backgate potential

To conclude this study on the spin-valley quantum bit, we present a new experimental result in a device similar to the one we studied in the simulations.

Several groups have demonstrated the electrical control of the valley splitting in planar Si/SiO_2 MOS quantum dots [50,56], showing linear dependence with gate bias. Up to date the valley splitting was not measured as a function of backgate in a nanowire device with at least one partially covering gate. Nevertheless this measurement has been performed at Hitachi Cambridge in a similar device with trigate geometry. This is a first experimental step in realizing the spin-valley qubit scheme. The device consists in a [110]-oriented nanowire with $W = 42$ nm, $H = 8$ nm and one overlapping gate of length $L_g = 44$ nm with the usual SiO_2/HfO_2 gate stack. The channel is doped with phosphorous at a concentration of 5×10^{17} cm^{-3}. The undoped silicon substrate is activated by flashing a
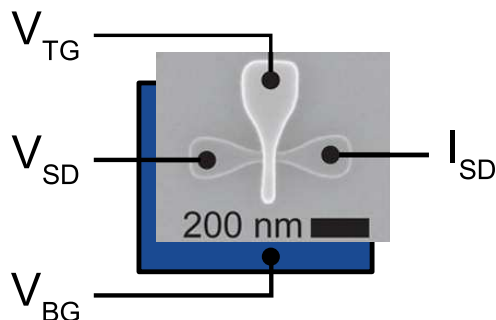
Figure 5.15: Device measured by David Ibberson at Hitachi Cambridge. From Ref. [57].
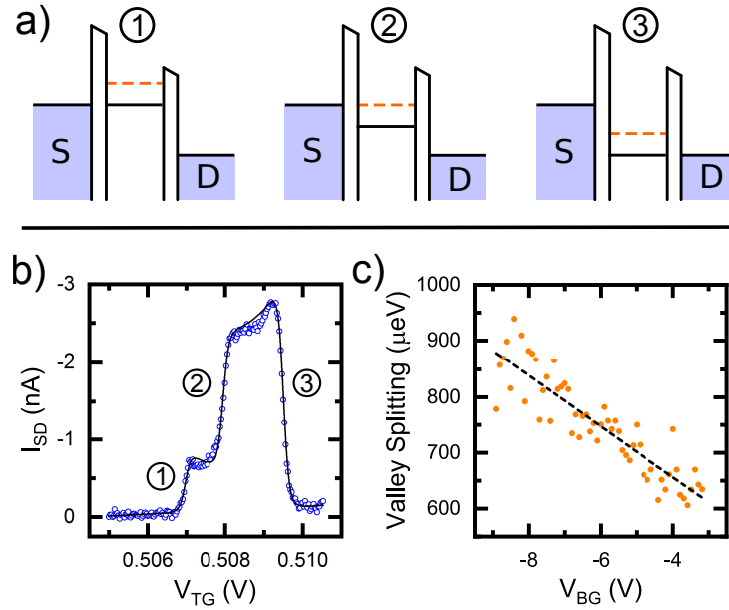
Figure 5.16: (a) Diagrams illustrating the respective alignment of the quantum dot and source and drain electrochemical levels at the three features observed in b). (b) Measured source-drain current (blue dots) in the first Coulomb oscillations at $V_{BG} = -7.8$ V. The black line is a fit considering that the system is in the sequential multi-level transport regime [43]. (c) Plot of valley splitting against V_{BG} with a best-fit line gradient of -45 ± 3 μeV/V. From Ref. [57] .
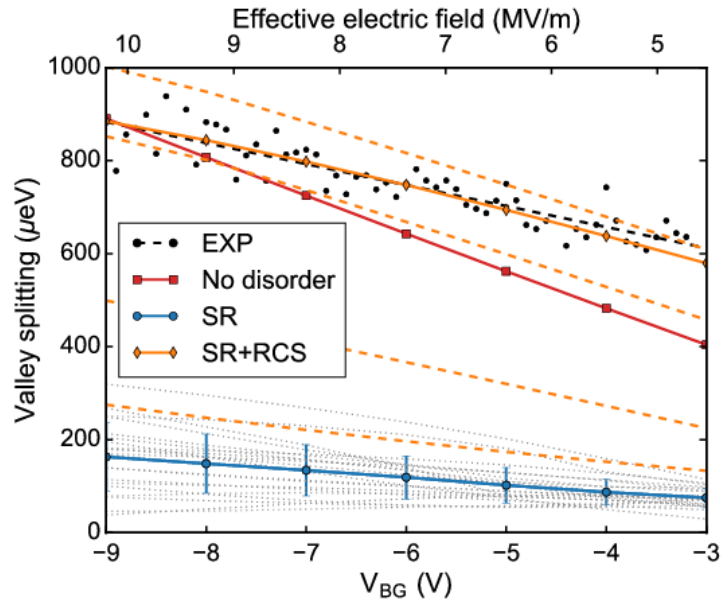
Figure 5.17: Tight-binding simulations of the valley splitting as a function of V_{BG}. The black dots are the experimental data points. The red line gives the trend for a perfect device with no defects or roughness. The blue line and error bars are the average an standard deviation for different SR profiles with rms 0.35 nm (each plotted as a dashed gray line). Finally, the orange lines are a few representative simulations with SR and RCS charges included (the best match with the experiment being highlighted by the solid line with diamond symbols). The top axis indicates the effective electric field felt by the electron.

surface-mounted blue LED to generate free carriers, then used as a back gate. A SEM picture of the device is shown Fig. 5.15.

For several backgate bias V_{BG}, Ibberson *et al* measured the source drain current while sweeping the top gate potential V_{TG}. This measurement, illustrated in Fig. 5.16a, presents three peaks. They correspond to three configurations shown Fig. 5.16b: ground state aligned with the source, excited state aligned with the source, ground state aligned with the drain. From this the ground state-excited state splitting is extracted as a function of V_{BG}, giving the curve Fig. 5.16c. This splitting shows a linear dependence with V_{BG} and goes from $880\,\mu$eV at $V_{BG} = -9$ V to $610\,\mu$eV at $V_{BG} = -3$, with a slope of $-45\pm3\,\mu$eV/V. To determine the nature of this excited state, we performed tight-binding calculations, that include several sources of disorder: dopants, surface roughness and charges in the gate stack.

First of all, the first orbital excited state is too far in energy, whatever the disorder, and does not show this linear dependence. The measured splitting is then most probably a valley splitting. We plot Fig. 5.17 the TB valley splitting in different cases. In the ideal case, the amplitude of the valley splitting is slightly lower than the experiment and indeed shows linear dependence but with a larger slope. As expected, surface roughness reduces the valley splitting amplitude and slope. Dopants could enhance Δ but then the slope is expected to be opposite if the wavefunction gets bound to a donor, as negative backgate voltages tend to transfer the electron from the dopant to the top interface thereby reducing the effects of the impurity potential (as already shown by Rahman *et al.* [149] and Roche *et al.* [97]). However we show that the measured Δ is compatible with the presence of charges in the gate stack. The presence of such charges at the Si/SiO$_2$ interface is supported by mobility measurements in similar devices and gives rise to "Remote Coulomb Scattering" (RCS) [87, 150]. The apparent density of these charges can be as large as a few 10^{13} cm^{-2}. In fact, the Coulomb disorder in the gate stack likely results from a combination of charge traps at this interface, local band offset fluctuations (interface dipoles), and possibly from work function fluctuations in granular metal gates [151]. Here we have modeled this disorder as a distribution of positive and negative charges at the SiO$_2$/HfSiO$_2$ interface with net density $n_{RCS} = 10^{13}$ cm^{-2}. In that case, the valley splitting depends strongly on the position of the charges. The localization is, indeed, much more efficient in a Coulomb than in a short-range SR potential, but also much more variable. For a given density of RCS charges, the valley splitting spans about one order of magnitude depending on their distribution. A statistical analysis of both mechanisms shows that 20 out of 20 simulated rough devices show well defined corner states at negative V_{BG}, while only 14 out of 20 simulated devices with RCS included still do so. In Fig. 5.17 a few representative samples are shown, illustrating this large variability, and a particular sample which reproduces perfectly the experimental results is highlighted. Coulomb disorder must, therefore, primarily be reduced in order to mitigate

device variability. As a matter of fact, the valley splitting has been measured in a similar device with two corner dots in parallel but with only SiO_2 as the gate dielectrics [94]. The valley splitting at $V_{BG} = -1$ V was found to be 145 μeV in one dot, which is more compatible with the TB valley splitting calculated with SR and no RCS. This calls for a careful assessment of the sources of disorder in silicon devices. Removing the HfO_2 oxide from the gate stack might help to reduce Coulomb disorder and variability.

As discussed earlier, the fact that Δ is linearly increasing with the gate potential, as the wavefunction is pushed at a Si/SiO_2 interface was already known. It was not obvious in our system since we have four interfaces. In fact, the lateral interfaces do not play a role because they are perpendicular to the most confined direction and therefore they do not act on the z valleys. We have verified this by computing the dependence of Δ with a pure lateral electric field and note no effect. We have thus computed the effective electric field felt by the electron, in the $\mathbf{z}$ direction, as $E_z^{\text{eff}} = \int E_z(r) \left| \Psi(r) \right|^2 dr$. That way the experimental slope of the valley splitting is 48 ± 3 μeV/(MV/m) with respect to the effective field. This is to be compared with the measured value in the planar MOS quantum dots of Refs. [50, 56], respectively 20.9 and 21.0 μeV/(MV/m). The order of magnitude is similar, but controlling the planar device seem less efficient.

In conclusion, this experiment is an important step towards the realization of the spin-valley qubit in a silicon nanowire. However it does not meet yet the requirements to implement our scheme. We would benefit from partially covering gates to create well controlled corner dots, and more importantly we should use devices with much smaller valley splitting. In order to make it easier to achieve and more reproducible, a message of these simulations is to suppress the HfO_2 oxide layer inherited from the ultra-scaled CMOS devices, and replace it with thicker SiO_2.

5.7   Conclusion

We have shown in chapter 4 that it was possible to manipulate electrically the spin of the electron in silicon, which is one of the main problem of current spin-based electron quantum bits. The electrical manipulation was allowed by the inter-valley spin-orbit interaction, coupling opposite spins of different valleys, and by the inter-valley dipolar interaction, coupling different valleys. In this chapter, we tailored these interactions in order to build a qubit which at the same time would have fast electrical control and preserve the good coherence properties of the electron spin. To achieve that we proposed a scheme, the spin-valley qubit, that consists in switching between a spin qubit where quantum information is well preserved, and a valley qubit for manipulation. The switch is made possible by the intervalley spin-orbit interaction and the electrical control over the valley splitting.

As we were working with the particular devices made at CEA in a silicon-on-insulator MOS technology, we leveraged on the backgate electrode to control the electric field, and thus the valley spitting. The nanowire and the partially covering gate are strong features of these devices because they easily break the symmetries of the electron wavefunction, thus allowing for sizable and reproducible inter-valley spin-orbit operation. Once in the valley mode, another requirement of the model is to be able to electrically couple the valley states. After demonstrating with tight-binding simulations that we had all this elements in our quantum dot device, we have studied the dynamics of the qubit with time-dependent simulations. We have derived the conditions on the control signals to operate properly the qubit, in order to keep the spin-valley passage adiabatic, and to compensate the systematic dephasing induced by this transition.

Once demonstrated how to operate the qubit, we have evaluated the decoherence and relaxation in both regimes to demonstrate the sustainability of the scheme. We have in particular dealt with pervasive sources of noise, phonons and Johnson-Nyquist, showing indeed the interest in switching modes for manipulation, but also the great advantage of having a small valley splitting. In order to asses further the feasibility of the protocol, we have studied the effect of surface roughness on the variability of the key figures of the qubit. The result is that the spin-orbit interaction is remarkably robust, so that the spin-valley switching is always possible. On the downside, as they depend on the atomic details of the interface, $D_{v_1v_2}$ (and Δ also to a lesser extent) has a large variability. We have also shown how the valley splitting depends on the thickness of the silicon layer, which must be optimized. Finally we have shown a new experiment on the measurement of the control of valley splitting with the backgate, the first step in the the realization of the spin-valley qubit.

Chapter 6

Hole spin qubits

Dans ce chapitre nous nous intéressons à la manipulation électrique des trous dans les qubits silicium. En effet, l'interaction spin-orbite est bien plus importante dans la bande de valence que dans la bande de conduction, et permet en principe de réaliser une manipulation du spin par EDSR. Dans le cadre de la réponse linéaire (en champ magnétique et en excitation électrique), deux mécanismes d'EDSR ont été identifiés. Le premier est la g-TMR ("g-Tensor Modulation Resonance") et repose sur le contrôle électrique des facteurs gyromagnétiques. Il requiert des facteurs g anisotropes et dépendant du potentiel. Un champ électrique crée une modulation du potentiel de confinement, qui se traduit par des facteurs g dépendant du temps, et donc en une modulation du vecteur de Larmor qui peut résulter en une rotation du spin. Le second mécanisme a été observé dans les semiconducteurs III-V, et la théorie a été donnée par Golovach, Borhani et Loss (GBL). Contrairement à la g-TMR, il n'est pas associé avec une variation des facteurs g. À la place, le champ électrique oscillant translate simplement la fonction d'onde sans changer sa forme. Pendant ce mouvement le couplage spin-orbite crée un champ magnétique effectif qui se couple au spin.

De manière générale il est attendu que ces deux mécanismes coexistent puisqu'ils partagent la même origine: le couplage spin-orbite. Notamment, dans les qubits de spin de trous dans le silicium ont été observées des oscillations de Rabi par EDSR [93], ainsi que des modulations électriques des facteurs g [152]. GBL et g-TMR doivent donc coexister dans ces dispositifs. Dans ce chapitre nous étudions cette coexistence dans un qubit de spin de trou, confiné dans une boîte quantique silicium. Pour cela, nous présentons tout d'abord des mesures d'anisotropie des facteurs g et de la fréquence de Rabi en fonction de l'orientation du champ magnétique. Après cela nous introduisons le formalisme de la matrice ĝ, qui est une généralisation de la g-TMR, et nous montrons comment il permet de séparer la fréquence de Rabi en deux contributions : la g-TMR, qui peut être extraite de mesures de splitting Zeeman, et l'iso-Zeeman EDSR, qui ne peut pas être extraite de telles mesures (le mécanisme GBL en est un exemple). Nous appliquons cette technique aux données expérimentales afin de déterminer ces deux contributions. Il appa-

raît que, comme attendu, les deux contributions coexistent. Le mécanisme dominant est l'iso-Zeeman EDSR, mais la contribution g-TMR est non négligeable. Finalement nous introduisons une méthode pour le calcul numérique de la matrice ĝ et nous l'appliquons à des des simulations **k.p** *pour reproduire qualitativement les cartographies de Rabi. Ces résultats mettent en évidence l'effet de la position de l'état dans le dispositif ainsi que l'impact important de la contrainte.*

In condensed matter, the spin-orbit (SO) interaction couples the motion of a particle to its spin state; in combination with a static magnetic field, alternate electric fields then result in intrinsic, effective magnetic fields able to rotate the spins [153]. Sufficiently strong SO can allow for electric-dipole spin resonance (EDSR). As we have seen, such a perspective is very attractive for quantum computation with confined spins in semiconductor as quantum bits (qubits) [154]. Indeed, it gets round the need of localized alternate magnetic fields [78, 155], rather challenging to generate, or magnetic field gradients [76, 156].

In the linear response regime where the Rabi frequency is proportional to th static magnetic and RF electric field, two mechanisms for spin rotations have been identified. The first one is called g-Tensor Modulation Resonance (g-TMR) and relies on the electrical tunability of the spin g-factors [157–159]. Indeed it requires anisotropic and gate dependent g-factors. In essence, an alternating electric field modulates the confinement potential and the shape of the electron wavefunction, which translates into time-dependent g factors and, therefore in a modulation of the Larmor vector which can result in a rotation of the spin. It is formally characterized by a tensor which describes g-factors variations. The second one was experimentally observed in a variety of III-V semiconductor quantum dots [22, 23, 32, 160] and the theory was given by Golovach, Borhani and Loss [161]. Contrarily to g-TMR, it is not associated with a variation of the g-factors. Instead, the alternating electric field shakes the wavefunction as a whole. During this motion, the spin-orbit interactions give rise to an effective time-dependent magnetic field proportional to the alternating electric field, to the static magnetic field, and to the inverse spin-orbit length. It can be characterized by an effective spin-orbit field $\mathbf{\Omega}_{\mathrm{SO}}$. Although sometimes called EDSR in the literature, in the following we call this mechanism GBL from the names of the authors of Ref. [161], in order to distinguish it from the more general concept of EDSR, that is the coherent control of a spin by a radio-frequency electric field, as introduced by Rashba [162, 163]. It is worth noting that the electrical spin-orbit mediated spin manipulation described in chapter IV does not belong to either of these categories. Indeed it involves an Hamiltonian that is not linear in magnetic field due to the coupling between different valley states.

In general, the above two mechanisms are expected to coexist, since they share a common SO origin. Besides, in the experimental realizations of Refs. [124, 157, 164], there is little proof that one of the mechanism is truly negligible. Interestingly, on p-type silicon devices, all-electrical coherent Rabi oscillations of the spin [93] and sizable, anisotropic electrical modulation of the g-factors have been demonstrated [152]. GBL and g-TMR must therefore coexist in hole silicon quantum dots. In this chapter we thus investigate this coexistence in a hole spin qubit confined in a silicon quantum dot. In this device a gate voltage microwave modulation has been applied to induce Rabi oscillations of the hole spin. The measured Rabi frequency is anisotropic with respect to the magnetic field orientation. By correlating this to the angular and gate-voltage dependence of the g

factors, we will discriminate the mechanisms contributing to EDSR. Then, we build a model that is a generalization of Ref. [157]. We relate EDSR to the electrical modulation of a g-matrix $\hat{g}$ in a unified description of GBL and g-TMR mechanisms. More precisely this model allows to distinguish two contributions to the Rabi frequency. The first one is due to the gate voltage dependence of the g factors $|g^*| = \left| \hat{g} \cdot \frac{\mathbf{B}}{|\mathbf{B}|} \right|$ (where $\mathbf{B}$ is the magnetic field), and therefore of the measured Zeeman splitting. This is a generalization of the g-TMR mechanism, which accounts for the variation of the g factors and of their principal axes with the gate voltage. The second contribution originates from unitary modulations of the $\hat{g}$ matrix, which do not results in variations of the g factors. In this case there is no Zeeman energy modulation, so we call this contribution iso-Zeeman EDSR (IZ-EDSR). It can only be extracted from measurements of the Rabi frequency as a function of the magnetic field orientation. The GBL mechanism is an example of this scenario. We will show how the g-matrix formalism provides a simple yet efficient way to analyze the experimental results, as well as a compact model for the qubit which allows for fast numerical calculations of the full Rabi frequency map.

In this chapter, we proceed in the following way. We first present the experiment of Ref. [100], and the results obtained on the Rabi frequency and g factor anisotropies with the magnetic field orientation. After that we introduce the g-matrix formalism and show how that it naturally leads us to separate the Rabi frequency into two contributions. We then apply it to the experimental data and show the angular maps of IZ-EDSR and and g-TMR. Finally we introduce the method for the numerical calculation of the g-matrix and use it to qualitatively reproduce the experimental Rabi maps, showing the importance of the position of the dot and of strain inside the device.

6.1   Measurement of g-factor and Rabi anisotropy

In this part we present the measurement of the Rabi frequency and of the g-factor as a function of the magnetic field orientation in a hole spin qubit, performed by Alessandro Crippa and Romain Maurand at CEA/INAC. We detail the device structure, the measurement set-up, and show the main results that we will analyze in the next paragraphs through the g-matrix formalism.

The device studied here is similar to the one used to make the CMOS hole qubit of Ref. [93], and the following measurements are reported in Ref [100]. It consists in a silicon nanowire ($H = 8$ nm, $W = 25$ nm) oriented along [110] in the so-called "pump geometry": two 35 nm-long metallic gates in series (G1 and G2) completely overlap the channel connected to the source (S) and drain (D) degenerately boron-doped contacts. Two hole quantum dots are formed under each gate in the Coulomb blockade regime at the base temperature $T = 15$ mK of the dilution cryostat. A small source-drain bias is applied to measure the current. The transport through the double quantum dot is possible
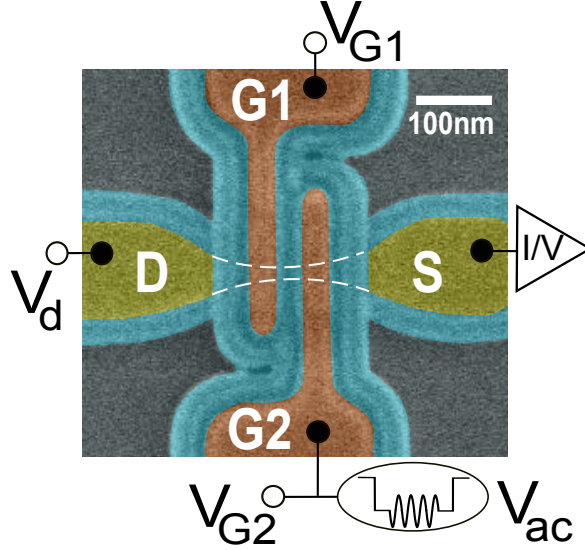
Figure 6.1: Scanning electron micrograph of a device similar to the one measured, with false colors. The white dashed lines outline the Si nanowire, 25 nm large and 8 nm thick, constituting the channel between S and D (yellow regions). Gates G1, G2 (in brown) are 35 nm long and separated by SiN$_3$ spacers (cyan); microwave bursts are applied to G2. The x, y, z axes define the lab frame. From Ref. [100].

in the triple-point regions characterized by pairs of triangles in the (V_{G1}, V_{G2}) diagram. We work at the triple point shown Fig. 6.2a in the Pauli spin blockade regime. In this figure ("1,1") and ("0,2") denote the excess charges of the double quantum dot, though each dot contains between 10 and 30 holes. The lever-arms parameters characterizing the influence of G1 and G2 on the chemical potentials of dot 1 and 2 are extracted from Fig. 6.2a [125]. With α_{ij} giving the influence of gate j on the levels of dot i, we have $\alpha_{11} = 0.7117$ eV/V, $\alpha_{12} = 0.0115$ eV/V, $\alpha_{21} = 0.2984$ eV/V and $\alpha_{22} = 0.264$ eV/V. This suggests that dot 1 is well coupled to gate 1, whereas dot 2 is similarly coupled to both gates, thus is most likely located under the spacer in between the two gates.

Starting from the Pauli spin blockade regime at the yellow star bias point of Fig. 6.2, a microwave signal of frequency f can be applied on gate 2. In the presence of a magnetic field, EDSR occurs when the microwave energy matches the Zeeman splitting. The Pauli blockade is lifted as hole spin transitions are driven. Hence at the resonance,

$$hf = |g^*| \mu_B B \tag{6.1}$$

where $|g^*|$ is the effective hole g factor of the resonant dot for this orientation of $\mathbf{B}$. This is illustrated in Fig. 6.2b, for a magnetic field along $\mathbf{x}$. In this plot we see two EDSR lines with different slopes and intensity, one for each dot. This shows, firstly, that the excitation on gate 2 affects also the quantum dot under gate 1, and secondly, that the g-factors in the two dots are different. The most intense line corresponds to the resonance of the right dot (located under G2 or between G1 and G2) whose gate receives directly
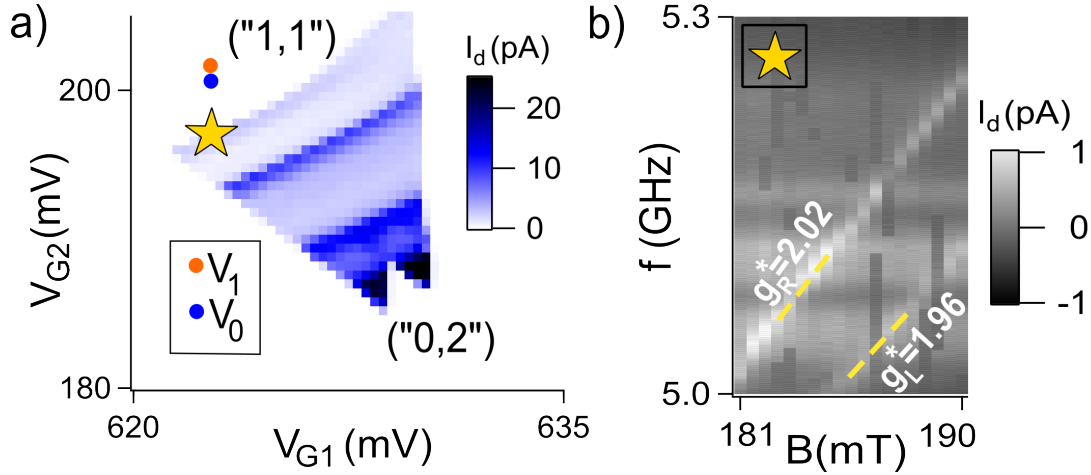
99

Figure 6.2: (a) Bias triangles of the double dot under study at $V_d = 5$ mV. Quoted numbers denote the equivalent excess charges deducible from Pauli spin blockade; points V_0, V_1 mark where spins are manipulated during pulse sequences. (b) Spectroscopy of the hole qubit under Pauli spin blockade (yellow star in (a)) via I_d as a function of a continuous microwave frequency f and $|\mathbf{B} = (B, 0, 0)|$. From Ref. [100].

the microwaves, whereas the less intense line corresponds to the left dot (located under G1) which only sees the cross-talk signal. Using Eq. 6.1, we obtain for the left dot $|g_L^*| = 1.96 \pm 0.02$ and for the right dot $|g_R^*| = 2.02 \pm 0.02$.

In order to operate the device as a spin qubit and perform and measure Rabi oscillations, the Koppens scheme [134] is used. This scheme is schematized in Fig. 6.3: starting from the spin blockade regime (yellow star in Fig. 6.2), the qubit (dot 2) is pulsed into the Coulomb blockade regime (bias point V_0), then a burst of resonant microwaves of duration τ is applied on G2 and rotates the spin. Finally the system is pulsed back to the spin blockade for spin projection. This sequence is repeated continuously, resulting in an measurable current I_d that oscillates as a function of τ, signature of the Rabi oscillations shown in Fig. 6.4. Remarkably the spin coherence seems quite good since we observe no decay over the 13 oscillations in this figure. This of course is just an indication, and a proper evaluation of the coherence times would be needed.

We can now characterize the full dependence of the qubit Rabi frequency on the magnetic field orientation. Fig. 6.5a displays the Rabi frequency for 291 directions of $\mathbf{B}$, defined by the angles θ and φ. θ is the angle with the $\mathbf{z}$ direction and φ is the angle with the $\mathbf{x}$ direction. For each pixel $|\mathbf{B}|$ is adjusted so that the spin resonance sticks to 9 GHz in order to drive the spin at same microwave power for each field direction. The Rabi frequency ranges from 3 MHz to 40 MHz, it is maximal for $\mathbf{B} \parallel \mathbf{z}$. Rabi oscillations are minimal for ($\varphi \approx 0°$, $\theta \approx 90°$) and ($\varphi \approx 180°$, $\theta \approx 90°$), that is along the $\mathbf{x}$ direction.

We then want to extract precisely $|g^*(V, \mathbf{B})|$, the g factor of the qubit for a given direction of the magnetic field, at the bias points V_0 and V_1. To do so the current trace is measured as a function of the microwave frequency for a burst duration $\tau = 20$ ns.
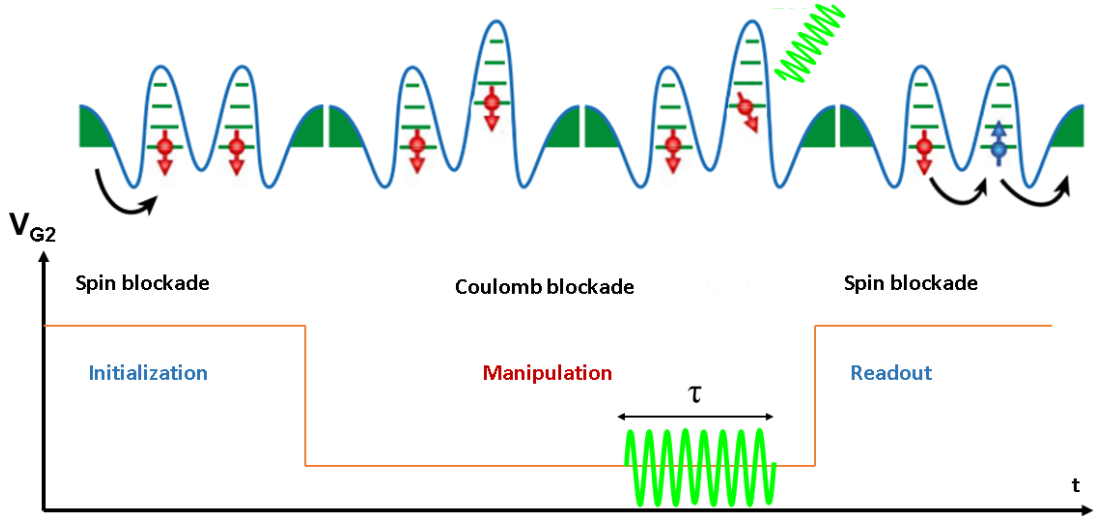
Figure 6.3: Protocol for manipulation and detection of the spin. Adapted from Ref. [93].
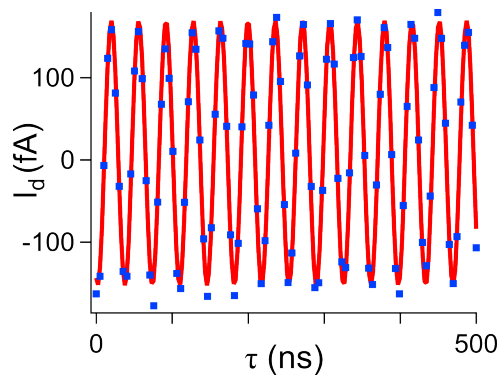

Figure 6.4: Rabi oscillations as a function of microwave burst time τ for $\mathbf{B} = (0, 0, -0.36)$ T. A current offset of 200 fA is subtracted for clarity. From Ref. [100].
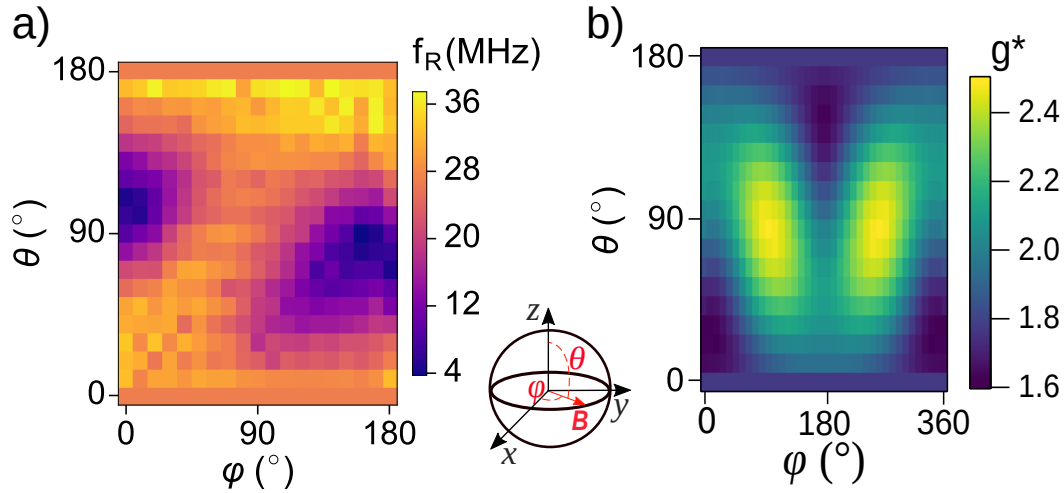
Figure 6.5: (a) Cartography the angular dependence of the Rabi frequency. The measurement is performed at constant Zeeman splitting (9 GHz). (b) Measured g^* carthography. θ, φ are stepped by 10° between 0° and 180°. The whole plot can be obtained by symmetry $(\mathbf{B} \to -\mathbf{B})$.

Following Ref. [122], the current is fitted with $I_d \propto (f_R^2/a) \sin^2(\pi \tau \sqrt{a})$, with $a = (f - f_0)^2 + f_R^2$ where f_R is the Rabi frequency and f_0 the resonance frequency. The histograms of f_0 for 400 such measurements are plotted in Fig. 6.6. Using Eq. 6.1 we can then deduce $|g^*|$ from the peak of f_0 for each direction of B.

By sweeping the magnetic field orientation in the same way as we did for the Rabi frequency cartography, the full angular dependence of $|g^*|$ at bias point V_0 can be characterized: in Fig. 6.5b, θ and φ are stepped between 0° and 180°, so that the full maps can be obtained by symmetry $(\mathbf{B} \to -\mathbf{B})$. $|g^*|$ ranges from 1.6 to 2.48, and the two strong minima are $(\varphi \approx 0°, \theta \approx 90°)$ and $(\varphi \approx 180°, \theta \approx 90°)$. Interestingly, a similar in plane $|g^*| \simeq 2\text{-}2.6$ (depending on the gate voltage) and out-of-plane $|g^*| \simeq 1.5$ have been measured in an other p-type nanowire quantum dot [152]. The fact that the ratio between the highest and the lowest g factors is not very large suggests a significant heavy-hole/light-hole mixing [165, 166].

In conclusion we have presented the measurement set-up for a full cartography of the Rabi frequency and g factors of a hole qubit. In the following we are going to present the g-matrix formalism which provides a unified description of the two maps.
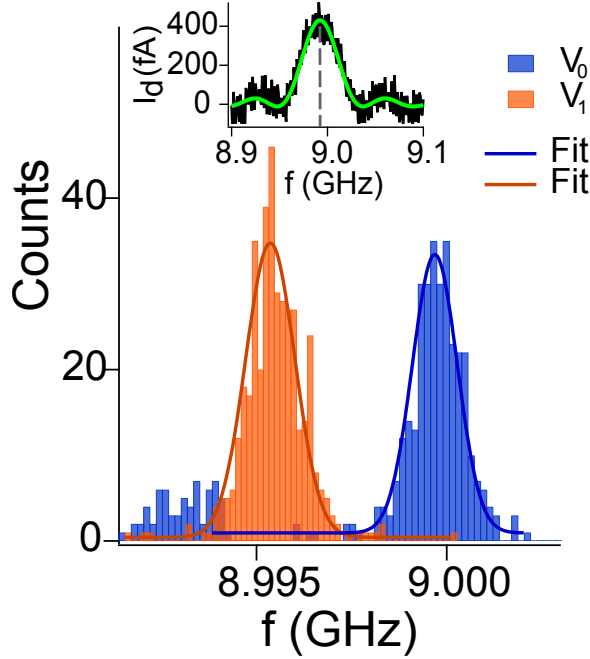
Figure 6.6: Inset: current trace as a function of microwave frequency f for burst duration $\tau = 20\,\text{ns}$ at $\mathbf{B} = (0, 216, 216)\,\text{mT}$. Blue and orange histograms display the dispersion of the resonance frequency when V_{G2} is pulsed to point V_0 and V_1, respectively. The Gaussian fits yield $g^*(V_0) = 2.013 \pm 0.001$ and $g^*(V_1) = 2.010 \pm 0.001$, taking into account the field uncertainty. From Ref. [100].

6.2 *g*-matrix formalism and data interpretation

In this section we introduce the *g*-matrix formalism and show that the Rabi frequency is linked to the derivative of the *g*-matrix with respect to the gate potential. The distinction between *g*-TMR and GBL mechanisms suggests to separate the Rabi frequency into two contributions depending if spin transitions are accompanied with a variation of the Zeeman tensor (TMR) or not (IZ-EDSR). These two contributions have particular relations with the *g*-matrix and its derivative. We finally show how to extract *g*-TMR and IZ-EDSR contributions from the experimental data.

6.2.1 The *g* matrix formalism.

The Hamiltonian of a Kramers doublet $\{|\Uparrow\rangle, |\Downarrow\rangle\}$ in a homogeneous magnetic field $\mathbf{B}$ can be written:

$$H = \frac{1}{2}\mu_B \,{}^t\boldsymbol{\sigma} \cdot \hat{g} \cdot \mathbf{B}\,,\tag{6.2}$$

where μ_B is Bohr's magneton, $\boldsymbol{\sigma} = (\sigma_1, \sigma_2, \sigma_3)$ is the vector of Pauli matrices, $\hat{g}$ is the *g*-matrix (a real 3×3 matrix), and $\cdot$ is the matrix product. Any linear-in-$\mathbf{B}$ two-level Hamiltonian can in principle be mapped onto Eq. (6.2) up to an irrelevant energy shift. The 9 elements of the *g*-matrix are independent unless symmetries reduce the number of degrees of freedom. In order to get further insights into the significance of the *g*-matrix,

we may factor $\hat{g} = \hat{U} \cdot \hat{g}_d \cdot {}^t\hat{V}$, where $\hat{g}_d = \text{diag}(g_1, g_2, g_3)$ is diagonal and $\hat{U}$, $\hat{V}$ are unitary matrices with determinant $+1$ (singular value decomposition):

$$ H = \frac{1}{2}\mu_B\,{}^t({}^t\hat{U} \cdot \boldsymbol{\sigma}) \cdot \hat{g}_d \cdot ({}^t\hat{V} \cdot \mathbf{B})\,. \tag{6.3} $$

The columns of $\hat{V}$ define three direct, orthonormal magnetic axes $\mathbf{X}$, $\mathbf{Y}$ and $\mathbf{Z}$. $\boldsymbol{\sigma}' = {}^t\hat{U} \cdot \boldsymbol{\sigma}$ sets three new spin matrices $(\sigma_1', \sigma_2', \sigma_3')$, or, equivalently, three new orthogonal quantization axes for the pseudo-spin of the Kramers doublet. Therefore, there must exist a unitary transform R in the $\{|\Uparrow\rangle, |\Downarrow\rangle\}$ subspace such that $R^\dagger \sigma_i' R = \sigma_i$ for all i's. The columns of R define a new basis $\{|\Uparrow\rangle_{\mathbf{Z}}, |\Downarrow\rangle_{\mathbf{Z}}\}$ for the two levels system in which:

$$ H = \frac{1}{2}\mu_B(g_1 B_1 \sigma_1 + g_2 B_2 \sigma_2 + g_3 B_3 \sigma_3)\,, \tag{6.4} $$

where B_1, B_2 and B_3 are the components of $\mathbf{B}$ along the magnetic axes $\mathbf{X}$, $\mathbf{Y}$ and $\mathbf{Z}$. Hence, the g-matrix can be made diagonal with an appropriate choice of real space axes for the magnetic field *and* basis set for the two levels system [167, 168]. The states $|\Uparrow\rangle_{\mathbf{Z}}$ and $|\Downarrow\rangle_{\mathbf{Z}}$ can be identified as the up and down pseudo-spin states along $\mathbf{Z}$ as they are the eigenstates of H for magnetic fields $\mathbf{B} \parallel \mathbf{Z}$.

Once the g-matrix is made diagonal, if we apply concomitant rotations on the magnetic axes ($\mathbf{B}'\hat{A}\mathbf{B}$) and pseudo-spin quantization axes ($\boldsymbol{\sigma}' = \hat{A}\boldsymbol{\sigma}$), with $\hat{A}$ unitary, then

$$ \hat{g}_T = \hat{A} \cdot \hat{g}_d \cdot {}^t\hat{A} \tag{6.5} $$

is symmetric and is usually known as the g-tensor in the literature. However, such a symmetric $\hat{g}_T$ may not be able to describe the system when the potential is varied. Indeed if we choose $\hat{g}$ symmetric at some bias point V_0, $\hat{g}(V_0 + \delta V)$ might not be symmetric because the $\hat{V}$ and $\hat{U}$ matrices that diagonalizes $\hat{g}$ can depend on the bias point.

6.2.2   The (symmetric) Zeeman tensor

In this paragraph we introduce on the Zeeman tensor, which can be obtained from magnetospectroscopy measurements.

Rewriting Eq. (6.2) as

$$ H = \frac{1}{2}\mu_B|\hat{g} \cdot \mathbf{B}|\sigma_{\mathbf{u}}\,, \tag{6.6} $$

where $\sigma_{\mathbf{u}} = {}^t\mathbf{u} \cdot \boldsymbol{\sigma}$ and $\mathbf{u} = \hat{g} \cdot \mathbf{B}/|\hat{g} \cdot \mathbf{B}|$, the Zeeman splitting ΔE between the eigenstates of H reads:

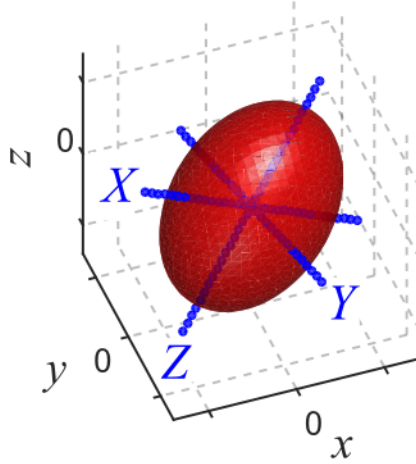$$ \Delta E = \mu_B|\hat{g} \cdot \mathbf{B}|\,. \tag{6.7} $$

Figure 6.7: Isosurface of $\Delta E^2 = g^{*2}\mu_B^2 B^2$ in the measurement frame $\{\mathbf{x}, \mathbf{y}, \mathbf{z}\}$. The blue lines are the principal magnetic axes $\mathbf{X}, \mathbf{Y}, \mathbf{Z}$ of the ellipsoid at $V_{G2} = V_0$. From Ref. [100].

This can be conveniently cast in the form:

$$\Delta E^2 = \mu_B^2(^t\mathbf{B} \cdot {}^t\hat{g} \cdot \hat{g} \cdot \mathbf{B}) = \mu_B^2(^t\mathbf{B} \cdot \hat{G} \cdot \mathbf{B}),\qquad(6.8)$$

where $\hat{G} = {}^t\hat{g} \cdot \hat{g}$ is the symmetric Zeeman tensor. From a practical point of view, $\hat{G}$ can be constructed from the measurement of ΔE^2 for six orientations of the magnetic field. Note that $\hat{G}$ only depends on the choice of a frame for the magnetic field. On the contrary $\hat{g}$ depends on the choice of a frame for the magnetic field and on a choice of basis set $\{|\Uparrow\rangle, |\Downarrow\rangle\}$ for the Kramers doublet. Any rotation R of the $\{|\Uparrow\rangle, |\Downarrow\rangle\}$ basis set results in a corresponding rotation $\hat{g}_R = {}^t\hat{U}(R) \cdot \hat{g}$ of the *g*-matrix (see note [169]), which leaves the Zeeman tensor $\hat{G}_R = {}^t\hat{g}_R \cdot \hat{g}_R = {}^t\hat{g} \cdot \hat{U}(R) \cdot {}^t\hat{U}(R) \cdot \hat{g} = {}^t\hat{g} \cdot \hat{g} = \hat{G}$ invariant, since $\hat{U}$ is a unitary matrix. This is expected, since the Zeeman splittings must not depend on the choice of the $\{|\Uparrow\rangle, |\Downarrow\rangle\}$ basis set. It follows from Eq. (6.4) that the eigenvalues of $\hat{G}$ are g_1^2, g_2^2, and g_3^2 while the eigenvectors of $\hat{G}$ are the magnetic axes $\mathbf{X}$, $\mathbf{Y}$ and $\mathbf{Z}$. The characterization of the Zeeman splittings therefore brings the principal *g*-factors and associated magnetic axes, but leaves $|\Uparrow\rangle_\mathbf{Z}$ and $|\Downarrow\rangle_\mathbf{Z}$ unspecified.

Coming back for a moment to the experimental results, we can apply Eq. 6.8 to the measurements and reconstruct $\hat{G}$ from six orientations of the magnetic field. We find at $V_G = V_0$, $|g_1^*| \simeq 2.08$, $|g_2^*| \simeq 2.48$ and $|g_3^*| \simeq 1.62$, and the associated principal magnetic axes in the lab frame (defined in Fig. 6.1) $\mathbf{X} = (0.82, 0.19, -0.53)$, $\mathbf{Y} = (-0.22, 0.98, 0.01)$ and $\mathbf{Z} = (0.52, 0.11, 0.84)$. Fig. 6.7 shows the ellipsoidal isosurfaces ΔE^2 in the lab frame ($\Delta E^2 = \mu_B^2(g_1^{*2}B_X^2 + g_2^{*2}B_Y^2 + g_3^{*2}B_Z^2)$). Fig. 6.8a and 6.8b compare the full angular dependence of g^* reconstructed from $\hat{G}$, to the experimental values as a function of θ and ϕ, showing a perfect agreement.

We have shown how to characterize the *g*-matrix at a given bias point from Zeeman
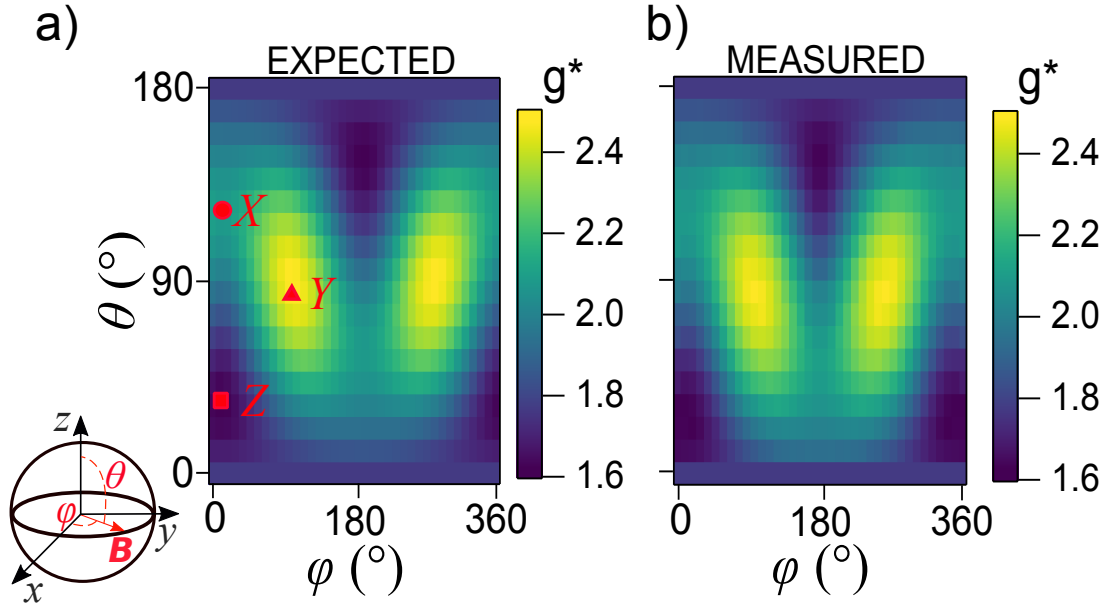
Figure 6.8: (a) g^* as a function of the field angles θ and φ, reconstructed from the six values of g^* defining the Zeeman tensor. (b) Experimental cartography of g^*, same as Fig. 6.5b), for comparison. From Ref. [100].

splitting measurements. In our problem, $\hat{g}$ depends on the gate potential V_G. Next we demonstrate the link between the Rabi frequency and the $\hat{g}\prime$ matrix, the derivative of $\hat{g}$ with respect to the gate voltage.

6.2.3   The Rabi frequency in the g-matrix formalism

We now derive the formula for the Rabi frequency when the g-matrix is dependent on a single control parameter, in this case a gate voltage V_G. When this gate voltage is varied around $V_G = V_0$, with $V_G(t) = V_0 + V_{ac}\sin(2\pi f_0 t)$, we can expand the g-matrix to first order as:

$$\hat{g}(V_G) \simeq \hat{g}(V_0) + (V_G - V_0)\hat{g}'(V_0) \tag{6.9}$$

where $\hat{g}'$ is the derivative of $\hat{g}$ with respect to V_G and $\delta V_G = V_G - V_0$. The Hamiltonian can then be written:

$$\begin{aligned} H(V_G) &= \frac{1}{2}\mu_B{}^t\boldsymbol{\sigma} \cdot \hat{g}(V_G) \cdot \mathbf{B} \\ &\simeq \frac{1}{2}\mu_B{}^t\boldsymbol{\sigma} \cdot [\hat{g}(V_0) + \hat{g}'(V_0)\delta V_G] \cdot \mathbf{B}, \end{aligned} \tag{6.10}$$

Let us introduce the Larmor vector $\hbar\boldsymbol{\Omega} = \mu_B\hat{g}(V_0) \cdot \mathbf{B}/2$ and its gate-voltage derivative $\hbar\boldsymbol{\Omega}' = \mu_B\hat{g}'(V_0) \cdot \mathbf{B}/2$. Then,

$$H(V_G) = \hbar|\boldsymbol{\Omega}|\sigma_\omega + \hbar|\boldsymbol{\Omega}'|\delta V_G\sigma_{\omega'}, \tag{6.11}$$

with $\omega = \boldsymbol{\Omega}/|\boldsymbol{\Omega}|$ and $\omega' = \boldsymbol{\Omega}'/|\boldsymbol{\Omega}'|$. Splitting $\boldsymbol{\Omega}' = \boldsymbol{\Omega}'_\parallel + \boldsymbol{\Omega}'_\perp$ into components parallel and perpendicular to $\boldsymbol{\Omega}$,

$$H(V_G) = \hbar|\boldsymbol{\Omega} + \boldsymbol{\Omega}'_\parallel \delta V_G|\sigma_\omega + \hbar|\boldsymbol{\Omega}'_\perp|\delta V_G \sigma_{\omega'_\perp}. \tag{6.12}$$

$\boldsymbol{\Omega}'_\parallel$ characterizes gate-driven modulations of the Larmor (spin precession) frequency, while $\boldsymbol{\Omega}'_\perp$ characterizes spin rotations. For a radio-frequency (RF) $\delta V_G = V_{ac}\sin(|\boldsymbol{\Omega}|t)$ resonant with the transition between the eigenstates of $H(V_0)$, the Rabi frequency f_R reads [157, 159]:

$$\begin{aligned} hf_R &= \hbar|\boldsymbol{\Omega}'_\perp|V_{ac} \\ &= \hbar|\omega \times \boldsymbol{\Omega}'|V_{ac} \\ &= \frac{\mu_B B V_{ac}}{2|g^*|}\Big|[\hat{g}(V_0)\cdot\mathbf{b}] \times [\hat{g}'(V_0)\cdot\mathbf{b}]\Big|, \end{aligned} \tag{6.13}$$

where $\mathbf{b} = \mathbf{B}/B$ is the unit vector along the magnetic field and $|g^*| = |\hat{g}(V_0)\cdot\mathbf{b}|$ is the effective *g*-factor along that direction. This may be conveniently written $f_R = |\mathbf{f}_R|$, with:

$$h\mathbf{f}_R = \frac{\mu_B B V_{ac}}{2|g^*|}[\hat{g}(V_0)\cdot\mathbf{b}] \times [\hat{g}'(V_0)\cdot\mathbf{b}]. \tag{6.14}$$

We can note that, as expected from the assumptions behind Eqs. 6.2 and 6.9, the Rabi frequency is linear in B and V_{ac}. Also, the Larmor frequency $|\boldsymbol{\Omega}|/(2\pi)$ and the Rabi frequency $|\mathbf{f_R}|$ do not depend on the choice of the basis set for the Kramers doublet (see note [170]).

From Eq. 6.13, we see that in order to predict the Rabi frequency, one only needs in principle to characterize $\hat{g}(V_0)$ and $\hat{g}'(V_0)$. As we have discussed in part 6.2.2, we can always write a diagonal *g*-matrix $\hat{g}(V_0)$ with an appropriate choice of real space axes for the magnetic field and basis set for the Kramers doublet. If the Kramers basis $\{|\Uparrow\rangle_\mathbf{z}, |\Downarrow\rangle_\mathbf{z}\}$ depends on V_G, then $\hat{g}(V_G)$ is diagonal in a different (yet implicit) basis set at each gate voltage. It is then not possible to reconstruct $\hat{g}'$ from the measurement of the Zeeman tensor at different gate voltages. Eq. 6.13 precisely provides a link between a measurable quantity, f_R, and $\hat{g}'$. In the following we will use this link to extract the $\hat{g}'$ matrix. To do so, we will first show how to split the Rabi frequency into two contributions, the *g*-TMR which is obtained from the measurement of the Zeeman tensor, and the iso-Zeeman EDSR which can not.

6.2.4 Iso-Zeeman EDSR and *g*-TMR.

Here we present in more detail the two contributions to the Rabi frequency, IZ-EDSR and *g*-TMR, and we show their relation to the *g*-matrix formalism.

A key feature here is the fact that a gate-voltage modulation of $\hat{g}$ can give rise to a finite Rabi frequency, but no variations in the Zeeman splitting, i.e $\hat{G}' = 0$. Indeed $\hat{G}'$ is related to the derivative of the g-matrix by

$$\hat{G}' = {}^t\hat{g} \cdot \hat{g}' + {}^t\hat{g}' \cdot \hat{g} \,. \tag{6.15}$$

Notably, $\hat{G}'$ is zero if ${}^t\hat{g} \cdot \hat{g}'$ is an antisymmetric matrix. We refer to such contributions to the Rabi frequency as the iso-Zeeman EDSR: it captures, in particular, the pure rotations of the basis $\{|\Uparrow\rangle_{\mathbf{z}}, |\Downarrow\rangle_{\mathbf{z}}\}$ that do not give rise to modulations of the Zeeman splittings. In a complementary manner, we refer to variations of the Zeeman tensor contributing to the Rabi frequency as g-Tensor Modulation Resonance (g-TMR). Let us formalize in more detail these definitions. We can always write ${}^t\hat{g} \cdot \hat{g}' = \hat{S} + \hat{A}$, where $\hat{S}$ is a symmetric matrix and $\hat{A}$ an antisymmetric matrix. Then Eq. 6.15 sets $\hat{S} = \hat{G}'/2$. We can then introduce the g-TMR matrix

$$\hat{g}'_{\text{TMR}} = {}^t\hat{g}^{-1} \cdot \hat{G}'/2 \tag{6.16}$$

and the IZR matrix

$$\hat{g}'_{\text{IZR}} = {}^t\hat{g}^{-1} \cdot \hat{A}, \tag{6.17}$$

so that $\hat{g}' = \hat{g_{\text{TMR}}}' + \hat{g_{\text{IZR}}}'$ and split accordingly Eq. 6.14 as

$$\mathbf{f_R} = \mathbf{f}_{\text{TMR}} + \mathbf{f}_{\text{IZR}} \tag{6.18}$$

where $\mathbf{f}_{\text{TMR}}$ and $\mathbf{f}_{\text{IZR}}$ are the contributions of $\hat{g}'_{\text{TMR}}$ and $\hat{g}'_{\text{IZR}}$ to the Rabi frequency.

A notable example of IZ-EDSR is the GBL mechanism of Ref. [161]. In their setup a harmonic potential define a quantum dot in a static magnetic field, and the dot is moved around its equilibrium position by an homogeneous alternating electric field, thus mediating EDSR by intrinsic SO coupling. In these conditions, $\hat{G}' = 0$, because the alternating electric field does not change the shape of the confinement potential, and therefore the Zeeman splitting. The electric field only moves the dot as a whole, however $\hat{g}' \neq 0$ since the vector potential breaks translational symmetry. In the end, for an isotropic g-tensor g_0, the GBL Rabi frequency can be put in the form:

$$h f_R = 2 g_0 \mu_B |\mathbf{B} \times \mathbf{\Omega}_{\text{SO}}| \,, \tag{6.19}$$

where $\mathbf{\Omega}_{\text{SO}}$ is a field describing the combined effect of the spin-orbit interaction and electric field excitation. It is, in particular, dependent on the direction of the excitation. From Eq. 6.19, the Rabi frequency is minimal when the magnetic field is parallel to $\mathbf{\Omega}_{\text{SO}}$. Eq. 6.19 being linear in B, it can be cast into the form of Eq. 6.13. Indeed we discuss in appendix C the reformulation of the GBL mechanism in the g-matrix formalism.

On the other hand g-TMR is a generalized version of the g-TMR of Ref. [157]. A
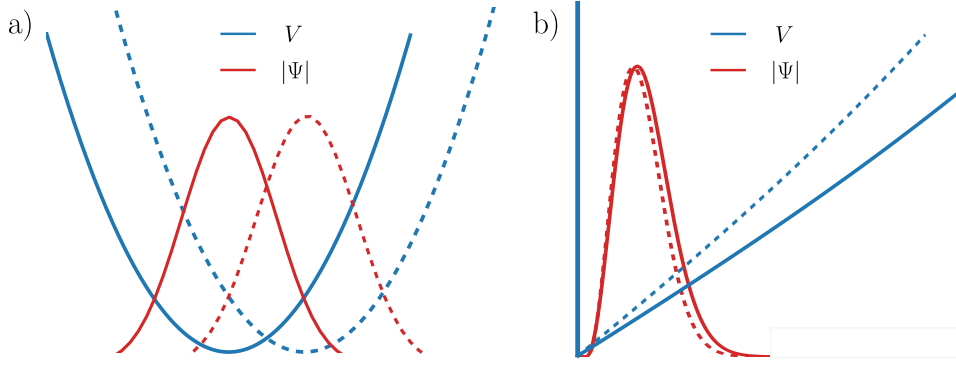
Figure 6.9: Potential and squared wavefunction; the dashed lines represents the same potential with a constant electric field added. (a) State confined in a harmonic confinement potential, an oscillating constant electric field leads to IZ-EDSR. (b) State confined at an interface, an oscillating constant electric field mostly leads to *g*-TMR.

change of the confinement potential modulates the principal *g* factors g_i^*, and therefore drives spin rotations. In the original scenario of Ref. [157], the magnetic axes are fixed by the symmetries of the system and do not rotate.

It is important to note that the case in which the confinement potential is harmonic and the alternative electric field is constant in space always leads to IZ-EDSR. Indeed in that case, the alternating electric field only translates the confinement potential, so that the Zeeman tensor is invariant. To put it in another way, for a constant electric field excitation, only the anharmonicity of the confinement potential can lead to *g*-TMR. This is illustrated in Fig. 6.9, with two typical cases for IZ-EDSR and *g*-TMR. The first one is a state confined in a harmonic potential: adding a constant electric field only translates the state. The second one is a state confined at an interface, with a potential that is almost triangular: the constant electric field barely translates the state position but change the stiffness of the confinement potential, leading mainly to *g*-TMR.

6.2.5 Interpretation of the Rabi map through the *g*-matrix formalism.

We have now all the tools needed to interpret the experimental data within the *g*-matrix formalism. We are going to start by extracting the IZR and *g*-TMR contributions from the experimental Rabi frequency. As we have discussed, the $\hat{g}'$ matrix cannot usually be reconstructed from the measurement of the Zeeman splittings, which can only provide $\hat{g}'_{\text{TMR}}$. Nonetheless, $\hat{g}'_{\text{IZR}}$ can be extracted from the Rabi frequency map. We detail the general procedure in the following, and after that we apply it to the experimental data of paragraph 6.1.

First, the symmetric Zeeman tensor $\hat{G} = {}^t\hat{g} \cdot \hat{g}$ is constructed from the measurement of the Zeeman splittings along 6 independent directions. The eigenvalues of $\hat{G}$ are the

square of the principal g-factors g_1^2, g_2^2, and g_3^2, while the eigenvectors of $\hat{G}$ are the principal magnetic axes $\mathbf{X}$, $\mathbf{Y}$ and $\mathbf{Z}$. In the magnetic axes frame, there exists a (yet implicit) basis set $\{|\Uparrow\rangle_{\mathbf{Z}}, |\Downarrow\rangle_{\mathbf{Z}}\}$ for the Kramers doublet such that:

$$\hat{g} \equiv \hat{g}_d = \begin{pmatrix} g_1 & 0 & 0 \\ 0 & g_2 & 0 \\ 0 & 0 & g_3 \end{pmatrix}. \tag{6.20}$$

Note that there might be an ambiguity on the sign of the g_i's (all assumed the same sign here).

The matrix $\hat{G}'$ can be extracted from the measurement of $\hat{G}$ for two nearby gate voltages $V_G = V_0$ and $V_G = V_0 + \delta V_G$. In the principal magnetic axes and $\{|\Uparrow\rangle_{\mathbf{Z}}, |\Downarrow\rangle_{\mathbf{Z}}\}$ basis set at $V_G = V_0$, the g-TMR matrix is then $\hat{g}'_{\text{TMR}} = \hat{g}_d^{-1} \cdot \hat{G}'/2$. We then need $\hat{g}'_{\text{IZR}} = \hat{g}_d^{-1} \cdot \hat{A}$. There are three independents elements in $\hat{A}$ (because $\hat{A}$ is antisymmetric), therefore using Eq. 6.13 one should be able to extract them from the measurement of the Rabi frequency along three directions of the magnetic field. The measurement of $\hat{G}$ and $\hat{G}'$ hence provides $\hat{g}$ and six out of the nine degrees of freedom of $\hat{g}'$. Only three degrees of freedom of $\hat{g}'$ are not accessible from a measurement of the Zeeman splitting and give rise to IZ-EDSR.

Let us apply this procedure to the experimental data. We first compute $\hat{G}'$ from the experimental tensors $G(\hat{V}_0)$ and $G(\hat{V}_1)$, with $V_1 - V_0 = 0.25$ mV $\simeq V_{ac}$. In the magnetic axes frame $\{\mathbf{X}, \mathbf{Y}, \mathbf{Z}\}$ at $V_{G2} = V_0$ we find

$$\hat{G}'(V_0) = \begin{bmatrix} -17.9 & 21.1 & 7.2 \\ 21.2 & 17.1 & -19.8 \\ 7.2 & -19.8 & 9.1 \end{bmatrix} \text{V}^{-1} \tag{6.21}$$

The fact that $\hat{G}'$ is not diagonal in this low-symmetry device shows that the principal magnetic axes (as well as, presumably, the basis set $\{|\Uparrow\rangle_{\mathbf{Z}}, |\Downarrow\rangle_{\mathbf{Z}}\}$) rotate with the gate voltage. With $\hat{g}_d = \text{diag}(2.08, 2.48, 1.62)$, we get

$$\hat{g}'_{\text{TMR}}(V_0) = \begin{bmatrix} -4.31 & 5.07 & 1.73 \\ 4.26 & 3.45 & -4.01 \\ 2.22 & -6.12 & 2.82 \end{bmatrix} \text{V}^{-1} \tag{6.22}$$

We can next fit the elements of $\hat{A}$ on at least three Rabi frequency measurements. For better accuracy, we also fit the amplitude V_{ac} of the RF field, and do a least-square
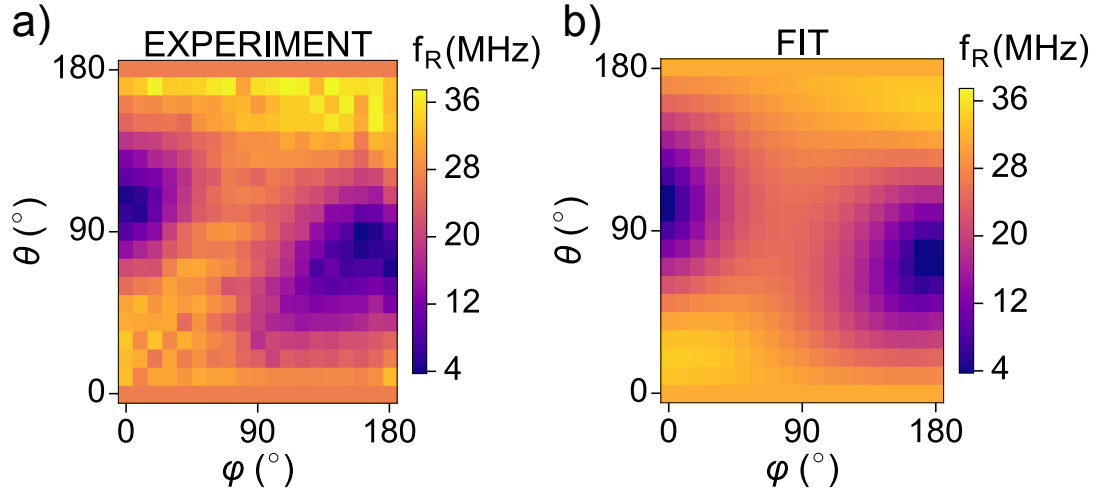
Figure 6.10: (a) Measured angular dependence of the Rabi frequency, as in Fig. 6.5a. (b) Analogous map obtained from the fit of (a) with Eq. 6.13.
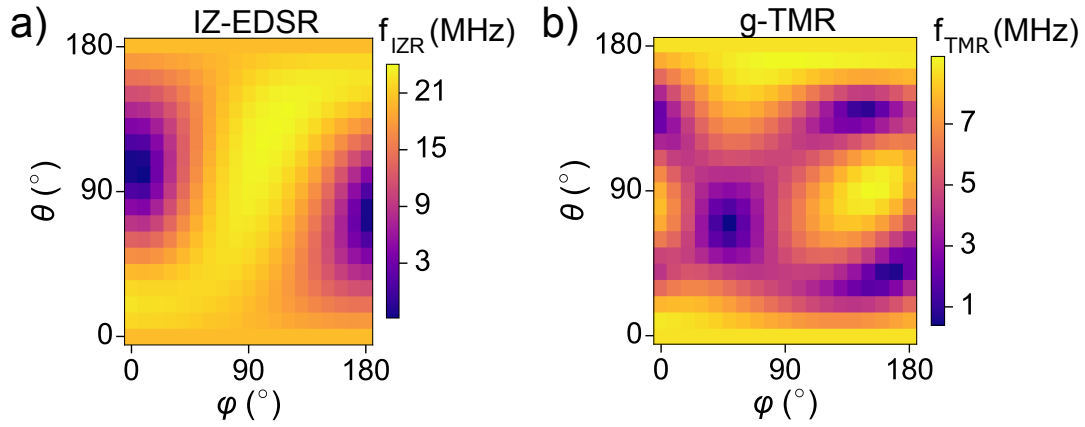
Figure 6.11: (a) IZ-EDSR and (b) *g*-TMR contributions to f_R.

regression on the whole Rabi map $f_R(\mathbf{B})$. This yields:

$$\hat{g}'_{\mathrm{IZR}}(V_0) = \begin{bmatrix} 0.0 & -7.45 & -4.97 \\ 6.26 & 0.0 & -23.99 \\ 6.38 & 36.60 & 0.0 \end{bmatrix} \mathrm{V}^{-1} \tag{6.23}$$

as well as $V_{ac} = 0.41$ mV, close to the value expected for the present RF setup. Finally in the same magnetic axes we can compute $\hat{g}' = \hat{g}'_{\mathrm{TMR}} + \hat{g}'_{\mathrm{IZR}}$,

$$\hat{g}'(V_0) = \begin{bmatrix} -4.3 & -2.4 & -3.2 \\ 10.5 & 3.4 & -28.0 \\ 8.6 & 30.5 & 2.8 \end{bmatrix} \mathrm{V}^{-1} \tag{6.24}$$

We plot on Fig. 6.10 the measured Rabi map along with the one calculated from $\hat{g}_d$ and $\hat{g}'$ via Eq. 6.13. There are only small discrepancies between the two that we ascribe to the experimental uncertainty on $\hat{G}'(V_0)$.

Finally we plot on Fig. 6.11 the contributions f_{IZR} and f_{TMR} computed using Eq. 6.13 with $\hat{g}_d$, $\hat{g}'_{\text{IZR}}$ and $\hat{g}'_{\text{TMR}}$. We can see that the dominant contribution is IZ-EDSR. Nevertheless the g-TMR part cannot be neglected since it can reach as much as 30 % of the total Rabi frequency. The g-TMR map of Fig. 6.11b shows a complex dependence on the magnetic field orientation that reflects the complex structure of the potential in the device. As for the IZ-EDSR contribution, we point out that, although the GBL model cannot be applied directly (because our $\hat{g}_d$ is not isotropic), f_{IZR} reproduces its most salient feature: two well-defined minima along $\mathbf{x}$ suggest that the effective spin-orbit field $\mathbf{\Omega}_{\text{SO}}$ is along $\mathbf{x}$. We have seen that the lever-arms parameters characterizing the influence of G1 and G2 on dot 2 respectively are $\alpha_{21} = 0.2984$ eV/V and $\alpha_{22} = 0.264$ eV/V, showing similar coupling to both gates. This suggests that the dot is most likely located under the spacer in between the two gates, therefore implies that the RF electric field on G2 drives the motion of the hole along the nanowire axis $\mathbf{y}$. In the simplest approximation (discarding the complex behavior of holes under magnetic field), it is possible to interpret the position of the minima. Indeed, the spin-orbit Hamiltonian $H_{SO} \propto (\mathbf{\nabla}V \times \mathbf{p})\boldsymbol{\sigma}$, for a static electric field $\mathbf{\nabla}V$ mostly along $\mathbf{z}$, and a motion mostly along the wire direction $\mathbf{y}$, becomes $H_{SO} \propto \sigma_x$, and does not couple spins when $\mathbf{B} \parallel \mathbf{x}$. Therefore, as the orientation of $\mathbf{\Omega}_{\text{SO}}$ depends on the direction of the electric field excitation, we may expect a different direction for the minimum of Rabi frequency if the dot is located under G2 (with electric field excitation along $\mathbf{x}$ and $\mathbf{z}$). We will verify this with numerical calculations in part 6.3.

It is in fact not surprising that with a quantum dot located between the gates and a RF electric field along the nanowire, the dominant contribution is IZ-EDSR. As we have seen before, one driving force of IZ-EDSR is the RF oscillations of a harmonic potential dot, whereas an anharmonic confinement potential also leads to g-TMR. Along the wire the potential is much more harmonic than perpendicular to it, where structural confinement is very sharp and strong. On the contrary, we shall then expect g-TMR to dominate for a dot under the gate, and that is indeed what we will verify with the numerical calculations.

Another point worth noting is the fact that $|\mathbf{f}_R| \leq |\mathbf{f}_{\text{TMR}}| + |\mathbf{f}_{\text{IZR}}|$, because $\mathbf{f}_{\text{IZR}}$ and $\mathbf{f}_{\text{TMR}}$ are in general not aligned, so Fig. 6.10b is not the exactly the sum of Fig. 6.11a and b. In order to highlight this correction, we have plotted in Fig. 6.12 the difference $|\mathbf{f_R}| - |\mathbf{f}_{\text{IZR}}| - |\mathbf{f}_{\text{TMR}}|$, along with $\cos(\theta_Z)$, where θ_Z is the angle between $\mathbf{f}_{\text{IZR}}$ and $\mathbf{f}_{\text{TMR}}$. There is a large sector around $\theta = 90°$, $\varphi = 135°$ where IZR and g-TMR tend to cancel each other. Elsewhere the two vectors are almost aligned.

We have thus shown that as expected the IZ-EDSR and g-TMR contributions to the Rabi frequency coexist in a silicon hole quantum dot made in nanowire FET technology. It is the first time that such coexistence is evidenced. The common origin of the two mechanisms is the spin-orbit interaction yet they manifest it in different ways. g-TMR
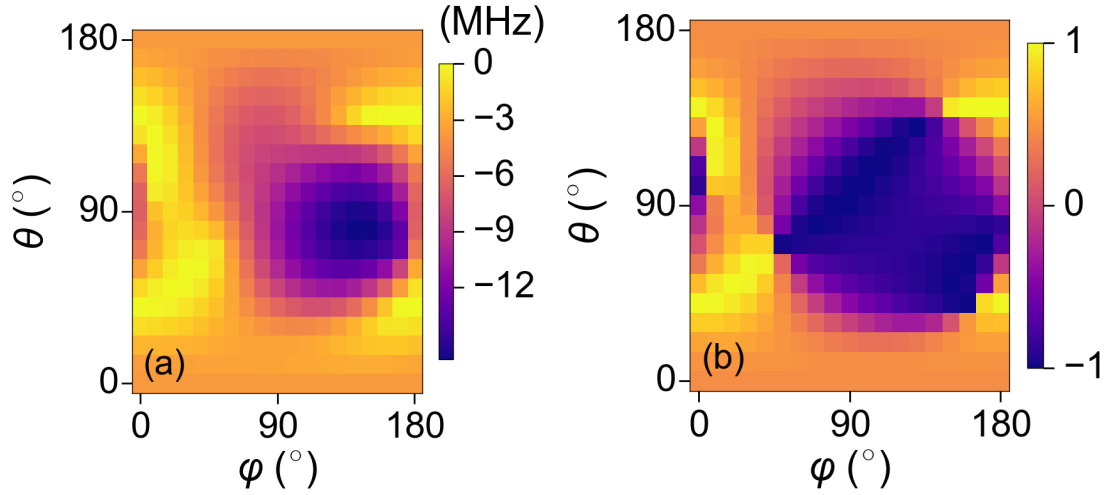
Figure 6.12: (a) Map of $|\mathbf{f}_R|-|\mathbf{f}_{\mathrm{IZR}}|-|\mathbf{f}_{\mathrm{TMR}}|$ as a function of the orientation of the magnetic field. (b) Map of $\cos(\theta_Z)$ as a function of the orientation of the magnetic field, where θ_Z is the angle between $\mathbf{f}_{\mathrm{IZR}}$ and $\mathbf{f}_{\mathrm{TMR}}$.

is driven by changes in the confinement potential resulting in a variation of the Zeeman tensor. IZ-EDSR is mostly driven by the alternating motion of the dot, which does not result in variations of the Zeeman splitting. The g-matrix formalism provides a unified description of both phenomena, allowing to separate them, and to evaluate the full angular dependence from a few measurements. In our particular sample IZ-EDSR has been found to be the most relevant contribution, probably because of the localization of the dot between the two gates promote the alternating motion of the dot over the change of confinement potential. We shall verify this with detailed simulations in the next part. Fortunately, the g-matrix formalism provides an easy way to compute the full map of Rabi frequencies. It is indeed possible to calculate the g-matrix from the wavefunctions at zero magnetic field.

6.3 Theoretical prediction of experimental Rabi map

In the previous part we have shown how the g-matrix formalism allowed us to interpret the angular dependence of the Rabi frequency. We have extracted the IZ-EDSR and g-TMR contributions, showing that they coexist. IZ-EDSR can be characterized by a spin-orbit field $\mathbf{\Omega}_{\mathrm{SO}} \parallel \mathbf{x}$, and g-TMR can be associated with the variations of the confinement potential. This calls for a precise modeling of the confinement potential and spin-orbit interaction, which would be very useful in order to understand the nature of the dot, why IZ-EDSR dominates over g-TMR, if these Rabi cartographies are reproducible, and ideally provide guidelines to optimize the qubits. Fortunately, the g-matrix formalism developed in part 6.2 provides a very efficient way to compute numerically the Rabi maps when associated to electronic structure calculations. Indeed we will show that the g-matrix

and its derivative can be easily calculated from the eigenstates at zero magnetic field using simple perturbation theory. We will use this methodology on top of 6-bands **k.p** calculations in order to study the effect of disorder and localization on the Rabi map. This alone cannot reproduce the experimental results but give interesting informations on the behavior of IZ-EDSR and g-TMR. With the introduction of strains in the system (known to be present in CMOS devices, but not precisely characterized), we are able to reproduce the experimental results. In this part, we first describe the general methodology for the numerical calculation of the g-matrix, then we use it to predict the Rabi frequencies in SOI devices.

6.3.1   Numerical calculation of the g-matrix and its derivative

First of all we present the methodology for the numerical calculation of $\hat{g}$ and $\hat{g}'$ in the general case. Then in order to verify it, we apply the methodology to a hole quantum dot, and compare the Rabi frequency map computed from $\hat{g}$, $\hat{g}'$, using Eq. 6.13, to the one obtained from a direct calculation using the equation:

$$f_R = \frac{eV_{ac}}{h} \left| \langle 0 | \hat{D} | 1 \rangle \right| \tag{6.25}$$

where $|0\rangle$ and $|1\rangle$ are the states of the qubit at finite magnetic field, and $\hat{D}(r) = \frac{\partial V_{\text{tot}}(\mathbf{r})}{\partial V_g}$ as in chapter IV and V.

We consider a quantum dot in a homogeneous magnetic field $\mathbf{B} = (B_x, B_y, B_z)$. The system can therefore be characterized by a Hamiltonian $\hat{H}(V, \mathbf{B})$ On one hand we can expand the Hamiltonian in power of $\mathbf{B}$, at $\mathbf{B} = \mathbf{0}$:

$$\begin{aligned} H(V, \mathbf{B}) &= H_0(V) - B_x M_{1,x} - B_y M_{1,y} - B_z M_{1,z} + \mathcal{O}(B^2) \\ &= H_0(V) - \mathbf{B} \cdot \mathbf{M_1} + \mathcal{O}(B^2) \,, \end{aligned} \tag{6.26}$$

where $M_{1,\alpha} \equiv -\partial H / \partial B_\alpha |_{\mathbf{B}=\mathbf{0}}$, and $H_0(V) = H(V, \mathbf{B} = \mathbf{0})$. We then consider a two-level qubit, based on a pair of Kramers-degenerate eigenstates of $H_0(V)$, $\{|\Psi_\Uparrow\rangle, |\Psi_\Downarrow\rangle\}$, at $\mathbf{B} = \mathbf{0}$. We wish to deal with the magnetic field as a perturbation. At finite B, the zeroth-order states and first order energies are the eigenpairs of:

$$H_1(V, \mathbf{B}) = -\mathbf{B} \cdot \mathbf{M_1} = - \begin{pmatrix} \langle \Psi_\Uparrow | \mathbf{B} \cdot \mathbf{M_1} | \Psi_\Uparrow \rangle & \langle \Psi_\Uparrow | \mathbf{B} \cdot \mathbf{M_1} | \Psi_\Downarrow \rangle \\ \langle \Psi_\Downarrow | \mathbf{B} \cdot \mathbf{M_1} | \Psi_\Uparrow \rangle & \langle \Psi_\Downarrow | \mathbf{B} \cdot \mathbf{M_1} | \Psi_\Downarrow \rangle \end{pmatrix} \tag{6.27}$$

On the other hand, we remind that any two-level system can be mapped to first order in

B onto the effective spin Hamiltonian (up to an energy shift):

$$\hat{H} = \frac{1}{2}\mu_B{}^t\boldsymbol{\sigma} \cdot \hat{g}(V) \cdot \mathbf{B} \tag{6.28}$$

with $\boldsymbol{\sigma} = (\sigma_1, \sigma_2, \sigma_3)$ the vector of Pauli matrices and $\hat{g}$ the 3×3 real g-matrix. We can write this Hamiltonian explicitly:

$$\hat{H} = \frac{1}{2}\mu_B \begin{pmatrix} \alpha & \beta^* \\ \beta & -\alpha \end{pmatrix} \tag{6.29}$$

with

$$\alpha = g_{zx}B_x + g_{zy}B_y + g_{zz}B_z \tag{6.30a}$$

$$\beta = (g_{xx} + ig_{yx})B_x + (g_{xy} + ig_{yy})B_y + (g_{xz} + ig_{yz})B_z \tag{6.30b}$$

We can then identify Eq. 6.29 and Eq. 6.27, which yields

$$\hat{g}(V) = -\frac{2}{\mu_B} \begin{pmatrix} \text{Re}\langle\Psi_\Downarrow|M_{1,x}|\Psi_\Uparrow\rangle & \text{Re}\langle\Psi_\Downarrow|M_{1,y}|\Psi_\Uparrow\rangle & \text{Re}\langle\Psi_\Downarrow|M_{1,z}|\Psi_\Uparrow\rangle \\ \text{Im}\langle\Psi_\Downarrow|M_{1,x}|\Psi_\Uparrow\rangle & \text{Im}\langle\Psi_\Downarrow|M_{1,y}|\Psi_\Uparrow\rangle & \text{Im}\langle\Psi_\Downarrow|M_{1,z}|\Psi_\Uparrow\rangle \\ \langle\Psi_\Uparrow|M_{1,x}|\Psi_\Uparrow\rangle & \langle\Psi_\Uparrow|M_{1,y}|\Psi_\Uparrow\rangle & \langle\Psi_\Uparrow|M_{1,z}|\Psi_\Uparrow\rangle \end{pmatrix} . \tag{6.31}$$

In practice, the states $\{|\Psi_\Uparrow\rangle, |\Psi_\Downarrow\rangle\}$ are computed at zero magnetic field with the **k.p** or tight-binding method. The operator $\mathbf{M_1}$ is not constructed explicitly. For instance the matrix elements of $M_{1,x}$ are evaluated from finite differences with a leapfrog scheme as

$$\langle\Psi_i|M_{1,x}|\Psi_j\rangle = \frac{\langle\Psi_i|H(V, +\delta B\mathbf{x})|\Psi_j\rangle - \langle\Psi_i|H(V, -\delta B\mathbf{x})|\Psi_j\rangle}{-2\delta B} \tag{6.32}$$

with $|\Psi_{i,j}\rangle \in \{|\Psi_\Uparrow\rangle, |\Psi_\Downarrow\rangle\}$. The leapfrog scheme allows to get rid of the small $\propto B^2$ terms that might develop at finite δB in the Hamiltonian. The g-matrix is then easily computed with Eqs. 6.31 and 6.32. We then need to compute $\hat{g}'$ at $V = V_0$. This can be done by computing the g-matrix $\hat{g}(V_0 \pm \delta V)$ at two close bias points $V = V_0 \pm \delta V$ in some basis sets $\{|\Psi_{\pm,\Uparrow}\rangle, |\Psi_{\pm,\Downarrow}\rangle\}$ and calculate $\hat{g}'$ from finite differences:

$$\hat{g}'(V_0) = \frac{\hat{g}(V_0 + \delta V) - \hat{g}(V_0 - \delta V)}{2\delta V} \tag{6.33}$$

However, the above equation is usually meaningless as $\{\Psi_{\pm,\Uparrow}, \Psi_{\pm,\Downarrow}\}$ are defined up to an arbitrary unitary transform $U_\pm$. We show in appendix D how to find the appropriate basis set $\{|\Psi_{\pm\Uparrow'}\rangle, |\Psi_{\pm\Downarrow'}\rangle\}$ which allow for a safe calculation of $\hat{g}'$ using Eq. 6.33.

As an example, we have applied this methodology to the same device as in chapters IV and V, a nanowire with $W = 30$ nm, $H = 10$ nm, and a gate covering half the width
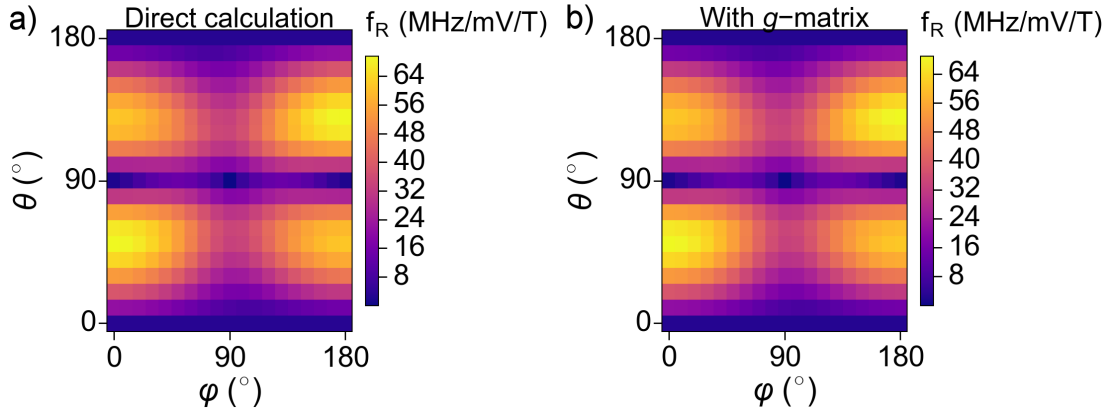
Figure 6.13: (a) Direct calculation of f_R using Eq. 6.25 (b) Calculation of f_R using the g-matrix formalism and Eq. 6.13.

with $L_g = 30$ nm. We apply $V_G = -0.1$ V on the gate in order to trap a hole. The convention for the axes and angular dependence are the same as for the experimental device. On one hand we have computed directly the Rabi frequency for a given magnetic field $\mathbf{B}$ using Eq. 6.25. We have then swept the magnetic field orientation (the magnetic field amplitude is kept constant $|\mathbf{B}| = 1$ T). On the other hand we have calculated $\hat{g}$ and $\hat{g}'$ and used Eq. 6.13 to compute the Rabi frequency with respect to the magnetic field orientation. The results, displayed Fig. 6.13, show that the two methods give almost identical numerical results on the full map of Rabi frequency. The difference between the two methods is less than 1%. The use of the g-matrix formalism for numerical calculation is however much more efficient: for an equal accuracy we just need three calculations of the two states $|\Psi_\Uparrow\rangle$ and $|\Psi_\Downarrow\rangle$ (at V_0 and $V_0 \pm \delta V$) and we can get very precisely the Rabi frequency for arbitrary $\mathbf{B}$ (the calculation of the g-matrix is very cheap). In the case of the direct calculation, the electronic structure of the qubit must be calculated for each $\mathbf{B}$.

For the same device we have also tested the assumption of a linear in B Rabi frequency. To that end, we have chosen a direction of the magnetic field, here $\mathbf{b} = (1, 0, 1)/\sqrt{2}$, and computed the dependence of the f_R with the magnetic field amplitude with Eq. 6.25 and with Eq. 6.13 (linear in B by construction). The results, plotted Fig. 6.14 show that f_R is indeed linear in B on a large range, up to a few Teslas. This is perfectly fine for qubit applications in which the magnetic field remains below 2 T, in order to reach EDSR frequency not larger than a few tens of GHZ.

The methodology now validated, we can use it to compute the Rabi maps from the electronic structure calculations and compare with the experimental map.
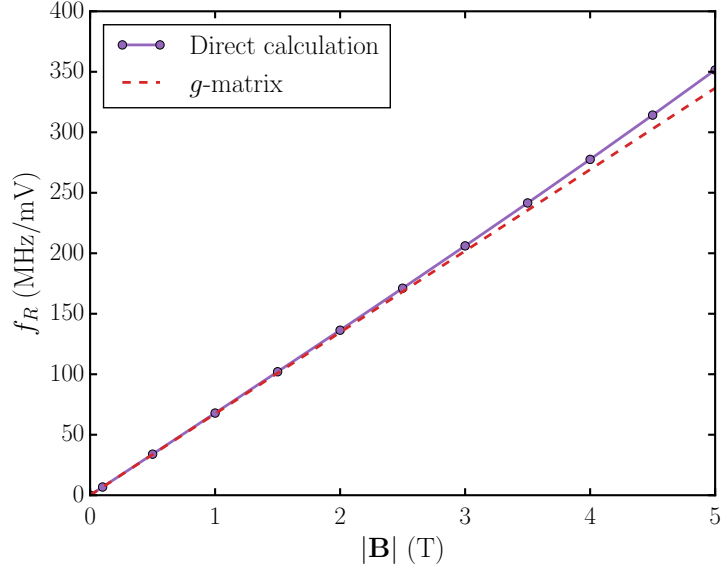
Figure 6.14: Rabi frequency from direct calculation and g-matrix formalism, as a function of magnetic field amplitude, with a field along $\mathbf{x} + \mathbf{z}$.

6.3.2 Calculations of the Rabi map.

We have used the g-matrix formalism to analyze the measured Rabi frequency anisotropy, and have shown that it can be used to efficiently calculate numerically the Rabi map. In this part we will use it along with 6 bands $\mathbf{k}.\mathbf{p}$ calculations on the hole qubit, in order to find which physical parameters reproduce the experimental Rabi map. The microscopic disorder in the device is not known, so it is illusory to look for a quantitative agreement, but we could seek at least for a qualitative agreement. We use a device similar to the experimental one, a nanowire with height $H = 8$ nm and $W = 25$ nm, and two gates in series of length $L_g = 30$ nm. As in the previous chapters, we place two side gates 30 nm to the left and right of the central gates, in order to mimic the quasi-metallic source/drain contacts. The schematic of the device is shown Fig. 6.15.

First let us examine the simplest case, a dot trapped under the gate, without any disorder. However, in this device with fully covering gates, the perfect symmetry hinders the formation of corners states, whereas in practice local disorder easily breaks this symmetry. Therefore, in that case we artificially break the symmetry by using gates covering only half of the width of the nanowire. We apply $V_{s1} = V_{s2} = 0.3$ V, in order to create the source/drain barriers, $V_{bg} = 0$ V, and $(V_{G1}, V_{G2}) = (-0.1, 0.0)$ V, in order to trap a hole under gate G1. Here the g-factors are $|g_1^*| = 1.97$, $|g_2^*| = 1.35$, $|g_3^*| = 3.27$ respectively along $\mathbf{x}$, $\mathbf{y}$, $\mathbf{z}$. The anisotropy of g factors is therefore very different from the experimental case, where the larger g factors are in-plane (2.08 and 2.48), and the smaller (1.62) is out of plane. We have computed the Rabi frequency in this system, and we have decomposed it into IZ-EDSR and g-TMR contributions, shown in Fig. 6.16, at constant Zeeman splitting $E_z/h = 9$ GHz, like in the experiment. Here the g-TMR is
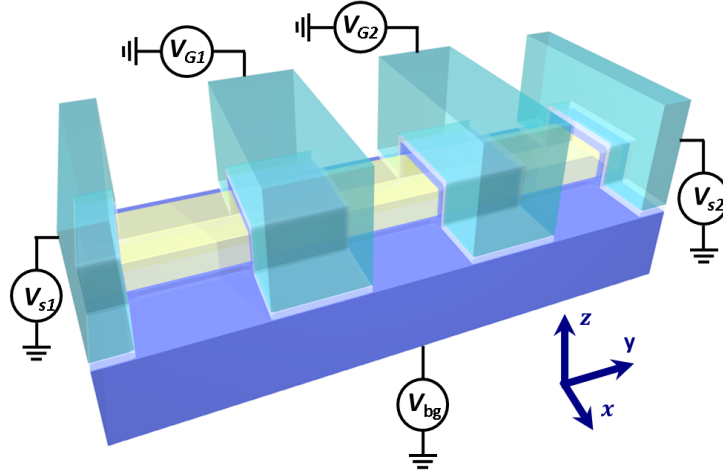
Figure 6.15: Schematic of the device. The silicon nanowire is in yellow, SiO$_2$ is in blue, HfO$_2$ in light gray and the gates are in dark green.
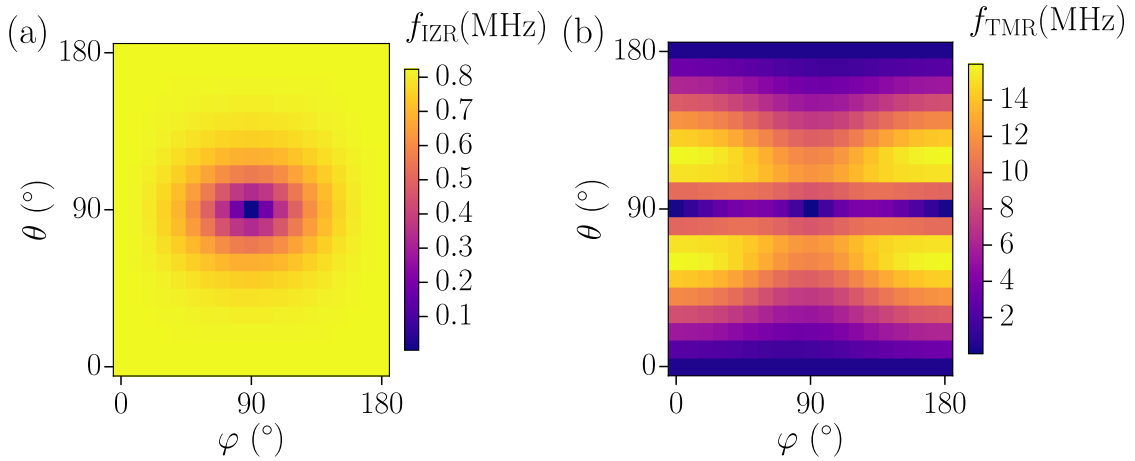
Figure 6.16: Rabi frequency cartography for a state located under the main gate, at constant Zeeman energy (9 GHz) (a) IZ-EDSR contribution (b) g-TMR contribution.

the dominant mechanism, as expected because the dot is confined close to two interfaces, leading to an anharmonic transverse potential, similar to Fig. 6.9a. The IZ-EDSR map present a minimum for $\theta = 90°$, $\varphi = 90°$ corresponding to a $\mathbf{\Omega}_{SO} \parallel \mathbf{y}$, orthogonal to the experimental one. This is also consistent with the GBL model, as $\mathbf{\Omega}_{SO}$ depends on the direction of the electric field excitation, which is here along $\mathbf{x}$ and $\mathbf{z}$, whereas it is mainly along $\mathbf{y}$ in the experimental case.

We have thus here three main inconsistencies with the experimental results: the g-factors anisotropy, the proportion between IZ-EDSR and g-TMR, and the orientation of the IZ-EDSR minima are not properly reproduced.

Let us start with the g-factor anisotropy. There could be different reasons that could explain this discrepancy. First, we are looking at the ground state. If tens of holes are present, the actual qubit state might have a different orbital shape, so a different g factor. In addition, the charge disorder could induce such variations. However, the
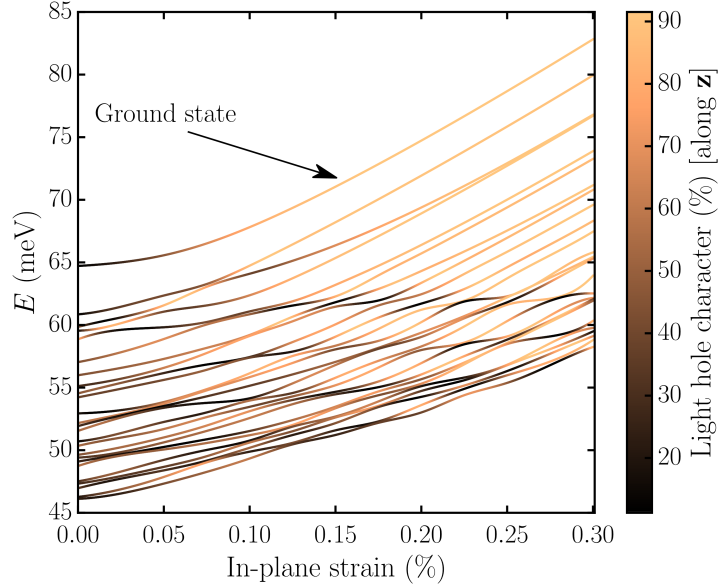
Figure 6.17: Energy of hole states as a function of the amplitude of an in-plane biaxial strain. The color code gives the light-hole character in %. The hole state higher in energy is the ground state.

same anisotropy is systematically measured in these devices, even for the first hole in a smaller wire [152]. This invites us to look for a reproducible feature. A possibility is the presence of non-intentional strain. Indeed, up to now in the simulations we have dealt with hole states which are mostly heavy holes in the $\mathbf{z}$ direction (higher g-factor along that direction). Experimentally, the small g-factor along $\mathbf{z}$ is more likely a signature of a light-hole state. In a planar device in-plane biaxial tensile strain promotes light-hole states [171]. We have verified that it is also the case in our device: in Fig. 6.17 we have plotted the energy of the first states as a function of the amplitude of in-plane biaxial strain and characterized their heavy or light hole nature by a color code. When increasing the strain amplitude more excited states have a light hole character, up to ten orbital states for $\epsilon_{xx} = \epsilon_{yy} = 0.2$ %. Such non-intentional strain are known to be present in MOSFET devices, due for instance to the deposition of metallic gates [172]. They are difficult to characterize and can be inhomogeneous [173]. Moreover, as we cool down the samples to sub-Kelvin temperatures, the difference of thermal dilatation between Si and the surrounding materials inevitably induces strain. Here we applied a small quasi-biaxial strain of $\epsilon_{xx} = \epsilon_{yy} = 0.2$ % and $\epsilon_{zz} = -0.15$ % and we obtained the correct anisotropy. We got $|g_1^*| = 2.48$, $|g_2^*| = 2.01$, $|g_3^*| = 0.80$ respectively along $\mathbf{x}$, $\mathbf{y}$, $\mathbf{z}$.

This leaves us with the discrepancies on the IZ-EDSR/g-TMR ratio, and on the angular position of the IZ-EDSR minima. We know from the measurement of the lever-arms parameters that the dot is localized between the two gates. Therefore an obvious way to reproduce the experimental maps is to start by putting the dot in that position. To do that, we cannot put 10 to 30 holes in each dot because it is too complicated to describe.
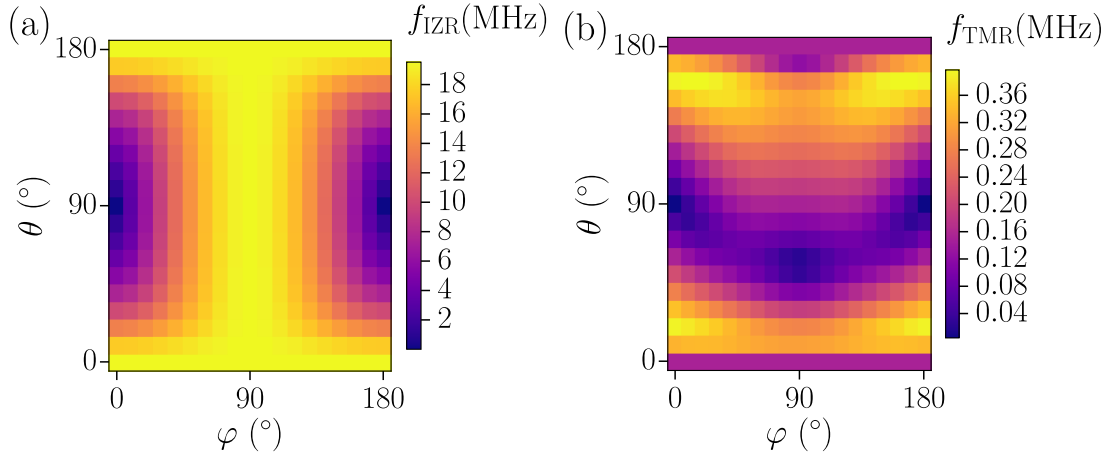
Figure 6.18: Rabi frequency cartography for a state located under between the two gates, at constant Zeeman energy (9 GHz), with tensile in-plane strain, without disorder. (a) IZ-EDSR contribution (b) g-TMR contribution.

We then simply adjust the bias on the different gates in our system to put a potential well in between two gates. We start with a device with fully covering gates but without disorder, and we will introduce disorder later. We apply $V_{s1} = V_{s2} = 0.3$ V in order to create the source/drain barriers, and $V_{G1} = V_{G2} = 0.1$ V in order to position the dot between the gates. We have again computed the Rabi frequency map and separated the two mechanisms. The IZ-EDSR and g-TMR maps are plotted in Fig. 6.18. The IZ-EDSR is the dominant mechanism, because the confinement potential is more harmonic. As expected $\mathbf{\Omega}_{SO}$ is this time almost aligned with $\mathbf{x}$, as we have shifted the direction of electric excitation by roughly 90°. The amplitude of g-TMR is very small and has a complex dependence.

In that ideal case, without any disorder, the electric field excitation is mostly along the wire direction, so the minima of IZ-EDSR are along the $\mathbf{x}$ direction. If we introduce disorder, such as surface roughness and RCS charges in the gate stack, the direction of the electric field excitation can be slightly shifted. To verify this we have introduced surface roughnes, and positive and negative charges trapped at the SiO_2/HfO_2 interface with density $n_{RCS} = 2 \times 10^{12}$ cm^{-2}, on top of the previous simulation. We have computed the Rabi frequency maps on a few samples, and the results for a typical example are shown in Fig. 6.19. The minima of IZ-EDSR are this time slightly shifted, and this example reproduces pretty well the experimental cartography of Fig. 6.11a. On the other samples, the minima can be shifted slightly differently in the $\mathbf{x}$-$\mathbf{y}$ plane depending on disorder. Moreover, the g-TMR/IZ-EDSR ratio as well as the g-TMR anisotropy seem to depend a lot on the distribution of charges in the gate stack.

Consequently, our simulations qualitatively reproduce the main experimental features for a dot positioned between two gates, and with an in-plane biaxial strain. We do not have a qualitative agreement on the values of the g-factors. This can be explained by the
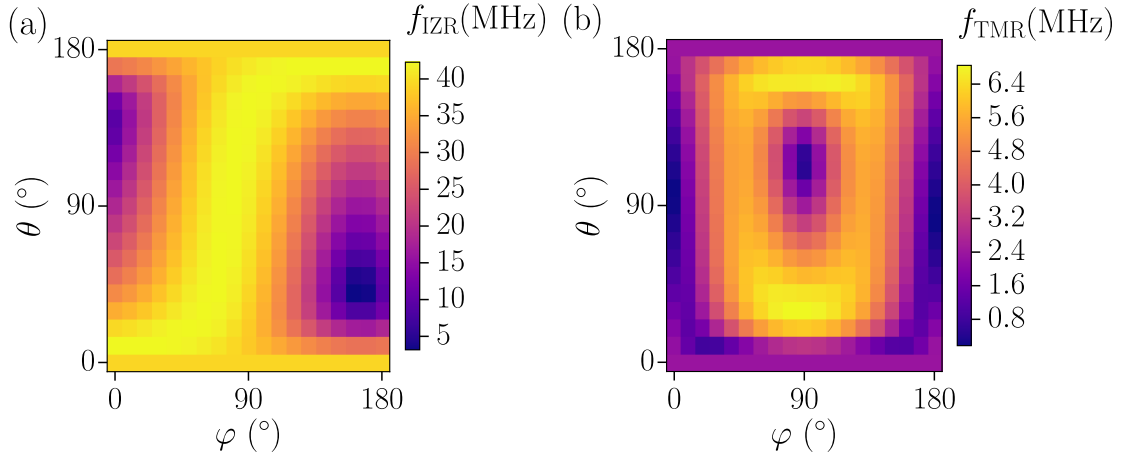
Figure 6.19: Rabi frequency cartography for a state located under between the two gates, at constant Zeeman energy (9 GHz), with tensile in-plane strain, with surface roughness and RCS charges with density $n_{\mathrm{RCS}} = 2 \times 10^{12}$ cm^{-2}. (a) IZ-EDSR contribution (b) g-TMR contribution.

fact that we consider only the ground state, so we need to look for the g-factors of higher orbital and the effect of Coulomb interactions. Moreover, the amplitude of the Rabi frequency is smaller in all the cases we presented (keeping in mind that the f_R are given in MHz/mV, and a gate excitation V_{ac} smaller than 1 mV is applied in the experiment). The dot is hence probably too confined in the simulations. However, in the experimental device, the dots contains between 10 and 30 holes which would screen and smoothen the potential, thus decreasing the confinement. Anyway, as the number of holes in the dots, the potential disorder and the inhomogeneous strains are not known in the device, we can only seek a qualitative agreement.

To conclude, in these hole spin qubits the dependence of the Rabi frequency with the magnetic field orientation can be very complex, and thus needs to be carefully characterized. In particular the influence of strain seems to be very important, even for small strains. It can then be interesting to add intentional strain to overcome the uncontrolled effect of non-intentional strains. Strain-engineering is straightforward in microelectronics [174, 175], so it could be used to optimize the properties of qubits.

On another note, in the perspective of the approach of a linear chain of face-to-face devices presented in chapter II, each dot is located under a gate, therefore the main mechanism is expected to be g-TMR. In that sense, the present experiment is not representative of these qubits. More detailed simulation studies are needed to determine the robustness of the two mechanisms with respect to disorder and how they can be engineered in these devices, in order to find the best qubit architectures.

6.4 Conclusion

The original motivation of the study of this chapter was the measurement by Crippa *et al.* of the Rabi frequency dependence on the magnetic field orientation in a hole spin qubit. In that experiment, the Rabi frequency is driven by EDSR, allowed by the spin-orbit coupling in the valence band of silicon. Therefore, a point to clarify was the relative role played by the two spin-orbit mechanisms identified in the literature, g-TMR and GBL. To that end we have developed a methodology based on the original g-TMR, the g-matrix formalism, which encompasses both mechanisms. This formalism allows to split the Rabi frequency into two contributions: one which is accessible via measurements of the Zeeman splittings (g-TMR), and one which is not (IZ-EDSR). We have applied this methodology to the experimental data and extracted these two contributions, showing that the main mechanism is IZ-EDSR and that g-TMR exists in a non-negligible proportion. Moreover, we have shown how to compute the g-matrices on top of 6-band $\mathbf{k}.\mathbf{p}$ calculations, which allowed to compute efficiently the Rabi maps. We have used these calculations to reproduce the main features of the experimental. In particular, we have shown that the g-factors anisotropy is compatible with in-plane tensile biaxial strain, and that the anisotropy of IZ-EDSR can be explained by the position of the dot between the two gates of the double quantum dot.

These results show some important points to be characterized in future works. The strain seem to have important effects on the Rabi frequencies and g-factors, so strain-engineering could be used to override the non-intentional strains and for qubit optimization. Then, the variability with local disorder on the Rabi maps need to be evaluated and controlled, because the orientation of the magnetic field will be the same for all the qubits.

Finally, it is worth noting that as long as the system is in the linear response regime (in $\mathbf{B}$ and electric field), the g-matrix formalism is applicable. Therefore, even if it has been used in the specific of silicon on insulator hole spin qubits, it can be applied to various materials and architectures of spin qubits.

Chapter 7

Conclusion

This thesis is focused on the numerical and theoretical study of the electrical manipulation of the spin in the electron and hole silicon qubits. It is included in a large program in CEA Grenoble whose purpose is to take advantage of the CMOS capabilities at Leti and low temperature physics expertise at INAC, in order to develop scalable spin quantum bits in silicon. Therefore, we tried to work as close as possible to the real experimental devices. To that end we have used a set of simulation tools presented in chapter 3, which allow for a faithful description of electrostatic potential and electronic structure of the qubits, hence for a reliable comparison with the measurements. We summarize our results in the next section, then we discuss the next steps that could be undertaken starting from the present work.

7.1   Main results

We started by investigating in chapter 4 the unexpected measurement of EDSR on electrons in a silicon double quantum dot, involving an excited valley state. We have developed an analytical model, validated by tight-binding calculations, and shown that EDSR is due to a combination of intervalley spin-orbit and dipolar interactions. Using group theory we have shown that the sizable spin-orbit coupling exists in dots with low symmetry (no more than one mirror plane). States localized at the corner of a nanowire have such symmetry, whereas planar quantum dots do not. This explains why EDSR was first observed in CEA particular devices. The anisotropy of the predicted spin-orbit interaction is consistent with the anisotropy of the measured current, thus validating the hypothesis of a spin-orbit driven EDSR. We have also computed the Rabi frequency as a function of the magnetic field amplitude, which shows a strong non-linearity: the main EDSR transition exhibits a sharp peak when the Zeeman splitting equals the valley splitting.

In chapter 5, we have built on these elements to create an efficient scheme for spin manipulation. This scheme is based on the tuning of the spin-valley mixing by the valley splitting, which is handily controlled by the backgate. Indeed, thanks to the intervalley

spin-orbit interaction we can switch between a spin qubit, where manipulation is slow but with good coherence properties, and a valley qubit, more prone to decoherence yet efficiently controllable electrically. The goal of this chapter is to determine the workability of this proposal, being as thorough as it is possible with the simulations. To that end, we have computed with tight-binding the evolution of the main elements of the model with the backgate potential, showing that the Rabi frequency can reach more than 100 MHz in the valley regime. After that, we have used time-dependent simulations to demonstrate the qubit operation. In order to give proof on the sustainability of the scheme we have computed the decoherence due to a few simple sources of noise. Then we have studied the effect of surface roughness on qubit variability, showing that an efficient scheme (with Rabi frequency of a few tens of MHz) can be achieved at the price of individual calibration of the qubits. Moreover we have investigated the effect of the wire height on the valley splitting, and have evidenced the significant impact of the interfaces. Finally, we have presented a recent measurement of the valley splitting as a function of the backgate bias. We have explained the large value observed by the presence of remote charges in the gate stack, which induce a lot of variability. This experiment constitutes a first step towards the experimental realization of our proposal.

In the last chapter, we focus on hole spin qubits. Contrarily to the conduction band, the spin-orbit coupling is intrinsically much larger in the valence band, therefore making holes natural candidates for electrical spin manipulation. We have presented a recent experiment in which the anisotropy of the Rabi frequency with the magnetic field direction is measured. In order to explain the obtained cartography, we have developed a formalism that allows for the description of the qubit via the g-matrix. In this model, the Rabi frequency can be computed (in the linear response regime) from the g-matrix and its derivative with respect to the gate voltage. With this formalism, we distinguish two contributions to the Rabi frequency: on one hand the g-Tensor Magnetic Resonance, analogous to the mechanism of Ref. [157], which can be extracted from measurements of the Zeeman splittings, and on the other hand Iso-Zeeman EDSR, including the EDSR mechanism of Ref. [161], which is not accessible from the Zeeman splittings. We have extracted the experimental maps of the g-TMR and IZ-EDSR contributions, showing that in that case the IZ-EDSR is the dominant mechanism, although g-TMR is not negligible. In order to interpret these results we have computed the g-matrices on top of 6-bands $\mathbf{k.p}$ calculations, and obtained the Rabi maps. We have shown that the g-factors anisotropy is compatible with non-intentional strain, and that the anisotropy and dominant proportion of IZ-EDSR are due to the position of the dot between the gates and to charge disorder in a lesser extent. Indeed, g-TMR is enhanced by the anharmonicity of the potential, which is much higher when the dot is shaken against an interface. We thus expect that in the intended corner dots, the dominant mechanism is g-TMR, so this will have to be taken into account in the analysis of the next experiments. In this chapter, the use of the

g-matrix formalism and **k.p** simulations provided us with a lot of new information on the measured system.

7.2 Outlook

The outlooks of this work are twofold: the continuation of the studies we have presented, and the use of unexploited features of the simulation tools.

Concerning the first, there is ongoing work that need to be completed. Regarding electrons, we need to develop a complete model for the valley describing the intervalley spin-orbit and dipolar interactions with the height of the nanowire. First calculations indeed show that the spin-orbit coupling is almost independent of the height, whereas the dipolar interaction shows large variations. More generally, we hope that this work will stimulate new experiments, not only in nanowire devices, but maybe also in other type of silicon devices, provided they have sizable spin-orbit interaction. As for holes, the studies are less advanced than electrons, and preliminary studies tend to show that there is room for improvement. For instance, by computing the Rabi frequency dependence with the backgate, we have observed that the symmetries are also important for holes: in some high-symmetry points the Rabi frequency vanishes. This is currently investigated as part of the PhD of Benjamin Venitucci, and a paper has just been submitted [176]. We could thus envision a scheme analogous to electrons, with a manipulation regime and a noise-protected regime, but this has to be carefully characterized. Moreover, the strain seem to have a great influence on the qubit properties and could be used for optimization of the Rabi frequency.

We have also presented in chapter 3 the numerical tools based on the configuration interaction method that can describe the many-particles interactions. An interesting prospect is then to use it to describe everything that make use of particle-particle interactions in the experiments. Namely, we could model the readout in a face-to-face device, and compare our results with the reflectometry measurements. We could also study the effects of the inner electrons/holes in a dot on the properties of the qubit, which were neglected in this thesis so far. Finally, we could model two-qubit gates, which is an ongoing experimental work and a key feature for quantum computing.

Bibliography

[1] D. Loss, D. P. DiVincenzo, Quantum computation with quantum dots, Physical Review A 57 (1998) 120–126. `doi:10.1103/PhysRevA.57.120`.

[2] S.-H. Lo, D. Buchanan, Y. Taur, W. Wang, Quantum-mechanical modeling of electron tunneling current from the inversion layer of ultra-thin-oxide nmosfet's, IEEE Electron Device Letters 18 (5) (1997) 209–211.

[3] H. Ishikuro, T. Fujii, T. Saraya, G. Hashiguchi, T. Hiramoto, T. Ikoma, Coulomb blockade oscillations at room temperature in a si quantum wire metal-oxide-semiconductor field-effect transistor fabricated by anisotropic etching on a silicon-on-insulator substrate, Applied physics letters 68 (25) (1996) 3585–3587.

[4] R. Lavieville, F. Triozon, S. Barraud, A. Corna, X. Jehl, M. Sanquer, J. Li, A. Abisset, I. Duchemin, Y.-M. Niquet, Quantum dot made in metal oxide silicon-nanowire field effect transistor working at room temperature., Nano letters 15 (5) (2015) 2958–2964.

[5] International technology roadmap for semiconductors - itrs 2.0, Tech. rep. (2015).

[6] R. Courtland, Transistors could stop shrinking in 2021, IEEE Spectrum 53 (9) (2016) 9–11.

[7] R. P. Feynman, There's plenty of room at the bottom, Miniaturization (1959) 282–296.

[8] S. Lloyd, Universal quantum simulators, Science (1996) 1073–1078.

[9] D. Deutsch, Quantum theory, the church–turing principle and the universal quantum computer, Proc. R. Soc. Lond. A 400 (1818) (1985) 97–117.

[10] D. Deutsch, R. Jozsa, Rapid solution of problems by quantum computation, Proc. R. Soc. Lond. A 439 (1907) (1992) 553–558.

[11] P. W. Shor, Polynomial-time algorithms for prime factorization and discrete logarithms on a quantum computer, SIAM review 41 (2) (1999) 303–332.

[12] S. Aaronson, Guest column: Np-complete problems and physical reality, ACM Sigact News 36 (1) (2005) 30–52.

[13] D. Aharonov, M. Ben-Or, Fault-tolerant quantum computation with constant error, in: Proceedings of the twenty-ninth annual ACM symposium on Theory of computing, ACM, 1997, pp. 176–188.

[14] D. P. DiVincenzo, The physical implementation of quantum computation, Fortschritte der Physik: Progress of Physics 48 (9-11) (2000) 771–783.

[15] A. G. Fowler, M. Mariantoni, J. M. Martinis, A. N. Cleland, Surface codes: Towards practical large-scale quantum computation, Physical Review A 86 (3) (2012) 032324.

[16] B. M. Terhal, Quantum error correction for quantum memories, Reviews of Modern Physics 87 (2) (2015) 307.

[17] M. Dyakonov, Prospects for quantum computing: Extremely doubtful, in: International Journal of Modern Physics: Conference Series, Vol. 33, World Scientific, 2014, p. 1460357.

[18] X. Waintal, What determines the ultimate precision of a quantum computer?, arXiv preprint arXiv:1702.07688.

[19] J. R. Petta, A. C. Johnson, J. M. Taylor, E. A. Laird, A. Yacoby, M. D. Lukin, C. M. Marcus, M. P. Hanson, A. C. Gossard, Coherent manipulation of coupled electron spins in semiconductor quantum dots, Science 309 (5744) (2005) 2180–2184.

[20] F. H. L. Koppens, C. Buizert, K. J. Tielrooij, I. T. Vink, K. C. Nowack, T. Meunier, L. P. Kouwenhoven, L. M. K. Vandersypen, Driven coherent oscillations of a single electron spin in a quantum dot., Nature 442 (7104) (2006) 766. `doi:10.1038/nature05065`.
URL `http://www.ncbi.nlm.nih.gov/pubmed/16915280`

[21] E. Rashba, A. L. Efros, Orbital mechanisms of electron-spin manipulation by an electric field, Phys. Rev. Lett. 91 (12) (2003) 126405.

[22] K. C. Nowack, F. H. L. Koppens, Y. V. Nazarov, L. M. K. Vandersypen, Coherent control of a single electron spin with electric fields., Science 318 (5855) (2007) 1430. `doi:10.1126/science.1148092`.
URL `http://www.ncbi.nlm.nih.gov/pubmed/17975030`

[23] S. Nadj-Perge, S. M. Frolov, E. P. A. M. Bakkers, L. P. Kouwenhoven, Spin-orbit qubit in a semiconductor nanowire., Nature 468 (7327) (2010) 1084. `doi:10.1038/nature09682`.
URL `http://www.ncbi.nlm.nih.gov/pubmed/21179164`

[24] E. A. Laird, C. Barthel, E. I. Rashba, C. M. Marcus, M. P. Hanson, A. C. Gossard, Hyperfine-mediated gate-driven electron spin resonance, Physical Review Letters 99 (2007) 246601. `doi:10.1103/PhysRevLett.99.246601`.
URL `https://link.aps.org/doi/10.1103/PhysRevLett.99.246601`

[25] M. Pioro-Ladrière, T. Obata, Y. Tokura, Y.-S. Shin, T. Kubo, K. Yoshida, T. Taniyama, S. Tarucha, Electrically driven single-electron spin resonance in a slanting Zeeman field, Nature Physics 4 (10) (2008) 776. `doi:10.1038/nphys1053`.
URL `http://www.nature.com/doifinder/10.1038/nphys1053`

[26] S. I. Erlingsson, Y. V. Nazarov, Hyperfine-mediated transitions between a zeeman split doublet in gaas quantum dots: The role of the internal field, Physical Review B 66 (15) (2002) 155327.

[27] J. Elzerman, R. Hanson, L. W. Van Beveren, B. Witkamp, L. Vandersypen, L. P. Kouwenhoven, Single-shot read-out of an individual electron spin in a quantum dot, nature 430 (6998) (2004) 431.

[28] A. Morello, J. J. Pla, F. A. Zwanenburg, K. W. Chan, K. Y. Tan, H. Huebl, M. Möttönen, C. D. Nugroho, C. Yang, J. A. van Donkelaar, et al., Single-shot readout of an electron spin in silicon, Nature 467 (7316) (2010) 687.

[29] K. Nowack, M. Shafiei, M. Laforest, G. Prawiroatmodjo, L. Schreiber, C. Reichl, W. Wegscheider, L. Vandersypen, Single-shot correlations and two-qubit gate of solid-state spins, Science 333 (6047) (2011) 1269–1272.

[30] K. Ono, D. G. Austing, Y. Tokura, S. Tarucha, Current Rectification by Pauli Exclusion in a Weakly Coupled Double Quantum Dot System, Science 297 (August) (2002) 1313. `doi:10.1126/science.1070958`.

[31] R. Brunner, Y.-S. Shin, T. Obata, M. Pioro-Ladrière, T. Kubo, K. Yoshida, T. Taniyama, Y. Tokura, S. Tarucha, Two-qubit gate of combined single-spin rotation and interdot spin exchange in a double quantum dot, Physical review letters 107 (14) (2011) 146801.

[32] K. Petersson, L. McFaul, M. Schroer, M. Jung, J. M. Taylor, A. A. Houck, J. Petta, Circuit quantum electrodynamics with a spin qubit, Nature 490 (7420) (2012) 380–383.

[33] X. Mi, J. Cady, D. Zajac, P. Deelman, J. Petta, Strong coupling of a single electron in silicon to a microwave photon, Science (2016) aal2469.

[34] N. Samkharadze, G. Zheng, N. Kalhor, D. Brousse, A. Sammak, U. Mendes, A. Blais, G. Scappucci, L. Vandersypen, Strong spin-photon coupling in silicon, Science 359 (6380) (2018) 1123–1127.

[35] X. Mi, M. Benito, S. Putz, D. M. Zajac, J. M. Taylor, G. Burkard, J. R. Petta, A coherent spin–photon interface in silicon, Nature 555 (7698) (2018) 599.

[36] B. E. Kane, A silicon-based nuclear spin quantum computer, nature 393 (6681) (1998) 133.

[37] T. D. Ladd, F. Jelezko, R. Laflamme, Y. Nakamura, C. Monroe, J. L. O'Brien, Quantum computers, Nature 464 (7285) (2010) 45.

[38] A. Imamoglu, D. D. Awschalom, G. Burkard, D. P. DiVincenzo, D. Loss, M. Sherwin, A. Small, et al., Quantum information processing using quantum dot spins and cavity qed, Physical review letters 83 (20) (1999) 4204.

[39] A. Blais, R.-S. Huang, A. Wallraff, S. M. Girvin, R. J. Schoelkopf, Cavity quantum electrodynamics for superconducting electrical circuits: An architecture for quantum computation, Physical Review A 69 (6) (2004) 062320.

[40] I. Chiorescu, Y. Nakamura, C. M. Harmans, J. Mooij, Coherent quantum dynamics of a superconducting flux qubit, Science 299 (5614) (2003) 1869–1871.

[41] E. Knill, R. Laflamme, G. J. Milburn, A scheme for efficient quantum computation with linear optics, nature 409 (6816) (2001) 46.

[42] J. I. Cirac, P. Zoller, Quantum computations with cold trapped ions, Physical review letters 74 (20) (1995) 4091.

[43] F. A. Zwanenburg, A. S. Dzurak, A. Morello, M. Y. Simmons, L. C. L. Hollenberg, G. Klimeck, S. Rogge, S. N. Coppersmith, M. A. Eriksson, Silicon quantum electronics, Review of Modern Physics 85 (2013) 961. `doi:10.1103/RevModPhys.85.961`. URL `https://link.aps.org/doi/10.1103/RevModPhys.85.961`

[44] J. J. Morton, D. R. McCamey, M. A. Eriksson, S. A. Lyon, Embracing the quantum limit in silicon computing, Nature 479 (7373) (2011) 345.

[45] A. Tyryshkin, J. Morton, S. Benjamin, A. Ardavan, G. Briggs, J. Ager, S. Lyon, Coherence of spin qubits in silicon, Journal of Physics: Condensed Matter 18 (21) (2006) S783.

[46] A. M. Tyryshkin, S. Tojo, J. J. L. Morton, H. Riemann, N. V. Abrosimov, P. Becker, P. H. J., T. Schenkel, M. L. W. Thewalt, K. M. Itoh, S. A. Lyon, Electron spin coherence exceeding seconds in high-purity silicon, Nature Materials

11 (2) (2012) 143. `doi:http://dx.doi.org/10.1038/nmat3182`.
URL `http://www.nature.com/nmat/journal/v11/n2/abs/nmat3182.html#supplementary-information`

[47] A. L. Saraiva, M. J. Calderon, X. Hu, S. Das Sarma, B. Koiller, Physical mechanisms of interface-mediated intervalley coupling in Si, Physical Review B 80 (2009) 081305(R). `doi:10.1103/PhysRevB.80.081305`.

[48] A. L. Saraiva, M. J. Calderon, R. B. Capaz, X. Hu, S. Das Sarma, B. Koiller, Intervalley coupling for interface-bound electrons in silicon : An effective mass study, Physical Review B 84 (2011) 155320. `doi:10.1103/PhysRevB.84.155320`.

[49] A. Saraiva, A. Baena, M. Calderón, B. Koiller, Theory of one and two donors in silicon, Journal of Physics: Condensed Matter 27 (15) (2015) 154208.

[50] C. H. Yang, A. Rossi, R. Ruskov, N. S. Lai, F. A. Mohiyaddin, S. Lee, C. Tahan, G. Klimeck, A. Morello, A. S. Dzurak, Spin-valley lifetimes in a silicon quantum dot with tunable valley splitting, Nature Communications 4 (2013) 2069 EP –, article.
URL `http://dx.doi.org/10.1038/ncomms3069`

[51] M. Friesen, S. N. Coppersmith, Theory of valley-orbit coupling in a si/sige quantum dot, Physical Review B 81 (2010) 115324. `doi:10.1103/PhysRevB.81.115324`.
URL `https://link.aps.org/doi/10.1103/PhysRevB.81.115324`

[52] P. Boross, G. Széchenyi, D. Culcer, A. Pályi, Control of valley dynamics in silicon quantum dots in the presence of an interface step, Physical Review B 94 (2016) 035438. `doi:10.1103/PhysRevB.94.035438`.
URL `https://link.aps.org/doi/10.1103/PhysRevB.94.035438`

[53] A. Corna, L. Bourdet, R. Maurand, A. Crippa, D. Kotekar-Patil, H. Bohuslavskyi, R. Laviéville, L. Hutin, S. Barraud, X. Jehl, M. Vinet, S. De Franceschi, Y.-M. Niquet, M. Sanquer, Electrically driven electron spin resonance mediated by spin–valley–orbit coupling in a silicon quantum dot, npj Quantum Information 4 (1) (2018) 6. `doi:10.1038/s41534-018-0059-1`.

[54] X. Hao, R. Ruskov, M. Xiao, C. Tahan, H. Jiang, Electron spin resonance and spin-valley physics in a silicon double quantum dot, Nature Communications 5 (2014) 3860. `doi:10.1038/ncomms4860`.
URL `https://www.nature.com/articles/ncomms4860#supplementary-information`

[55] W. H. Lim, C. H. Yang, F. A. Zwanenburg, A. S. Dzurak, Spin filling of valley-orbit states in a silicon quantum dot, Nanotechnology 22 (33) (2011) 335704. `doi:10.1088/0957-4484/22/33/335704`.

[56] J. K. Gamble, P. Harvey-Collard, N. T. Jacobson, A. D. Baczewski, E. Nielsen, L. Maurer, I. Montaño, M. Rudolph, M. S. Carroll, C. H. Yang, A. Rossi, A. S. Dzurak, R. P. Muller, Valley splitting of single-electron si mos quantum dots, Applied Physics Letters 109 (25) (2016) 253101. `doi:10.1063/1.4972514`.

[57] D. J. Ibberson, L. Bourdet, J. C. Abadillo-Uriel, I. Ahmed, S. Barraud, M. J. Calderón, Y.-M. Niquet, M. F. Gonzalez-Zalba, Electric-field tuning of the valley splitting in silicon corner dots, arXiv preprint arXiv:1805.07981.

[58] M. G. Borselli, R. S. Ross, A. A. Kiselev, E. T. Croke, K. S. Holabird, P. W. Deelman, L. D. Warren, I. Alvarado-Rodriguez, I. Milosavljevic, F. C. Ku, et al., Measurement of valley splitting in high-symmetry si/sige quantum dots, Applied Physics Letters 98 (12) (2011) 123118.

[59] Z. Shi, C. Simmons, J. Prance, J. King Gamble, M. Friesen, D. Savage, M. Lagally, S. Coppersmith, M. Eriksson, Tunable singlet-triplet splitting in a few-electron si/sige quantum dot, Applied Physics Letters 99 (23) (2011) 233108.

[60] K. Wang, C. Payette, Y. Dovzhenko, P. Deelman, J. Petta, Charge relaxation in a single-electron si/sige double quantum dot, Physical review letters 111 (4) (2013) 046801.

[61] P. Scarlino, E. Kawakami, T. Jullien, D. R. Ward, D. E. Savage, M. G. Lagally, M. Friesen, S. N. Coppersmith, M. A. Eriksson, L. M. K. Vandersypen, Dressed photon-orbital states in a quantum dot: Intervalley spin resonance, Phys. Rev. B 95 (2017) 165429. `doi:10.1103/PhysRevB.95.165429`.
URL `https://link.aps.org/doi/10.1103/PhysRevB.95.165429`

[62] S. F. Neyens, R. H. Foote, B. Thorgrimsson, T. Knapp, T. McJunkin, L. Vandersypen, P. Amin, N. K. Thomas, J. S. Clarke, D. Savage, et al., Transport and valley splitting in si quantum wells with pure ge at the top interface, arXiv preprint arXiv:1804.01914.

[63] G. Dresselhaus, Spin-orbit coupling effects in zinc blende structures, Physical Review 100 (2) (1955) 580.

[64] M. O. Nestoklon, L. E. Golub, E. L. Ivchenko, Spin and valley-orbit splittings in SiGeSi heterostructures, Physical Review B 73 (2006) 235334. `doi:10.1103/PhysRevB.73.235334`.
URL `https://link.aps.org/doi/10.1103/PhysRevB.73.235334`

[65] L. Golub, E. Ivchenko, Spin splitting in symmetrical sige quantum wells, Physical Review B 69 (11) (2004) 115333.

[66] D. Culcer, A. Saraiva, B. Koiller, X. Hu, S. D. Sarma, Valley-based noise-resistant quantum computation using si quantum dots, Physical review letters 108 (12) (2012) 126804.

[67] J. S. Schoenfield, B. M. Freeman, H. Jiang, Coherent manipulation of valley states at multiple charge configurations of a silicon quantum dot device, Nature Communications 8 (1) (2017) 64. `doi:https://doi.org/10.1038/s41467-017-00073-x`.

[68] A. Laucht, J. T. Muhonen, F. A. Mohiyaddin, R. Kalra, J. P. Dehollain, S. Freer, F. E. Hudson, M. Veldhorst, R. Rahman, G. Klimeck, K. M. Itoh, D. N. Jamieson, J. C. Mccallum, A. S. Dzurak, A. Morello, Electrically controlling single-spin qubits in a continuous microwave field, Science Advances 1 (2015) e1500022. `doi:10.1126/sciadv.1500022`.

[69] J. Salfi, J. Mol, R. Rahman, G. Klimeck, M. Simmons, L. Hollenberg, S. Rogge, Spatially resolving valley quantum interference of a donor in silicon, Nature materials 13 (6) (2014) 605.

[70] B. Koiller, X. Hu, S. D. Sarma, Strain effects on silicon donor exchange: Quantum computer architecture considerations, Physical Review B 66 (11) (2002) 115201.

[71] S. Schofield, N. Curson, M. Simmons, F. Rueß, T. Hallam, L. Oberbeck, R. Clark, Atomically precise placement of single dopants in si, Physical review letters 91 (13) (2003) 136104.

[72] D. N. Jamieson, C. Yang, T. Hopf, S. Hearne, C. I. Pakes, S. Prawer, M. Mitic, E. Gauja, S. Andresen, F. Hudson, et al., Controlled shallow single-ion implantation in silicon using an active substrate for sub-20-kev ions, Applied Physics Letters 86 (20) (2005) 202101.

[73] P. Harvey-Collard, N. T. Jacobson, M. Rudolph, J. Dominguez, G. A. Ten Eyck, J. R. Wendt, T. Pluym, J. K. Gamble, M. P. Lilly, M. Pioro-Ladrière, et al., Coherent coupling between a quantum dot and a donor in silicon, Nature communications 8 (1) (2017) 1029.

[74] G. Tosi, F. A. Mohiyaddin, V. Schmitt, S. Tenberg, R. Rahman, G. Klimeck, A. Morello, Silicon quantum processor with robust long-distance qubit couplings, Nature Communications 8 (1) (2017) 450. `doi:10.1038/s41467-017-00378-x`. URL `https://doi.org/10.1038/s41467-017-00378-x`

[75] L. M. K. Vandersypen, H. Bluhm, J. S. Clarke, A. S. Dzurak, R. Ishihara, A. Morello, D. J. Reilly, L. R. Schreiber, M. Veldhorst, Interfacing spin qubits in quantum dots and donors–hot, dense, and coherent, npj Quantum Information

3 (1) (2017) 34. `doi:10.1038/s41534-017-0038-y`.
URL `https://doi.org/10.1038/s41534-017-0038-y`

[76] E. Kawakami, P. Scarlino, D. R. Ward, F. R. Braakman, D. E. Savage, M. G. Lagally, M. Friesen, S. N. Coppersmith, M. A. Eriksson, L. M. K. Vandersypen, Electrical control of a long-lived spin qubit in a Si/SiGe quantum dot, Nat. Nanotech. 9 (9) (2014) 666–670.

[77] S. Goswami, K. A. Slinker, M. Friesen, L. M. McGuire, J. L. Truitt, C. Tahan, L. J. Klein, J. O. Chu, P. M. Mooney, D. W. van der Weide, R. Joynt, S. N. Coppersmith, M. A. Eriksson, Controllable valley splitting in silicon quantum devices, Nature Physics 3 (1) (2007) 41. `doi:http://dx.doi.org/10.1038/nphys475`.
URL `http://www.nature.com/nphys/journal/v3/n1/suppinfo/nphys475_S1.html`

[78] M. Veldhorst, J. C. C. Hwang, C. H. Yang, A. W. Leenstra, B. de Ronde, J. P. Dehollain, J. T. Muhonen, F. E. Hudson, K. M. Itoh, A. Morello, A. S. Dzurak, An addressable quantum dot qubit with fault-tolerant control-fidelity., Nature Nanotechnology 9 (12) (2014) 981. `doi:10.1038/nnano.2014.216`.
URL `http://www.ncbi.nlm.nih.gov/pubmed/25305743`

[79] D. M. Zajac, A. J. Sigillito, M. Russ, F. Borjans, J. M. Taylor, G. Burkard, J. R. Petta, Resonantly driven cnot gate for electron spins, Science 359 (6374) (2018) 439–442. `doi:10.1126/science.aao5965`.

[80] K. Takeda, J. Kamioka, T. Otsuka, J. Yoneda, T. Nakajima, M. R. Delbecq, S. Amaha, G. Allison, T. Kodera, S. Oda, S. Tarucha, A fault-tolerant addressable spin qubit in a natural silicon quantum dot, Science Advances 2 (2016) e1600694. `doi:10.1126/sciadv.1600694`.

[81] C. Jones, M. A. Fogarty, A. Morello, M. F. Gyure, A. S. Dzurak, T. D. Ladd, Logical qubit in a linear array of semiconductor quantum dots, Physical Review X 8 (2) (2018) 021058.

[82] B. M. Maune, M. G. Borselli, B. Huang, T. D. Ladd, P. W. Deelman, K. S. Holabird, A. A. Kiselev, I. Alvarado-Rodriguez, R. S. Ross, A. E. Schmitz, et al., Coherent singlet-triplet oscillations in a silicon-based double quantum dot, Nature 481 (7381) (2012) 344.

[83] Z. Shi, C. Simmons, J. Prance, J. K. Gamble, T. S. Koh, Y.-P. Shim, X. Hu, D. Savage, M. Lagally, M. Eriksson, et al., Fast hybrid silicon double-quantum-dot qubit, Physical review letters 108 (14) (2012) 140503.

[84] B. Thorgrimsson, D. Kim, Y.-C. Yang, L. W. Smith, C. B. Simmons, D. R. Ward, R. H. Foote, J. Corrigan, D. E. Savage, M. G. Lagally, M. Friesen, S. N. Coppersmith, M. A. Eriksson, Extending the coherence of a quantum dot hybrid qubit, npj Quantum Information 3 (1) (2017) 32. doi:https://doi.org/10.1038/s41534-017-0034-2.

[85] M. Veldhorst, C. H. Yang, J. C. C. Hwang, W. Huang, J. P. Dehollain, J. T. Muhonen, S. Simmons, A. Laucht, F. E. Hudson, K. M. Itoh, A. Morello, A. S. Dzurak, A two-qubit logic gate in silicon, Nature 526 (2015) 410–414. doi:10.1038/nature15263.

[86] T. F. Watson, S. G. J. Philips, E. Kawakami, D. R. Ward, P. Scarlino, M. Veldhorst, D. E. Savage, M. G. Lagally, M. Friesen, S. N. Coppersmith, M. A. Eriksson, L. M. K. Vandersypen, A programmable two-qubit quantum processor in silicon, Nature 555 (2018) 633–637. doi:10.1038/nature25766.

[87] L. Bourdet, J. Li, J. Pelloux-Prayer, F. Triozon, M. Cassé, S. Barraud, S. Martinie, D. Rideau, Y.-M. Niquet, Contact resistances in trigate and finfet devices in a non-equilibrium green's functions approach, Journal of Applied Physics 119 (8) (2016) 084503. doi:10.1063/1.4942217.
URL http://dx.doi.org/10.1063/1.4942217

[88] L. Bourdet, J. Li, J. Pelloux-Prayer, F. Triozon, M. Cassé, S. Barraud, S. Martinie, D. Rideau, Y.-M. Niquet, High and low-field contact resistances in trigate devices in a non-equilibrium green's functions framework, in: Simulation of Semiconductor Processes and Devices (SISPAD), 2016 International Conference on, IEEE, 2016, pp. 291–294.

[89] Z. Zeng, F. Triozon, S. Barraud, Y.-M. Niquet, A simple interpolation model for the carrier mobility in trigate and gate-all-around silicon nwfets, IEEE Transactions on Electron Devices 64 (6) (2017) 2485–2491.

[90] M. Hofheinz, X. Jehl, M. Sanquer, G. Molas, M. Vinet, S. Deleonibus, Simple and controlled single electron transistor based on doping modulation in silicon nanowires, Applied Physics Letters 89 (14) (2006) 143504. doi:10.1063/1.2358812.
URL http://scitation.aip.org/content/aip/journal/apl/89/14/10.1063/1.2358812

[91] D. Kotekar-Patil, A. Corna, R. Maurand, A. Crippa, A. Orlov, S. Barraud, L. Hutin, M. Vinet, X. Jehl, S. De Franceschi, M. Sanquer, Pauli spin blockade in cmos double quantum dot devices, Phys. S. Sol. (b) 254 (3).

[92] H. Bohuslavskyi, D. Kotekar-Patil, R. Maurand, A. Corna, S. Barraud, L. Bourdet, L. Hutin, Y.-M. Niquet, X. Jehl, S. De Franceschi, M. Sanquer, Pauli blockade in a few-hole pmos double quantum dot limited by spin-orbit interaction, Appl. Phys. Lett. 109 (19) (2016) 193101.

[93] R. Maurand, X. Jehl, D. Kotekar-Patil, A. Corna, H. Bohuslavskyi, R. Laviéville, L. Hutin, S. Barraud, M. Vinet, M. Sanquer, S. De Franceschi, A cmos silicon spin qubit, Nature Comm. 7 (2016) 13575.

[94] A. C. Betz, R. Wacquez, M. Vinet, X. Jehl, A. L. Saraiva, M. Sanquer, A. J. Ferguson, M. F. Gonzalez-Zalba, Dispersively detected pauli spin-blockade in a silicon nanowire field-effect transistor, Nano letters 15 (7) (2015) 4622–4627. `doi:10.1021/acs.nanolett.5b01306`.

[95] M. F. Gonzalez-Zalba, S. Barraud, A. J. Ferguson, A. C. Betz, Probing the limits of gate-based charge sensing, Nature Communications 6 (2015) 6084. `doi:10.1038/ncomms7084`.

[96] A. Crippa, R. Maurand, D. Kotekar-Patil, A. Corna, H. Bohuslavskyi, A. O. Orlov, P. Fay, R. Laviéville, S. Barraud, M. Vinet, et al., Level spectrum and charge relaxation in a silicon double quantum dot probed by dual-gate reflectometry, Nano letters 17 (2) (2017) 1001–1006.

[97] B. Roche, E. Dupont-Ferrier, B. Voisin, M. Cobian, X. Jehl, R. Wacquez, M. Vinet, Y. M. Niquet, M. Sanquer, Detection of a large valley-orbit splitting in silicon with two-donor spectroscopy 108 (2012) 206812–. `doi:10.1103/PhysRevLett.108.206812`.

[98] S. De Franceschi, L. Hutin, R. Maurand, L. Bourdet, H. Bohuslavskyi, A. Corna, D. Kotekar-Patil, S. Barraud, X. Jehl, Y.-M. Niquet, et al., Soi technology for quantum information processing, in: Electron Devices Meeting (IEDM), 2016 IEEE International, IEEE, 2016, pp. 13–4.

[99] H. Watzinger, J. Kukučka, L. Vukušić, F. Gao, T. Wang, F. Schäffler, J.-J. Zhang, G. Katsaros, Hole spin resonance in ge double quantum dots, arXiv preprint arXiv:1802.00395.

[100] A. Crippa, R. Maurand, L. Bourdet, D. Kotekar-Patil, A. Amisse, X. Jehl, M. Sanquer, R. Laviéville, H. Bohuslavskyi, L. Hutin, S. Barraud, M. Vinet, Y.-M. Niquet, S. De Franceschi, Electrical spin driving by g-matrix modulation in spin-orbit qubits, Phys. Rev. Lett. 120 (2018) 137702. `doi:10.1103/PhysRevLett.120.137702`. URL `https://link.aps.org/doi/10.1103/PhysRevLett.120.137702`

[101] R. Barrett, M. W. Berry, T. F. Chan, J. Demmel, J. Donato, J. Dongarra, V. Ei-
jkhout, R. Pozo, C. Romine, H. Van der Vorst, Templates for the solution of linear
systems: building blocks for iterative methods, Vol. 43, Siam, 1994.

[102] S. M. Goodnick, D. K. Ferry, C. W. Wilmsen, Z. Liliental, D. Fathy, O. L. Krivanek,
Surface roughness at the si(100)-sio$_2$ interface, Physical Review B 32 (1985) 8171.
`doi:10.1103/PhysRevB.32.8171`.
URL `https://link.aps.org/doi/10.1103/PhysRevB.32.8171`

[103] Y.-M. Niquet, V.-H. Nguyen, F. Triozon, I. Duchemin, O. Nier, D. Rideau, Quan-
tum calculations of the carrier mobility: Methodology, matthiessen's rule, and com-
parison with semi-classical approaches, Journal of Applied Physics 115 (5) (2014)
054512.

[104] M. Casse, L. Thevenod, B. Guillaumot, L. Tosti, F. Martin, J. Mitard, O. Weber,
F. Andrieu, T. Ernst, G. Reimbold, T. Billon, M. Mouis, F. Boulanger, Carrier
transport in hfo2/metal gate mosfets: physical insight into critical parameters, IEEE
Transactions on Electron Devices 53 (4) (2006) 759–768. `doi:10.1109/TED.2006.`
`870888`.

[105] J. C. Slater, G. F. Koster, Simplified lcao method for the periodic potential problem,
Physical Review 94 (6) (1954) 1498.

[106] J. M. Luttinger, W. Kohn, Motion of electrons and holes in perturbed periodic
fields, Physical Review 97 (4) (1955) 869.

[107] A. Di Carlo, Microscopic theory of nanostructured semiconductor devices: beyond
the envelope-function approximation, Semiconductor Science and Technology 18 (1)
(2003) R1.
URL `http://stacks.iop.org/0268-1242/18/i=1/a=201`

[108] C. Delerue, M. Lannoo, Nanostructures: Theory and Modelling, Springer, New-
York, 2004.

[109] Y. M. Niquet, D. Rideau, C. Tavernier, H. Jaouen, X. Blase, Onsite matrix ele-
ments of the tight-binding Hamiltonian of a strained crystal: Application to sil-
icon, germanium, and their alloys, Physical Review B 79 (2009) 245201. `doi:`
`10.1103/PhysRevB.79.245201`.
URL `https://link.aps.org/doi/10.1103/PhysRevB.79.245201`

[110] M. Graf, P. Vogl, Electromagnetic fields and dielectric response in empirical tight-
binding theory, Physical Review B 51 (8) (1995) 4940.

[111] S. Kim, M. Luisier, A. Paul, T. B. Boykin, G. Klimeck, Full Three-Dimensional Quantum Transport Simulation of Atomistic Interface Roughness in Silicon Nanowire FETs, IEEE Transactions on Electron Devices 58 (5) (2011) 1371. `doi:10.1109/TED.2011.2118213`.

[112] G. Sleijpen, H. Van der Vorst, A jacobi–davidson iteration method for linear eigenvalue problems, SIAM Review 42 (2) (2000) 267. `doi:10.1137/S0036144599363084`.

[113] Z. Bai, J. Demmel, J. Dongarra, A. Ruhe, H. van der Vorst (Eds.), SIAM, Philadelphia, 2000. `doi:10.1137/1.9780898719581`.

[114] V. Sverdlov, E. Ungersboeck, H. Kosina, S. Selberherr, Effects of shear strain on the conduction band in silicon: An efficient two-band k.p theory, in: Solid State Device Research Conference, 2007. ESSDERC 2007. 37th European, IEEE, 2007, pp. 386–389.

[115] G. Dresselhaus, A. F. Kip, C. Kittel, Cyclotron resonance of electrons and holes in silicon and germanium crystals, Physical Review 98 (1955) 368. `doi:10.1103/PhysRev.98.368`.

[116] L. C. Lew Yan Voon, M. Willatzen, The k p Method, Springer, Berlin, 2009. `doi:10.1007/978-3-540-92872-0`.

[117] J. M. Luttinger, Quantum theory of cyclotron resonance in semiconductors: General theory, Physical Review 102 (1956) 1030. `doi:10.1103/PhysRev.102.1030`.

[118] A. Szabo, N. S. Ostlund, Modern quantum chemistry: introduction to advanced electronic structure theory, Courier Corporation, 2012.

[119] S. Roche, D. Mayou, Conductivity of Quasiperiodic Systems: A Numerical Study, Physical Review Letters 79 (1997) 2518. `doi:10.1103/PhysRevLett.79.2518`.

[120] M. Veldhorst, H. G. J. Eenink, C. H. Yang, A. S. Dzurak, Silicon cmos architecture for a spin-based quantum computer, Nature Communications 8 (1) (2017) 1766. `doi:10.1038/s41467-017-01905-6`.
URL `https://doi.org/10.1038/s41467-017-01905-6`

[121] J. Yoneda, T. Otsuka, T. Nakajima, T. Takakura, T. Obata, M. Pioro-Ladriére, H. Lu, C. Palmstrøm, A. Gossard, S. Tarucha, Fast electrical control of single electron spins in quantum dots with vanishing influence from nuclear spins, Phys. Rev. Lett. 113 (26) (2014) 267601.

[122] E. Kawakami, P. Scarlino, D. R. Ward, F. R. Braakman, D. E. Savage, M. G. Lagally, M. Friesen, S. N. Coppersmith, M. A. Eriksson, L. M. K. Vandersypen, Electrical control of a long-lived spin qubit in a Si/SiGe quantum dot., Nature Nanotechnology 9 (9) (2014) 666. `doi:10.1038/nnano.2014.153`. URL `http://www.ncbi.nlm.nih.gov/pubmed/25108810`

[123] A. Corna, Single spin control and readout in silicon coupled quantum dots, Theses, Université Grenoble Alpes (Jan. 2017). URL `https://tel.archives-ouvertes.fr/tel-01586070`

[124] S. Nadj-Perge, S. Frolov, E. Bakkers, L. P. Kouwenhoven, Spin-orbit qubit in a semiconductor nanowire, Nature 468 (7327) (2010) 1084–1087.

[125] W. G. van der Wiel, S. De Franceschi, J. M. Elzerman, T. Fujisawa, S. Tarucha, L. P. Kouwenhoven, Electron transport through double quantum dots, Rev. Mod. Phys. 75 (2002) 1–22. `doi:10.1103/RevModPhys.75.1`. URL `https://link.aps.org/doi/10.1103/RevModPhys.75.1`

[126] G. Feher, Electron Spin Resonance Experiments on Donors in Silicon. I. Electronic Structure of Donors by the Electron Nuclear Double Resonance Technique, Physical Review 114 (5) (1959) 1219. `doi:10.1103/PhysRev.114.1219`. URL `http://link.aps.org/doi/10.1103/PhysRev.114.1219`

[127] L. J. Sham, M. Nakayama, Effective-mass approximation in the presence of an interface, Physical Review B 20 (2) (1979) 734. `doi:10.1103/PhysRevB.20.734`.

[128] C. Tahan, R. Joynt, Relaxation of excited spin, orbital, and valley qubit states in ideal silicon quantum dots, Physical Review B 89 (2014) 075302. `doi:10.1103/PhysRevB.89.075302`.

[129] P. Huang, X. Hu, Spin relaxation in a Si quantum dot due to spin-valley mixing, Physical Review B 90 (2014) 235315. `doi:10.1103/PhysRevB.90.235315`.

[130] M. Veldhorst, R. Ruskov, C. H. Yang, J. C. C. Hwang, F. E. Hudson, M. E. Flatté, C. Tahan, K. M. Itoh, A. Morello, A. S. Dzurak, Spin-orbit coupling and operation of multivalley spin qubits, Physical Review B 92 (2015) 201401(R). `doi:10.1103/PhysRevB.92.201401`. URL `https://link.aps.org/doi/10.1103/PhysRevB.92.201401`

[131] W. Huang, M. Veldhorst, N. M. Zimmerman, A. S. Dzurak, D. Culcer, Electrically driven spin qubit based on valley mixing, Physical Review B 95 (2017) 075403. `doi:10.1103/PhysRevB.95.075403`. URL `https://link.aps.org/doi/10.1103/PhysRevB.95.075403`

[132] D. Culcer, X. Hu, S. Das Sarma, Interface roughness, valley-orbit coupling, and valley manipulation in quantum dots, Physical Review B 82 (2010) 205315. `doi:10.1103/PhysRevB.82.205315`.
URL `https://link.aps.org/doi/10.1103/PhysRevB.82.205315`

[133] J. K. Gamble, M. A. Eriksson, S. N. Coppersmith, M. Friesen, Disorder-induced valley-orbit hybrid states in si quantum dots, Physical Review B 88 (2013) 035310. `doi:10.1103/PhysRevB.88.035310`.
URL `https://link.aps.org/doi/10.1103/PhysRevB.88.035310`

[134] F. H. L. Koppens, C. Buizert, I. T. Vink, K. C. Nowack, T. Meunier, L. P. Kouwenhoven, L. M. K. Vandersypen, Detection of single electron spin resonance in a double quantum dot, Journal of Applied Physics 101 (2007) 081706. `doi:10.1063/1.2722734`.

[135] M. Schroer, K. Petersson, M. Jung, J. Petta, Field tuning the g factor in inas nanowire double quantum dots, Phys. Rev. Lett. 107 (17) (2011) 176811.

[136] R. M. Jock, N. T. Jacobson, P. Harvey-Collard, A. M. Mounce, V. Srinivasa, D. R. Ward, J. Anderson, R. Manginell, J. R. Wendt, M. Rudolph, et al., A silicon metal-oxide-semiconductor electron spin-orbit qubit, Nature communications 9 (1) (2018) 1768.

[137] M. Born, V. Fock, Beweis des adiabatensatzes, Zeitschrift für Physik 51 (3-4) (1928) 165–180.

[138] C. Zener, Non-adiabatic crossing of energy levels, Proceedings of the Royal Society of London A: Mathematical, Physical and Engineering Sciences 137 (833) (1932) 6962. `doi:10.1098/rspa.1932.0165`.

[139] L. D. Landau, Zur theorie der energieubertragung. ii, Phys. Z. Sowjetunion 2 (46) (1932) 1–13.

[140] A. A. Clerk, M. H. Devoret, S. M. Girvin, F. Marquardt, R. J. Schoelkopf, Introduction to quantum noise, measurement, and amplification, Review of Modern Physics 82 (2010) 1155. `doi:10.1103/RevModPhys.82.1155`.

[141] E. Paladino, Y. M. Galperin, G. Falci, B. L. Altshuler, $1/f$ noise: Implications for solid-state quantum information, Review of Modern Physics 86 (2014) 361. `doi:10.1103/RevModPhys.86.361`.

[142] K. K. Hung, P. K. Ko, C. Hu, Y. C. Cheng, Random telegraph noise of deep-submicrometer mosfets, IEEE electron device letters 11 (2) (1990) 90–92.

[143] C. Chang, S. S. Chung, Y. Hsieh, L. Cheng, C. Tsai, G. Ma, S. Chien, S. Sun, The observation of trapping and detrapping effects in high-k gate dielectric mosfets by a new gate current random telegraph noise (ig-rtn) approach, in: Electron Devices Meeting, 2008. IEDM 2008. IEEE International, IEEE, 2008, pp. 1–4.

[144] M. Hofheinz, X. Jehl, M. Sanquer, G. Molas, M. Vinet, S. Deleonibus, Individual charge traps in silicon nanowires, The European Physical Journal B - Condensed Matter and Complex Systems 54 (3) (2006) 299–307. `doi:10.1140/epjb/e2006-00452-x`.
URL `https://doi.org/10.1140/epjb/e2006-00452-x`

[145] Z. Li, M. Sotto, F. Liu, M. K. Husain, H. Yoshimoto, Y. Sasago, D. Hisamoto, I. Tomita, Y. Tsuchiya, S. Saito, Random telegraph noise from resonant tunnelling at low temperatures, Scientific reports 8 (1) (2018) 250.

[146] E. Dornel, T. Ernst, J. C. Barbé, J. M. Hartmann, V. Delaye, F. Aussenac, C. Vizioz, S. Borel, V. Maffini-Alvaro, C. Isheden, J. Foucher, Hydrogen annealing of arrays of planar and vertically stacked Si nanowires, Applied Physics Letters 91 (23) (2007) 233502. `doi:10.1063/1.2818678`.

[147] N. M. Zimmerman, P. Huang, D. Culcer, Valley phase and voltage control of coherent manipulation in si quantum dots, Nano Letters 17 (7) (2017) 4461–4465, pMID: 28657758. `arXiv:https://doi.org/10.1021/acs.nanolett.7b01677`, `doi:10.1021/acs.nanolett.7b01677`.
URL `https://doi.org/10.1021/acs.nanolett.7b01677`

[148] V. Volkov, T. Pinsker, Boundary conditions, energy spectrum, and optical transitions of electrons in bounded narrow gap crystals, Surface Science 81 (1) (1979) 181 – 192. `doi:https://doi.org/10.1016/0039-6028(79)90512-0`.
URL `http://www.sciencedirect.com/science/article/pii/0039602879905120`

[149] R. Rahman, J. Verduijn, N. Kharche, G. P. Lansbergen, G. Klimeck, L. C. L. Hollenberg, S. Rogge, Engineered valley-orbit splittings in quantum-confined nanostructures in silicon, Phys. Rev. B 83 (2011) 195323. `doi:10.1103/PhysRevB.83.195323`.
URL `https://link.aps.org/doi/10.1103/PhysRevB.83.195323`

[150] S. Barraud, O. Bonno, M. Cassé, The influence of coulomb centers located in hfo 2/sio 2 gate stacks on the effective electron mobility, Journal of Applied Physics 104 (7) (2008) 073725.

[151] Z. Zeng, F. Triozon, Y.-M. Niquet, Carrier scattering in high-κ/metal gate stacks, Journal of Applied Physics 121 (11) (2017) 114503.

[152] B. Voisin, R. Maurand, S. Barraud, M. Vinet, X. Jehl, M. Sanquer, J. Renard, S. De Franceschi, Electrical control of g-factors in a few-hole silicon nanowire mosfet, Nano Lett. 16 (7) (2016) 88–92.

[153] E. I. Rashba, Theory of electric dipole spin resonance in quantum dots: Mean field theory with gaussian fluctuations and beyond, Phys. Rev. B 78 (19) (2008) 195302.

[154] S. Nadj-Perge, V. Pribiag, J. Van den Berg, K. Zuo, S. Plissard, E. Bakkers, S. Frolov, L. Kouwenhoven, Spectroscopy of spin-orbit quantum bits in indium antimonide nanowires, Phys. Rev. Lett. 108 (16) (2012) 166801.

[155] J. J. Pla, K. Y. Tan, J. P. Dehollain, W. H. Lim, J. J. Morton, D. N. Jamieson, A. S. Dzurak, A. Morello, A single-atom electron spin qubit in silicon, Nature 489 (7417) (2012) 541–545.

[156] Y. Tokura, W. G. van der Wiel, T. Obata, S. Tarucha, Coherent single electron spin control in a slanting zeeman field, Phys. Rev. Lett. 96 (4) (2006) 047202.

[157] Y. Kato, R. Myers, D. Driscoll, A. Gossard, J. Levy, D. Awschalom, Gigahertz electron spin manipulation using voltage-controlled g-tensor modulation, Science 299 (5610) (2003) 1201–1204.

[158] J. Pingenot, C. E. Pryor, M. E. Flatté, Electric-field manipulation of the landé g tensor of a hole in an in 0.5 ga 0.5 as/gaas self-assembled quantum dot, Phys. Rev. B 84 (19) (2011) 195403.

[159] N. Ares, G. Katsaros, V. Golovach, J. Zhang, A. Prager, L. Glazman, O. Schmidt, S. De Franceschi, Sige quantum dots for fast hole spin rabi oscillations, Appl. Phys. Lett. 103 (26) (2013) 263113.

[160] S. Debald, C. Emary, Spin-orbit-driven coherent oscillations in a few-electron quantum dot, Phys. Rev. Lett. 94 (22) (2005) 226803.

[161] V. N. Golovach, M. Borhani, D. Loss, Electric-dipole-induced spin resonance in quantum dots, Physical Review B 74 (2006) 165319. `doi:10.1103/PhysRevB.74.165319`.
URL `https://link.aps.org/doi/10.1103/PhysRevB.74.165319`

[162] E. Rashba, V. Sheka, Electric-dipole spin resonances, in: Modern Problems in Condensed Matter Sciences, Vol. 27, Elsevier, 1991, pp. 131–206.

[163] E. I. Rashba, Theory of electric dipole spin resonance in quantum dots: Mean field theory with gaussian fluctuations and beyond, Physical Review B 78 (2008) 195302. doi:10.1103/PhysRevB.78.195302.
URL https://link.aps.org/doi/10.1103/PhysRevB.78.195302

[164] J. Van den Berg, S. Nadj-Perge, V. Pribiag, S. Plissard, E. Bakkers, S. Frolov, L. Kouwenhoven, Fast spin-orbit qubit in an indium antimonide nanowire, Phys. Rev. Lett. 110 (6) (2013) 066806.

[165] R. Li, F. E. Hudson, A. S. Dzurak, A. R. Hamilton, Pauli spin blockade of heavy holes in a silicon double quantum dot, Nano Lett. 15 (2015) 7314–7318.

[166] R. Winkler, S. Papadakis, E. De Poortere, M. Shayegan, Spin-Orbit Coupling in Two-Dimensional Electron and Hole Systems, Vol. 41, Springer, 2003.

[167] L. Chibotaru, A. Ceulemans, H. Bolvin, Unique definition of the zeeman-splitting g tensor of a kramers doublet, Phys. Rev. Lett. 101 (3) (2008) 033003.

[168] J. A. Weil, J. R. Bolton, Electron paramagnetic resonance: elementary theory and practical applications, John Wiley & Sons, 2007.

[169] Let R be an unitary transform in the $\{|\Uparrow\rangle, |\Downarrow\rangle\}$ subspace. R can be cast in the form

$$R = \begin{pmatrix} \alpha e^{i\theta} & -\beta^* \\ \beta e^{i\theta} & \alpha^* \end{pmatrix} \qquad (7.1)$$

with $|\alpha|^2 + |\beta|^2 = 1$. In the basis set $\{|\Uparrow\rangle', |\Downarrow\rangle'\} = R\{|\Uparrow\rangle, |\Downarrow\rangle\}$, the Hamiltonian reads $H' = \mu_B{}^t\sigma' \cdot \hat{g} \cdot \mathbf{B}/2$, with $\sigma_i' = R^\dagger \sigma_i R$. Yet $\sigma' = \hat{U} \cdot \sigma$, with:

$$\hat{U} = \begin{pmatrix} \mathrm{Re}[(\alpha^2 - \beta^2)e^{i\theta}] & \mathrm{Im}[(\alpha^2 - \beta^2)e^{i\theta}] & 2\mathrm{Re}(\alpha^*\beta) \\ -\mathrm{Im}[(\alpha^2 + \beta^2)e^{i\theta}] & \mathrm{Re}[(\alpha^2 + \beta^2)e^{i\theta}] & 2\mathrm{Im}(\alpha^*\beta) \\ -2\mathrm{Re}(\alpha\beta e^{i\theta}) & -2\mathrm{Im}(\alpha\beta e^{i\theta}) & |\alpha|^2 - |\beta|^2 \end{pmatrix}. \qquad (7.2)$$

Hence $H' = \mu_B{}^t\sigma \cdot \hat{g}' \cdot \mathbf{B}/2$, with $\hat{g}' = {}^t\hat{U} \cdot \hat{g}$. The $\hat{U}$ matrix is unitary with determinant $+1$. Therefore, any rotation of the $\{|\Uparrow\rangle, |\Downarrow\rangle\}$ basis set results in a corresponding rotation of the g-matrix. Conversely, any unitary 3×3 matrix $\hat{U}$ with determinant $+1$ can be mapped onto Eq. (7.2), and associated with a unitary transform R in the $\{|\Uparrow\rangle, |\Downarrow\rangle\}$ subspace.

[170] We use the following property: for two vectors $\mathbf{a}, \mathbf{b}$ and a unitary matrix $\hat{U}$, $\hat{U}\mathbf{a} \times \hat{U}\mathbf{b} = \det(\hat{U}){}^t\hat{U}^{-1}(\mathbf{a} \times \mathbf{b})$. Then under the transformation $\hat{g} \to {}^t\hat{U}\hat{g}$ and $\hat{g}' \to {}^t\hat{U}\hat{g}'$,

the Rabi frequency reads:

$$|\tilde{\mathbf{f}}_{\mathbf{R}}| = \frac{\mu_B B V_{ac}}{2h|g^*|} \left| [^t\hat{U}\hat{g}(V_0) \cdot \mathbf{b}] \times [^t\hat{U}\hat{g}'(V_0) \cdot \mathbf{b}] \right| \tag{7.3a}$$

$$= \frac{\mu_B B V_{ac}}{2h|g^*|} |\det(\hat{U})| \left| {}^t R[\hat{g}(V_0) \cdot \mathbf{b}] \times [\hat{g}'(V_0) \cdot \mathbf{b}] \right| \tag{7.3b}$$

$$= |\mathbf{f}_{\mathbf{R}}| \tag{7.3c}$$

because the unitary transformations preserve the norm and $|\det(\hat{U})| = 1$.

[171] G. L. Bir, G. E. Pikus, Symmetry and strain-induced effects in semiconductors.

[172] C. Y. Kang, R. Choi, M. Hussain, J. Wang, Y. J. Suh, H. Floresca, M. J. Kim, J. Kim, B. H. Lee, R. Jammy, Effects of metal gate-induced strain on the performance of metal-oxide-semiconductor field effect transistors with titanium nitride gate electrode and hafnium oxide dielectric, Applied Physics Letters 91 (3) (2007) 033511.

[173] R. Coquand, M. Casse, S. Barraud, D. Cooper, V. Maffini-Alvaro, M.-P. Samson, S. Monfray, F. Boeuf, G. Ghibaudo, O. Faynot, et al., Strain-induced performance enhancement of trigate and omega-gate nanowire fets scaled down to 10-nm width, IEEE Transactions on Electron Devices 60 (2) (2013) 727–732.

[174] M. L. Lee, E. A. Fitzgerald, M. T. Bulsara, M. T. Currie, A. Lochtefeld, Strained si, sige, and ge channels for high-mobility metal-oxide-semiconductor field-effect transistors, Journal of Applied Physics 97 (2005) 011101. `doi:10.1063/1.1819976`.

[175] Y. Sun, S. E. Thompson, T. Nishida, Physics of strain effects in semiconductors and metal-oxide-semiconductor field-effect transistors, Journal of Applied Physics 101 (2007) 104503. `doi:10.1063/1.2730561`.

[176] B. Venitucci, L. Bourdet, D. Pouzada, Y.-M. Niquet, Modeling of spin qubits manipulation in the g-matrix formalism: Application to a hole qubit on silicon-on-insulator, arXiv preprint arXiv:1807.09185.

[177] R. Hanson, J. R. Petta, S. Tarucha, L. M. K. Vandersypen, Spins in few-electron quantum dots, Reviews of Modern Physics 79 (4) (2007) 1217. `doi:10.1103/RevModPhys.79.1217`.
URL `http://link.aps.org/doi/10.1103/RevModPhys.79.1217`

[178] F. H. L. Koppens, J. A. Folk, J. M. Elzerman, R. Hanson, L. H. W. van Beveren, I. T. Vink, H. P. Tranitz, W. Wegscheider, L. P. Kouwenhoven, L. M. K. Vandersypen, Control and Detection of Singlet-Triplet Mixing in a Random Nuclear Field, Science

309 (5739) (2005) 1346. `doi:10.1126/science.1113719`.
URL `http://science.sciencemag.org/content/309/5739/1346`

[179] S. Nadj-Perge, S. M. Frolov, J. W. W. van Tilburg, J. Danon, Y. V. Nazarov, R. Algra, E. P. A. M. Bakkers, L. P. Kouwenhoven, Disentangling the effects of spin-orbit and hyperfine interactions on spin blockade, Physical Review B 81 (2010) 201305(R). `doi:10.1103/PhysRevB.81.201305`.
URL `https://link.aps.org/doi/10.1103/PhysRevB.81.201305`

[180] V. N. Golovach, M. Borhani, D. Loss, Holonomic quantum computation with electron spins in quantum dots, Phys. Rev. A 81 (2010) 022315. `doi:10.1103/PhysRevA.81.022315`.

Appendix A

H_{Bloch} matrices

As discussed in chapter III, the effect of the magnetic field on the Bloch functions and the spin is described buy the following Hamiltonian:

$$H_{\text{Bloch}} = -(3\kappa + 1)\mu_B \mathbf{B.L} + g_0\mu_B \mathbf{B.S} = \mu_B \mathbf{B.K} \tag{A.1}$$

For completeness, we give below the expression of the matrices K_x, K_y, K_z consistent with our choice of phases for the Bloch functions [1]:

$$K_x = - \begin{pmatrix} 0 & \sqrt{3}\kappa & 0 & 0 & -\sqrt{\frac{3}{2}}\kappa' & 0 \\ \sqrt{3}\kappa & 0 & 2\kappa & 0 & 0 & -\frac{\kappa'}{\sqrt{2}} \\ 0 & 2\kappa & 0 & \sqrt{3}\kappa & \frac{\kappa'}{\sqrt{2}} & 0 \\ 0 & 0 & \sqrt{3}\kappa & 0 & 0 & \sqrt{\frac{3}{2}}\kappa' \\ -\sqrt{\frac{3}{2}}\kappa' & 0 & \frac{\kappa'}{\sqrt{2}} & 0 & 0 & \kappa'' \\ 0 & -\frac{\kappa'}{\sqrt{2}} & 0 & \sqrt{\frac{3}{2}}\kappa' & \kappa'' & 0 \end{pmatrix} \tag{A.2a}$$

$$K_y = i \begin{pmatrix} 0 & \sqrt{3}\kappa & 0 & 0 & -\sqrt{\frac{3}{2}}\kappa' & 0 \\ -\sqrt{3}\kappa & 0 & 2\kappa & 0 & 0 & -\frac{\kappa'}{\sqrt{2}} \\ 0 & -2\kappa & 0 & \sqrt{3}\kappa & -\frac{\kappa'}{\sqrt{2}} & 0 \\ 0 & 0 & -\sqrt{3}\kappa & 0 & 0 & -\sqrt{\frac{3}{2}}\kappa' \\ \sqrt{\frac{3}{2}}\kappa' & 0 & \frac{\kappa'}{\sqrt{2}} & 0 & 0 & \kappa'' \\ 0 & \frac{\kappa'}{\sqrt{2}} & 0 & \sqrt{\frac{3}{2}}\kappa' & -\kappa'' & 0 \end{pmatrix} \tag{A.2b}$$

$$K_z = - \begin{pmatrix} 3\kappa & 0 & 0 & 0 & 0 & 0 \\ 0 & \kappa & 0 & 0 & \sqrt{2}\kappa' & 0 \\ 0 & 0 & -\kappa & 0 & 0 & \sqrt{2}\kappa' \\ 0 & 0 & 0 & -3\kappa & 0 & 0 \\ 0 & \sqrt{2}\kappa' & 0 & 0 & \kappa'' & 0 \\ 0 & 0 & \sqrt{2}\kappa' & 0 & 0 & -\kappa'' \end{pmatrix}, \tag{A.2c}$$

---

[1] We assume $g_0 = 2$ in Eq. (A.1).

with $\kappa' = 1 + \kappa$ and $\kappa'' = 1 + 2\kappa$.

Appendix B

Pauli blockade in a spin-valley system

In chapter IV, we have discussed the nature of the A, B, C and V line in a one-particle picture. In this appendix, we introduce a two-particle picture for the blockade, which accounts for the valley degree of freedom and gives a better description of the V line.

Spin blockade can arise when the current flows through the sequence of charge configurations $(n_1, n_2) \equiv (2n + 1, 2m + 1) \to (2n, 2m + 2) \to (2n, 2m + 1) \to (2n + 1, 2m + 1)...,$ where n_1 and n_2 are the number of electrons in dots 1 and 2. [30, 177] Indeed, the $(2n + 1, 2m + 1)$ states can be mapped onto singlet $S(1, 1)$ and triplet $T(1, 1)$ states, while the $(2n, 2m+2)$ states can be mapped onto singlet $S(0, 2)$ and triplet $T(0, 2)$ states. While the $S(1, 1)$ and $T(1, 1)$ states are almost degenerate, the $S(0, 2)$ and $T(0, 2)$ states can be significantly split because the $T(0, 2)$ state must involve some orbital excitation. The $(2n + 1)^{\text{th}}$ electron may enter in dot 1 through any of the $(1, 1)$ configurations at high enough source-drain bias. Once in a $T(1, 1)$ state, the system may, however, get trapped for a long time if the $T(0, 2)$ states are still out of the bias window, because tunneling from $T(1, 1)$ to $S(0, 2)$ requires a spin flip. The current is hence suppressed. At reverse source-drain bias, the current flows through the sequence of charge configurations $(2n + 1, 2m + 1) \to (2n, 2m + 1) \to (2n + 1, 2m) \to (2n + 1, 2m + 1)...,$ which can not be spin-blocked, giving rise to current rectification.

The observation of inter-valleys resonances suggests that m is even (otherwise only transitions between v_2 states would be observed in dot 2). We assume from now on that n is also even. As a matter of fact, the absence of *visible* bias triangles for lower gate voltages suggests $m = n = 0$.

We discuss below the role of valley blockade in the present experiments. We assume the valley splitting is much larger in dot 1 (Δ_1) than in dot 2 ($\Delta_2 = 36 \, \mu\text{eV}$) due to disorder and bias conditions. The valley splitting in dot 1 is actually beyond the bandwidth of the EDSR setup. This reflects the stochastic variations from one dot to an other, as confirmed by tight-binding simulations.
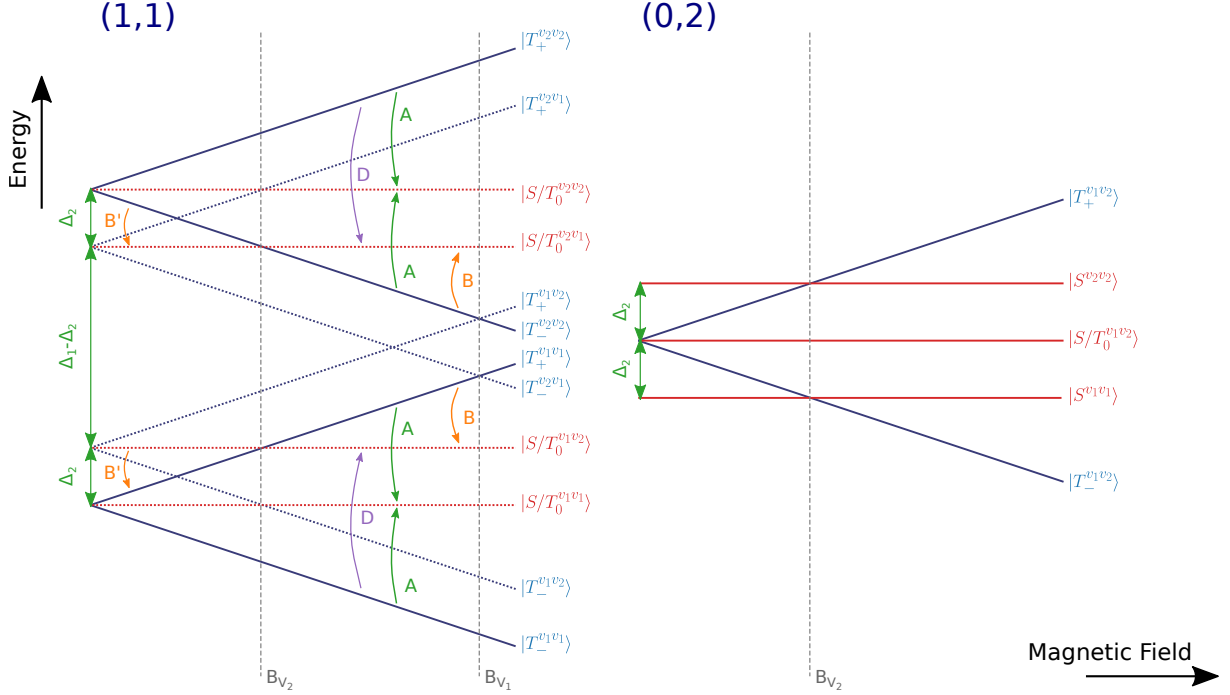
Figure B.1: Scheme of the energy levels for a system with two dots, filled with two electrons in the $(1,1)$ and $(0,2)$ charge configurations, as a function of magnetic field. We assume different valley splittings in the two dots (respectively $\Delta_1 > \Delta_2$). Triplets in the $(0,2)$ configurations with two electrons in the same valley are not represented, since they are energetically far away.

In the $(1,1)$ charge configuration, the low-energy states can be characterized by their spin component [singlet (S) or triplet (T_0, T_-, T_+)] and by the valley occupied in each dot (v_1 or v_2). Sixteen states can be constructed in this way (see Fig. B.1). We neglect in a first approximation the small exchange splitting between singlet and triplet states with same valley indices. The magnetic field $\mathbf{B} = B\mathbf{b}$ splits the T_- (total spin $\langle S_\mathbf{b} \rangle = -1$) and T_+ states ($\langle S_\mathbf{b} \rangle = +1$) from the S and T_0 states ($\langle S_\mathbf{b} \rangle = 0$). The splitting between T_+ and T_- is $E_z = 2g\mu_B B$.

Similar states can be constructed in the $(0,2)$ charge configuration. The $S^{v_1 v_1}(0,2)$ and $S^{v_1 v_1}(1,1)$ are detuned by the bias on gates 1 and 2. We focus on detunings smaller than the orbital singlet-triplet splitting $\Delta_{\mathrm{ST}} = 1.9$ meV, so that neither the $v_1 v_1$ nor the $v_2 v_2$ triplets can be reached from the $(1,1)$ states.

Given the small $\Delta_2 = 36\,\mu\mathrm{eV}$ extracted from spin resonance, we need, however, to reconsider the mechanisms for current rectification. Indeed, the system must be spin-and-valley blocked [54] since the detuning is typically much larger than Δ_2 so that $T^{v_1 v_2}(0,2)$ states are accessible in the bias window. Assuming that both spin and valley are conserved during tunneling, the spin and valley blocked $(1,1)$ states are actually $T_-^{v_1 v_1}$, $T_+^{v_1 v_1}$, $T_-^{v_2 v_2}$ and $T_+^{v_2 v_2}$. Although $T_0^{v_1 v_1}$ and $T_0^{v_2 v_2}$ are, in principle, also spin and valley blocked, they may be mixed with the nearly degenerate $S^{v_1 v_1}$ and $S^{v_2 v_2}$ states by, e.g., spin-orbit coupling and nuclear spin disorder, [178, 179] and be therefore practically unblocked.

We can now refine the interpretation of the different lines. Each one corresponds to a different set of transitions between blocked and unblocked $(1, 1)$ states. Line A corresponds to transitions between $T_\pm^{v_1 v_1}$ and $T_0^{v_1 v_1}/S^{v_1 v_1}$ states, and to transitions between $T_\pm^{v_2 v_2}$ and $T_0^{v_2 v_2}/S^{v_2 v_2}$ states. Line B corresponds to transitions between $T_+^{v_1 v_1}$ and $T_0^{v_1 v_2}/S^{v_1 v_2}$ states, and between $T_-^{v_2 v_2}$ and $T_0^{v_2 v_1}/S^{v_2 v_1}$ states. The line D on Fig. 3 of the main text would correspond to transitions between $T_-^{v_1 v_1}$ and $T_0^{v_1 v_2}/S^{v_1 v_2}$ states, and between $T_+^{v_2 v_2}$ and $T_0^{v_2 v_1}/S^{v_2 v_1}$ states. These transitions give rise to the same spectrum as in the one-particle picture.

Line V is independent on the microwave frequency and also appears when no microwaves are applied. At the magnetic field $B_V \simeq \Delta_2/(g\mu_B)$, the states $T_+^{v_1 v_1}$ and $T_0^{v_1 v_2}/S^{v_1 v_2}$, as well as the states $T_-^{v_2 v_2}$ and $T_0^{v_2 v_1}/S^{v_2 v_1}$ are almost degenerate. The mixing of these near degenerate blocked and unblocked states by SOC lifts spin and valley blockade of the $T_+^{v_1 v_1}$ and $T_-^{v_2 v_2}$ states, giving rise to an excess of current at $B \simeq B_V$ independent on the microwave excitation.

Appendix C

g-matrix formulation of the GBL mechanism

Any mechanism giving rise to Rabi oscillations with frequency proportional to B and V_{ac} shall be captured by Eq. 6.13. This excludes spin rotations at zero-field [180] or showing significant non-linearities [53].

As an example, we can cast the spin-orbit mechanism of Ref. [161] (GBL mechanism) in the g-matrix formalism. We consider a quantum dot in the effective mass approximation, with strong confinement along $\boldsymbol{z}$, harmonic confinement $V(x,y) = m\omega_0^2(x^2 + y^2)/2$ in the (xy) plane, and in-plane Rashba plus Dresselhaus spin-orbit coupling [161]. We assume an isotropic g-factor g_0. An electric field $\mathbf{E} = E_0(e_x\mathbf{x} + e_y\mathbf{y})\sin(\omega t)$ is applied in the (xy) plane in order to drive Rabi oscillations between the $|\downarrow\rangle$ and $|\uparrow\rangle$ states ($e_x^2 + e_y^2 = 1$, the spin being quantized along $\boldsymbol{z}$). Then, according to Ref. [161],

$$hf_R = 2g_0\mu_B|\mathbf{B} \times \boldsymbol{\Omega}_{\mathrm{SO}}| \tag{C.1}$$

at resonance, where:

$$\boldsymbol{\Omega}_{\mathrm{SO}} = -\frac{eE_0}{m\omega_0^2}\left(\frac{e_y}{\lambda_-}, \frac{e_x}{\lambda_+}, 0\right) \tag{C.2}$$

wuth $\lambda_\pm = \hbar/[m(\beta \pm \alpha)]$, (α, β) being the Rashba and Dresselhaus spin-orbit constants. From the effective Hamiltonian of the quantum dot in the static limit ($\omega \to 0$) [161],

$$H_{\mathrm{eff}} = \frac{1}{2}g_0\mu_B\mathbf{B} \cdot \sigma + g_0\mu_B(\mathbf{B} \times \boldsymbol{\Omega}_{\mathrm{SO}}) \cdot \sigma\,, \tag{C.3}$$

the matrices $\hat{g}$ and $\hat{g}'$ can be readily identified (the derivative being taken with respect to

E_0 instead of V):

$$\hat{g} = g_0 \begin{pmatrix} 1 & 0 & 0 \\ 0 & 1 & 0 \\ 0 & 0 & 1 \end{pmatrix} \tag{C.4a}$$

$$\hat{g}' = 2g_0 \begin{pmatrix} 0 & 0 & -\Theta_{0,y} \\ 0 & 0 & +\Theta_{0,x} \\ +\Theta_{0,y} & -\Theta_{0,x} & 0 \end{pmatrix} \tag{C.4b}$$

with $\boldsymbol{\Theta}_0 = \boldsymbol{\Omega}_{\mathrm{SO}}/E_0$. Insertion of Eqs. (C.4) into Eqs. (6.13) yields back Eq. (6.19), showing that the present g-matrix formalism indeed captures the EDSR mechanism of Ref. [161].

Appendix D

Numerical calculation of g-matrix derivative

We detail here the calculation of $\hat{g}'$ the derivative of $\hat{g}$ with respect to V. As shown in chapter VI, the g-matrix $\hat{g}(V_0)$ can be obtained in the Kramers basis set $\{|0, \Uparrow\rangle, |0, \Downarrow\rangle\}$ (the states are written in the form $|n, \sigma\rangle$, where n is the orbital index). Doing so again at $V = V_0 \pm \delta V$ yields $\hat{g}(V_0 \pm \delta V)$ in some basis sets $\{|0_\pm, \Uparrow\rangle, |0_\pm, \Downarrow\rangle\}$. We cannot compute directly $\hat{g}'$ from the leapfrog scheme of Eq. 6.32, because $\{|0, \Uparrow\rangle, |0, \Downarrow\rangle\}$ may differ from $\{|0_\pm, \Uparrow\rangle, |0_\pm, \Downarrow\rangle\}$ by an arbitrary transform $U_\pm$.

In order to choose the appropriate basis $\{|0_\pm, \Uparrow'\rangle, |0_\pm, \Downarrow'\rangle\}$, we first notice that although $|0, \Uparrow\rangle$ and $|0, \Downarrow\rangle$ are degenerate eigenstates of $H(V_0, \mathbf{B})$ (with H from Eq. 6.28), they are not coupled by the electric field, so that non-degenerate perturbation theory applies for our purpose:

$$\frac{\partial}{\partial V}|0, \Uparrow\rangle = -e \sum_{n>0, \sigma} \frac{\langle n, \sigma | D_1 | 0, \Uparrow\rangle}{E_0 - E_n} |n, \sigma\rangle \tag{D.1a}$$

$$\frac{\partial}{\partial V}|0, \Downarrow\rangle = -e \sum_{n>0, \sigma} \frac{\langle n, \sigma | D_1 | 0, \Downarrow\rangle}{E_0 - E_n} |n, \sigma\rangle \tag{D.1b}$$

Eqs. D.1 actually suggest that the appropriate $\{|0_\pm, \Uparrow'\rangle, |0_\pm, \Downarrow'\rangle\}$ must fulfill:

$$\begin{pmatrix} \langle 0_\pm, \Uparrow' | 0, \Uparrow\rangle & \langle 0_\pm, \Uparrow' | 0, \Downarrow\rangle \\ \langle 0_\pm, \Downarrow' | 0, \Uparrow\rangle & \langle 0_\pm, \Downarrow' | 0, \Downarrow\rangle \end{pmatrix} = \alpha_\pm I, \tag{D.2}$$

where I is the identity matrix and $0 < \alpha_\pm \leq 1$. We therefore seek the unitary transformation $P_\pm \equiv R_\pm^\dagger$ in the $\{|0_\pm, \Uparrow\rangle, |0_\pm, \Downarrow\rangle\}$ subspace such that the states $|0_\pm, \sigma'\rangle = P_\pm|0_\pm, \sigma\rangle$ satisfy the above relations. Solving this problem for Kramers degenerate states uniquely defines $P_\pm$:

$$P_\pm = \beta_\pm \begin{pmatrix} \langle 0_\pm, \Uparrow | 0, \Uparrow\rangle & \langle 0_\pm, \Downarrow | 0, \Uparrow\rangle \\ \langle 0_\pm, \Uparrow | 0, \Downarrow\rangle & \langle 0_\pm, \Downarrow | 0, \Downarrow\rangle \end{pmatrix}, \tag{D.3}$$

where:

$$\beta_\pm^{-2} = |\langle 0_\pm, \Uparrow\, |0, \Uparrow\rangle|^2 + |\langle 0_\pm, \Downarrow\, |0, \Uparrow\rangle|^2 \tag{D.4a}$$

$$= |\langle 0_\pm, \Uparrow\, |0, \Downarrow\rangle|^2 + |\langle 0_\pm, \Downarrow\, |0, \Downarrow\rangle|^2 \ . \tag{D.4b}$$

Finite differences (Eq. 6.32) can then be safely calculated in the basis sets $\{|0_\pm, \Uparrow'\rangle, |0_\pm, \Downarrow'\rangle\}$:

$$|0_\pm, \Uparrow'\rangle = \beta_\pm \left(\langle 0_\pm, \Uparrow\, |0, \Uparrow\rangle|0_\pm, \Uparrow\rangle + \langle 0_\pm, \Downarrow\, |0, \Uparrow\rangle|0_\pm, \Downarrow\rangle \right) \tag{D.5a}$$

$$|0_\pm, \Downarrow'\rangle = \beta_\pm \left(\langle 0_\pm, \Uparrow\, |0, \Downarrow\rangle|0_\pm, \Uparrow\rangle + \langle 0_\pm, \Downarrow\, |0, \Downarrow\rangle|0_\pm, \Downarrow\rangle \right) \ . \tag{D.5b}$$

We practically use $\delta V = 1$ mV.

Résumé

Dans la course à l'ordinateur quantique, le silicium est devenu ces dernières années un matériau de choix pour limplémentation des qubits de spin. De tels dispositifs sont fabriqués au CEA en utilisant les technologies CMOS, afin de faciliter leur intégration à grande échelle. Cette thèse porte sur la modélisation de ces qubits, et en particulier sur la manipulation de l'état de spin par un champ électrique. Pour cela nous utilisons un ensemble de techniques numériques avancées pour calculer le potentiel et la structure électronique des qubits (notamment les méthodes de liaisons fortes et k.p), afin d'être le plus proche possible des dispositifs expérimentaux. Ces simulations nous ont permis d'étudier deux résultats expérimentaux d'importance : l'observation de la manipulation par champ électrique du spin d'un électron d'une part, et la caractérisation de l'anisotropie de la fréquence de Rabi d'un qubit de trou d'autre part. Le premier résultat était plutôt inattendu, étant donné le très faible couplage spin-orbite dans la bande de conduction du silicium. Nous développons un modèle, validé par les simulations et certains résultats expérimentaux, qui met en évidence le rôle essentiel du couplage spin-orbite inter-vallée, exacerbé par la faible symétrie du système. Nous utilisons ces résultats pour proposer et tester numériquement un schéma de manipulation électrique consistant à passer réversiblement d'un qubit de spin à un qubit de vallée. Concernant les qubits de trous, le couplage spin-orbite relativement élevé autorise la manipulation du spin par champ électrique, toutefois les mesures expérimentales d'anisotropie donnent à voir une physique complexe, insuffisamment bien décrite par les modèles actuels. Nous développons donc un formalisme permettant de caractériser simplement la fréquence de Rabi en fonction du champ magnétique, et qui peut s'appliquer à d'autre type de qubit spin-orbite. Les simulations permettent de reproduire les résultats expérimentaux, et de souligner le rôle important de la contrainte.

Abstract

In the race for quantum computing, these last years silicon has become a material of choice for the implementation of spin qubits. Such devices are fabricated in CEA using CMOS technologies, in order to facilitate their large-scale integration. This thesis covers the modeling of these qubits and in particular the manipulation of the spin state with an electric field. To that end, we use a set numerical tools to compute the potential and electronic structure in the qubits (in particular tight-binding and k.p methods), in order to be as close as possible to the experimental devices. These simulations allowed us to study two important experimental results: on one hand the observation of the electrical manipulation of an electron spin, and on the other hand the characterization of the anisotropy of the Rabi frequency of a hole spin qubit. The first one was rather unexpected, since the spin-orbit coupling is very low in the silicon conduction band. We develop a model, confirmed by the simulations and some experimental results, that highlights the essential role of the intervalley spin-orbit coupling, enhanced by the low symmetry of the system. We use these results to propose and test numerically a scheme for electrical manipulation which consists in switching reversibly between a spin qubit and a valley qubit. Concerning the hole qubits, the relatively large spin-orbit coupling allows for electrical spin manipulation. However the experimental measurements of Rabi frequency anisotropy show a complex physics, insufficiently described by the usual models. Therefore we develop a formalism which allows to characterize simply the Rabi frequency as a function of the magnetic field, and that can be applied to other types of spin-orbit qubits. The simulations reproduce the experimental features, underline the important role of strain.